

Understanding Sea-Level Change Using Global and Regional Models

Hermans, T.H.J.

DOI

[10.4233/uuid:ad44006f-b50d-49b9-bf64-ee5cb7a55980](https://doi.org/10.4233/uuid:ad44006f-b50d-49b9-bf64-ee5cb7a55980)

Publication date

2022

Document Version

Final published version

Citation (APA)

Hermans, T. H. J. (2022). *Understanding Sea-Level Change Using Global and Regional Models*. [Dissertation (TU Delft), Delft University of Technology]. <https://doi.org/10.4233/uuid:ad44006f-b50d-49b9-bf64-ee5cb7a55980>

Important note

To cite this publication, please use the final published version (if applicable).
Please check the document version above.

Copyright

Other than for strictly personal use, it is not permitted to download, forward or distribute the text or part of it, without the consent of the author(s) and/or copyright holder(s), unless the work is under an open content license such as Creative Commons.

Takedown policy

Please contact us and provide details if you believe this document breaches copyrights.
We will remove access to the work immediately and investigate your claim.

Understanding Sea-Level Change Using Global and Regional Models

Understanding Sea-Level Change Using Global and Regional Models

Proefschrift

ter verkrijging van de graad van doctor
aan de Technische Universiteit Delft,
op gezag van de Rector Magnificus prof. dr. ir. T.H.J.J. van der Hagen,
voorzitter van het College voor Promoties,
in het openbaar te verdedigen op donderdag 7 juli 2022 om 12:30 uur

door

Tim Henri Josephus HERMANS

Ingenieur in Luchtvaart en Ruimtevaart,
Technische Universiteit Delft, Nederland
geboren te Alphen aan den Rijn, Nederland.

Dit proefschrift is goedgekeurd door de

promotor: prof. dr. L.L.A. Vermeersen

promotor: prof. dr. C.A. Katsman

Samenstelling promotiecommissie:

Rector Magnificus,

Prof. dr. L.L.A. Vermeersen

Prof. dr. C.A. Katsman

voorzitter

Technische Universiteit Delft & NIOZ

Technische Universiteit Delft

Onafhankelijke leden:

Prof. dr. C.W. Hughes

Prof. dr. J.D. Pietrzak

Prof. dr. R.S.W. van de Wal

Dr. A.J. Garner

Prof. dr. -ing. habil. R. Klees

University of Liverpool

Technische Universiteit Delft

Universiteit Utrecht

Rowan University

Technische Universiteit Delft, reservelid

Overige leden:

Dr. ir. A.B.A. Slangen

NIOZ

Dr. ir. A.B.A. Slangen heeft in belangrijke mate aan de totstandkoming van het proefschrift bijgedragen.



Keywords: sea-level change, sea-level variability, projections, modeling

Printed by: Gildeprint

Front & Back: ECCO2 model output visualized by NASA/Goddard Space Flight Center Scientific Visualization Studio

Copyright © 2022 by T.H.J. Hermans

ISBN 978-94-6419-524-8

An electronic version of this dissertation is available at

<http://repository.tudelft.nl/>.

Contents

Summary	vii
Samenvatting	xi
List of Abbreviations	xv
1 Introduction	1
1.1 Climate change and sea-level projections	1
1.2 Processes causing sea-level change	2
1.3 Sea-level change in the instrumental era.	6
1.4 Projecting sea-level change	8
1.5 Challenges of projecting sea-level change	11
1.6 Thesis aims and outline	14
2 Projecting Global Mean Sea-Level Change Using CMIP6 Models	17
2.1 Introduction.	18
2.2 Data and methods	19
2.3 Results	22
2.4 Discussion and conclusions	28
2.5 Supplementary information.	30
3 Improving Sea-Level Projections Using Dynamical Downscaling	45
3.1 Introduction.	46
3.2 Data and methods	48
3.3 The impact of dynamical downscaling on historical simulations	55
3.4 The impact of dynamical downscaling on future DSLC	65
3.5 Projected changes in the seasonal sea-level cycle	73
3.6 Discussion and conclusions	75
3.7 Supplementary information.	78
4 Drivers of Interannual Sea-Level Variability	85
4.1 Introduction.	86
4.2 Data and methods	87
4.3 Evaluation of model results.	91
4.4 The contributions of different drivers	97
4.5 Discussion.	105
4.6 Conclusions	106
4.7 Supplementary information.	108

5	The Effect Of Wind Stress on Seasonal Sea-Level Change	113
5.1	Introduction	114
5.2	CMIP6 simulations and regional model experiments . .	115
5.3	Seasonal DSLC simulated by CMIP6 models.	118
5.4	The effect of wind stress on the seasonality of DSLC. .	121
5.5	Discussion and conclusions	129
5.6	Supplementary information.	132
6	Conclusions and Recommendations	141
6.1	Conclusions	141
6.2	Recommendations	144
	Bibliography	147
	Data Statements	167
	Acknowledgements	169
	Curriculum Vitæ	171
	List of Publications	172

Summary

The Earth's climate is changing due to the greenhouse gases that we emit by burning fossil fuels. Consequently, the ocean is heating up and glaciers and ice sheets are melting, which causes the global mean sea level to rise. However, how much the sea level is rising regionally varies due to complex dynamical processes. In some places, the sea level is even falling instead of rising. To decide how to mitigate and adapt to sea-level change, estimating how much the (regional) sea level will change is crucial.

In addition to the sea-level change driven by greenhouse gas emissions (*externally forced* sea-level change), the sea level also varies over time naturally (*internal sea-level variability*). This complicates estimating forced sea-level change from the measurements of satellites and tide gauges: is an observed change simply a natural variation or the result of climate change? To filter out natural variations from the observations, the processes causing temporal sea-level variability need to be understood.

Estimates of future sea-level change (so-called *sea-level projections*) can be made by simulating the different processes causing sea-level change using numerical models. The behavior of the ocean and the atmosphere can be simulated with global climate models. These simulations are used to project dynamic changes in sea level. Dynamic sea-level change is caused by for instance the expansion of the warming ocean or the redistribution of the water within the ocean when the dominant wind patterns in a region change. Global climate models also provide the input to models that can be used to simulate other contributions to sea-level change, such as the melt of glaciers and the Antarctic and Greenland ice sheets.

There are dozens of different global climate models, developed and continuously improved by various modeling centers around the world. The differences between these models introduce uncertainties in sea-level projections. Furthermore, running global climate models is computationally very expensive. Consequently, the spatial resolution of these models is limited. For example, most global climate models compute the properties of the ocean only approximately every 100 km. This is far from optimal for coastal regions, in which sea-level change is influenced by ocean currents and topographic features on scales smaller than the typical resolution of global climate models. How this limited resolution affects sea-level projections for coastal regions is not yet clear. Techniques to refine the simulations of global climate models using regional models (*dynamical downscaling*) have rarely been applied in the context of sea-level projections.

In this thesis, I address several aspects of sea-level change and sea-level variability

using a combination of global and regional models. I start by showing how global mean sea-level projections are affected by the simulations of a new generation of global climate models (Chapter 2). Next, I focus on the sea level in the Northwestern European Shelf region. Using ocean models configured specifically for this region, I study the impact of dynamical downscaling on the simulations of global climate models (Chapter 3) and investigate what causes sea level to vary from year to year (Chapter 4). Finally, I investigate the seasonal mean changes in sea level that global climate models simulate and explain the differences in the changes between the different seasons using a regional model (Chapter 5).

In Chapter 2, I compare global mean sea-level projections based on two generations of global climate models. This is motivated by the sensitivity of the new generation of models (CMIP6 models) to CO₂ emissions, which exceeds that of the previous generation (CMIP5 models). Due to their higher sensitivity, the CMIP6 models simulate a larger increase in surface air temperature on average. However, I show that the higher temperature increase does not translate into much higher projections of global mean sea-level rise for 2100. In contrast, the projections of the rate of sea-level change by 2100 increase substantially. I explain how this is partially caused by the relationship between sea-level rise and cumulative surface air temperature, a relationship which has important implications for the mitigation of greenhouse gas emissions. Furthermore, I argue that the simulations of the most sensitive CMIP6 models are useful for projecting large changes in sea level that are less likely to occur but would have a big impact.

In Chapter 3, I use a regional ocean model to dynamically downscale the simulations of two global climate models on the Northwestern European Shelf. The results demonstrate that dynamical downscaling regionally improves the historical simulations of both global climate models. It also substantially affects their simulations of future ocean dynamic sea-level change, including along the coast. Importantly, the impact of dynamical downscaling is largest for the climate model with the lowest horizontal resolution and the least realistic land mask and bathymetry. For example, that model has a too low resolution to resolve the flow through the English Channel, which likely strongly affects the simulations of sea-level change. This applies to several other global climate models as well. Based on the results of Chapter 3, I therefore conclude that dynamical downscaling is a valuable and important method to improve regional sea-level projections.

In Chapter 4, I perform sensitivity tests with another regional ocean model for the Northwestern European Shelf. In these sensitivity tests, the different boundary conditions imposed on the model, such as the properties of the atmosphere and the neighboring ocean, are only allowed to vary from year to year (interannually) one by one. The results show how much among others the wind, air pressure and the processes in the neighboring ocean contribute to the interannual variability of the sea level on the Northwestern European Shelf. This is used to explain the differences and similarities of the temporal sea-level variability observed at different coastal locations. The tests also demonstrate that non-linear interactions between the different drivers of interannual sea-level variability do not play a large role.

In Chapter 5, I investigate the changes in seasonal mean sea level on the Northwestern European Shelf using a set of global climate models from the CMIP6 generation. I show that there can be substantial differences between the amount of sea-level rise in each season, which are typically not considered in sea-level projections. Using tests with the regional model of Chapter 4, I find that the deviations of sea-level rise in winter and summer are mainly caused by changes in regional wind stress. In spring and autumn, wind-stress changes play a smaller role, and changes in ocean density are likely more important. The tests also demonstrate that global climate models that do not resolve currents through the English Channel cannot accurately simulate the effect of wind-stress changes on the regional sea level, strengthening the case for dynamical downscaling as in Chapter 3.

In summary, this thesis highlights the value of complementing the sea-level simulations of global climate models with regional ocean models. Using both types of models, this thesis enhances our understanding of sea-level change and variability and provides a basis for improving sea-level projections on both the global and the regional scale.

Samenvatting

Het klimaat op aarde is aan het veranderen vanwege de broeikasgassen die we uitstoten door het gebruik van fossiele brandstoffen. Als gevolg daarvan warmt de oceaan op en smelten de gletsjers en ijskappen, waardoor de zeespiegel gemiddeld genomen stijgt. Hoeveel de zeespiegel precies stijgt kan echter behoorlijk verschillen per regio, vanwege complexe dynamische processen. Sterker nog, op sommige plekken daalt de zeespiegel zelfs. Om te bepalen hoe we ons het beste kunnen aanpassen aan zeespiegelverandering is het erg belangrijk om in te schatten hoeveel de (regionale) zeespiegel in de toekomst zal veranderen.

Naast de zeespiegelverandering ten gevolge van de uitstoot van broeikasgassen (*extern veroorzaakte zeespiegelverandering*) vertoont de zeespiegel ook natuurlijke schommelingen (*interne zeespiegelvariabiliteit*). Dit maakt het lastig om de extern veroorzaakte zeespiegelverandering af te leiden uit satellietmetingen en peilmetingen aan de kust: is een waargenomen verandering een natuurlijke schommeling of daadwerkelijk het resultaat van klimaatverandering? Om natuurlijke schommelingen uit de meetsignalen te filteren is het belangrijk om goed te begrijpen waardoor temporele zeespiegelvariabiliteit wordt veroorzaakt.

Het is mogelijk om schattingen te maken van de toekomstige zeespiegelverandering (zogenoeten *zeespiegelprojecties*) aan de hand van modelberekeningen. Het gedrag van de oceaan en de atmosfeer kan worden gesimuleerd met mondiale klimaatmodellen. Die simulaties worden gebruikt om lange termijn projecties te maken van de dynamische veranderingen van de zeespiegel. Dat zijn veranderingen die worden veroorzaakt door bijvoorbeeld de uitzetting van de oceaan als die warmer wordt, of door de herverdeling van het water in de oceaan als de overheersende windrichting in een bepaalde regio verandert. Mondiale klimaatmodellen leveren ook de input waarmee andere bijdrages aan zeespiegelverandering doorgerekend kunnen worden, zoals het smelten van gletsjers en de ijskappen op Groenland en Antarctica.

Er zijn tientallen verschillende klimaatmodellen, die voortdurend worden ontwikkeld en verbeterd door verschillende instituten op de wereld. De verschillen tussen klimaatmodellen zorgen voor onzekerheden in zeespiegelprojecties. Bovendien kost het gebruik van mondiale klimaatmodellen veel tijd en rekenkracht. De ruimtelijke resolutie van die modellen is daarom beperkt: de meeste mondiale klimaatmodellen berekenen bijvoorbeeld de eigenschappen van de oceaan alleen maar ongeveer elke 100 kilometer. Dat is allesbehalve optimaal voor kustgebieden, waarin de zeespiegelverandering wordt beïnvloed door zeestromingen en variaties in de kustlijn en de bodemdiepte op een kleinere schaal. De consequenties van die beperkte resolutie voor het maken van zeespiegelprojecties voor kustgebieden zijn nog niet

goed onderzocht. Er bestaan wel technieken om de simulaties van mondiale klimaatmodellen te verfijnen met behulp van regionale modellen (*dynamische schaalverkleining*), maar die zijn nog niet vaak gebruikt voor zeespiegelprojecties.

In deze scriptie bestudeer ik een aantal aspecten van zeespiegelverandering en zeespiegelvariabiliteit met een combinatie van mondiale en regionale modellen. Ik laat eerst zien hoe projecties van de wereldgemiddelde zeespiegelverandering worden beïnvloed door de simulaties van een nieuwe generatie mondiale klimaatmodellen (Hoofdstuk 2). Daarna concentreer ik me op de zeespiegel op het continentale plat ten noordwesten van Europa (het Noordwest-Europese Plat). Met behulp van oceaanmodellen die speciaal voor deze regio zijn ingesteld, bekijk ik de invloed van dynamische schaalverkleining op de simulaties van mondiale klimaatmodellen (Hoofdstuk 3) en onderzoek ik de oorzaken van schommelingen in de zeespiegel van jaar tot jaar (Hoofdstuk 4). Tot slot bestudeer ik de gemiddelde zeespiegelverandering die mondiale klimaatmodellen simuleren per seizoen en verklaar ik de verschillen tussen de veranderingen in de verschillende seizoenen aan de hand van een regionaal model (Hoofdstuk 5).

In Hoofdstuk 2 vergelijk ik de wereldwijd gemiddelde zeespiegelprojecties gebaseerd op twee verschillende generaties mondiale klimaatmodellen. De aanleiding hiertoe is dat de nieuwste generatie modellen (CMIP6 modellen) gevoeliger zijn voor CO₂-uitstoot dan de vorige generatie modellen (CMIP5 modellen) en daarom gemiddeld genomen een sterkere temperatuurstijging aan het aardoppervlak simuleren. Ik toon aan dat die sterkere temperatuurstijging echter niet leidt tot veel hogere projecties van de wereldwijd gemiddelde zeespiegelstijging in 2100. De projecties van de snelheid van die stijging in 2100 nemen daarentegen wel behoorlijk toe. Ik leg uit hoe dit deels te maken heeft met de relatie tussen zeespiegelstijging en cumulatieve temperatuurstijging - een relatie met belangrijke implicaties voor hoe snel we onze uitstoot van broeikasgassen zouden moeten verminderen. Bovendien beargumenteer ik dat de meest gevoelige CMIP6 modellen nuttig zijn voor het doorrekenen van worst-case zeespiegelscenario's.

In Hoofdstuk 3 gebruik ik een regionaal oceaanmodel voor de dynamische schaalverkleining van de simulaties van twee mondiale klimaatmodellen op het Noordwest-Europese Plat. De resultaten tonen aan dat dit de historische simulaties van beide klimaatmodellen regionaal verbetert. De schaalverkleining heeft ook invloed op de simulaties van de toekomstige zeespiegelverandering in de regio, inclusief aan de kust. De invloed van de schaalverkleining blijkt het grootst voor het klimaatmodel met de laagste resolutie en de minst realistische kustlijn en bodemdiepte. Dat model is bijvoorbeeld te grof om de stroming door het Engelse Kanaal uit te kunnen rekenen, wat de simulaties van zeespiegelverandering waarschijnlijk sterk beïnvloedt. Hetzelfde geldt voor meerdere andere klimaatmodellen. Op basis van de resultaten in Hoofdstuk 3 concludeer ik daarom dat dynamische schaalverkleining een waardevolle en belangrijke methode is om regionale zeespiegelprojecties te verbeteren.

In Hoofdstuk 4 voer ik gevoeligheidstests uit met een ander regionaal oceaanmodel van het Noordwest-Europese Plat. In die gevoeligheidstests leg ik het model bepaalde randvoorwaardes op, zoals de eigenschappen van de atmosfeer en de aangrenzende oceaan. Ik laat steeds één type randvoorwaarde variëren van jaar tot jaar, terwijl de andere randvoorwaardes elk jaar hetzelfde blijven. De resultaten laten zien hoeveel onder andere de wind, luchtdruk en de processen in de aangrenzende oceaan bijdragen aan de jaarlijkse schommelingen in de zeespiegel op het Noordwest-Europese Plat. Die informatie gebruik ik om de overeenkomsten en verschillen in de zeespiegelvariabiliteit die in verschillende kustplaatsen wordt waargenomen te verklaren. De gevoeligheidstests laten ook zien dat de niet-lineaire interacties tussen de verschillende factoren die bijdragen aan de zeespiegelvariabiliteit van jaar tot jaar geen grote rol spelen.

In Hoofdstuk 5 onderzoek ik de gemiddelde zeespiegelverandering op het Noordwest-Europese Plat per seizoen, aan de hand van de simulaties van een groep mondiale klimaatmodellen. Ik laat zien dat de zeespiegelstijging per seizoen flink kan verschillen. Tot nu toe wordt daar in zeespiegelprojecties echter vaak nog geen rekening mee gehouden. Door middel van tests met het regionale model uit Hoofdstuk 4 vind ik dat de afwijkingen van de zeespiegelstijging in de winter en de zomer vooral komen door regionale veranderingen in de wind. In de lente en de herfst spelen de veranderingen in de wind een kleinere rol, en zijn veranderingen in de dichtheid van het zeewater waarschijnlijk belangrijker. De tests laten ook zien dat mondiale klimaatmodellen die te grof zijn om de stroming door het Engelse Kanaal uit te kunnen rekenen niet geschikt zijn om het effect van windveranderingen op de zeespiegel in de regio te simuleren. Dit vormt een extra motivatie voor het toepassen van dynamische schaalverkleining zoals in Hoofdstuk 3.

Samengevat laat mijn proefschrift het belang zien van het gebruik van regionale oceaanmodellen als aanvulling op de simulaties van mondiale klimaatmodellen. Door beide soorten modellen te gebruiken vergroot dit proefschrift ons begrip van zeespiegelverandering en zeespiegelvariabiliteit. Daarmee draagt mijn onderzoek bij aan het verbeteren van zeespiegelprojecties op zowel mondiale als regionale schaal.

List of Abbreviations

AMM7	Atlantic Margin Model 7
CDF	Cumulative Distribution Function
CMIP5	Coupled Model Intercomparison Project 5
CMIP6	Coupled Model Intercomparison Project 6
CTW	Coastally Trapped Wave
DJF	December, January, February
DSLC	Ocean Dynamic Sea-Level Change
ECS	Equilibrium Climate Sensitivity
EffCS	Effective Climate Sensitivity
ESGF	Earth System Grid Federation
GMSL	Global Mean Sea Level
GSAT	Global Mean Surface Air Temperature
GTE	Global Mean Thermal Expansion
GCM	Global Climate Model
GCM-HAD	The GCM HadGEM2-ES
GCM-MPI	The GCM MPI-ESM-LR
GIA	Glacial Isostatic Adjustment
GRD	Gravitational, Rotational, Deformational
GSW	Gibbs SeaWater
IB	Inverse Barometer
IPCC	Intergovernmental Panel on Climate Change
IPCC AR5	5th Assessment Report of the IPCC
IPCC AR6	6th Assessment Report of the IPCC
JJA	June, July, August
LSW	Longshore Wind
MAM	March, April, May
MDT	Mean Dynamic Topography
NAO	North Atlantic Oscillation
NEMO	Nucleus for European Modelling of the Ocean
NWES	Northwestern European Shelf
OHU	Ocean Heat Uptake
OSTIA	Operational Sea Surface Temperature and Sea Ice Analysis
PCC	Pattern Correlation Coefficient
PSMSL	Permanent Service for Mean Sea Level
RCA4	Rosby Centre Regional Atmospheric Climate Model 4
RCM	Regional Climate Model
RCM-HAD	Dynamically downscaled HadGEM2-ES
RCM-MPI	Dynamically downscaled MPI-ESM-LR

RCP	Representative Concentration Pathway
ROMS	Regional Ocean Modeling System
RS LC	Relative Sea-Level Change
RMSE	Root Mean Square Error
SD	Standard Deviation
SLC	Sea-Level Change
SLP	Sea-Level Pressure
SON	September, October, November
SSH	Sea Surface Height
SSLA	Seasonal Sea-Level Anomaly
SSP	Shared Socioeconomic Pathway
SST	Sea Surface Temperature
SSS	Sea Surface Salinity
SWSA	Seasonal Wind-Stress Anomaly
SWVA	Seasonal Wind-Velocity Anomaly
TCR	Transient Climate Response
ToE	Time of Emergence
TG	Tide Gauge
VLM	Vertical Land Motion

1

Introduction

1.1. Climate change and sea-level projections

The headline statements of the recently published Working Group 1 contribution to the Sixth Assessment Report of the Intergovernmental Panel on Climate Change (IPCC AR6) are clear: our climate has been warming at a rate that is “unprecedented over at least the last 2,000 years”, and this warming is “unequivocally caused by human activities” ([Masson-Delmotte et al., 2021](#)). As a result, the ocean is heating up and ice sheets and glaciers are melting. This causes sea-level rise in many regions around the world, which increases the risk of coastal flooding and can even lead to the permanent loss of coastline through submergence. Sea-level rise can also enhance saltwater intrusion and coastal erosion and result in the loss of coastal wetlands and ecosystems ([Oppenheimer et al., 2019](#)). The consequences of sea-level rise will be felt especially by the communities located in coastal regions and call for the mitigation of climate change. However, the sea level will change substantially even if we reduce our greenhouse gas emissions today, because the ice sheets and the deep ocean are still responding to the greenhouse gases that we have emitted in the past ([Mengel et al., 2018](#)).

Coastal communities may use different strategies to adapt to sea-level change, such as protecting, accommodating, advancing, retreating and using nature-based solutions ([Oppenheimer et al., 2019](#)). To decide how and when to act, projections of sea-level change at a regional to local scale are crucial. Therefore, regional sea-level projections are being developed in individual studies (e.g., [Kopp et al., 2014](#); [Jackson and Jevrejeva, 2016](#)) and in national and intergovernmental assessments (e.g., [Church et al., 2013](#); [Fox-Kemper et al., 2021](#); [Oppenheimer et al., 2019](#); [Palmer et al., 2018b](#); [van den Hurk et al., 2014](#)).

Uncertainties in sea-level projections arise from the different approaches to modeling sea-level change, but also from the uncertainty in future greenhouse gas emissions and from natural climate variability, which masks externally forced changes in sea level ([Palmer et al., 2020](#); [Kopp et al., 2019](#); [Little et al., 2015](#); [Hawkins and Sutton, 2009](#)). The uncertainties in sea-level projections are important because

stakeholders are not only interested in the most likely sea-level rise outcomes, but also in the potential for larger sea-level rise ([Hinkel et al., 2019](#)). Scientists are continuously trying to improve sea-level projections by better defining and reducing their uncertainties, building on the latest understanding of all contributing physical processes and considering the kind of information that stakeholders need.

This thesis uses global climate models and regional ocean models to improve our understanding of sea-level change and sea-level variability. Before discussing the aims of this thesis in more detail, I will first introduce the processes causing sea-level change (Section 1.2) and the methods available to observe sea-level change (Section 1.3). Next, I will discuss how sea-level projections can be developed (Section 1.4) and what challenges this currently involves (Section 1.5). Finally, I will state the aims of this thesis and provide an outline of the chapters that follow (Section 1.6).

1.2. Processes causing sea-level change

Changes in sea level are caused by a combination of physical processes that act on global to local scales (Figure 1.1). To understand these processes, it is easiest to first think about the global mean sea level (GMSL). The GMSL rises or falls when the volume of the ocean increases or decreases. This may happen for two reasons. First, the volume of the ocean changes when water is added to or removed from the ocean, for example due to the melt or growth of glaciers and ice caps, the Greenland ice sheet or the Antarctic ice sheet. Changing the amount of the water stored on land, for example by groundwater extraction, deforestation or building dams, also affects the ocean volume (e.g., [Wada et al., 2017](#)). The GMSL change due to the exchange of water between the land, the cryosphere and the ocean is called *barystatic sea-level change* ([Gregory et al., 2019](#)). Second, the volume of the ocean changes when the average density of the seawater changes. As a result, the ocean expands or contracts, leading to so-called *steric sea-level change* ([Gregory et al., 2019](#)). Steric GMSL rise occurs mainly due to the increasing ocean temperature (thermal expansion) ([Lowe and Gregory, 2006](#)). The melt of glaciers and the global mean thermal expansion of the ocean have contributed to the GMSL rise from 1901 to 2018 by about 38 and 41%, respectively ([Fox-Kemper et al., 2021](#)).

While GMSL rise is a useful metric of the effects of climate change, sea-level change varies on regional to local scales (Figure 1.1) and this is what we ultimately experience at the coast. The main processes that cause regional variations in sea-level change are the gravitational, deformational and rotational response of the Earth to mass redistribution (Section 1.2.1), glacial isostatic adjustment (Section 1.2.2) and ocean dynamics (Section 1.2.3). Locally, also the vertical motion of the land surface (Section 1.2.4) and changes in extreme sea levels (Section 1.2.5) come into play. The reference frame plays an important role for sea-level change: we distinguish *geocentric* sea-level change (sea-level change relative to the Earth's center of mass) from *relative* sea-level change (sea-level change relative to the ocean floor).

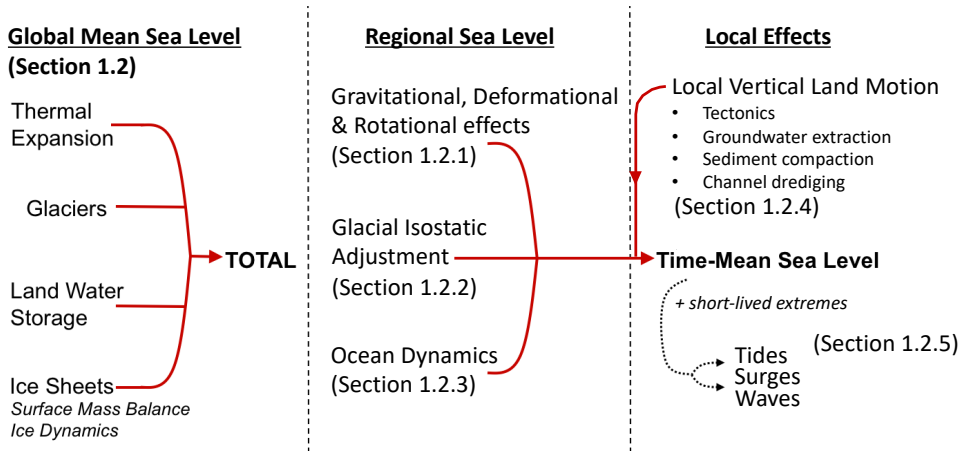


Figure 1.1: Overview of the physical processes causing sea-level change on different spatial and temporal scales. Adapted from Figure 2.1.1 of [Palmer et al. \(2018b\)](#).

1.2.1. Contemporary gravitational, rotational and deformational effects

If the ocean was at rest, the sea surface would have the shape of the geoid. The geoid is a non-uniform surface of equal gravitational and rotational potential, which depends on the mass distribution and the rotation of the Earth. When mass is exchanged between the land and the ocean, for example through ice melt or changes in land-water storage, the Earth's gravity field and rotation change. This affects the shape of the geoid. Additionally, the Earth deforms in response to the changes in surface loads. The so-called gravitational, rotational and deformational (GRD) effects ([Gregory et al., 2019](#)) of mass redistribution cause a distinct pattern of regional sea-level change called a sea-level fingerprint (e.g., [Mitrovica et al., 2001](#)).

For example, consider a melting ice sheet (Figure 1.2). In an equilibrium state, the sea level is relatively high near the ice sheet and low farther away due to the gravitational attraction of the ice sheet. When the ice sheet starts to melt and meltwater is added to the ocean, the sea level near the ice sheet falls because of the decreasing gravitational attraction of the ice. To compensate, the sea level far away from the ice sheet rises more than when the meltwater would have been redistributed over the ocean evenly. This has important consequences. For example, since The Netherlands is relatively close to Greenland but far away from Antarctica, the melt on Greenland results in less sea-level rise at our coasts than the same amount of melt on Antarctica would.

Changes in the Earth's rotation due to the ice melt further modify the shape of the geoid. Additionally, the solid Earth will deform in response to the ice melt (Figure 1.2), both instantaneously due to the elastic response of the crust, and on longer timescales due to the viscous response of the mantle (see Section 1.2.2). Under-

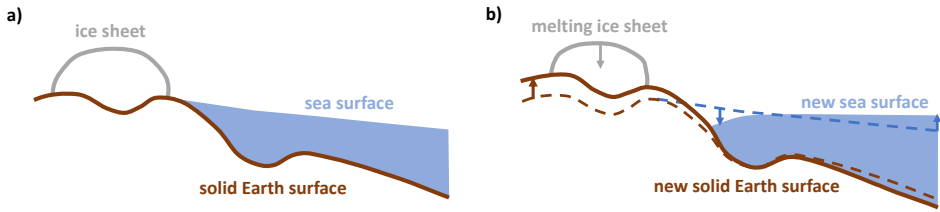


Figure 1.2: Schematic representation of the gravitational and deformational effects of the Earth on sea level in response to a melting ice sheet: **(a)** before the ice melt has started; **(b)** after the ice melt has started. Adapted from Figure 2 of [Whitehouse \(2018\)](#).

neath and near the melting ice sheet, the land surface lifts because the surface load decreases, leading to a relative sea-level fall. In contrast, the sea-level rise far away from the ice increases the load on the ocean floor, causing the solid Earth to deform again. Hence, the GRD effects due to the mass redistribution caused by for example changes in land ice and land-water storage will in turn affect that mass redistribution itself.

1.2.2. Glacial isostatic adjustment

In addition to the GRD effects due to contemporary mass redistribution, the solid Earth is also still responding to the redistribution of mass that occurred in the past. The GRD effects due to the on-going viscous deformation of the Earth's mantle in response to the past unloading of ice sheets is called glacial isostatic adjustment (GIA). The solid Earth deformation due to GIA is especially large in areas that were covered by large ice sheets during the Last Glacial Maximum (approximately 26,500 to 20,000 years ago). For example, in Scandinavia, land uplift rates can exceed 10 mm/yr ([Lidberg et al., 2007](#)). In regions adjacent to former ice sheets, the surface is sinking because the mantle material that has been pushed outward by the ice is now slowly flowing back, restoring isostatic equilibrium.

1.2.3. Ocean dynamics

In reality, the sea level differs from the geoid due to spatial variations in ocean density and ocean circulation. For example, wind-driven subtropical and subpolar ocean gyres revolve around large areas of relatively high and low sea level, respectively. In high-latitude regions, where deep water forms as part of the thermohaline circulation, the average sea level is relatively low ([Levermann et al., 2005](#)). These and other features can be recognized when looking at the average shape of the sea surface relative to the geoid (Figure 1.3), which is called the mean dynamic topography.

Changes in the density and the circulation of the ocean, both due to internal climate variability and in response to external forcing such as greenhouse gas emissions, cause the sea level to vary on a range of timescales (e.g., [Yin et al., 2010](#)). Examples are transient phenomena such as tides, surges, waves and ocean eddies, but also

longer lasting effects such as the redistribution of ocean water following shifts in dominant wind patterns and the slowdown of the thermohaline circulation due to surface warming and freshening. Such changes result in differences in the mean state of the sea surface between different periods, referred to as ocean dynamic sea-level change (DSLCL). The sea level is also affected by regional atmospheric pressure anomalies which, depending on their sign, depress or raise the sea surface through the inverse barometer effect (Stammer and Hüttemann, 2008).

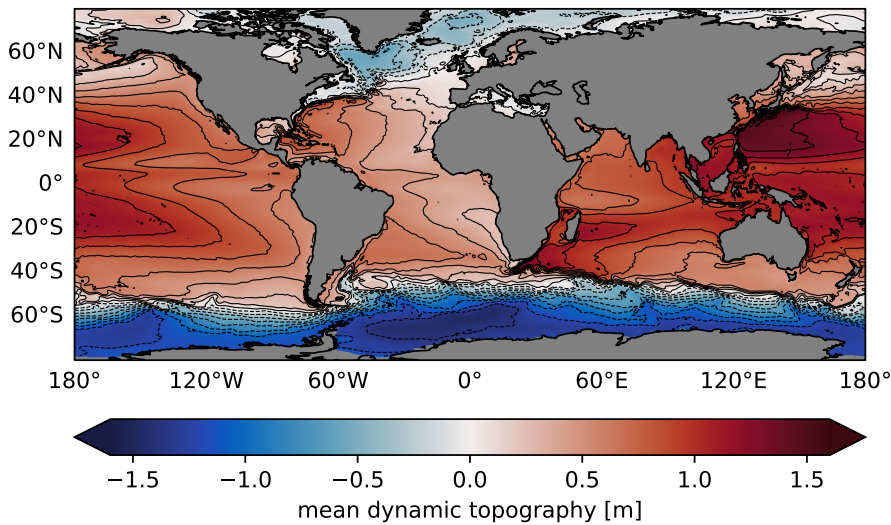


Figure 1.3: Mean dynamic topography from 1993 to 2012 [m] based on (CNES, 2019) data.

1.2.4. Local vertical land motion

As mentioned in Sections 1.2.1 & 1.2.2, contemporary GRD effects and GIA result in vertical land motion (VLM), which causes relative sea-level change. Locally, VLM also occurs due to seismicity (e.g., Klos et al., 2019) and land subsidence, following for example sediment compaction (e.g., Brain, 2016). Human activity, such as the extraction of minerals and fluids from the ground, can accelerate land subsidence, as is happening in deltaic megacities (Cao et al., 2021; Syvitski et al., 2009). Sediment transport may also partially offset relative sea-level change and could be considered part of VLM.

1.2.5. Changes in extreme sea levels

Changes in the time-mean state of the sea level due to the processes described above change the baseline elevation of tides, surges, and waves. This is the main cause of future changes in the frequency of extreme sea levels (Howard et al., 2019; Vousdoukas et al., 2018). Additional changes in extreme sea levels can be caused by dynamic changes in tides, surges and waves, for instance due to changes in storminess. The time-mean sea-level change may also cause changes in tides,

surges and waves, for instance through altering the local water depth (e.g., [Arns et al., 2017](#)). Since extreme sea levels cause coastal flooding, projecting their change is an active area of research (e.g., [Vousdoukas et al., 2018](#); [Muis et al., 2020](#); [Tebaldi et al., 2021](#); [Fox-Kemper et al., 2021](#)).

In summary, sea-level change varies on a range of spatial and temporal scales due to the combination of the processes described above. To develop comprehensive sea-level projections, they all need to be considered (Section 1.4).

1.3. Sea-level change in the instrumental era

Over the past century or so (1901–2010), GMSL has risen by approximately 17.5 cm ([Palmer et al., 2021](#)) (Figure 1.4a). We know this mainly because of long tide gauge records. Tide gauges are coastal monitoring stations that record the height of the sea level relative to the land to which they are anchored. This means that tide gauges measure relative sea-level change and that their measurements are affected by local VLM (Section 1.2.4). The VLM at a tide gauge can be estimated using nearby GPS observations, if available ([Wöppelmann and Marcos, 2016](#)). Tide gauge records, available from global databases such as the Permanent Service for Mean Sea Level (PSMSL, [Holgate et al., 2013](#)), are indispensable for reconstructing sea-level change over the last century (Figure 1.4a). However, since tide gauges are situated at the coast and are not evenly distributed around the world (Figure 1.4b), reconstructing GMSL rise from their records is not straightforward.

Since the launch of the TOPEX/Poseidon satellite altimeter mission in 1992 ([Fu et al., 1994](#)), spaceborne observations of sea level with a near-global coverage have become available. Satellite altimeters take repeated measurements of geocentric sea level (relative to the Earth’s center of mass) at a regular time interval depending on the orbit of the satellite. They do so by sending out radar pulses to the ocean surface and measuring the time it takes for these pulses to return. The altimetry measurements therefore depend on, among others, the determination of the orbit of the satellite and geophysical corrections such as for atmospheric propagation delays and sea state biases ([Escudier et al., 2017](#)).

Based on satellite altimetry, GMSL has very likely risen at a rate of 2.88 to 3.61 mm/yr over 1993–2018 ([Fox-Kemper et al., 2021](#)). Altimetry measurements also expose distinct spatial features of sea-level change such as the zonal contrast in the Tropical Pacific Ocean, the meridional dipole in the North Atlantic Ocean and the relatively low rates near Antarctica and Greenland (Figure 1.5). In Figure 1.5, mesoscale eddies in regions with strong currents are visible as near-circular features of anomalous sea-level change. The altimetry records are crucial for understanding DSLC (e.g., [Chafik et al., 2019](#); [Thompson et al., 2016](#)) and can be used to evaluate ocean models (e.g., [Bilbao et al., 2015](#); [Landerer et al., 2014](#); [Richter et al., 2017](#)). To distinguish DSLC from sea-level change due to changes in the geoid, altimetry measurements need to be corrected for the latter, for example using satellite measurements of the Earth’s gravity field (e.g., from the Gravity Field and Steady-State Ocean Circulation Explorer).

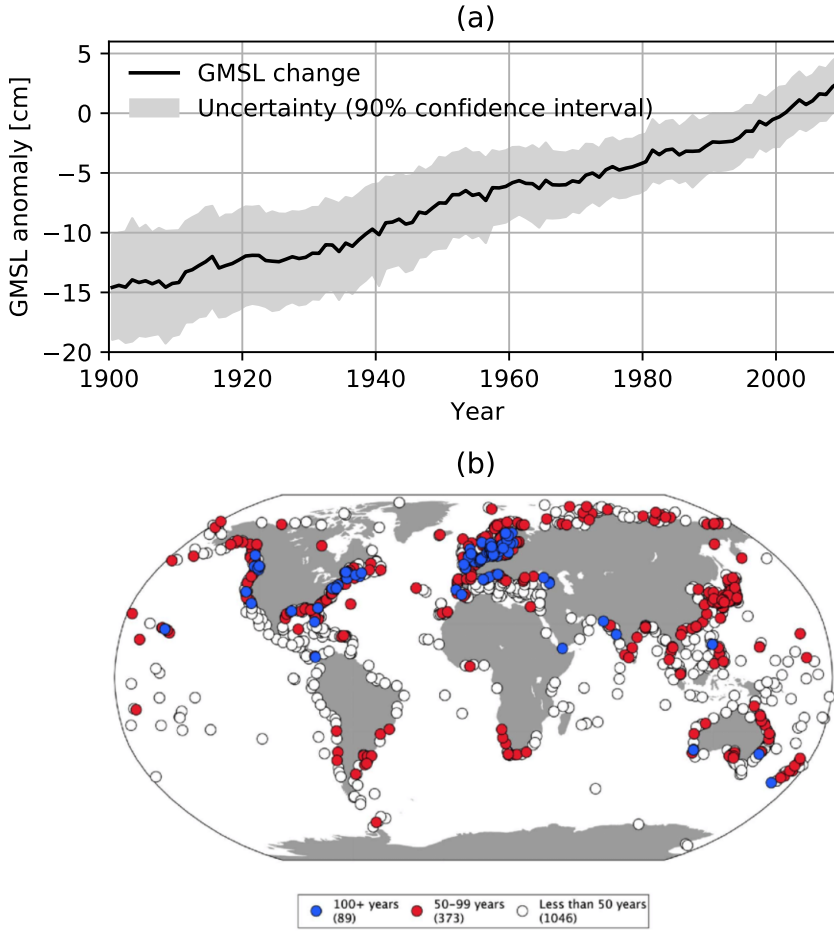


Figure 1.4: (a) Historical GMSL rise relative to 1991-2010 based on an ensemble of tide gauge reconstructions. The black line shows the ensemble mean of the reconstructions and the light grey shading shows the uncertainty (90% confidence interval). Based on the data of [Palmer et al. \(2021\)](#); (b) the global coverage of tide gauges based on the records made available by the PSMSL. The colors indicate the record lengths. Obtained from [Ponte et al. \(2019\)](#), their Figure 2.

To compare satellite altimetry records with tide gauge records, VLM needs to be added to the first or subtracted from the latter. Compared to most tide gauge records, the altimetry record is short. Especially at a regional scale, this complicates distinguishing externally forced sea-level change and its acceleration from internal sea-level variability (e.g., [Hamlington et al., 2020](#)). Moreover, the waveforms of the radar pulses of altimeters are affected by the presence of land, reducing the accuracy of satellite altimetry near the coasts ([Cipollini et al., 2017](#)). Tide gauges and satellite altimetry are therefore complementary observation tools.

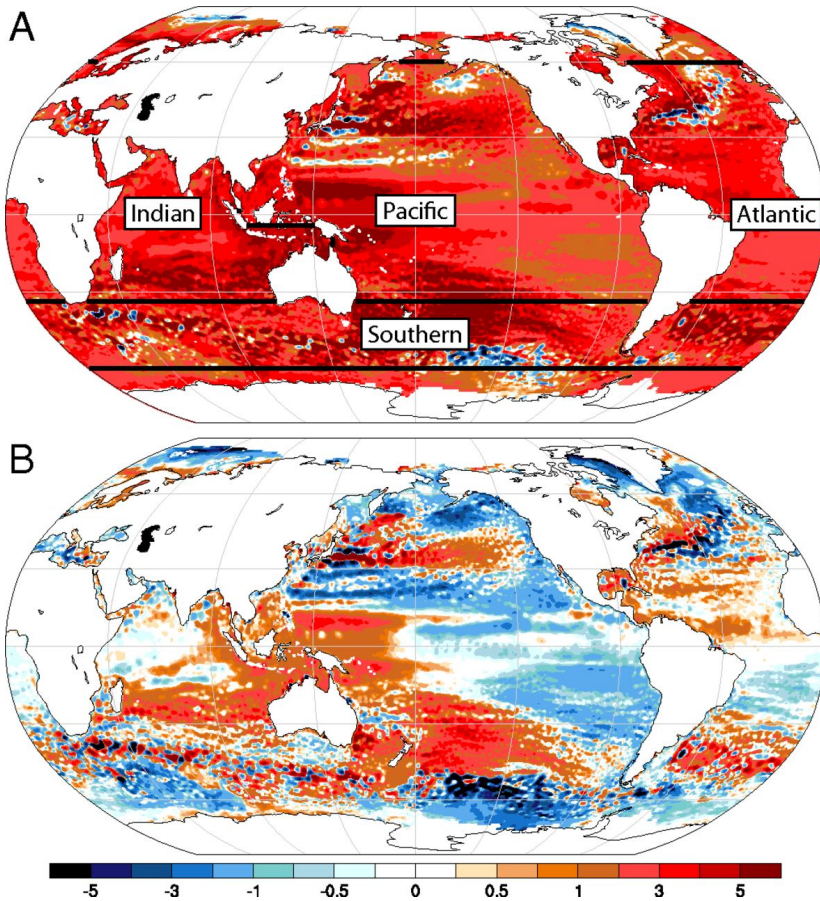


Figure 1.5: Regional trends of annual mean sea level derived from satellite altimetry over 1993-2018 [mm/yr], (a) with and (b) without GMSL rise. Obtained from [Fasullo and Nerem \(2018\)](#), their Figure 1.

1.4. Projecting sea-level change

One way to project future sea-level change is to use the relationship between observed sea-level change (Section 1.3) and a relevant global climate parameter such as the global mean surface air temperature. For a certain projected change in global mean surface air temperature, sea-level change can then be projected (e.g., [Rahmstorf et al., 2007](#); [Mengel et al., 2016](#)). Such semi-empirical methods are relatively simple and computationally cheap but assume that the relationships on which they are based are adequate representations of the physical processes involved. These relationships therefore need to be well constrained by observations. Additionally, semi-empirical methods assume that the relationships involved will not change in the future; an assumption which may be invalidated by non-linear changes in the processes causing sea-level change. Alternatively, process-based methods that rely on complex numerical models may be used to project the contribution of each of

the processes introduced in Section 1.2 (e.g., [Fox-Kemper et al., 2021](#); [Kopp et al., 2014](#); [Oppenheimer et al., 2019](#); [Palmer et al., 2018b](#); [Slangen et al., 2014](#)). Crucially, our ability to make process-based projections depends on our understanding of the relevant physical processes and how best to model them, which motivates this thesis.

1.4.1. Global climate models

Global climate models (GCMs) can be used to simulate the response of the Earth system to radiative forcing. Radiative forcings are factors that alter the energy imbalance at the top of the Earth's atmosphere ([Forster et al., 2021](#)), such as solar variability and changes in the concentration of greenhouse gases and aerosols in the atmosphere due to human activity and volcanism. The input to GCMs can either be based on observed radiative forcing or on radiative forcing under different future scenarios, such as representative concentration pathways (RCPs, [Meinshausen et al., 2011](#)) and the scenarios tied to shared socioeconomic pathways (SSPs, [Meinshausen et al., 2020](#)).

The output of GCMs consists of the time-dependent response of many climate variables, including global mean thermal expansion and DSLC (see Section 1.2). GCMs simulate these variables by dividing the climate system in many different grid cells. For each grid cell, the equations describing the relevant physical processes are solved numerically. Computational constraints limit the number of grid cells of GCMs and therefore their average grid resolution. The different components of the climate system are coupled within a GCM. For example, the wind may affect the ocean circulation, whereas the sea surface temperature may influence the atmospheric circulation.

There are dozens of different GCMs, developed and continuously improved by various modeling centers around the world. These modeling centers participate in so-called Coupled Model Intercomparison Projects (CMIPs) to provide a systematic comparison of their models for a well-defined set of common experiments. These model ensembles allow scientists to study the response of the climate system to changes in greenhouse gas concentrations and to identify model biases. Simulations of GCMs participating in the fifth intercomparison project (CMIP5, [Taylor et al., 2012](#)) have been available since the start of writing this thesis, whereas simulations from the latest intercomparison project (CMIP6, [Eyring et al., 2016](#)) have only started to become available in 2019.

1.4.2. Projecting barystatic sea-level change, GIA and VLM

Ice sheets and glaciers are typically not included in GCMs, mainly due to the discrepancy between the resolution of most GCMs and the resolution appropriate for ice models ([Vizcaino, 2014](#)). Instead, the contributions of ice sheets and glaciers to sea-level change are projected using dedicated ice sheet and glacier models and parameterizations, driven by the output of GCMs. For example, glacier mass changes are typically projected using global mass balance models driven by the precipitation and surface air temperature output of GCMs (e.g., [Marzeion et al., 2020](#)). Projec-

tions of the mass change of the Greenland and Antarctic ice sheets often rely on regional ice sheet models forced with the precipitation, surface air temperature, and ocean temperature and salinity output of GCMs (e.g., [Nowicki et al., 2020](#); [Goelzer et al., 2020](#)). Importantly, this means that the interactions of the ice sheets with the atmosphere and the ocean are not resolved. To estimate the contribution of ice sheet processes which we cannot yet model well, structured expert judgement can be used ([Bamber and Aspinall, 2013](#); [Bamber et al., 2019](#), see Section 1.5.1). The contribution of land-water storage to sea-level change is often projected using hydrological models ([Konikow, 2011](#); [Wada et al., 2016](#)) and relationships between land-water storage and the global population (e.g., [Fox-Kemper et al., 2021](#); [Kopp et al., 2014](#)).

The regional sea-level change due to the GRD effects caused by the projected terrestrial mass changes is often computed by solving the sea-level equation ([Farrell and Clark, 1976](#)) for a rotating elastic Earth (e.g., [Mitrovica et al., 2011](#)). To account for GIA, typically global models are used that solve the sea-level equation using a radially symmetric viscoelastic Earth model combined with a spatially varying ice history over the last glacial cycle (e.g., [Lambeck et al., 2014](#); [Peltier et al., 2014](#)). Alternatively, GIA can be estimated in conjunction with VLM by statistically extrapolating the linear background trends observed at tide gauges (e.g., [Kopp et al., 2014](#); [Fox-Kemper et al., 2021](#)). To sum all the separately estimated components of sea-level change and their uncertainties, the dependence between processes must be considered.

1.4.3. Recent projections

Updated sea-level projections, based on CMIP6 models, have recently been published by the IPCC AR6 ([Fox-Kemper et al., 2021](#)). Their projections of GMSL rise by 2100 range from 0.28 to 1.01 m (relative to 1995-2014), depending on the emissions scenario. This range excludes ice-sheet dynamics that are currently poorly understood but may lead to higher sea-level projections (see Section 1.5.1). Regionally, the relative sea-level projections of the IPCC AR6 show some distinct deviations from the global mean (Figure 1.6). Generally, due to GRD effects, the sea level will fall near large sources of terrestrial mass loss (e.g., Greenland and West Antarctica) and rise farther from them. Due to ocean dynamics, the projected sea-level rise is relatively high for example northeast of the US and relatively low for example south of the Antarctic Circumpolar Current ([Slangen et al., 2014](#)). Due to GIA, relative sea level is projected to fall strongly in regions that were covered by large ice sheets in the past (e.g., Scandinavia, Alaska, Greenland, Antarctica and Patagonia). High rates of relative sea-level rise are found at locations experiencing large land subsidence, for example in Asian deltas and in the Gulf of Mexico.

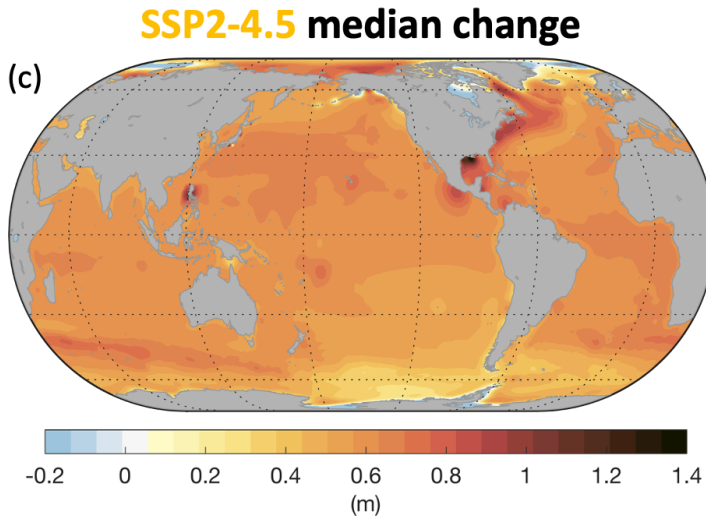


Figure 1.6: The median projections of relative sea-level change by 2100 [m] of the IPCC AR6 for an intermediate emissions scenario (SSP2-4.5), relative to 1995-2014. Obtained from [Fox-Kemper et al. \(2021\)](#), their Figure 9.28c. Note that the colormap does not distinguish values below -0.2 m.

1.5. Challenges of projecting sea-level change

In the recent decades, the development of sea-level projections has progressed substantially, particularly with regards to the regional variations of sea-level change. However, the range of sea-level projections in the literature has widened over time ([Garner et al., 2018](#)) and substantial challenges remain. This section outlines some of the main uncertainties involved in projecting sea-level change (Section 1.5.1) and then introduces the uncertainties that this thesis addresses in more detail (Sections 1.5.2, 1.5.3 & 1.5.4).

1.5.1. Main uncertainties in sea-level projections

Different types of uncertainty in sea-level projections exist and their relative importance varies by location and through time ([Little et al., 2015](#); [Palmer et al., 2020](#); [Hawkins and Sutton, 2009](#)). One type of uncertainty is the uncertainty in the future emissions of greenhouse gases. This uncertainty is typically addressed by developing sea-level projections for different emissions scenarios (Section 1.4.1). A second type of uncertainty stems from the uncertainties in modeling the different components of sea-level change. Some of the largest uncertainties of this type are related to the dynamics of the Greenland and Antarctic ice sheets, which are not well understood.

Given the lack of consensus among experts on how best to model the Greenland and Antarctic Ice Sheets, their contributions to sea-level change can be considered *deeply* uncertain ([Fox-Kemper et al., 2021](#)). The main difficulties relate to processes that are poorly constrained by observations and that existing models cannot resolve

well (see also Section 1.4.2). For the Antarctic ice sheet, examples are the marine ice sheet and ice cliff instabilities, the sensitivity of marine-grounded ice shelves to ocean warming, and the effect of ice-ocean feedbacks (e.g., [DeConto et al., 2021](#); [Golledge et al., 2019](#); [Levermann et al., 2020](#); [Nowicki et al., 2020](#); [Fox-Kemper et al., 2021](#)). For the Greenland Ice Sheet, examples are atmospheric forcing, surface processes, and ice-climate interactions (e.g., [Muntjewerf et al., 2020](#); [Goelzer et al., 2020](#); [Fox-Kemper et al., 2021](#)).

Modeling VLM is also challenging. Only a few models provide global estimates of VLM due to GIA (e.g., [Lambeck et al., 2014](#); [Peltier et al., 2014](#)). Except for the model of [Caron et al. \(2018\)](#), forward GIA models do not provide formal uncertainty estimates. Moreover, most global GIA models assume that the Earth is radially symmetric, neglecting potentially important lateral variations in lithospheric thickness and mantle viscosity. Projections of other types of VLM are not available at a global scale. As an alternative, some studies have extrapolated linear background rates in tide gauge records to account for GIA in combination with other long-term VLM components (e.g., [Fox-Kemper et al., 2021](#); [Kopp et al., 2014](#)). This is inaccurate at locations with non-linear VLM caused by seismicity or anthropogenic land subsidence.

Additional modeling uncertainties arise from the use of GCMs to develop sea-level projections, which is a central theme of this thesis. Many components of sea-level projections rely directly or indirectly on the simulations of GCMs (Section 1.4). Therefore, uncertainties are introduced by the discrepancies between the simulations of different GCMs, which will be discussed in more detail in Section 1.5.2. Furthermore, even though different GCMs have different ocean and atmosphere grids, most of them have a relatively low grid resolution (Section 1.4.1). This may affect their simulations of DSLC in coastal regions, which will be discussed in more detail in Section 1.5.3.

A third type of uncertainty in sea-level projections is caused by internal sea-level variability, which refers to the natural fluctuations in sea level within the climate system. Internal sea-level variability is important because it can temporarily alter long-term sea-level trends. Essentially, internal sea-level acts as noise, obscuring the externally forced sea-level change. As such, it is the main source of uncertainty in local sea-level projections for the next few decades ([Palmer et al., 2020](#)). Sea-level variability therefore forms another important theme of this thesis and will be further introduced in Section 1.5.4.

1.5.2. Differences between GCMs

Ensembles of GCMs like the CMIP5 and CMIP6 ensembles typically consist of a few tens of models from modeling centers willing to participate. Such ensembles are therefore called ‘ensembles of opportunity’: unlike perturbed physics ensembles, they were not designed to fully and systematically sample uncertainty ([Tebaldi and Knutti, 2007](#)). Consequently, the spread between the GCMs in an ensemble does not necessarily reflect the true uncertainty of a quantity of interest. Subsequent ensembles of GCMs may well have different distributions of a variable, which af-

fects the sea-level projections derived from them. The different distributions of the climate sensitivity of the CMIP5 and CMIP6 ensembles form an important example. Primarily due to stronger positive cloud feedbacks, CMIP6 models tend to be more sensitive to radiative forcing than CMIP5 models (Zelinka et al., 2020), leading to higher projections of global mean surface air temperature increase (Forster et al., 2020). The implications of the differences between the CMIP5 and CMIP6 models for global mean sea-level projections will be studied in Chapter 2.

To develop sea-level projections, the simulations of all GCMs in an ensemble are typically weighted equally (e.g., Slangen et al., 2014; Kopp et al., 2014). This may not be the most appropriate strategy, since structural differences between GCMs introduce differences in model performance. Additionally, GCMs can be interdependent, especially when developed by the same modeling center or when based on the same code. Weighting schemes accounting for model performance and interdependence have been developed (e.g., Knutti et al., 2017; Brunner et al., 2020), but their application to sea-level projections remains largely unexplored. Weighting schemes have to rely on evaluating historical simulations. However, physically plausible relationships between historical performance metrics and future change ('emergent constraints') are challenging to determine (Eyring et al., 2019).

1.5.3. Using GCMs for coastal sea-level projections

The horizontal grid resolution of CMIP5 and CMIP6 models is typically around 100 km for the ocean and around 150-200 km for the atmosphere (see Chapters 3 & 5). Additionally, the number of vertical levels in most GCMs is limited, especially in the shallow parts of the ocean. Consequently, processes occurring at scales smaller than the grid resolution must be parameterized and small-scale topographic features cannot be represented. These are major limitations especially for shallow shelf seas, in which the coastline, bathymetric features and small-scale processes strongly influence the ocean dynamics. Examples are water transport along and across the shelf break, coastal upwelling and downwelling, mesoscale eddies, freshwater inflow and fronts, mixing, frictional boundary layers and ocean currents through narrow seas and channels (e.g., O'Dea et al., 2012; Holt et al., 2017). The limited resolution of GCMs also prevents them from resolving tides, waves and surges and their interaction with time-mean sea-level change. The dissipation of tidal energy is an important source of mixing in shelf seas. How these limitations affect coastal sea-level projections based on GCMs is not yet clear.

Running multiple centennial experiments with high-resolution GCMs is computationally very expensive. Alternatively, GCM simulations may be refined regionally using high-resolution regional models, a technique called dynamical downscaling. While dynamical downscaling is commonly applied for the atmosphere (e.g., Jacob et al., 2020), only few dynamical-downscaling studies have been carried out for sea-level change. High-resolution regional ocean models also offer the possibility to resolve tides, waves and surges. In Chapter 3, I therefore apply dynamical downscaling to two GCMs and study its impact on their simulations of ocean dynamic sea-level change and sea-level variability.

1.5.4. Sea-level variability and projections

Evaluating sea-level projections and determining the current pathway of sea-level change based on observations is important for adaptive coastal planning (Haasnoot et al., 2018, 2019). However, interannual to decadal sea-level variability complicates interpreting the discrepancies between sea-level projections and observations (e.g., Baart et al., 2018). Externally forced sea-level change can be estimated from the observations with higher confidence if internal sea-level variability is removed first (e.g., Calafat and Chambers, 2013; Haigh et al., 2014; Hamlington et al., 2019). In this context, a good understanding of the drivers of regional sea-level variability is important, motivating the research presented in Chapter 4.

The sea level does not only vary interannually to decadal, but also has a pronounced seasonal cycle at many locations, mainly driven by oceanic and meteorological effects (Tsimplis and Woodworth, 1994). However, sea-level projections are typically provided on an annual mean time scale, meaning that the seasonal sea-level cycle is filtered out. Consequently, potential changes in the characteristics of the seasonal sea-level cycle are not included. Chapter 5 explores this research gap by studying projections of seasonal mean sea-level change and its causes.

1.6. Thesis aims and outline

This thesis aims to improve our understanding of the uncertainties in sea-level projections based on GCMs, and of sea-level variability and its future changes, using a combination of global climate models and regional ocean models. The thesis starts by studying GMSL rise and then proceeds to investigate regional sea-level change (Figure 1.7), taking the Northwestern European Shelf (NWES) as an example study region. The NWES is a continental shelf northwest of Europe (Figure 1.8) and a typical example of a region which is not well represented in most GCMs. At the same time, the NWES is rich of oceanographic observations spanning long time periods (e.g., from PSMSL and the Copernicus Marine Service), which facilitates sea-level research and the evaluation of ocean models for this region.

The following research questions will be addressed in this thesis:

Chapter 2 - How do the global mean sea-level projections based on CMIP5 and CMIP6 models differ?

As discussed in Section 1.5.2, the distributions of the climate sensitivity of the CMIP5 and CMIP6 ensembles differ. Chapter 2 therefore investigates how the global mean sea-level projections based on these ensembles differ. First, the simulations of global mean thermal expansion and surface air temperature increase are compared. Next, these simulations are used to derive global mean sea-level projections using the methods of the Fifth Assessment Report of the IPCC (Church et al., 2013). The resulting projections are compared across the ensembles and across individual models, gaining insight into the implications of the increased climate sensitivity of CMIP6 models.

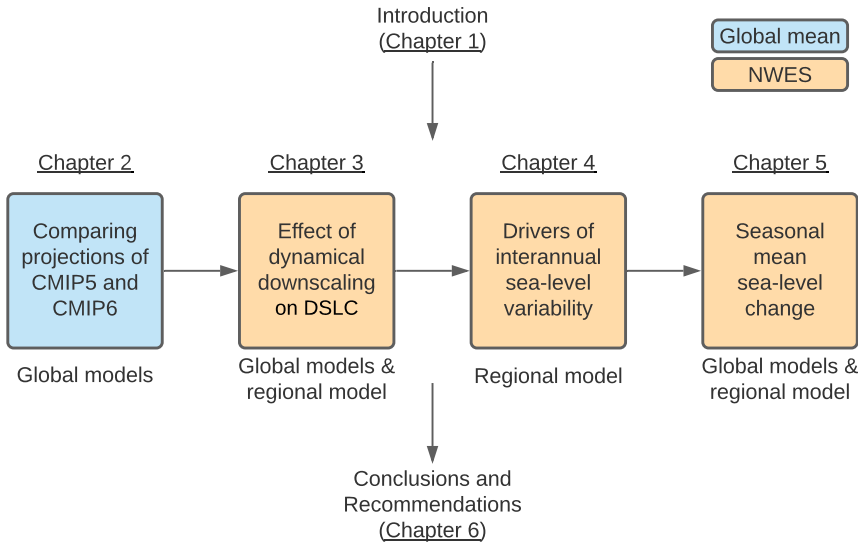


Figure 1.7: Overview of the topics of this thesis, highlighting the temporal and spatial scales studied and the types of models used in each chapter.

Chapter 3 - How does dynamical downscaling affect the simulations of ocean dynamic sea-level change of global climate models?

Moving to the regional scale, Chapter 3 focuses on the limitations of GCMs regarding their simulations of DSLC on the NWES (see Section 1.5.3). To this end, Chapter 3 uses a high-resolution regional ocean model to dynamically downscale the simulations of two CMIP5 models on and around the NWES. First, the original and downscaled simulations are evaluated against observations. Next, the simulations of future DSLC are compared to study the impact of dynamical downscaling. The impact of dynamical downscaling on the simulations of the time of emergence and changes in the seasonal sea-level cycle is also discussed.

Chapter 4 - What drives the interannual sea-level variability on the NWES?

Removing natural sea-level variability from observations helps to estimate externally forced sea-level change and to compare observed sea-level change with projections with higher confidence (Section 1.5.4). To this end, the respective roles of the different drivers of interannual sea-level variability need to be understood and quantified. In Chapter 4, I therefore perform sensitivity experiments with a high-resolution regional ocean model to investigate the drivers of the interannual sea-level variability on the NWES. The results complement prior observation-based studies and provide new insights into the spatial correlation pattern of sea level on the NWES.

Chapter 5 - How will seasonal mean sea level on the NWES change in the future?

Sea-level projections are often provided at an annual mean basis, which means that potential changes in the seasonal sea-level cycle are not considered (Section 1.5.4). Chapter 5 therefore studies the seasonality of future sea-level change on the NWES, using the simulations of an ensemble of CMIP6 models. The causal role of seasonal wind-stress change is investigated using experiments performed with the regional ocean model of Chapter 4. Additional model experiments are performed to study the ability of CMIP6 models to simulate the response of sea level on the NWES to regional wind-stress change, connecting the findings of Chapters 3 & 5.

In Chapter 6, I discuss the outcomes of my research and provide recommendations for future work.

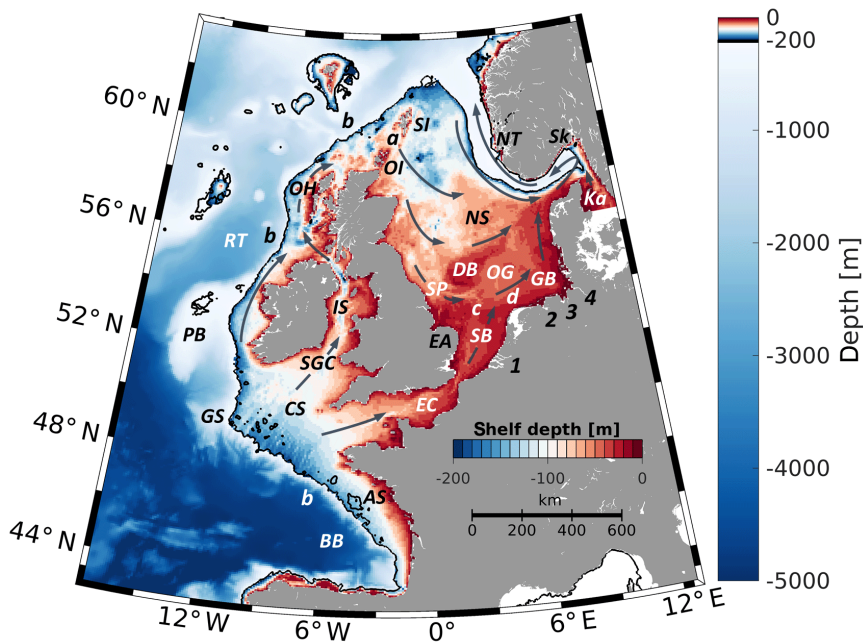


Figure 1.8: Bathymetry of the NWES and the surrounding North Atlantic Ocean, together with a schematic overview of the general circulation on the NWES (arrows). The black line indicates the 200 m isobath approximating the shelf break. Figure obtained from [Ricker and Stanev \(2020\)](#), their Figure 1. The abbreviations and numbers denote the "Armorican Shelf (AS), Bay of Biscay (BB), Celtic Sea (CS), Dogger Bank (DB), East Anglia (EA), English Channel (EC), German Bight (GB), Goban Spur (GS), Irish Sea (IS), Kattegat (Ka), North Sea (NS), Norwegian Trench (NT), Oyster Ground (OG), Outer Hebrides (OH), Orkney Islands (OI), Porcupine Bank (PB), Rockall Trough (RT), Skagerrak (Sk), Southern Bight (SB), St. George's Channel (SGC), Shetland Islands (SI), Silver Pit (SP), Fair Isle Current (a), European Slope Current (b), East Anglia Plume (c), Frisian Front (d), Rhine (1), Ems (2), Weser (3), and Elbe (4)" (p. 638) ([Ricker and Stanev, 2020](#)).

2

Projecting Global Mean Sea-Level Change Using CMIP6 Models

Abstract

The effective climate sensitivity (EffCS) of the models in the Coupled Model Inter-comparison Project 6 (CMIP6) has increased relative to CMIP5. We explore the implications of this for projections of global mean sea-level (GMSL) rise by 2100 for three emissions scenarios. CMIP6 projections of global surface air temperature are substantially higher than in CMIP5, but this is not the case for the projections of global mean thermal expansion. Using these projections as input to construct GMSL projections with the methods of the IPCC AR5, the 95th percentile projections of GMSL rise by 2100 only increase by 3-7 cm. The projected rates of GMSL rise around 2100 increase more strongly, though, implying more pronounced differences beyond 2100 and greater committed sea-level rise. Inter-model differences in GMSL projections indicate that EffCS-based model selection may substantially alter the ensemble projections. GMSL change in 2100 is accurately predicted by time-integrated temperature change, and thus requires reducing emissions early to be mitigated.

2.1. Introduction

Global mean sea level (GMSL) has risen by around 1.5 mm/yr since the 1960s (Dangendorf et al., 2017; Frederikse et al., 2018) and is projected to rise at an accelerated pace unless greenhouse gas emissions are substantially reduced (Oppenheimer et al., 2019). Limiting the adverse impacts of sea-level rise (Nicholls and Cazenave, 2010) requires accurate sea-level projections to underpin effective coastal decision making and adaptation planning. GMSL change results from both ocean density changes (steric sea-level change) and the exchange of mass (barystatic sea-level change) between the ocean and the cryosphere or the land. Global mean steric sea-level change is nearly equal to global mean thermal expansion (GTE), since global mean halosteric change is negligible (Gregory and Lowe, 2000; Gregory et al., 2019).

Ensembles of complex, coupled global climate models (GCMs), for example from the Coupled Model Intercomparison Project Phase 5 (CMIP5, Taylor et al., 2012), form the basis of many GMSL projections (e.g., Church et al., 2013; Kopp et al., 2014; Oppenheimer et al., 2019; Palmer et al., 2018b, 2020; Slangen et al., 2012, 2014). The Fifth Assessment Report of the Intergovernmental Panel on Climate Change (IPCC AR5) constructed a Monte Carlo ensemble of GMSL projections from CMIP5 simulations of GTE and global mean surface air temperature (GSAT), with GSAT-driven parameterizations of the surface mass balance components of land-based ice melt (Church et al., 2013). Several subsequent studies built on this approach (Oppenheimer et al., 2019; Palmer et al., 2018b, 2020), updating the contribution of the dynamics of the Antarctic ice sheet based on post-AR5 modeling studies.

The GSAT response to radiative forcing varies across GCMs according to the strength of different climate feedbacks, and can be characterized by estimates of climate sensitivity. In particular, equilibrium climate sensitivity (ECS) measures the GSAT response in GCMs upon reaching equilibrium following an instantaneous doubling of CO₂ concentration in the atmosphere. Since running coupled GCMs to equilibrium is computationally very expensive, ECS is often approximated with effective climate sensitivity (EffCS). EffCS is obtained through linearly regressing the top-of-atmosphere radiative flux anomaly on GSAT in idealized experiments in which a GCM has not yet reached equilibrium (Gregory et al., 2004).

The current generation of GCMs in CMIP6 (Eyring et al., 2016) has a positively skewed EffCS distribution, including multiple models with a higher EffCS than the CMIP5 range (2.1–4.7 K; Andrews et al., 2012) and the 5–95% range constrained by multiple lines of evidence (2.3–4.7 K; Sherwood et al., 2020). Consequently, CMIP6 models project a larger GSAT increase for a given emissions scenario (Forster et al., 2020). This has sparked an important debate about what model developments have caused the increase in EffCS and whether these developments have improved model physics. The increased EffCS in CMIP6 has been attributed to stronger positive cloud feedback (Meehl et al., 2020; Zelinka et al., 2020), and the representation of clouds has improved in several CMIP6 models compared to CMIP5 (e.g., Bodas-Salcedo et al., 2019; Gettelmann et al., 2019; Voldoire et al., 2019;

Bjordal et al., 2020; Swart et al., 2019; Williams et al., 2020). On the other hand, some high-EffCS CMIP6 models overestimate historical warming, suggesting their future warming may be too large (Brunner et al., 2020; Forster et al., 2020; Nijssen et al., 2020; Tokarska et al., 2020). Still, an EffCS higher than 5 K cannot be discounted as physically implausible (Bjordal et al., 2020). Thus, investigating the consequences of the increased EffCS in CMIP6 for projections of climate change is important.

Although multiple studies have investigated the consequences of the increased EffCS in CMIP6 for GSAT change projections, the consequences for GMSL projections have only been studied using a reduced complexity model (Vega-Westhoff et al., 2020). Here, we generate GMSL projections based on CMIP6 using the Monte Carlo approach of IPCC AR5 (Church et al., 2013), including both GTE and the GSAT-driven barystatic contributions, and compare these to CMIP5-based projections. Isolating the impact of CMIP6 simulations using consistent methods is an important step to ensure traceability to past IPCC projections of global and regional sea-level change. Given the complex correlations among different GMSL change components (Palmer et al., 2020), increased EffCS may not simply lead to increased GMSL projections. Additionally, the increased EffCS in CMIP6 motivates us to premise high-risk, low-probability GMSL projections on individual models, exploring high-end projections to a fuller extent than was previously possible with CMIP5.

In Section 2.3.1, we compare CMIP5 and CMIP6 projections of GTE and GSAT change, which form the input to the GMSL projections. Next, we investigate their relationship with EffCS in Section 2.3.2. We include their relationship with the transient climate response (TCR), another policy-relevant metric of climate sensitivity, in the supporting information. In Section 2.3.3, we compare CMIP5- and CMIP6-based GMSL projections and show GMSL projections based on individual CMIP6 models. Since we focus on the impact of increased EffCS on inter-ensemble and inter-model uncertainties using IPCC AR5 methods, we acknowledge but do not consider more recent insights into the potential instability of the Antarctic ice sheet (e.g., DeConto and Pollard, 2016; Edwards et al., 2019).

2.2. Data and methods

2.2.1. CMIP5 and CMIP6 model data

We use monthly mean CMIP5 GTE and GSAT data ('zostoga' and global area-weighted mean 'tas' variables) from the IPCC AR5 (Church et al., 2013) for the representative concentration pathways (RCPs, Meinshausen et al., 2011) 8.5, 4.5 and 2.6. This ensemble contains 21 models from 13 modeling centers. For three models, the RCP2.6 data was not provided and instead emulated by IPCC AR5 using the simple climate model of Good et al. (2011, 2013).

The CMIP6 data were downloaded from the Earth System Grid Federation (ESGF) for three shared socioeconomic pathways (SSPs, O'Neill et al., 2014). We picked SSPs with high fossil-fueled, middle-of-the-road and sustainable-development narratives, with nameplate radiative forcing in 2100 approximately corresponding with the

forementioned RCPs. Thus, we use the RCP-SSP pairs SSP5-RCP8.5, SSP2-RCP4.5 and SSP1-RCP2.6, respectively. Only for the CMIP6 model CanESM5, both RCP- and SSP-forced simulations were available from ESGF. The median GSAT change in 2081-2100 (relative to 1986-2005) of the 5 RCP-forced and 25 SSP-forced variants of CanESM5 differ by 0.27, 0.19 and -0.15 K (SSP minus RCP) for SSP5-RCP8.5, SSP2-RCP4.5 and SSP1-RCP2.6, respectively. These differences are likely smaller for the multi-model mean, so based on this preliminary comparison we assume that differences in GSAT change between CMIP5 and CMIP6 are mainly due to increased EffCS (following [Forster et al. \(2020\)](#)). Differences between RCPs and SSPs may have a larger relative effect on GTE, because the inter-ensemble differences in GTE are smaller (Section 2.3.1).

Our CMIP6 ensemble includes 20 models from 12 modeling centers (Table S2.1). For these models both GTE and GSAT were available by November 2nd, 2020, for the historical simulation (1850-2014) and all three emissions scenarios (2015-2100). We use the first available simulation variant ('ripf', Table S2.1) of each model. Additionally, we require models to provide fully overlapping pre-industrial control runs for GTE to allow us to correct for model drift, and the idealized model experiments required to compute EffCS and TCR (see Section 2.2.2). All CMIP6 GCMs providing GSAT but not necessarily GTE ($n=31$, Table S2.1) are used for context in Figures S2.2, S2.3 and Table S2.3.

We corrected GTE for model drift, which can arise from the slow adjustment of the deep ocean to initial conditions and/or imperfect representation of energy conservation in the model simulations ([Hobbs et al., 2016](#); [Sen Gupta et al., 2013](#)). To remove drift, we apply a least-squares quadratic fit to the full control experiment of each model and subtract the overlapping part of the fit from the historical and scenario runs. Although we chose a quadratic fit for consistency with IPCC AR5 ([Church et al., 2013](#)), the drift is nearly linear for most CMIP6 models (Figure S2.1). This is consistent with the analysis of [Hobbs et al. \(2016\)](#) for CMIP5 models. The difference between linear and quadratic drift-correction (2081-2100 minus 1986-2005) is largest for INM-CM5-0 (0.32 cm), which is small compared to the projected GTE (8-37 cm; Figure 2.1). Finally, the monthly mean GTE and GSAT data were annually averaged.

2.2.2. Calculating EffCS and TCR

The EffCS and TCR of the CMIP5 models were obtained from [Andrews et al. \(2012\)](#) and [Forster et al. \(2013\)](#), respectively. For the CMIP6 models, we compute these using the same methods (see Table S2.1 for the results). Namely, to obtain EffCS, for each GCM we linearly regress the top-of-atmosphere radiative flux anomaly ΔN on GSAT over 150 simulation years in experiments of abrupt CO₂ quadrupling. ([Gregory et al., 2004](#)). We use the CO₂ quadrupling instead of doubling experiment, because the signal-to-noise ratio is higher. Additionally, we assume that the 4xCO₂ forcing is equal to twice the 2xCO₂ forcing and that the climate feedback parameter is constant. Extrapolating ΔN to zero to approximate equilibrium, EffCS is found as 0.5 times the x-intercept. EffCS underestimates ECS in GCMs because the net

climate feedback becomes less effective at restoring radiative equilibrium over time (Andrews et al., 2012; Rugenstein et al., 2020). Nevertheless, EffCS is a widely used metric relevant to 21st-century climate change (Grose et al., 2018) and thus a useful basis of comparison between CMIP5 and CMIP6. To obtain TCR, we compute the mean GSAT change in the simulation years 61–80 in experiments of 1% CO₂ increase per year (i.e., the window centered around the time of CO₂ doubling). For the CMIP5 model MIROC-ESM-CHEM, these idealized model experiments were not available.

2.2.3. GMSL projection methodology

To ensure traceability to previous GMSL projections, we compute CMIP6-based projections using the same approach as in IPCC AR5 (Church et al., 2013). For each emissions scenario, we generate a 450,000-member Monte Carlo ensemble of GMSL projections. These projections contain the contributions of thermal expansion, land-ice mass changes and land-water storage changes. The inputs to these projections are the time-dependent CMIP6 mean and standard deviation of GTE and GSAT change, from which 450 samples are drawn (see Section 2.5.3 and the flowchart therein for details). Through parameterization schemes (Section 2.5.3), the contribution of glaciers and the surface mass balance of the Greenland and Antarctic ice sheets depend on GSAT change, while the other barystatic contributions depend only on time. For comparison with the projections of Palmer et al. (2020), and indirectly with the projections of Oppenheimer et al. (2019), we also use an alternative parameterization of Antarctic dynamical ice discharge based on the projections of Levermann et al. (2014).

For each GTE and GSAT sample pair, one thousand samples are generated to represent methodological uncertainty in the parameterization schemes. This results in an ensemble of GMSL projections of 450x1,000=450,000 members. These projections converge with a 0.01 m uncertainty for GMSL change and its components and with a 0.1 mm/yr uncertainty for its rate (Church et al., 2013). Thus, subsequently computed GMSL projections can differ randomly by these amounts. We present a flowchart and a summary of the methods in Section 2.5.3, and refer to Church et al. (2013) and Palmer et al. (2020) for further information.

Finally, we also derive GMSL projections based on the GTE and GSAT simulations of each of the 20 CMIP6 models individually (Section 2.5.3). This results in 20 ensembles of one thousand members each, which allow us to study inter-model uncertainty related to EffCS. Additionally, equally weighting all models these ensembles can be joined into a 20,000-member ensemble to test the sensitivity to the assumptions made in constructing the 450,000-member ensemble (Section 2.3.3).

2.3. Results

2.3.1. Comparing CMIP5 and CMIP6 projections of GTE and GSAT change

We first compare CMIP5 and CMIP6 GTE and GSAT change projections, which form the input to the GMSL projections in Section 2.3.3. Despite the increased EffCS in CMIP6, the CMIP5 and CMIP6 ensemble means and medians of GTE, averaged over the period 2081-2100, are similar (Figures 2.1a-c & key statistics in Table S2.2). The 5-95% range has widened from CMIP5 to CMIP6, particularly toward lower values, mainly due to the GTE projections of INM-CM4-8 (EffCS=1.82 K) and INM-CM5-0 (EffCS=1.92 K). Relative to CMIP5, the 95th percentiles of CMIP6 GTE increased by 1 cm (+4, +5, and +3%) under SSP5-RCP8.5, SSP2-RCP4.5 and SSP1-RCP2.6, respectively. The 5th percentiles of GTE correspondingly decreased by 4, 2 and 2 cm (-17, -13 and -22%). However, a two-sided Kolmogorov-Smirnov test suggests we cannot reject the null hypothesis that the CMIP5 and CMIP6 GTEs are drawn from the same underlying distribution ($p \geq 0.05$, Figure S2.2).

In contrast to GTE, the mean, median and 5-95% range of CMIP6 GSAT change are substantially higher than in CMIP5 for all emissions scenarios (Figures 2.1d-f & Table S2.2). The CMIP6 medians, averaged over 2081-2100, are 0.80, 0.60 and 0.43 K higher than for CMIP5 for SSP5-RCP8.5, SSP2-RCP4.5, and SSP1-RCP2.6, respectively (+22, +31 and +41%; the relative difference due to increased EffCS could be larger in stabilization scenarios because the ocean heat uptake (OHU) efficiency declines faster than in higher emissions scenarios). Relative to CMIP5, the 95th percentile changes of CMIP6 increased by 1.36, 0.91 and 0.55 K (+29, +35 and +31%). Nevertheless, the CMIP5 and CMIP6 distributions of GSAT change are only statistically different for SSP2-RCP4.5 ($p < 0.05$, Figure S2.2). However, this does not mean that the inter-ensemble differences for SSP5-RCP8.5 and SSP1-RCP2.6 are unimportant.

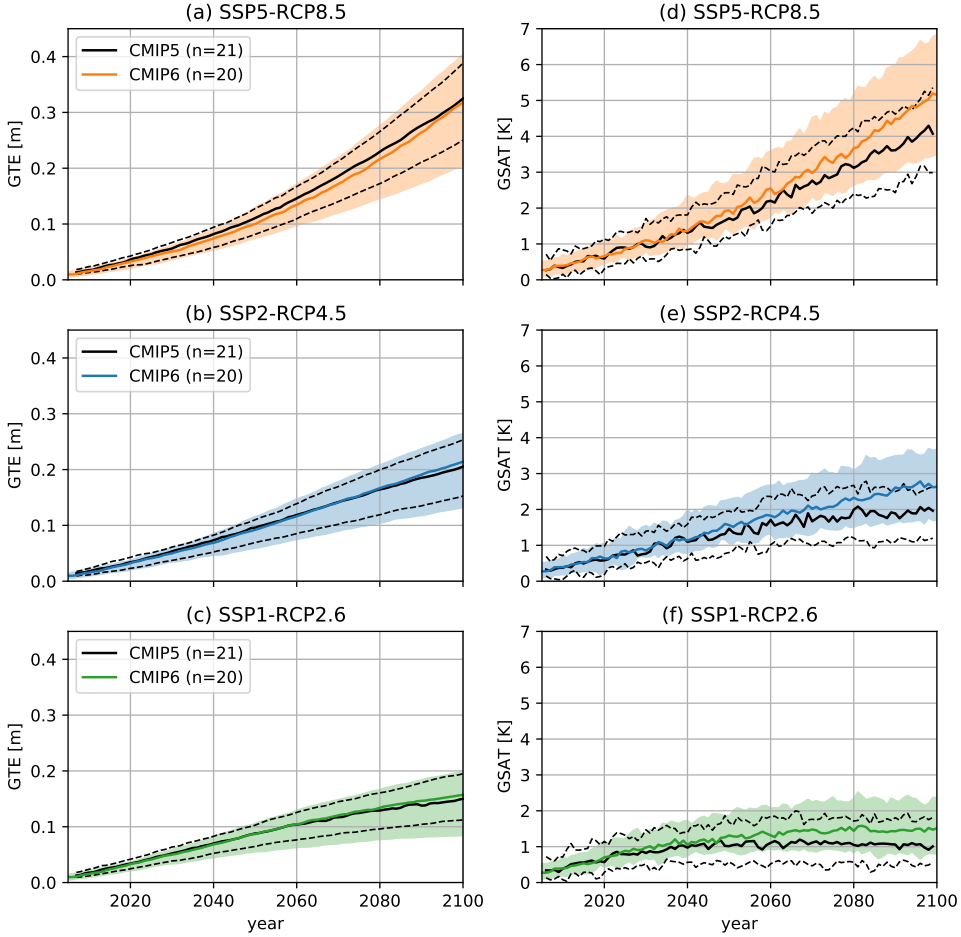


Figure 2.1: Ensemble median (CMIP6: colored solid lines; CMIP5: black solid lines) and 5-95% range (CMIP6: colored shaded area; CMIP5: black dashed lines) of **(a-c)** global mean thermal expansion [GTE, m] and **(d-f)** global mean surface air temperature [GSAT, K] change of the 20-member CMIP6 and 21-member CMIP5 ensembles, relative to the 1986-2005 average, for SSP5-RCP8.5 (orange, **a/d**), SSP2-RCP4.5 (blue, **b/e**) and SSP1-RCP2.6 (green, **c/f**).

2.3.2. Relation of GTE and GSAT change with climate sensitivity

The 20-member CMIP6 ensemble has a higher median EffCS and TCR than the CMIP5 ensemble (4.04 and 2.00 K compared to 3.50 and 1.88 K, respectively), and spans a larger range (EffCS of 1.83-5.62 K compared to 2.08-4.67 K; Table S2.2). However, insufficient evidence exists for significant statistical difference between the CMIP5 and CMIP6 distributions (Figure S2.3). Nevertheless, the higher upper tail of CMIP6 motivates investigating the differences further.

To interpret the inter-ensemble differences in GTE and GSAT change given the increased climate sensitivity in CMIP6, we linearly regress GTE and GSAT change in 2081-2100 on EffCS (Figure 2.2). We find statistically significant linear relationships with EffCS for both GTE (Figures 2.2a-c) and GSAT change (Figures 2.2d-f), except for CMIP5 GTE under SSP1-RCP2.6 (Figure 2.2c). Thus, EffCS is a relevant metric for 21st-century climate change. However, since EffCS represents the GSAT response to CO₂-doubling, it explains much but not all of the inter-model variance of GSAT change in emissions scenarios with multiple forcing agents (Figures 2.2d-f, R^2 values). The role of OHU in determining the tendency of the curve of GSAT against EffCS to flatten for increasing EffCS likely causes the non-zero y-intercepts.

Linear regression against EffCS explains much less of the variance of GTE than of GSAT change (10-63% versus 59-91%; Figure 2.2). While GTE correlates positively with GSAT change ($r=0.59-0.80$; Figure S2.5), GTE is also controlled by the ocean dynamics governing OHU and expansion efficiency, which cause inter-model spread (Melet and Meyssignac, 2015). For example, OHU in CMIP6 models could partially occur in regions contributing little to increased GSAT change, or be driven by wind-driven subduction unrelated to GSAT change. Aspects like these could explain why GTE projections have not substantially increased from CMIP5 to CMIP6, despite the increased EffCS.

For both GTE and GSAT change, the correlations with EffCS are higher for higher emissions scenarios (Figure 2.2), consistent with previous results for GSAT change in CMIP5 (Große et al., 2018). The reason is likely the larger ratio of forced signal to internal variability for higher emissions scenarios (Lyu et al., 2015). Additionally, more of the inter-model variance of CMIP6 than of CMIP5 is explained by EffCS for all emissions scenarios, suggesting that the increased spread of EffCS causes the increased spread of GTE and GSAT change (Table S2.2). The correlations of both GTE and GSAT change with TCR are lower than with EffCS (Figure S2.4), consistent with previous CMIP5-based studies (Gregory et al., 2015; Große et al., 2018, 2016). Thus, TCR is less useful than EffCS for characterizing GMSL projections.

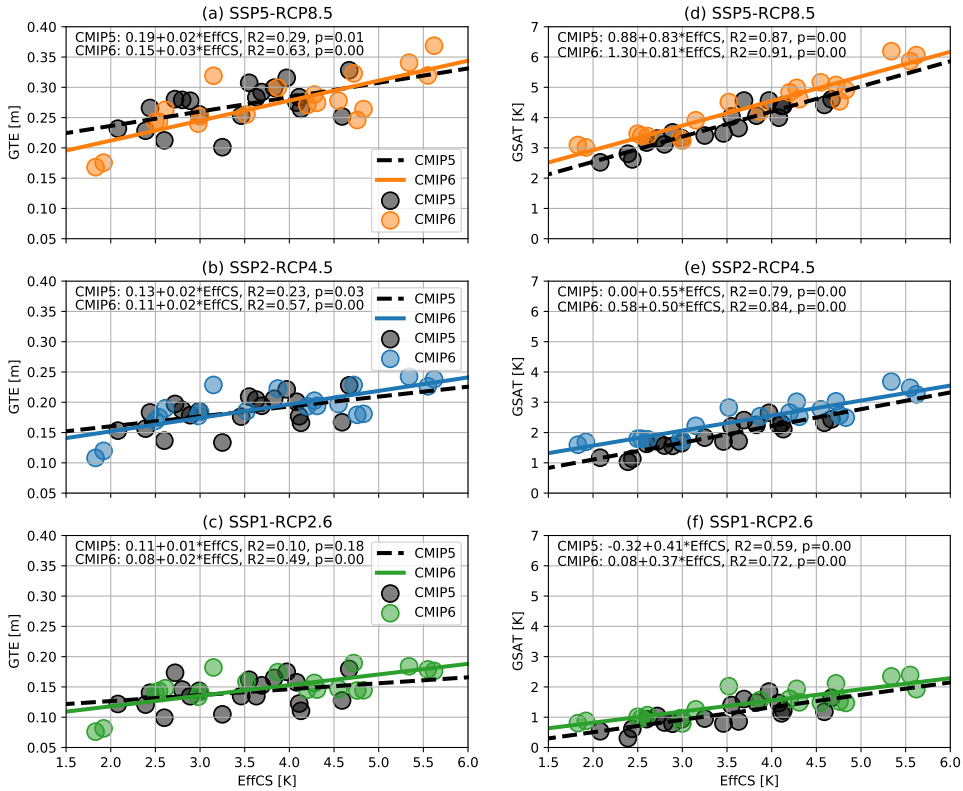


Figure 2.2: (a-c) Global mean thermal expansion [GTE, m] and (d-f) global mean surface air temperature [GSAT, K] change (2081-2100 minus 1986-2005) of the CMIP6 (colored circles) and CMIP5 (black circles) models against their effective climate sensitivity [EffCS, K], together with a least-squares linear regression (CMIP6: colored, solid; CMIP5: black, dashed) on EffCS for SSP5-RCP8.5 (orange, a/d), SSP2-RCP4.5 (blue, b/e) and SSP1-RCP2.6 (green, c/f). The intercept, slope, R-squared and p-value of the regression are indicated in each panel.

2.3.3. CMIP6-based GMSL projections

Applying the IPCC AR5 methods (Church et al., 2013) to the CMIP6 simulations results in ensemble-median projections of GMSL rise of 0.76, 0.56 and 0.47 m in 2100 for SSP5-RCP8.5, SSP2-RCP4.5 and SSP1-RCP2.6, respectively (Figures 2.3a-c; see Table S2.4 for 2081-2100 and Table S2.5 for a component breakdown). This represents a modest increase of 2, 3 and 3 cm (+3, +6 and +7%) relative to CMIP5. The 5-95% range shifted up from 0.52-0.98, 0.36-0.71 and 0.28-0.61 m to 0.52-1.05, 0.38-0.76 and 0.30-0.64 m, respectively. For the 95th percentile, this is an increase of 7, 5 and 3 cm (+7, +7 and +5%). In comparison, the projected rates of GMSL rise (average rates during 2095-2100) increase more strongly: 1.4, 0.9 and 0.4 mm/yr for the medians (+12, +15 and +9%) and 3.5, 1.6 and 0.5 mm/yr for the 95th percentiles (+21, +18 and +8%), respectively. Projections made with the methods of Palmer et al. (2020) show a comparable increase from CMIP5 to CMIP6 (Figure S2.6). Thus, updating existing GMSL projections with CMIP6 data affects projections for 2100 only moderately, but has a more pronounced impact beyond 2100.

To study inter-model differences, we also generate GMSL projections based on the 20 individual CMIP6 models directly (explained in Sections 2.2.2 & 2.5.3). The 5-95% range for individual models can fall substantially outside the CMIP6 ensemble 5-95% range (Figure S2.7) and may therefore be used to describe the outer envelope of GMSL projections. Large inter-model differences exist: the CMIP6 model with the highest EffCS (CanESM5; Swart et al., 2019) projects 5-95% ranges of 0.81-1.24, 0.51-0.82, and 0.39-0.67 m for SSP5-RCP8.5, SSP2-RCP4.5 and SSP1-RCP2.6, respectively, whereas the model with the lowest EffCS (INM-CM4-8; Volodin and Gritsun, 2018) projects 0.43-0.73, 0.29-0.56 and 0.23-0.48 m (Figures 2.3a-c).

The differences between the 20,000-member ensemble consisting of the individual model projections combined (20x1,000) and the 450,000-member ensemble of GMSL projections constructed by sampling from GTE and GSAT change (Section 2.5.3) are mostly below the random uncertainty of the Monte Carlo method. However, the 5-95% range of the thermal expansion of the 20,000-member ensemble is around 2 cm lower than that of the 450,000-member ensemble because the GTE distribution of CMIP6 is negatively skewed (Figures 2.1a-c). Thus, the assumptions made in constructing the 450,000-member ensemble (i.e., that GTE and GSAT change are normally distributed and perfectly correlated to one another) are reasonable but imperfect. The actual correlation structure (Figure S2.5) can be preserved by directly sampling from the CMIP6 ensemble, but the number of models is likely insufficient for a proper representation.

For both CMIP5 and CMIP6, the relationship between the median projection of GMSL and GSAT change becomes less linear toward 2100 under most scenarios (Figure 2.3d). In contrast, GMSL change and the time-integrated (cumulative sum of) GSAT change have a nearly linear and approximately scenario-independent relationship toward 2100 (Figure 2.3e). We explain why and discuss the implications for mitigation in the next section.

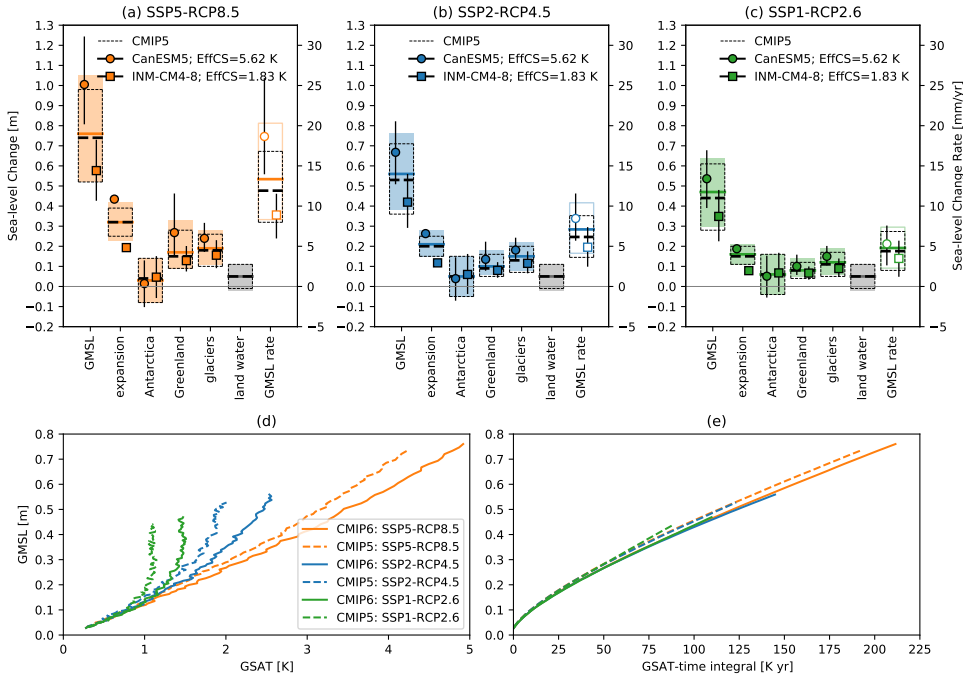


Figure 2.3: CMIP6-based projections of global mean sea-level (GMSL) change and its components in 2100 relative to 1986-2005 [m] and the average rate during 2095-2100 [mm/yr], computed using IPCC AR5 methods, for **(a)** SSP5-RCP8.5 (orange), **(b)** SSP2-RCP4.5 (blue) and **(c)** SSP1-RCP2.6 (green), overlaid by CMIP5-based projections (Church et al., 2013, Table 13.SM.1); and the CMIP6 (solid curves) and CMIP5 (dashed curves) ensemble-median GMSL change [m] against **(d)** ensemble-median GSAT [K] and **(e)** time-integrated ensemble-median GSAT change [K yr] for 2007-2100, for the same emissions scenarios. The colored solid lines and boxes in **(a-c)** represent the CMIP6 ensemble-medians and 5-95% ranges, and the black dashed lines those for CMIP5. The symbols and whiskers represent the median and 5-95% for the two CMIP6 models with the highest and lowest EffCS, respectively. Note the secondary y-axes for the average rate of GMSL change.

2.4. Discussion and conclusions

The increased EffCS in CMIP6 translates into substantially higher (e.g., 0.82, 0.56 and 0.41 K for the medians) projections of 21st-century GSAT change than the CMIP5 GSAT change for SSP5-RCP8.5, SSP2-RCP4.5 and SSP1-RCP2.6, consistent with previous findings (Forster et al., 2020; Tokarska et al., 2020). However, the differences between the CMIP5- and CMIP6-based GMSL projections are relatively modest. Updating the IPCC AR5 projections with CMIP6 input leads to 5-95% ranges of 0.52-1.05, 0.38-0.76 and 0.30-0.64 m in 2100 for SSP5-RCP8.5, SSP2-RCP4.5 and SSP1-RCP2.6, respectively. The medians have increased by 2-3 cm only and the 95th percentiles by 3-7 cm (see Table S2.4 for the projections of other studies that used IPCC AR5 methods). This is caused by multiple factors.

First, a higher GSAT increase results in a lower Antarctic GMSL contribution through increased snowfall accumulation. Moreover, the total land-ice contribution to GMSL is a (nearly linear) function of time-integrated GSAT change, since the rate of ice mass loss from the Greenland and Antarctic ice sheets and glaciers is related to GSAT change (Section 2.5.3). Since the relative difference in time-integrated GSAT change between CMIP5 and CMIP6 is smaller than the relative difference in GSAT change itself, the relative difference in GMSL rise in 2100 is also smaller. This additionally explains why projected GMSL rise rates around 2100 increase considerably from CMIP5 to CMIP6 (Figures 2.3a-c), implying that GMSL projections beyond 2100 (e.g., Nauels et al., 2017; Palmer et al., 2018a, 2020) will be affected more strongly by the increased EffCS. It also implies that time-integrated GSAT change up to 2100 is a better and more scenario-independent descriptor of the total GMSL rise in 2100 than the GSAT change in 2100. The approximate proportionality between the rate of OHU and GSAT change (Gregory et al., 2015; Gregory and Mitchell, 1997) further contributes to this. To minimize the time-integral of GSAT change, emissions should be reduced early (e.g., Mengel et al., 2018), making time-integrated emissions metrics more relevant for GMSL rise targets than endpoint metrics (Collins et al., 2020; Oliv   and Peters, 2013).

Second, GTE is not substantially higher in CMIP6 than in CMIP5 and correlates with EffCS less strongly than GSAT change (Section 2.3.2). Given the increase in GSAT change, our results suggest that the average OHU efficiency (e.g., Kuhlbrodt and Gregory, 2012) in CMIP6 is lower than in CMIP5. While the reasons for this are unclear (it could reflect increases in mean ocean stratification or differences in the patterns of projected surface warming), the inter-model differences in OHU efficiency may be dominated by the inter-model differences in the representation of ocean circulation processes (Newsom et al., 2020). Also, larger differences in GTE may only emerge after 2100, given the slow response of the deep ocean (Geoffroy and Saint-Martin, 2013; Held et al., 2010).

Third, the effect of the high EffCS in some CMIP6 models on differences between CMIP5 and CMIP6 is partially balanced by the very low EffCS in others, such as INM-CM4-8 and INM-CM5-0. Thus, the lower end of the CMIP6 EffCS distribution also needs to be scrutinized. Additionally, the 20 models in our CMIP6 ensemble come

from only 12 different modeling centers. Consequently, model weighting based on model interdependence (e.g., [Brunner et al., 2020](#)) may influence our results.

For consistency between GTE and GSAT change (Section 2.5.3), we only used CMIP6 models that provide simulations of both GTE and GSAT. Since the ensemble-mean GSAT change of all 31 CMIP6 models providing GSAT simulations is 0.11–0.24 K lower than that of the 20-member CMIP6 ensemble (Table S2.3), our GMSL projections might change when GTE simulations from additional models become available. Alternatively, for these models GTE could be derived from ocean temperature simulations (e.g., [Lorbacher et al., 2015](#); [Melet and Meyssignac, 2015](#)), or by emulation with simple climate models (e.g., [Geoffroy and Saint-Martin, 2013](#); [Good et al., 2013](#); [Palmer et al., 2018a](#)).

Although the EffCS range of CMIP6 lies partially outside the range recently assessed by the World Climate Research Programme ([Sherwood et al., 2020](#)), the increased EffCS appears to result from an improved representation of the atmosphere in at least some of the CMIP6 models (e.g., [Gettelmann et al., 2019](#); [Bjordal et al., 2020](#); [Williams et al., 2020](#)). Even though the differences in GMSL projections for 2100 between CMIP5 and CMIP6 are modest, the uncertainty around what constitutes EffCS in GCMs combined with the interest of risk-averse stakeholders in low-probability/high-impact GMSL projections ([Hinkel et al., 2019](#); [Stammer et al., 2019](#)) clearly motivates exploring the outer envelope of GMSL projections by premising projections on individual CMIP6 GCMs (Figures 2.3a–c & S2.7).

If the real world behaves as simulated with CanESM5 (highest EffCS of CMIP6: 5.62 K), we cannot exclude a GMSL rise of 1.24 m for SSP5-RCP8.5 with more than 95% confidence based on the methods of the IPCC AR5. This is 51 cm more than for INM-CM4-8 (lowest EffCS of CMIP6: 1.83 K). Incorporating marine ice cliff instability in Antarctica in our projections may further augment this difference ([Vega-Westhoff et al., 2020](#)). Thus, the choice between characterizing the central part of the probability distribution and more comprehensively sampling the high end of the GMSL projection space, through subsetting the CMIP6 ensemble using EffCS, has a substantial impact on GMSL projections. Our results underline the need to constrain EffCS, GTE and GSAT in global climate models in order to better characterize the uncertainty in sea-level projections.

2.5. Supplementary information

2.5.1. Supplementary figures

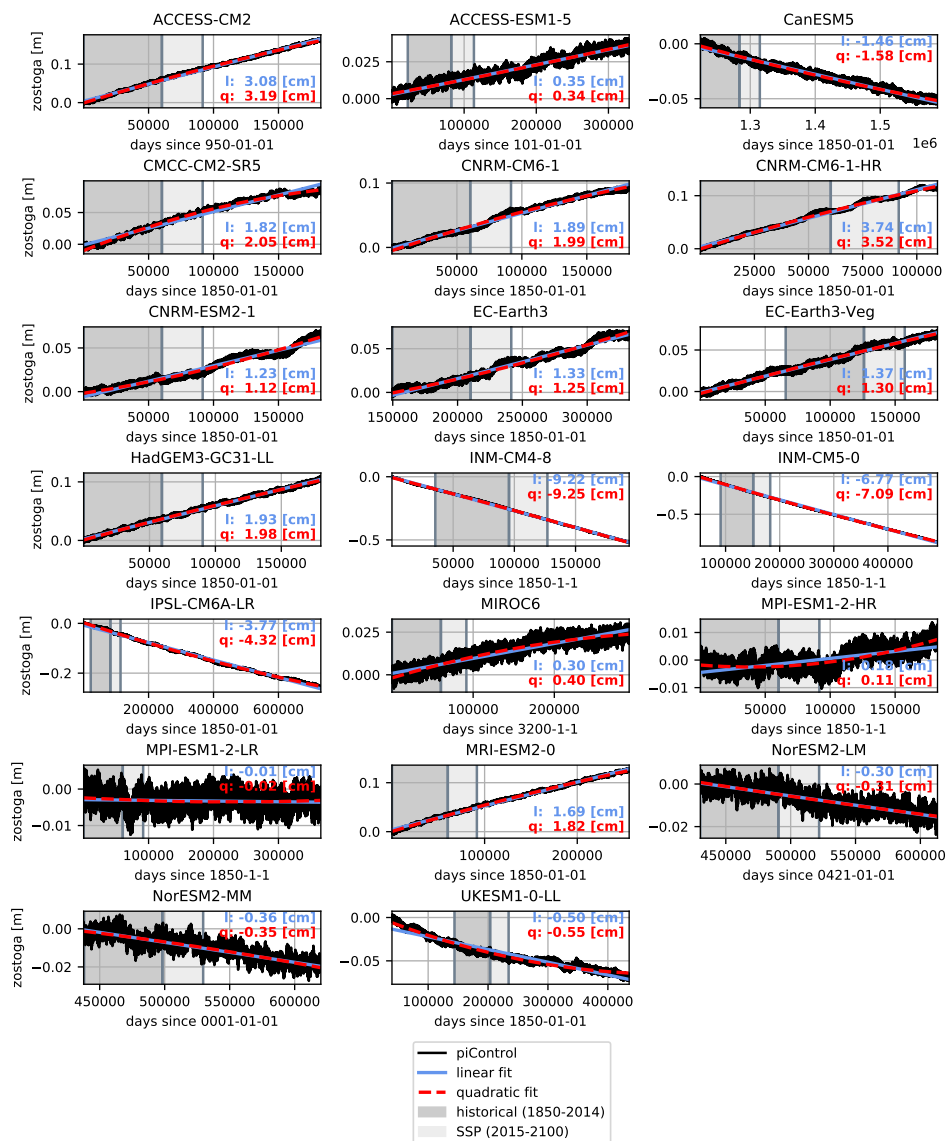


Figure S2.1: Pre-industrial control time series of GTE ('zostoga') [m] (black) for the 20 CMIP6 models used in this study and linear (blue, solid) and quadratic (red, dashed) polynomials fitted to the control runs for dedrifting. The total linear (blue text) and quadratic drift (red text) in 2081-2100 relative to 1986-2100 is indicated in [cm]. The overlap of the control run with the historical and scenario runs is indicated with the grey and light grey boxes.

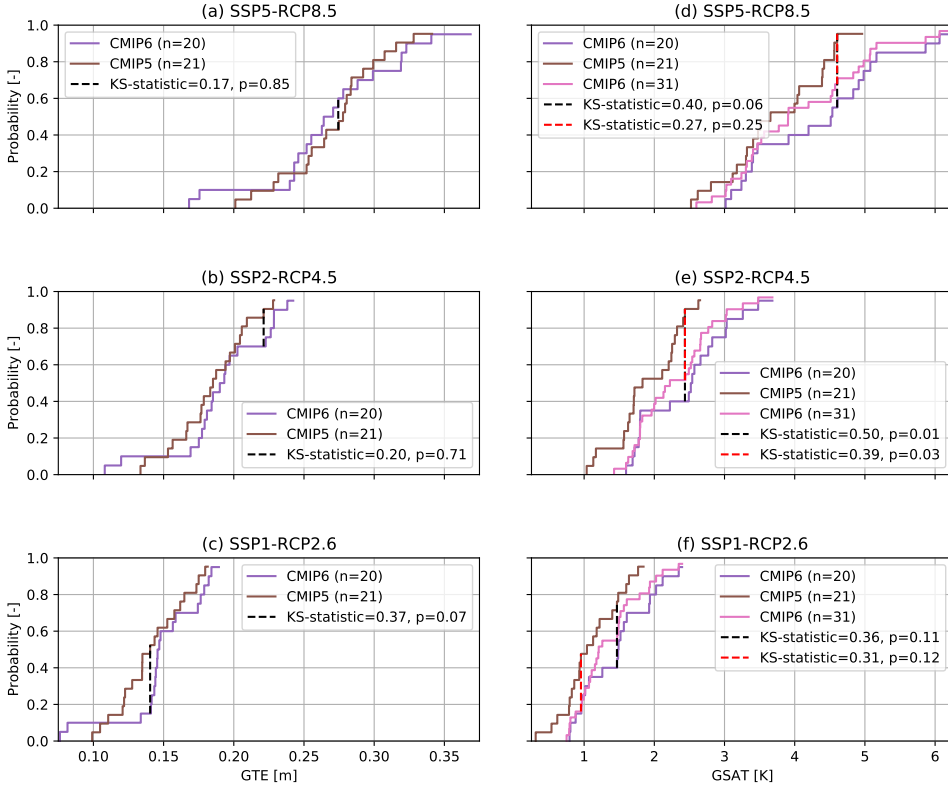


Figure S2.2: Cumulative distribution functions (CDFs) of the **(a-c)** global mean thermal expansion [GTE, m] and **(d-f)** global mean surface air temperature [GSAT, K] change in 2081-2100 relative to 1986-2005 for the 20-member CMIP6 ensemble, the IPCC AR5 CMIP5 ensemble (n=21), and the CMIP6 ensemble with all models that provide GSAT simulations (n=31), for SSP5-RCP8.5, SSP2-RCP4.5 and SSP1-RCP2.6. The Kolmogorov-Smirnov test statistics (i.e., the maximum difference between two CDFs) and corresponding p-values are indicated. A small p-value implies high confidence in that the maximum distance between two CDFs drawn from the same underlying distribution will not exceed the reported test statistic.

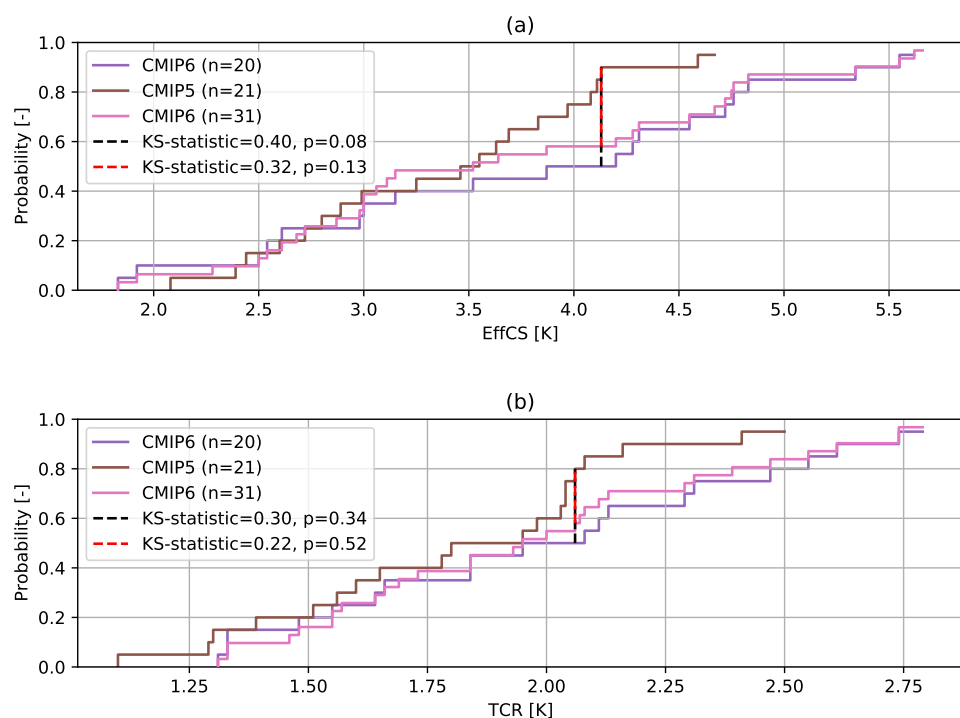


Figure S2.3: Cumulative distribution functions (CDFs) of the **(a)** effective climate sensitivity [EffCS, K] and **(b)** transient climate response [TCR, K] for the 20-member CMIP6 ensemble, the IPCC AR5 CMIP5 ensemble (n=21), and the CMIP6 ensemble with all models that provide GSAT simulations (n=31). The Kolmogorov-Smirnov test statistics (i.e., the maximum difference between two CDFs) and corresponding p-values are indicated. A small p-value implies high confidence in that the maximum distance between two CDFs drawn from the same underlying distribution will not exceed the reported test statistic.

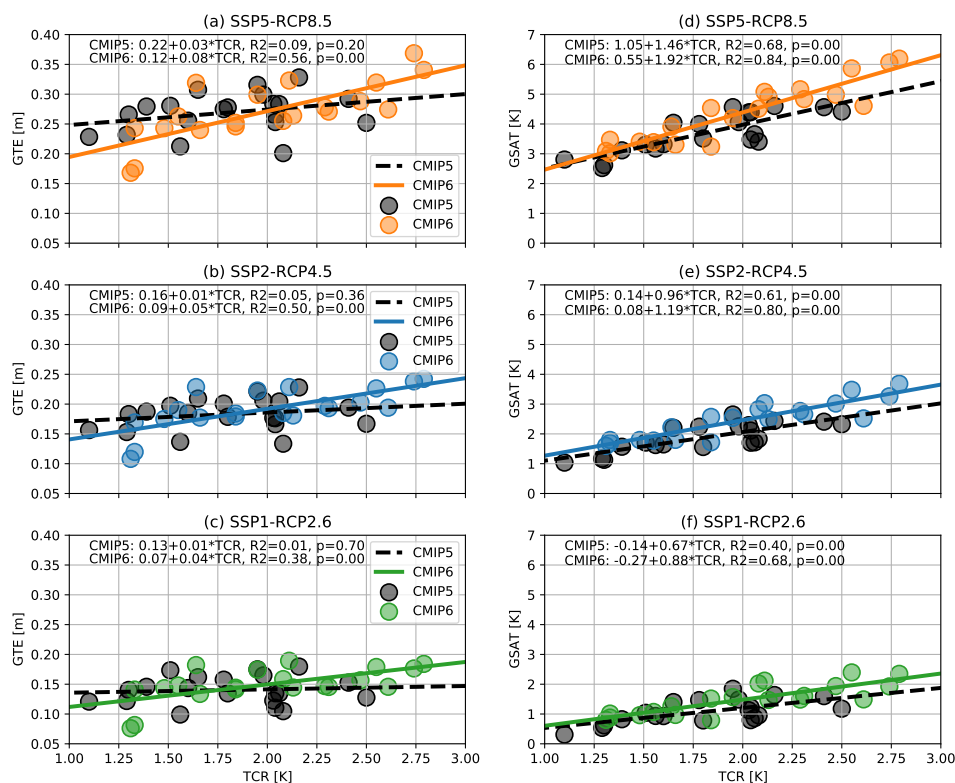


Figure S2.4: (a-c) Global mean thermal expansion [GTE, m] and (d-f) global mean surface air temperature [GSAT, K] change (mean 2081-2100 minus 1986-2005) of the CMIP6 (colored circles) and CMIP5 (black circles) models against their transient climate response [TCR, K], together with a least-squares linear regression (CMIP6: colored, solid; CMIP5: black, dashed) against TCR for SSP5-RCP8.5 (orange, a/d), SSP2-RCP4.5 (blue, b/e) and SSP1-RCP2.6 (green, c/f). The intercept, slope, R-squared and p-value of the regression are indicated in each panel.

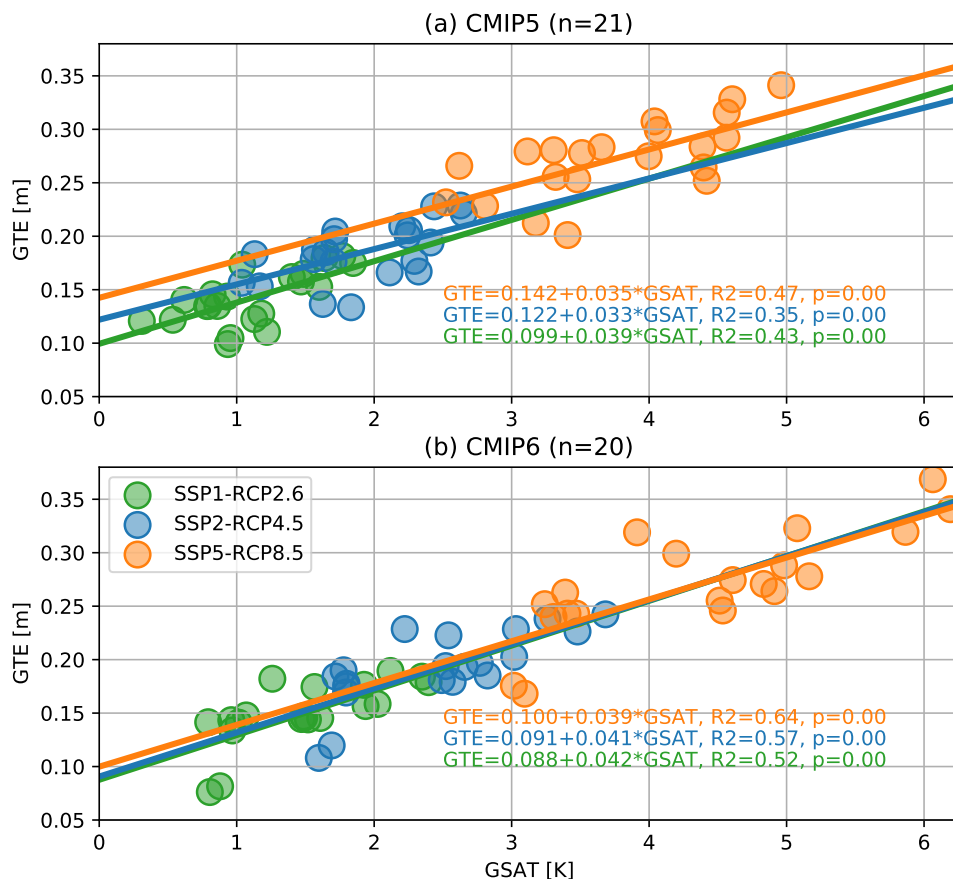


Figure S2.5: Least-squares linear regression of global mean thermal expansion [GTE, m] against global mean surface air temperature [GSAT, K] change (mean 2081-2100 minus 1986-2005) for **(a)** the 21-member CMIP5 ensemble and **(b)** the 20-member CMIP6 ensemble, for SSP5-RCP8.5 (orange), SSP2-RCP4.5 (blue) and SSP1-RCP2.6 (green). The intercept, slope, R-squared and p-value of the regression for each emissions scenario are indicated.

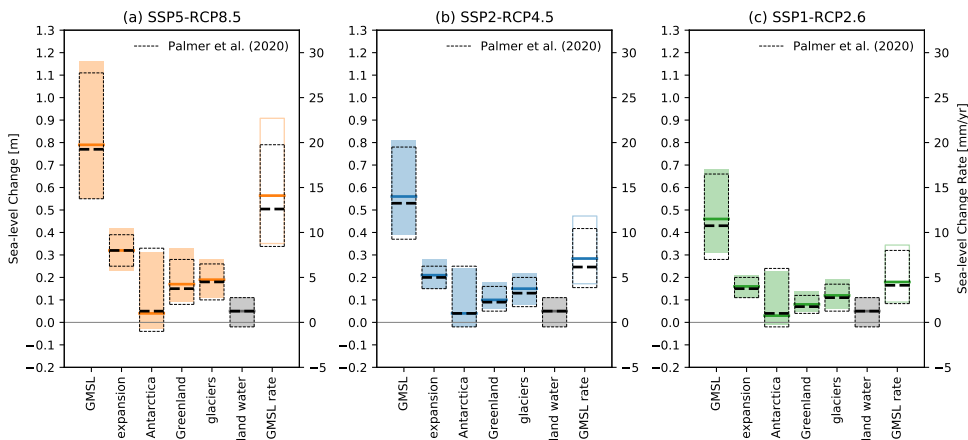


Figure S2.6: CMIP6-based projections of global mean sea-level (GMSL) change and its components in 2100 relative to 1986-2005 [m] and the average rate during 2095-2100 [mm/yr], computed using IPCC AR5 methods with (Levermann et al., 2014) parameterizations for Antarctic ice dynamics, for (a) SSP5-RCP8.5 (orange), (b) SSP2-RCP4.5 (blue) and (c) SSP1-RCP2.6 (green), overlaid by the projections of Palmer et al. (2020) (black dashed lines). The colored solid lines and boxes represent the CMIP6 ensemble-medians and 5-95% ranges, and the black dashed lines those of Palmer et al. (2020).

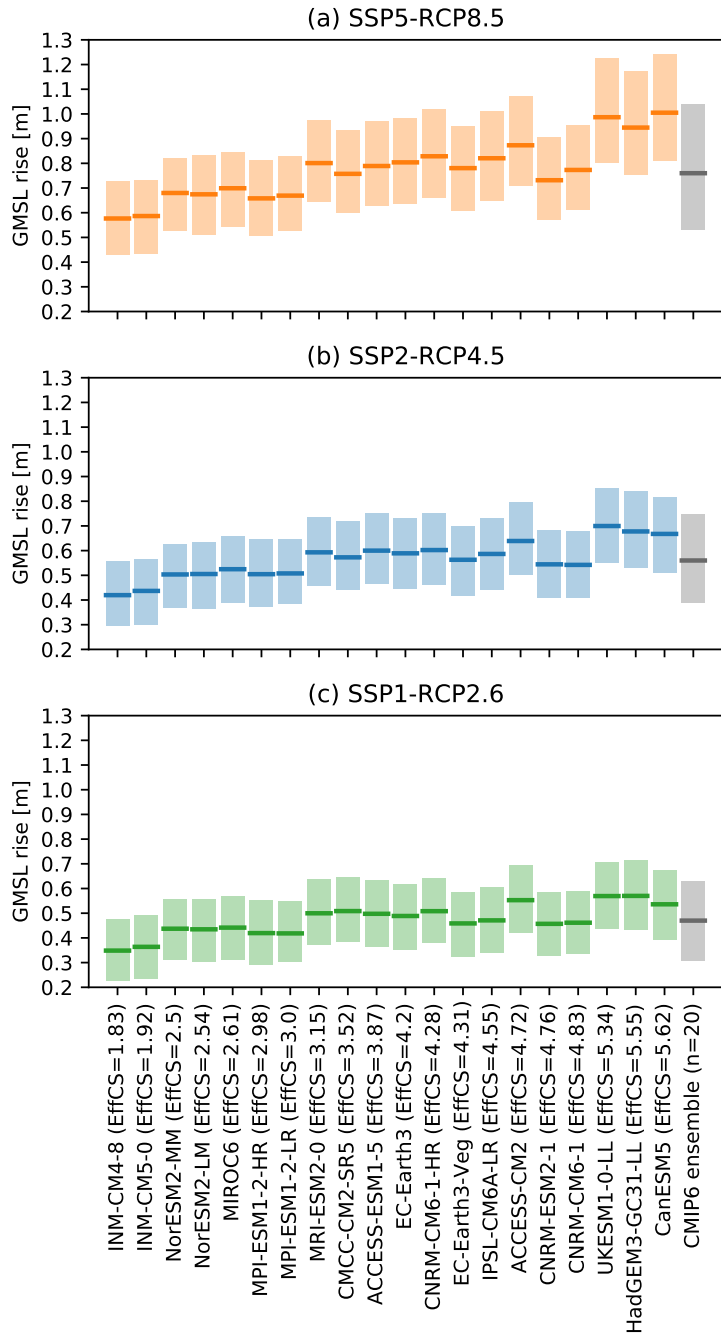


Figure S2.7: Projected median (solid lines) and 5-95% range (shaded boxes) of global mean sea-level (GMSL) rise at 2100 relative to 1986-2005 [m] for the 20-member CMIP6 ensemble (grey) computed using IPCC AR5 methods, and for individual CMIP6 models (colored) sorted by EffCS in ascending order, computed using IPCC AR5 methods adapted to sample directly from the 20-member CMIP6 ensemble (explained in Sections 2.2.3 & 2.5.3) for **(a)** SSP5-RCP8.5 (orange), **(b)** SSP2-RCP4.5 (blue) and **(c)** SSP1-RCP2.6 (green).

2.5.2. Supplementary tables

Table S2.1: CMIP6 models used in this study and their modeling centers, their effective climate sensitivity [EffCS, K] and transient climate response [TCR, K] derived from idealized model experiments (Section 2.2.2), and whether (x) or not () they provide the required GTE simulations. For the drift-corrected global mean thermal expansion and global mean surface air temperature change of the models, see Table S1 of [Hermans et al. \(2021\)](#). The data was downloaded on the 2nd of November, 2020. Results for GISS-E2-1-G were excluded as its historical GTE decrease of over 4 m may indicate data errors (r1i1p1f2).

Model (institute)	EffCS [K]	TCR [K]	Variant	GTE
ACCESS-CM2 (CSIRO & ARCCS)	4.72	2.11	r1i1p1f1	x
ACCESS-ESM1-5 (CSIRO & ARCCSS)	3.87	1.95	r1i1p1f1	x
AWI-CM-1-1-MR (AWI)	3.11	2.07	r1i1p1f1	
BCC-CSM2-MR (BCC)	3.06	1.73	r1i1p1f1	
CAMS-CSM1-0 (CAMS)	2.28	1.69	r1i1p1f1	
CanESM5 (CCCma)	5.62	2.74	r1i1p1f1	x
CESM2-WACCM (NCAR)	4.75	2.00	r1i1p1f1	
CIESM (THU)	5.66	2.39	r1i1p1f1	
CMCC-CM2-SR5 (CMCC)	3.52	2.08	r1i1p1f1	x
CNRM-CM6-1 (CNRM & CERFACS)	4.83	2.13	r1i1p1f2	x
CNRM-CM6-1-HR (CNRM & CERFACS)	4.28	2.47	r1i1p1f2	x
CNRM-ESM2-1 (CNRM & CERFACS)	4.76	1.84	r1i1p1f2	x
EC-Earth3 (EC-Earth-Consortium)	4.20	2.31	r1i1p1f1	x
EC-Earth3-Veg (EC-Earth-Consortium)	4.31	2.61	r1i1p1f1	x
FGOALS-g3 (CAS)	2.87	1.46	r1i1p1f1	
FGOALS-f3-L (CAS)	3.00	2.06	r1i1p1f1	
GFDL-ESM4 (NOAA & GFDL)	2.72	1.57	r1i1p1f1	
HadGEM3-GC31-LL (MOHC)	5.55	2.55	r1i1f1p3	x
INM-CM4-8 (INM)	1.83	1.31	r1i1p1f1	x
INM-CM5-0 (INM)	1.92	1.33	r1i1p1f1	x
IPSL-CM6A-LR (IPSL)	4.55	2.29	r1i1p1f1	x
MCM-UA-1-0 (UA)	3.64	1.93	r1i1p1f2	
MIROC-ES2L (MIROC)	2.68	1.55	r1i1p1f2	
MIROC6 (MIROC)	2.61	1.55	r1i1p1f1	x
MPI-ESM1-2-HR (MPI-M)	2.98	1.66	r1i1p1f1	x
MPI-ESM1-2-LR (MPI-M)	3.00	1.84	r1i1p1f1	x
MRI-ESM2-0 (MRI)	3.15	1.64	r1i1p1f1	x
NESM3 (NUIST)	4.67	2.74	r1i1p1f1	
NorESM2-LM (NCC)	2.54	1.48	r1i1p1f1	x
NorESM2-MM (NCC)	2.50	1.33	r1i1p1f1	x
UKESM1-0-LL (MOHC)	5.34	2.79	r1i1p1f2	x

CMIP5 (n=21)								
	EffCS [K]	TCR [K]	Δ GSAT [K]			GTE [m]		
			SSP-RCP 1-2.6	2-4.5	5-8.5	SSP-RCP 1-2.6	2-4.5	5-8.5
Mean	3.39	1.81	0.14	0.19	0.27	1.11	1.92	3.76
St. Dev.	0.74	0.37	0.02	0.03	0.04	0.44	0.50	0.72
Median	3.50	1.88	0.14	0.19	0.28	1.04	1.92	3.70
5-95%	2.37-4.59	1.28-2.41	0.10-0.18	0.14-0.23	0.21-0.33	0.49-1.78	1.12-2.58	2.64-4.70
Min.-Max.	2.08-4.67	1.10-2.50	0.10-0.18	0.13-0.23	0.20-0.34	0.31-1.85	1.04-2.65	2.52-4.96

CMIP6 (n=20)								
	EffCS [K]	TCR [K]	Δ GSAT [K]			GTE [m]		
			SSP-RCP 1-2.6	2-4.5	5-8.5	SSP-RCP 1-2.6	2-4.5	5-8.5
Mean	3.80	2.00	0.15	0.19	0.27	1.48	2.46	4.39
St. Dev.	1.16	0.47	0.03	0.03	0.05	0.51	0.63	0.99
Median	4.04	2.02	0.15	0.19	0.27	1.47	2.52	4.50
5-95%	1.92-5.55	1.33-2.74	0.08-0.18	0.12-0.24	0.18-0.34	0.80-2.32	1.63-3.49	3.10-6.06
Min.-Max.	1.83-5.62	1.31-2.79	0.08-0.19	0.11-0.24	0.17-0.37	0.79-2.40	1.60-3.68	3.02-6.19

Table S2.2: Summary of effective climate sensitivity [EffCS, K] and transient climate response [TCR, K], and projected global mean thermal expansion [GTE, m] and surface air temperature [GSAT, K] change for SSP1-RCP2.6, SSP2-RCP4.5 and SSP5-RCP8.5 (2081-2100 minus 1986-2005) for the IPCC AR5 CMIP5 ensemble and the CMIP6 ensemble introduced in Section 2.2.1.

Table S2.3: Summary of effective climate sensitivity [EffCS, K] and transient climate response [TCR, K], and projected global surface air temperature [GSAT, K] change for SSP1-RCP2.6, SSP2-RCP4.5 and SSP5-RCP8.5 (2081-2100 minus 1986-2005) for the CMIP6 ensemble including all models with GSAT simulations (n=31, see Section 2.2.1).

	EffCS [K]	TCR [K]	Δ GSAT [K]		
			SSP-RCP 1-2.6	2-4.5	5-8.5
Mean	3.69	1.97	1.37	2.33	4.15
St. Dev.	1.12	0.44	0.47	0.59	1.11
Median	3.52	1.95	1.27	2.27	3.98
5-95%	2.10-5.58	1.33-2.74	0.77-2.24	1.59-3.37	2.91-5.96
Min.-Max.	1.83-5.66	1.31-2.79	0.75-2.40	1.43-3.68	2.60-6.19

Table S2.4: Comparison of the 5-95% GMSL change projections computed using the IPCC AR5 Monte Carlo approach as presented in this study and in previous studies for 2100 and 2081-2100. All change values are expressed relative to the 1986-2005 average.

Projected GMSL rise in 2100 (5-95%) [m]			
	SSP1-RCP2.6	SSP2-RCP4.5	SSP5-RCP8.5
This study (CMIP6)	0.30-0.64	0.38-0.76	0.52-1.05
This study (CMIP6), Antarctica using (Levermann et al., 2014)	0.31-0.68	0.39-0.81	0.55-1.16
IPCC AR5 (CMIP5)	0.28-0.61	0.36-0.71	0.52-0.98
IPCC SROCC (CMIP5)	0.28-0.59	0.38-0.72	0.61-1.11
UKCP18 ¹ /Palmer et al. (2020) (CMIP5)	0.28-0.66	0.37-0.78	0.55-1.11
Projected GMSL rise averaged over 2081-2100 (5-95%) [m]			
	SSP1-RCP2.6	SSP2-RCP4.5	SSP5-RCP8.5
This study (CMIP6)	0.28-0.57	0.34-0.66	0.44-0.87
This study (CMIP6), Antarctica using (Levermann et al., 2014)	0.29-0.60	0.35-0.70	0.47-0.95
IPCC AR5 (CMIP5)	0.26-0.55	0.32-0.63	0.45-0.82
IPCC SROCC (CMIP5)	0.26-0.53	0.34-0.64	0.51-0.92
UKCP18 ¹ /Palmer et al. (2020) (CMIP5)	0.26-0.58	0.33-0.68	0.47-0.93

¹The UK Climate Projections 2018 (UKCP18) used a baseline of 1981-2000, resulting in change values approximately 1 cm higher than the values reported here from Palmer et al. (2020).

Table S2.5: CMIP6-based median and [5-95%] range projections of GMSL change [m] and its components at 2100 relative to 1986-2005, computed using the IPCC AR5 Monte Carlo approach. For comparison with CMIP5, see Table 13.SM.1 of [Church et al. \(2013\)](#).

	SSP1-RCP2.6	SSP2-RCP4.5	SSP5-RCP8.5
GTE [m]	0.16 [0.11-0.22]	0.21 [0.15-0.28]	0.32 [0.23-0.42]
Glaciers [m]	0.12 [0.06-0.19]	0.15 [0.08-0.22]	0.19 [0.11-0.28]
Net Greenland [m]	0.08 [0.05-0.14]	0.10 [0.06-0.18]	0.17 [0.09-0.33]
Greenland SMB [m]	0.04 [0.02-0.09]	0.06 [0.02-0.14]	0.11 [0.04-0.27]
Greenland dynamics [m]	0.04 [0.02-0.06]	0.04 [0.02-0.06]	0.05 [0.02-0.09]
Net Antarctica [m]	0.06 [-0.04-0.16]	0.05 [-0.05-0.15]	0.03 [-0.08-0.14]
Antarctica SMB [m]	-0.03 [-0.05-0.01]	-0.03 [-0.07-0.01]	-0.05 [-0.10-0.02]
Antarctica dynamics [m]	0.09 [-0.02-0.19]	0.09 [-0.02-0.19]	0.09 [-0.02-0.19]
Land water [m]	0.05 [-0.02-0.11]	0.05 [-0.02-0.11]	0.05 [-0.02-0.11]
GMSL [m]	0.47 [0.30-0.64]	0.56 [0.38-0.76]	0.76 [0.52-1.05]
GMSL rate [mm/yr]	4.79 [2.28-7.38]	7.10 [4.13-10.41]	13.35 [8.32-20.31]

2.5.3. Supplementary text

Using the Monte Carlo GMSL projection method of IPCC AR5

With the methods presented in IPCC AR5 ([Church et al., 2013](#)), GMSL projections can be derived for a given multi-model ensemble using annual mean GTE and GSAT time series (see flowchart). In IPCC AR5, projections were based on a CMIP5 ensemble, whereas we use a CMIP6 ensemble. First, we reference the 20 model-dependent GTE and GSAT time series to their averages in a common base period. To enable one-on-one comparison to IPCC AR5 ([Church et al., 2013](#)), we adhere to their base period of 1986-2005. Subsequently, for both the GTE and GSAT anomalies the multi-model mean and standard deviation are calculated. To generate continuous probability distribution functions, we assume both GTE and GSAT change are normally distributed, and draw 450 samples each of GTE and GSAT change using a common normal variate (this process is denoted by **(1)** in the flowchart in Figure S2.8). Thus, GTE and GSAT change are assumed to be perfectly correlated, meaning that a model with high GTE is implied to have a high GSAT change as well. This introduces a correlation structure between thermal expansion and the GSAT-driven barystatic contributions ([Palmer et al., 2020](#)). In the absence of strong constraints on the value to choose for a less than perfect correlation between GTE and GSAT, assuming a perfect correlation is a simplification which tends to overestimate uncertainty (and thus high-end sea-level rise), which is more cautious than assuming GTE and GSAT change are fully independent.

As seen in Figure S2.8, the GTE samples are used to estimate the contribution of thermal expansion to total GMSL change, whereas the GSAT change samples are used to estimate the contributions of glaciers and the surface mass balance of the Greenland and Antarctic ice sheets through parameterization schemes ([Church et al., 2013](#)). The contributions from Greenland ice dynamics, Antarctic ice dynamics and land-water storage are parameterized only as a function of time, so do not depend on GSAT change. The parameterization schemes for the barystatic components are based on global and regional models, and observations, and have

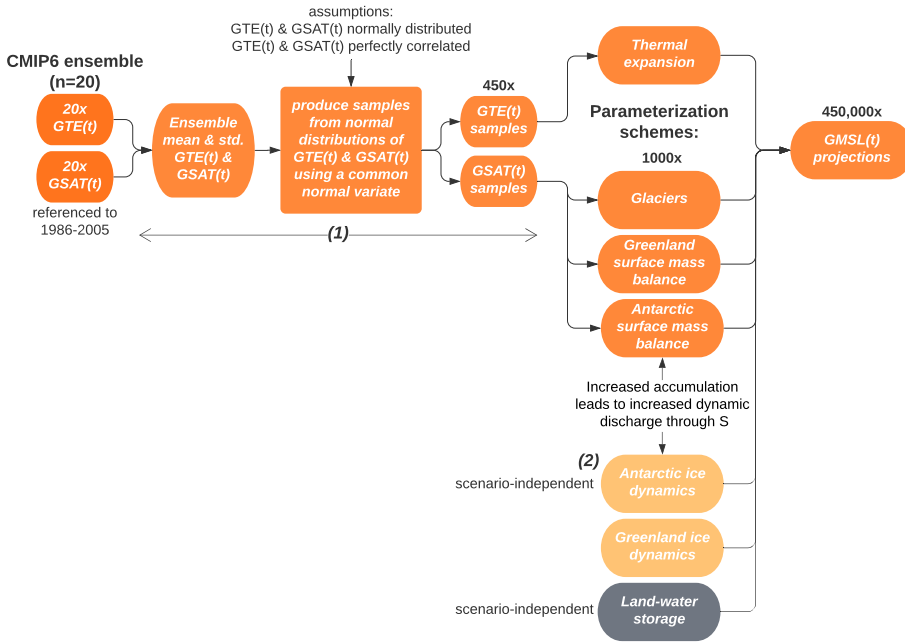


Figure S2.8: Flowchart of the Monte Carlo method of IPCC AR5 (Church et al., 2013) for producing GMSL projections.

been motivated and explained extensively by IPCC AR5 (Church et al., 2013) and Palmer et al. (2020). We summarize them here to clarify how the land-ice components depend on GSAT change and how methodological uncertainty is accounted for:

- Glaciers:** changes in global glacier mass were estimated by the IPCC AR5 (Church et al., 2013) using a parameterization based on four equally weighted global glacier models. The time-dependent contribution of glaciers to GSML change was modeled as $fI(t)^p$, in which $I(t)$ refers to the time-integral (cumulative sum) of GSAT change, and f and p are coefficients estimated through linear regression for each global glacier model separately. Systematic uncertainty is represented by assuming a time-dependent standard deviation equal to 20% of the contribution of glaciers projected with the aforementioned expression and using the ensemble-mean $I(t)$ as input. The standard deviation is multiplied by a random normally distributed factor.
- Greenland ice sheet:** the surface mass balance of the Greenland ice sheet in Gt/yr was estimated by the IPCC AR5 (Church et al., 2013) from GSAT using the cubic polynomial $-71.5GSAT - 20.4GSAT^2 - 2.8GSAT^3$, based on regional climate model projections. Since in this parameterization the rate of ice mass change depends on GSAT, the sea-level contribution of the surface mass balance of the Greenland ice sheet also scales with the time-integral of GSAT. To

represent methodological uncertainties, the cubic polynomial was multiplied by a log-normally distributed factor $F = e^N$, with N a normal distribution with zero mean and standard deviation 0.4. Another factor E , varying randomly between 1 and 1.15, was used to account for positive elevation feedback.

Projections of the contribution of ice dynamics of the Greenland ice sheet were estimated by fitting a quadratic function of time, starting at half of the observed rate of loss from Greenland during 2005-2010, toward lower and upper limits of 0.014 to 0.063 m for SSP1-RCP2.6 and SSP2-RCP4.5, and 0.020 to 0.085 for SSP5-RCP85, based on a number of different ice-sheet model projections (discussed by Church et al. (2013)). In between, a uniform probability density was assumed. Thus, the parameterization of the ice dynamic part of the net Greenland contribution does not depend on GSAT change.

- **Antarctic ice sheet:** the surface mass balance of the Antarctic ice sheet was estimated by the IPCC AR5 (Church et al., 2013) based on combined information from GCMs, high-resolution regional climate models and an ice-sheet mass balance model. The accumulation $A(t)$ was related to warming in Antarctica with $5.1 \pm 1.5\% \text{ } ^\circ\text{C}^{-1}$, and the ratio of warming in Antarctica to GSAT was assumed to be 1.1 ± 0.2 . The standard deviations of these ratios were assumed to be normally distributed uncertainties. The effect of increased accumulation on increased dynamic ice discharge was accounted for by adding $-SA(t)$ to $A(t)$, with S a factor varying randomly with a uniform probability distribution between 0 and 0.35. To obtain the contribution of the Antarctic surface mass balance to GMSL change, the mass balance changes are time-integrated. Thus, the accumulation in Antarctica depends on time-integrated GSAT.

Similar to the Greenland ice dynamics parameterization, the dynamics of the Antarctic ice sheet were parameterized in IPCC AR5 by fitting a quadratic function of time, starting at the observed rate of loss during 2005-2010, toward lower and upper limits of -0.029 and 0.185 m for all emissions scenarios. These were based on an assessment of the literature available at the time of the IPCC AR5. Thus, the parameterization of the ice dynamic part of the net Antarctic contribution does not depend on the GSAT change input nor on the emissions scenario. Again, in between the lower and upper limits a uniform probability density was assumed. The factor S mentioned above was assumed to be perfectly correlated with this distribution.

- **Land-water storage:** similar to the ice dynamic parameterizations, the contribution of land-water storage to GMSL change was estimated by the IPCC AR5 (Church et al., 2013) by fitting a quadratic function of time, starting at the observed rate of the land-water storage contribution to GMSL change, toward the assessed lower and upper limits of the time-mean of 2081-2100, for all emissions scenarios (-0.01 to 0.09 m; Church et al., 2013). The uncertainty was treated in the same way as for the ice dynamics.

For each of the 450 GTE and GSAT samples drawn (see flowchart), 1,000 additional

random samples are generated to represent methodological uncertainty in the parameterizations through varying parameters as explained above. For this number of samples, results converge to a random uncertainty of 0.01 m for GMSL rise and its components, and 0.1 mm/yr for its rate (Church et al., 2013). Combining the steric and barystatic contributions, an ensemble of 450,000 GMSL projections is obtained.

Parameterizing Antarctic ice dynamics based on projections of Levermann et al. (2014)

After the IPCC AR5 (Church et al., 2013) was published, Levermann et al. (2014) generated projections of Antarctic dynamic ice discharge for RCP 8.5, 6.0, 4.5 and 2.6 through employing linear response functions fitted to basal-melt sensitivity experiments of five different ice-sheet models for Antarctica. Levermann et al. (2014) related sub-surface ocean warming in Antarctica to GSAT change based on an ensemble of CMIP5 models, and estimated basal melt sensitivities from observations to translate sub-surface ocean warming into enhanced basal ice-shelf melting. This was translated into the ice dynamical response for each emissions scenario using the linear response functions.

As an alternative to the scenario-independent parameterization of the Antarctic ice dynamic contribution to GMSL change in IPCC AR5 (Church et al., 2013), Palmer et al. (2018b) and Palmer et al. (2020) parameterized the scenario-dependent projections of Levermann et al. (2014). This was done by estimating a log-normal fit of the form Ae^N , with A a constant and N a normal distribution with zero mean, to the percentiles of the probability distributions of projections reported by Levermann et al. (2014) for each RCP separately. The contribution of Antarctic ice sheet dynamics to GMSL change was then modeled as a quadratic function of time, starting at the observed rate of loss, toward Ae^N in 2100. Thus, with this parameterization, the Antarctic dynamic contribution to GMSL change depends on the emissions scenario, but similar to the scenario-independent parameterization used by Church et al. (2013), does not depend on the GSAT input. To compare our GMSL projections with the projections of Palmer et al. (2020), we also generate GMSL projections incorporating their parameterization, replacing the scenario-independent parameterization of IPCC AR5 denoted by **(2)** in the flowchart (Figure S2.8).

Producing GMSL projections for individual CMIP6 models

We also use a variation of the Monte Carlo approach to produce GMSL projections based on each individual CMIP6 model separately instead of based on the CMIP6 multi-model ensemble. With this approach, we bypass the process denoted with **(1)** in the flowchart (Figure S2.8). Thus, instead of generating 450 samples using the multi-model mean and standard deviation of GTE and GSAT change, we use the GTE and GSAT change time series of the 20 individual CMIP6 models directly as input to the parameterization schemes. As before, an additional one thousand independent samples are used to represent methodological uncertainty in the parameterization schemes for each CMIP6 model. This results in 20 ensembles of GMSL projections, one for each CMIP6 model, with 1,000 members in each ensemble.

3

Improving Sea-Level Projections Using Dynamical Downscaling

Abstract

Changes in ocean properties and circulation lead to a spatially non-uniform pattern of ocean dynamic sea-level change (DSLCL). The projections of DSLCL that the IPCC AR5 presented were constructed with global climate models (GCMs) from the Coupled Model Intercomparison Project 5 (CMIP5). Since CMIP5 GCMs have a relatively coarse resolution and exclude tides and surges it is unclear whether they are suitable for providing DSLCL projections in shallow coastal regions such as the Northwestern European Shelf (NWES). One approach to addressing these shortcomings is dynamical downscaling – i.e., using a high-resolution regional model to refine the output of GCMs. Here, we use the regional shelf seas model AMM7 to show that, depending on the driving CMIP5 GCM, dynamical downscaling can have a large impact on the simulations of DSLCL in the NWES region. For a high-end greenhouse gas concentration scenario, we find that the downscaled simulations of 21st century DSLCL are up to 15.5 cm smaller than the DSLCL originally simulated along the North Sea coastline, owing to unresolved processes in the GCM. This is of a magnitude similar to the inter-model uncertainty of the CMIP5 ensembles used for previous DSLCL projections. Furthermore, dynamical downscaling affects the simulated time of emergence of externally forced sea-level change from background sea-level variability, and can result in differences in the projected change of the amplitude of the seasonal cycle of sea level of over 0.3 mm/yr. Our results therefore support a role for dynamical downscaling in future regional sea-level projections to aid coastal decision makers.

Published as: Hermans, T.H.J., Tinker, J., Palmer, M.D., Katsman, C.A., Vermeersen, B.L.A., & Slangen, A.B.A. (2020). *Improving Sea-Level Projections on the Northwestern European Shelf Using Dynamical Downscaling*, Climate Dynamics, 54, 1987-2011. [10.1007/s00382-019-05104-5](https://doi.org/10.1007/s00382-019-05104-5)

3.1. Introduction

An increase in coastal sea level has major socioeconomic and environmental impacts as it can lead to, for instance, flooding, erosion, saltwater intrusion and the decline of coastal wetlands (Nicholls and Cazenave, 2010). However, the magnitude of sea-level change (SLC) varies for different locations (Church et al., 2013). Regionally, projected SLC can deviate up to 50% from the global mean (Kopp et al., 2014; Slangen et al., 2014). This spatially non-uniform pattern of relative SLC is the result of different contributions, such as changes in the ocean and atmosphere, land ice mass change, vertical land motion (VLM), glacial isostatic adjustment (GIA) and terrestrial water storage (TWS) (Church et al., 2013). Here, we focus on ocean dynamic sea-level change (DSLCL) due to local changes in seawater density and local convergence or divergence of mass (steric and manometric SLC, respectively; Gregory et al., 2019).

Projections of DSLCL driven by greenhouse gas concentration scenarios are commonly made with the output of coupled global climate models (GCMs, e.g., Slangen et al., 2012, 2014; Church et al., 2013; de Vries et al., 2014; Kopp et al., 2014; Palmer et al., 2018b). Simulations of these models can be obtained from the Coupled Model Intercomparison Project Phase 5 (CMIP5) database (Taylor et al., 2012). At the time of writing CMIP6 models are being released (Eyring et al., 2016). Computational constraints limit the horizontal ocean resolution of CMIP5 GCMs to about 100 by 100 km, but the horizontal resolution varies considerably across the CMIP5 model ensemble. The vertical resolution of most GCMs is limited in shallow regions due to their unevenly spaced vertical levels at fixed depths (z-coordinates). Additionally, GCMs do not resolve tides and storm surges. However, in shallow shelf seas such as the North Sea, small-scale bathymetric features and hydrodynamical processes such as tidal mixing can be important for simulating DSLCL. Furthermore, an increased horizontal ocean resolution can give enhanced eddy activity (Suzuki et al., 2005; Penduff et al., 2010), which affects the simulated sea-level variability. Thus, GCMs may not be the most appropriate means for providing DSLCL projections in coastal regions. For local stakeholders and impact studies, projections at a finer spatial resolution are also desired.

Sea-level projections at a finer spatial resolution can be obtained by downscaling, which is a technique to obtain regional to local detail from larger scale information (Rummukainen, 2010). Here, we focus on dynamical downscaling by using a high-resolution regional climate model (RCM). Dynamical downscaling has previously been applied to study present-day hydrodynamics and the regional impact of future climate change for the North Sea and the Northwestern European Shelf (NWES) region (see (Schrum et al., 2016) for a comprehensive review). These studies have mainly focused on future changes in ocean temperature, salinity and circulation (e.g., Ådlandsvik, 2008; Holt et al., 2010, 2018; Mathis, 2013; Tinker et al., 2015, 2016; Mathis et al., 2017) and primary production and biochemistry (e.g., Wakelin et al., 2015; Holt et al., 2016). Extreme sea levels and tides have mainly been studied with barotropic models (e.g., Sterl et al., 2009; Howard et al., 2010; Pickering et al., 2012; Ward et al., 2012; Pelling et al., 2013; Pelling and

Green, 2014; Cannaby et al., 2016; Idier et al., 2017; Palmer et al., 2018b; Howard et al., 2019). DSLC on the NWES however, has not extensively been studied with RCMs, with the exception of Mathis (2013) who analyzed the seasonal variation of 100-yr sea-level trends in the North Sea with the HAMSOM model. Consequently, the effects of downscaling DSLC simulations for this region are not yet clear.

In other geographic regions dynamical downscaling has been shown to affect DSLC simulations substantially. Zhang et al. (2017) used a $1/10^\circ$ near-global ocean model (75°S to 75°N) driven by the atmospheric forcing of an ensemble of 17 CMIP5 GCMs for Australia. The downscaled DSLC was found to differ 1-3 cm from the original projections along the Australian coast, and was up to 20 cm larger further offshore. For the North Pacific, downscaled DSLC was computed with a regional model ($1/4^\circ$ by $1/4^\circ$) for three different driving CMIP5 GCMs (Liu et al., 2016). They found that along the coast of Japan, downscaled DSLC can differ up to 10 cm from the original DSLC depending on the driving GCM.

In this study we assess the importance of dynamical downscaling for the NWES region and quantify the uncertainties related to basing DSLC projections on coarse-resolution GCMs. We do this by downscaling the simulations of two CMIP5 GCMs with a regional shelf seas model (the Atlantic Margin Model (AMM7), O'Dea et al., 2017) and comparing the results with the original simulations for two different representative concentration pathways (RCPs, Meinshausen et al., 2011). In addition, we discuss the changes in the seasonal cycle of sea level in our simulations, which appears to be a gap in the current literature (e.g., Slangen et al., 2014; Kopp et al., 2014; Meyssignac et al., 2017; Palmer et al., 2018b) but is an important aspect of extreme sea levels and tides (Pugh, 1987). We assess whether the increased spatial and temporal resolution of our downscaled simulations leads to more realistic simulations of sea level on subannual timescales.

We start by presenting our downscaling set-up and the methods and observational data used to evaluate our simulations in Section 3.2. Next, we show in Section 3.3 that dynamical downscaling improves the historical GCM simulations based on comparisons with observations of sea surface temperature (SST), sea surface salinity (SSS), mean dynamic topography (MDT) and sea-level variability on seasonal and interannual timescales. We will discuss the large differences that dynamical downscaling can introduce in terms of annual mean DSLC and its different components in Section 3.4, and how these differences depend on the driving GCM and the climate change scenario. In Section 3.5 we focus on subannual timescales and compare the original and downscaled simulations of changes in the seasonal sea-level cycle. We end with a discussion and our conclusions in Section 3.6.

3.2. Data and methods

Here, we introduce AMM7 and the GCMs (Section 3.2.1) followed by our dynamical downscaling set-up (Section 3.2.2). Next, we discuss how we decompose DSLC in our analysis (Section 3.2.3). Finally, we present our framework to compare the sea surface height (SSH) output of the different models (Section 3.2.4) and to compare the output with observational data (Section 3.2.5).

3.2.1. NEMO AMM7 and the CMIP5 GCMs

We use the AMM7 (Coastal Ocean version 6) configuration of the primitive-equation modeling framework Nucleus for European Modelling of the Ocean (NEMO) V3.6 (Madec and NEMO Team, 2016) to downscale long-term simulations of two CMIP5 GCMs. AMM7 is a hydrodynamic model of the NWES region that has been extensively described and validated, and is being used for operational ocean forecasting (O'Dea et al., 2012; O'Dea et al., 2017) and marine reanalyses (Renshaw et al., 2019). Its domain (henceforth the NWES region) extends from 20°W to 13°E and from 40°N to 65°N (Figure 3.1a), allowing to internally resolve the exchange of water across the shelf break. The horizontal resolution is 1/15° latitude by 1/9° longitude, or nominally 7 by 7 km. Thus, on the shelf, AMM7 does not resolve the internal Rossby radius (≈ 4 km) (O'Dea et al., 2012) and is not eddy-resolving, but can capture small-scale topographical features that GCMs cannot. AMM7 has 50 vertical levels with hybrid z - σ coordinates (Siddorn and Furner, 2013). Details on how horizontal pressure gradient errors are handled are given by O'Dea et al. (2012) and Madec and NEMO Team (2016). Due to the terrain-following vertical levels, processes such as vertical mixing and bottom boundary layers are handled better than in CMIP5 GCMs, in which the mean depth of the North Sea (≈ 80 m) is represented by only 7 to 8 vertical levels.

We downscale the simulations of two example CMIP5 GCMs (Taylor et al., 2012) commonly used for sea-level projections, namely HadGEM2-ES (Collins et al., 2011) and MPI-ESM-LR (Giorgetta et al., 2013). Up to 2005, the CMIP5 GCMs are forced by observed greenhouse gas concentrations. For 2006–2099, the simulations forced with the RCP4.5 (intermediate) and RCP8.5 (high-end) scenarios (Meinshausen et al., 2011) are used. Together, these simulations are used to force AMM7 from 1972–2099. AMM7 is spun up from 1972 to 1979 and analyses are done for 1980–2099. In the main manuscript, we only show results for RCP8.5. We show the results for RCP4.5 in the Supplementary Information, as DSLC for RCP4.5 is spatially similar to that for RCP8.5 but smaller in magnitude.

The ocean component of HadGEM2-ES has 40 vertical z -levels (max. 17 on the shelf) and a horizontal resolution of 1° by 1° (≈ 85 km) on the NWES. The ocean component of MPI-ESM-LR also has 40 vertical z -levels (max. 12 on the shelf) and a bipolar grid with poles on Greenland and in the Weddell Sea. The curvilinear grid has an approximate resolution of 0.45° latitude by 0.82° longitude (≈ 50 km) in the central North Sea, which increases toward Greenland. As a result, MPI-ESM-LR includes several topographical features which HadGEM2-ES does not, such as the Norwegian Trench, the English Channel and the Irish Sea (Figures 3.1b & c).

3.2.2. Downscaling set-up

The GCM simulations are prescribed to AMM7 as boundary conditions at the lateral ocean boundaries and at the surface in a “one-way nesting” approach. For clarity, from now on we will refer to the simulations of HadGEM2-ES and MPI-ESM-LR as *GCM-HAD* and *GCM-MPI*, respectively. The downscaled simulations from AMM7, driven by HadGEM2-ES and MPI-ESM-LR, will be referred to as *RCM-HAD* and *RCM-MPI*, respectively.

Atmospheric forcing

The atmospheric surface forcing is obtained from simulations of the Rossby Centre regional atmospheric model RCA4 (Strandberg et al., 2014). RCA4 has been used to dynamically downscale the atmosphere component of GCM-HAD and GCM-MPI for the European Coordinated Regional Downscaling Experiment domain (Giorgi et al., 2009). Direct fluxes are used rather than bulk formulae: atmospheric pressure, precipitation minus evaporation and long-wave radiation are prescribed daily and 10 m wind and short-wave radiation 6-hourly.

Since no downscaled preindustrial atmospheric forcing is available from RCA4, we did not downscale the preindustrial control runs of GCM-HAD and GCM-MPI. Control runs can be used to correct SLC for spurious model drift (Sen Gupta et al., 2013). As model drift is small compared to forced trends especially on the shallow continental shelf (Sen Gupta et al., 2013), we expect that dedrifted will not significantly impact our findings, in particular not the comparison between the GCM and the downscaled simulations.

Lateral boundary conditions

The lateral boundary conditions consist of monthly mean temperature and salinity, barotropic currents and SSH, which are derived from the GCMs and interpolated onto the AMM7 grid. Temperature, salinity and barotropic currents are directly prescribed, and a relaxation zone of 10 grid points with a *tanh*-shaped relaxation parameter relaxes the internal solution to the prescribed boundary values (Madec and NEMO Team, 2016). SSH, and additionally 15 tidal constituents, are indirectly prescribed: a Flather radiation condition (Flather, 1976) corrects the depth-mean velocity normal to the lateral boundaries based on the SSH gradients between the internal solution and the lateral boundaries (Madec and NEMO Team, 2016). Directly prescribing SSH and prescribing barotropic currents through radiation conditions instead was found to be detrimental to the simulation of tides. SSH is derived from the ‘zos’ field of the driving CMIP5 GCMs, which gives SSH anomalies with respect to a time-invariant geoid. We ensured that global mean ‘zos’ is 0 m by removing the global mean at each timestep prior to generating the boundary conditions. The SSH boundary conditions were anomalized with respect to their spatial and temporal mean and for reasons of numerical stability an offset of 0.5 m was added.

River run-off and Baltic outflow

We simulate river run-off with the Total Runoff Integration Pathways river routing model (Oki and Sud, 1998) using the daily run-off from RCA4. Exchange with the

Baltic Sea through the Danish Straits and the Kattegat occurs at too small scales to resolve in AMM7. Instead, a climatology is used for temperature, salinity and barotropic currents for the Baltic inflow to the North Sea following O'Dea et al. (2017). As a consequence, downscaled DSLC along the Norwegian coast will be biased to present-day conditions.

3.2.3. Computing changes in bottom and atmospheric pressure and the local steric effect

To analyze the drivers of DSLC (Section 3.4.2), we decompose simulated DSLC into changes due to manometric change (local convergence/divergence of mass, which is related to bottom pressure change) and due to the local steric effect (depth-integrated density changes of the water column) as follows (Ponte, 1999; Gregory et al., 2019):

$$\frac{\delta\eta}{\delta t} = \frac{1}{g\rho_0} \frac{\delta(p_b - p_a)}{\delta t} - \frac{1}{\rho_0} \int_{-H}^{\eta} \frac{\delta\rho}{\delta t} dz \quad (3.1)$$

where η refers to SSH, t to time, g is the gravitational acceleration, ρ the density and ρ_0 a constant reference density at sea level, p_b the bottom pressure, p_a the atmospheric pressure and H the local ocean depth.

Bottom pressure changes (r.h.s. of Equation 3.1, first term) and local steric changes (r.h.s. of Equation 3.1, second term) are directly available from AMM7 output, but not for the GCMs. For the GCMs we therefore compute local steric change from the 3D fields of temperature and salinity, using the Gibbs SeaWater (GSW) toolbox (McDougall and Barker, 2011) of the Thermodynamic Equation of SeaWater 2010. Thermosteric and halosteric SLC can be computed similarly, keeping respectively salinity and temperature constant. We subsequently compute bottom pressure change from Equation 3.1. Differences in 21st century local steric SLC on the NWES between the direct AMM7 output and the GSW computation are less than 4 mm, so the methods are comparable.

Atmospheric pressure (p_a) changes also contribute to bottom pressure (p_b) changes. Their effect on sea level, referred to as the inverse barometer (IB) effect η_{IB} , is computed as follows (Stammer and Hüttemann, 2008):

$$\eta_{IB}(x, y, t) = -\frac{\rho'_a(x, y, t)}{g\rho_0} \quad (3.2)$$

where ρ'_a is defined as the local pressure anomaly with respect to the global area-weighted mean atmospheric pressure over the oceans $\overline{p_a}$, as a function of location x and y , and time t . Here, for both the GCMs and AMM7 we compute ρ'_a in Equation 3.2 with respect to the global mean ($\overline{p_a}$) obtained from the GCM simulations. We include the IB effect in the presented sea-level results unless stated otherwise.

3.2.4. Comparing DSLC in the GCMs with DSLC in AMM7

Both the CMIP5 GCMs and AMM7 apply the Boussinesq approximation. The Boussinesq approximation refers to replacing in-situ density by a reference density in all equations except the vertical momentum equation and the equation of state (Gill, 1983). As a result, Boussinesq models conserve volume rather than mass, and for global Boussinesq models the global mean thermosteric sea-level change ('zostoga' in CMIP5 models) needs to be diagnosed. Boussinesq models are still influenced by a local steric effect (Griffies et al., 2014). Since we use one-way dynamical downscaling in a relatively small domain, we neglect the effect that refining the GCM regionally has on 'zostoga'.

Since the spatial mean density changes in Boussinesq models while the volume is conserved, the bottom pressure shows a physically spurious change (Griffies and Greatbatch, 2012) according to Equation 3.1 (Section 3.2.3). AMM7 has Boussinesq dynamics like the GCMs, but only covers a limited region. Consequently, AMM7 does not conserve the same volume as the GCMs, leading to a different regional mean DSLC and a different (spurious) bottom pressure change. Additionally, discrepancies between the GCMs and AMM7 in the mass transport across the boundaries of the NWES region can result from the interpolation of the lateral boundary conditions (e.g., the ocean currents) from the parent grid onto the AMM7 grid and from the different representations of bathymetry, atmosphere and river run-off.

To directly compare DSLC in the GCMs with DSLC in AMM7, we correct the DSLC output of AMM7 for the differences in regional mean DSLC resulting from the Boussinesq approximation and from discrepancies in mass transport due to artefacts of the downscaling set-up. A spatially uniform correction to prognostic Boussinesq SSH can be made a posteriori based on the spatial mean density change, but only for models with closed boundaries (Greatbatch, 1994). This applies to CMIP5 GCMs, but not to a nested regional model. Instead, we apply a spatially uniform correction to the DSLC simulations of AMM7 by enforcing global mass conservation. To this end, we replace the regional area-weighted mean manometric SLC of AMM7 (regional mean DSLC due to bottom pressure change only, or equivalently, the total regional mass change) with the regional area-weighted mean manometric SLC in the driving GCMs:

$$\Delta\eta_{AMM7}^*(x, y, t) = \Delta\eta_{AMM7}(x, y, t) - \Delta\bar{\eta}_{AMM7}^{P_b}(t) + \Delta\bar{\eta}_{GCM}^{P_b}(t) \quad (3.3)$$

where $\Delta\eta_{AMM7}^*$ and $\Delta\eta_{AMM7}$ refer to corrected and uncorrected DSLC of AMM7, respectively, as a function of location and time. $\Delta\bar{\eta}_{AMM7}^{P_b}$ and $\Delta\bar{\eta}_{GCM}^{P_b}$ refer to the area-weighted mean DSLC due to bottom pressure changes only (first term on the l.h.s. of Equation 3.1, excluding atmospheric pressure changes) in the NWES region, as simulated by AMM7 and the GCMs, respectively.

3.2.5. Observational data for model evaluation

AMM7 has been extensively tested and downscaling setups similar to ours have been validated against observations in previous studies (e.g., Tinker et al., 2015). When

forced by a preindustrial control run of HadGEM3, AMM7 reproduces interannual sea-level variability observed with satellite altimetry and tide gauges well (Tinker et al., 2020). As different forcing introduces different biases, we will evaluate our historical simulations against observations in Section 3.3.

Model evaluation is complicated by internal variability: although the historical portion of the CMIP5 simulations is forced by observed changes in greenhouse gas concentrations (Taylor et al., 2012), the timing of internal variability in the models is not expected to match the timing of observed variability. Therefore, we focus on the capability of the models to reproduce the observations in a statistical sense. We extend the historical period 1980-2005 of our simulations to 2017 using RCP8.5. The time periods used for the evaluation within this window depend on the availability of each observational dataset.

Richter et al. (2017) compared 20-yr sliding windows of historical CMIP5 simulations (1850-2005) with satellite altimetry (1993-2012) in the Northern North Atlantic. They found little effect of internal variability on the correlation between simulated and observed mean dynamic topography (MDT), a measure of the average strength of geostrophic circulation. However, internal variability had a larger effect on the correlation with observed interannual sea-level variability and linear trends. Therefore, we compare satellite altimetry to simulated MDT, but use the longer records that tide gauges (TGs) provide to compare to simulated sea-level variability. A comprehensive comparison of TG records with simulated sea-level trends including the contributions of VLM, GIA, TWS and land ice mass change is beyond the scope of this study.

For MDT, we use the MDT CNES CLS18 product (Rio et al., 2014), which provides the mean SSH above the GOCO05S geoid model for the period 1993-2012. The CNES MDT is based on a combination of GRACE and GOCE data, satellite altimetry and in-situ data, and is provided on a $1/8^\circ$ by $1/8^\circ$ grid.

Observations of SST are obtained from the Operational Sea Surface Temperature and Sea Ice Analysis (OSTIA) (Donlon et al., 2012; Roberts-Jones et al., 2012), which combines satellite data and in-situ data. It is available at a resolution of $1/20^\circ$ by $1/20^\circ$ for the period 1992-2010.

Observations of SSS for 1980-2017 are derived from the EN4.2.0 dataset (Good et al., 2013), which provides quality-controlled sub-surface temperature and salinity measurements from profiling instruments and Argo floats. As the spatial and temporal resolution of EN4 in the NWES region are limited, we use EN4 only qualitatively. Similarly to Tinker et al. (2015), we do not use the optimally interpolated dataset. Instead, we average salinity observations within the first 10 m below the surface over winter (DJF) and summer (JJA) months and assign them to the nearest grid cell of a $1/4^\circ$ by $1/4^\circ$ grid. Mean salinity values computed from less than 4 years of data are rejected.

We use monthly and annual TG records from the revised local reference dataset obtained from the Permanent Service for Mean Sea Level (PSMSL) website (Holgate

et al., 2013; PSMSL, 2018). We select TGs on the NWES (Figure S3.1) with a series length of over 50 years and with a data coverage of at least 28 years during 1980-2017 ($\geq 75\%$). Stations in near proximity of the Baltic outflow are excluded, because exchange with the Baltic Sea is not resolved in any of our models (Section 3.2.2). Simulated annual mean SSH nearest to the TGs is subsampled based on the temporal coverage of each individual TG record.

The comparison of the GCM simulations with the AMM7 simulations, and of simulations with observations, involves datasets provided at different grids and resolutions. Throughout the paper, we will show all data on their original grids, as this best shows their spatial characteristics. When analyzing the differences between models, and between models and observations, computations are made and presented on the AMM7 grid to avoid losing the high-resolution information of AMM7. To this end, data with a different resolution and/or land mask are bilinearly interpolated and ocean grid cells that were originally land are filled with nearest-neighbor interpolation.

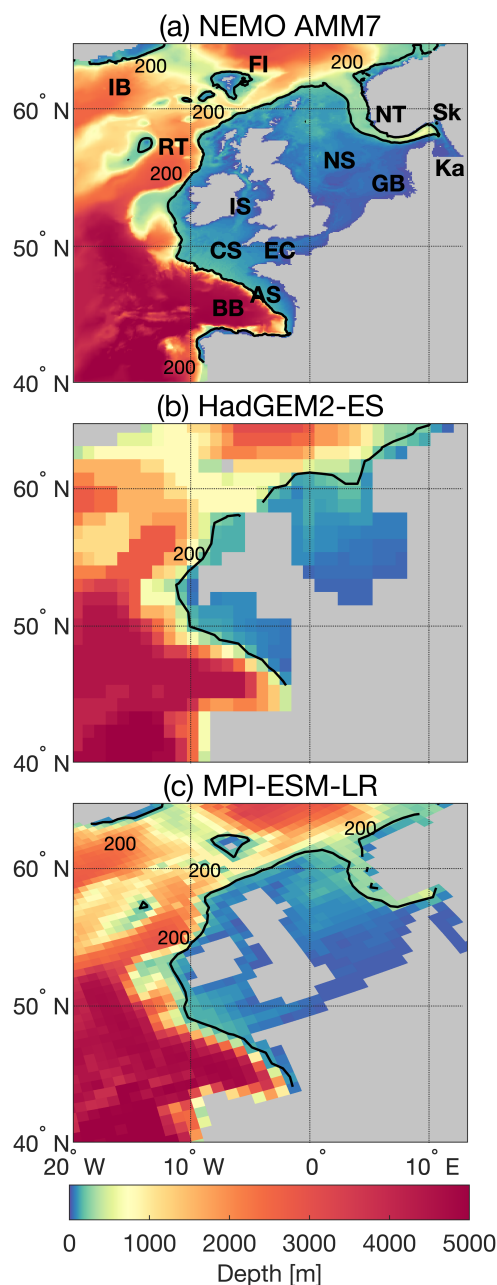


Figure 3.1: Bathymetry of (a) NEMO AMM7, (b) HadGEM2-ES, and (c) MPI-ESM-LR. The land mask is grey; the black lines denote the 200 m isobath approximating the shelf break. The abbreviations in (a) denote the American Shelf (AS), Bay of Biscay (BB), Celtic Sea (CS), English Channel (EC), Faroe Islands (FI), German Bight (GB), Iceland Basin (IB), Irish Sea (IS), Kattegat (Ka), North Sea (NS), Norwegian Trench (NT), Rockal Trough (RT) and Skagerrak (Sk) (see also Figure 1.8).

3.3. The impact of dynamical downscaling on historical simulations

In the following sections we compare the historical GCM and downscaled simulations of MDT (Section 3.3.1), SST and SSS (Section 3.3.2) and sea-level variability (Section 3.3.3) with observations and investigate the information that dynamical downscaling with AMM7 adds.

3.3.1. Mean dynamic topography

The observed MDT CNES CLS18 anomalies (w.r.t. the regional mean) for 1993–2012 show a northwest to southeast gradient (Figure 3.2a) perpendicular to the North Atlantic Current that flows along the shelf break. This slope current is driven by the combination of a horizontal density gradient and a sloping bathymetry (Huthnance, 1984). Along the southeastern North Sea coastline and in the Kattegat (see Figure 3.1 for a map), observed MDT is higher than elsewhere on the shelf.

Simulated MDT generally agrees well with the observations: we find pattern correlation coefficients (PCCs) with the observations of 0.86 and 0.90 for respectively GCM-HAD and GCM-MPI in the NWES region (Figures 3.2b & d). The accuracy of satellite altimetry is lower near the coasts than in the deep ocean due to land contamination (e.g., Deng et al., 2002), while we expect downscaling to provide added value especially on the shelf. Additionally, the across-track resolution of satellite altimetry is much lower than the resolution of AMM7. Despite these limitations, we find that after downscaling the PCCs of GCM-HAD and GCM-MPI improve to 0.94 and 0.94, respectively (Figures 3.2c & e). The MDT of GCM-HAD is improved most. The root mean square error (RMSE) changes slightly after downscaling (0.07 m for GCM-HAD and RCM-HAD, and 0.08 and 0.06 m for GCM-MPI and RCM-MPI, respectively).

All models reproduce the observed northwest to southeast MDT gradient reflecting the slope current, but this is captured only crudely by GCM-HAD (Figure 3.2b). The gradient of high to low MDT off the coast of Norway, perpendicular to the Norwegian Coastal Current and Atlantic inflow through the Norwegian Trench, is present in all models except GCM-HAD (Figures 3.2c–e). These topographically-steered currents cannot be resolved by GCM-HAD since its horizontal resolution is insufficient for a realistic bathymetry. However, the high MDT along the Norwegian coast is not clearly present in the MDT CNES CLS18 product either (Figure 3.2a), most likely due to insufficient resolution and land contamination (Ophaug et al., 2015; Idžanovic and Ophaug, 2017).

Along the southeastern North Sea coastline all models show elevated MDT similar to the observations, but for GCM-HAD this is obscured by a checkerboard pattern (Figures 3.2b). Such a checkerboard pattern may be related to numerical instabilities in horizontal diffusivity. Along the western boundary of the NWES region, simulated MDT is lower than observed MDT for all models. In the Norwegian Sea, simulated MDT is too low in GCM-MPI, RCM-HAD and RCM-MPI, and does not agree spatially with the observations in GCM-HAD.

Overall, dynamical downscaling with AMM7 adds value to the CMIP5 GCM simulations of MDT. The spatial improvement is largest for GCM-HAD, which has a lower horizontal resolution than GCM-MPI. Horizontal resolution is important to resolve the North Atlantic Current and Norwegian Coastal Current. This is in line with previous findings on the impact of dynamical downscaling of GCMs on the simulation of ocean circulation in the NWES region (e.g., [Ådlandsvik and Bentsen, 2007](#)). Resolving these currents is important for the exchange of heat and salt between the deep ocean and the shelf ([Huthnance, 1995](#)) and therefore likely to impact the emergent patterns of DSLC in climate change simulations.

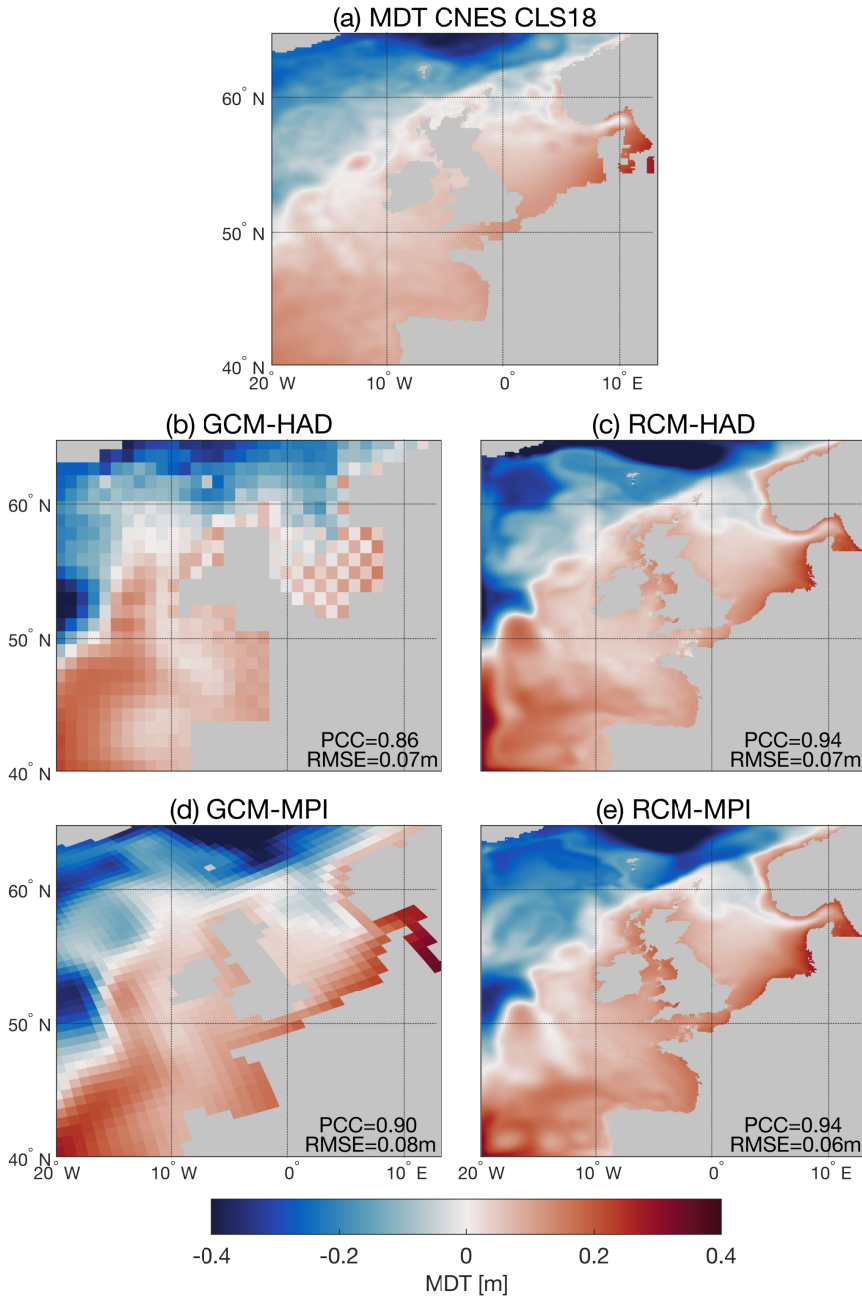


Figure 3.2: MDT anomalies (1993-2012), observed: **(a)** MDT CNES CLS18 and simulated: **(b)** GCM-HAD, **(c)** RCM-HAD, **(d)** GCM-MPI and **(e)** RCM-MPI. Simulated MDT is the time-mean of annual mean sea level, excluding the IB effect. The historical simulations are extended with the RCP8.5 scenario for 2006-2012. The regional mean MDT was removed from all fields. The PCCs and RMSEs of simulations v.s. observations are indicated in the panels.

3.3.2. Sea surface temperature and sea surface salinity

Next, we assess model skill at resolving the lateral transport and surface fluxes of heat and freshwater in the NWES region by comparing the historical simulations with observations of climatological SST and SSS. In winter, observed SST from OSTIA is relatively warm in the southwest of the NWES region (Figure 3.3a). The warm Atlantic water flows northward following the shelf break and enters the North Sea via its southern and northern entrances (as schematically shown in Figure 1.8). SST is colder in the east of the North Sea, along Norway and in the Norwegian Sea. In summer, observed SST is relatively high in the east of the North Sea (Figure 3.3b) and the SST of the slope current is less pronounced.

Compared to OSTIA, GCM-HAD is around 0.5-1.5 °C too warm at the surface on the shelf in winter (Figure 3.3c). Along the coasts, biases are larger and can reach up to 3 °C near the Danish coast (see Figure S3.2 for anomalies w.r.t. the observations). The SST of the slope current and the inflow of Atlantic water into the North Sea are not well reproduced by GCM-HAD. The English Channel in GCM-HAD is closed and we find cold biases of channel water of up to 0.9 °C with respect to the observations. In summer, GCM-HAD (Figure 3.3a) is around 2.5 °C colder than OSTIA near the Danish coast, and up to 5.2 °C warmer around the coast of the UK. Evaluated on the shelf, the PCCs and RMSEs of GCM-HAD with observations are 0.92 and 1.09 °C in winter, and 0.50 and 2.13 °C in summer, respectively. Dynamical downscaling of GCM-HAD clearly improves the representation of SST (Figures 3.3e & f). Similar to previous downscaled simulations (Holt et al., 2010; Tinker et al., 2015), RCM-HAD spatially reproduces the observed SST pattern in winter of the warm North Atlantic Current flowing along the shelf break and into the North Sea (Figure 3.3e). The biases in summer SST around the UK of RCM-HAD are reduced compared to GCM-HAD (Figure 3.3f). The PCCs increase and RMSEs reduce to 0.97 and 0.88 °C in winter, and to 0.88 and 1.16 °C in summer, respectively.

In winter, GCM-MPI is mostly around 0.3-1.4 °C warmer than the observations in the northern North Sea and north of Scotland, and around 0.6-1.1 °C colder west of the UK (Figure 3.3g). Like GCM-HAD, GCM-MPI is also too warm along the southeastern coasts of the North Sea (up to 2.6 °C) in winter compared to OSTIA. GCM-MPI resolves the SST of the slope current and the SST in the English Channel in winter better than GCM-HAD. In summer, GCM-MPI is around 1 °C warmer than the observations north of the UK and in the English Channel, and around 0.8-2.2 °C colder in the central and eastern North Sea (Figure 3.3h). On the shelf, GCM-MPI has PCCs and RMSEs of 0.91 and 0.69 °C in winter, and 0.82 and 0.86 °C in summer, respectively, so has smaller biases than GCM-HAD. Dynamical downscaling adds more spatial information and reduces biases with respect to the observations in both seasons (Figures 3.3i & j). The PCCs increase and RMSEs reduce to 0.96 and 0.54 °C in winter, and 0.90 and 0.66 °C in summer, respectively.

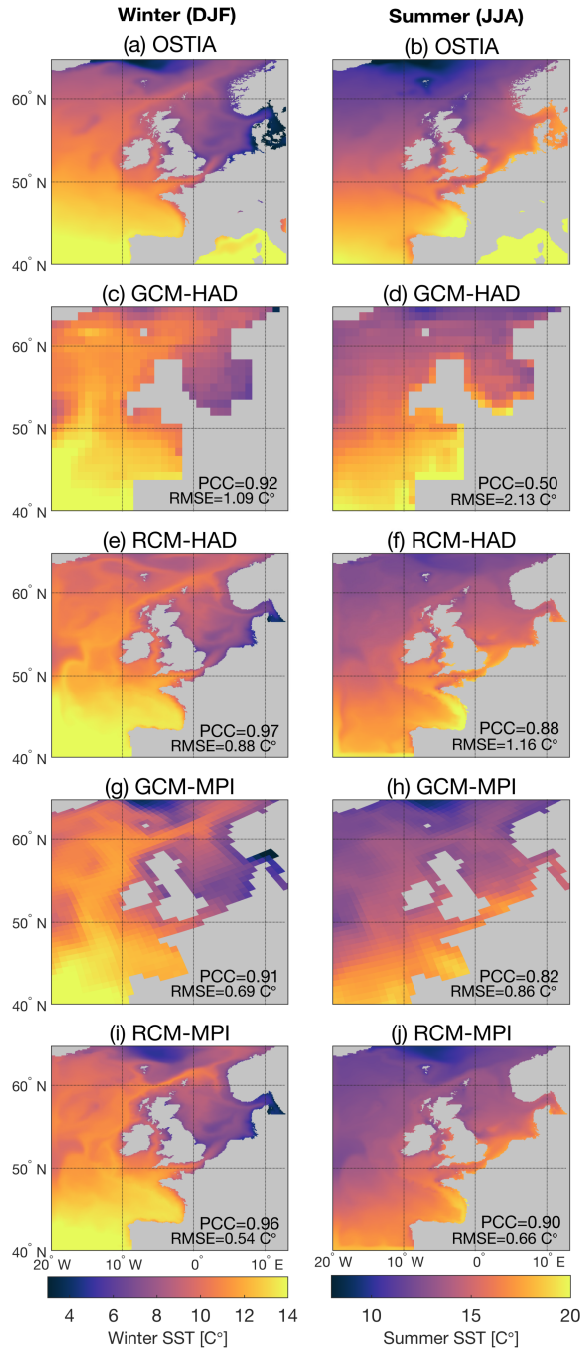


Figure 3.3: Climatological SST (1992-2010) in winter (DJF) and summer (JJA) from (a-b) the observational dataset OSTIA, and simulated for (c-d) GCM-HAD, (e-f) RCM-HAD, (g-h) GCM-MPI and (i-j) RCM-MPI. Note the different scales used for winter and summer. The historical simulations are extended with the RCP8.5 scenario for 2006-2010. The PCCs and RMSEs of simulations v.s. observations on the shelf are indicated in the panels. Biases relative to the observations are shown in Figure S3.2.

Similar to MDT, the biases of simulated SST with respect to the observations are larger for GCM-HAD than for GCM-MPI, and the improvement for GCM-HAD after downscaling is also larger. Part of this might be explained by the more realistic bathymetry and land mask of GCM-MPI. Near the boundaries of the NWES region, biases of RCM-HAD and RCM-MPI with observations are larger than in the interior, and the downscaled simulations are closer to their driving GCMs, due to the applied boundary conditions.

3

The observed climatological SSS is low in the German Bight, along part of the Dutch coast, in the Skagerrak and around Norway, owing to the freshwater outflow of rivers and the Baltic Sea (Huthnance, 1991), with moderate seasonal variation (Figures 3.4a & b). In contrast to the observations, in GCM-HAD low SSS is not confined to the coasts but spread out through most of the southeastern North Sea (Figures 3.4c & d). Simulated SSS there is around 1.5-2 PSU lower than EN4 (see also Figure S3.3). The observed low SSS around Norway is not reproduced by GCM-HAD, pointing to the misrepresentation of the Norwegian Coastal Current and/or Baltic outflow. RCM-HAD (Figures 3.4e & f) is more similar to the observations than GCM-HAD, but is fresher than EN4 in the German Bight, and more saline around Norway.

GCM-MPI displays low SSS around Norway like the EN4 observations, but does not reproduce the low SSS confined to the southeastern coast of the North Sea (Figures 3.4g & h). GCM-MPI is 4 to 6 psu too fresh in the Skagerrak compared to EN4. Downscaling also improves GCM-MPI, but like RCM-HAD, RCM-MPI (Figures 3.4i & j) is too fresh in the German Bight and too saline around Norway. The SSS of RCM-HAD and RCM-MPI are similar. This indicates that SSS on the shelf is controlled more strongly by freshwater input from evaporation/precipitation, river run-off, Baltic outflow and the circulation on the shelf than by dynamics outside of the domain. Compared to the GCMs, AMM7 also simulates lower SSS around the UK and west of France near freshwater input from river run-off. However, the EN4 observations are too sparse to facilitate a meaningful evaluation in those regions.

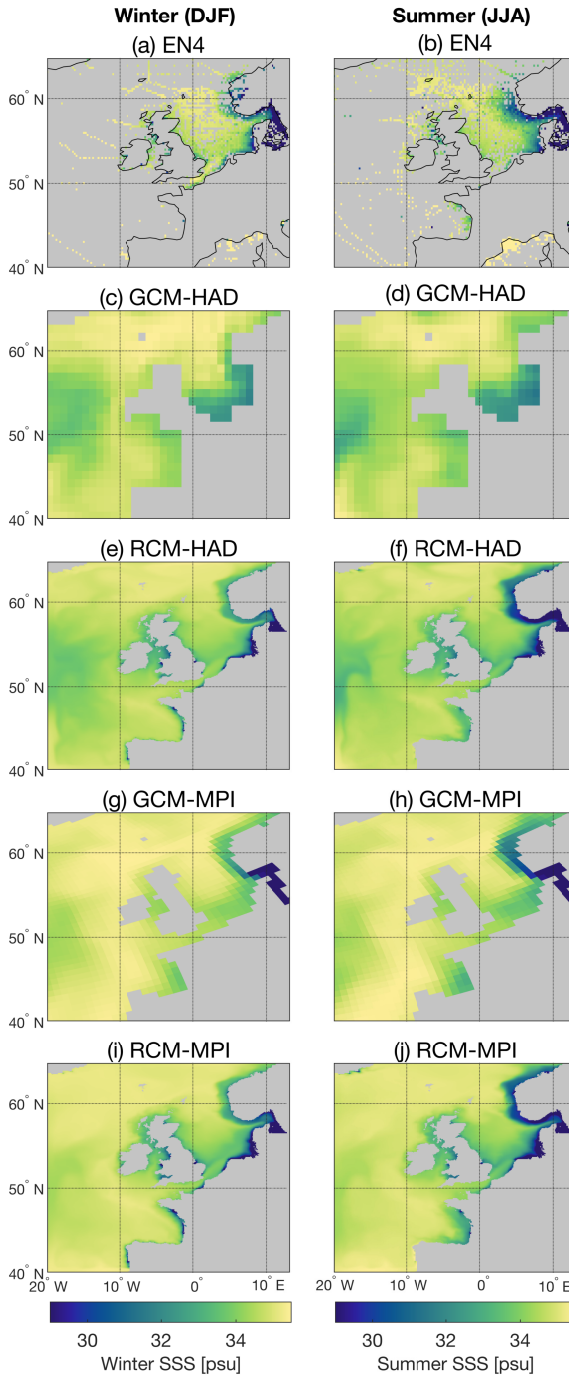


Figure 3.4: Climatological SSS (1980-2017) in winter (DJF) and summer (JJA) for **(a-b)** the observational dataset EN4, and simulated for **(c-d)** GCM-HAD, **(e-f)** RCM-HAD, **(g-h)** GCM-MPI and **(i-j)** RCM-MPI. The historical simulations are extended with the RCP8.5 scenario for 2006-2017. Biases relative to the observations are shown in Figure S3.3.

3.3.3. Interannual and seasonal sea-level variability

In addition to MDT (geostrophic circulation), SST and SSS, which have been used to evaluate downscaled simulations before (e.g., Ådlandsvik and Bentsen, 2007; Holt et al., 2010; Mathis, 2013; Tinker et al., 2015), we also evaluate the historical simulations of seasonal and interannual sea-level variability. As our metrics, we use the standard deviation of the detrended annual mean sea level and the mean amplitude of the seasonal sea-level cycle during 1980–2017. The TG observations (colored circles) show relatively large interannual variability in the German Bight and north of the Netherlands (Figure 3.5a), and slightly increased variability around the north of Norway. The large variability in the German Bight is also observed with satellite altimetry and can be explained well with a regression against local wind, SST and sea-level pressure (Sterlini et al., 2016).

GCM-HAD displays a relatively large interannual variability in the German Bight (Figure 3.5a), but in contrast to the observations this extends to the coast of Norway as well. In the deep ocean, GCM-HAD simulates a large interannual variability, especially near the western boundary of the NWES region. Comparing simulated interannual variability near TG stations to the observed TG data, GCM-HAD has a PCC of 0.7 and an RMSE of 1.12 cm. Dynamical downscaling improves the interannual sea-level variability of GCM-HAD compared to the TG records (Figure 3.5c), mainly along the Norwegian coast. Indeed, RCM-HAD (Figure 3.5b) has an increased PCC of 0.90 and a decreased RMSE of 0.84 cm.

The observed interannual sea-level variability at TGs is better reproduced by GCM-MPI (Figure 3.5d) than by GCM-HAD, which is reflected by a PCC of 0.83 and an RMSE of 0.55 cm with respect to the observations. Similar to GCM-HAD, the interannual sea-level variability in GCM-MPI is larger in parts of the deep ocean than on the shelf. In contrast to GCM-HAD, the skill of GCM-MPI at reproducing observed variability is only marginally affected by downscaling (Figures 3.5e & f). The PCC remains unchanged after downscaling, and the RMSE decreases from 0.55 to 0.52 cm for RCM-MPI. The comparison suggests that the impact of dynamical downscaling on simulations of interannual sea-level variability along the coast depends strongly on the driving GCM. The patterns of large interannual sea-level variability in the deep ocean are roughly similar between the original and downscaled simulations. The transition near the shelf break from small variability on the shelf to large variability in the deep ocean is more pronounced in the downscaled simulations, likely because the shelf break is better resolved in AMM7.

TGs in the German Bight and along the north coast of Norway show the highest seasonal sea-level variability (Figure 3.6, colored circles). The observed seasonal amplitude gradually increases northward along the Dutch coast. The simulated seasonal amplitude is typically smaller in the southwest of the NWES region and increases toward the north and northeast for all models (Figures 3.6a, b, d & e). Although GCM-HAD simulates high seasonal sea-level variability in the German Bight and around Norway, its variability has little spatial coherency in the North Sea and along the Norwegian coast (Figure 3.6a) and does not compare well with the TGs (Figure 3.6c). The PCC and RMSE of GCM-HAD with the observations are 0.84

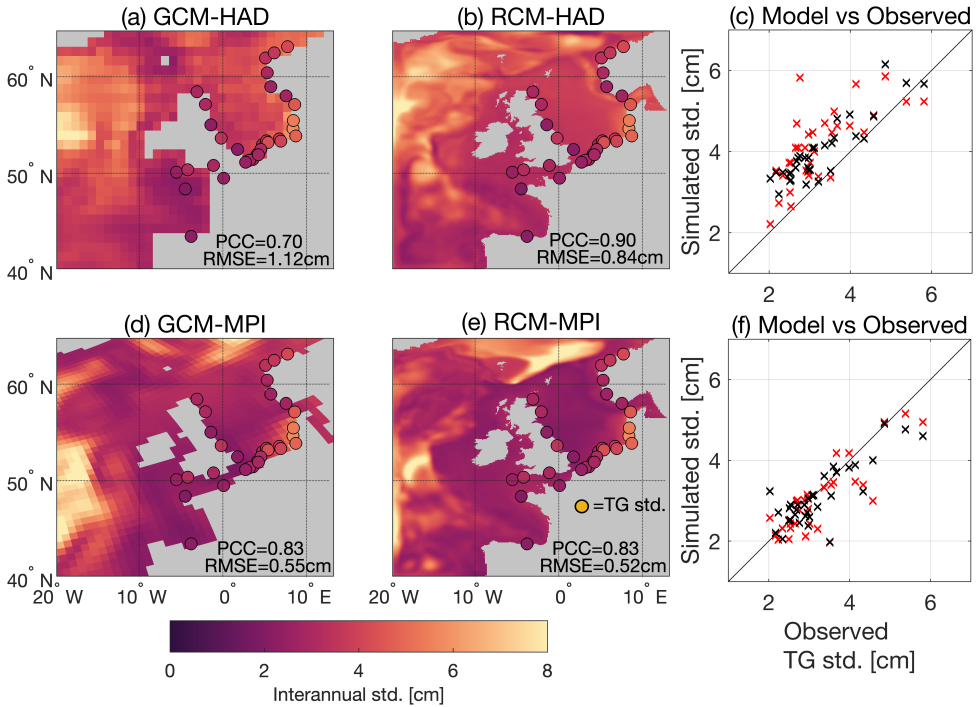


Figure 3.5: Simulated interannual sea-level variability (1980-2017) calculated as the standard deviation (std.) of detrended annual mean sea level for **(a)** GCM-HAD, **(b)** RCM-HAD, **(d)** GCM-MPI and **(e)** RCM-MPI, with colored circles depicting observed interannual variability at TGs. The historical simulations are extended with the RCP8.5 scenario for 2006-2017. The PCCs and RMSEs of simulations v.s. observations are indicated in the panels; scatter plots of simulated v.s. observed interannual variability at TGs for **(c)** GCM-HAD (red) and RCM-HAD (black) and for **(f)** GCM-MPI (red) and RCM-MPI (black).

and 2.18 cm, respectively. Dynamical downscaling strongly improves the fit with observations: RCM-HAD has a PCC of 0.94 and an RMSE of 1.57 cm (Figures 3.6b & c). Especially in the central North Sea, the seasonal amplitude is larger for RCM-HAD than for GCM-HAD.

GCM-MPI also displays high seasonal sea-level variability in the German Bight, but its variability extends too far south along the Dutch and Belgian coasts (Figure 3.6d). This leads to a poor fit with the observations: the PCC and RMSE of GCM-MPI are 0.67 and 2.99 cm, respectively. Around Norway, the simulation agrees with the observations better. Again, dynamical downscaling leads to a much better fit (Figures 3.6e & f), especially along the southeastern coast of the North Sea. The PCC and RMSE of RCM-MPI are 0.95 and 0.94 cm, respectively.

The improved model skill likely results from the increased ocean resolution and downscaled atmospheric forcing in our setup. However, the seasonal cycle is also affected by river run-off and tides (Tsimplis and Woodworth, 1994), of which the latter is not resolved in the GCMs. Seasonal sea-level variability in RCM-HAD and

RCM-MPI (Figures 3.6b & d) is remarkably similar (PCC of 0.82 over the NWES region, and similar biases w.r.t. TGs) despite the different driving GCMs, indicating that the boundary conditions have a lesser influence. Comparing Figures 3.5 & 3.6 shows that particularly along the coasts, the seasonal sea-level cycle benefits more from dynamical downscaling than interannual sea-level variability, which appears to have a larger dependency on the lateral boundary conditions.

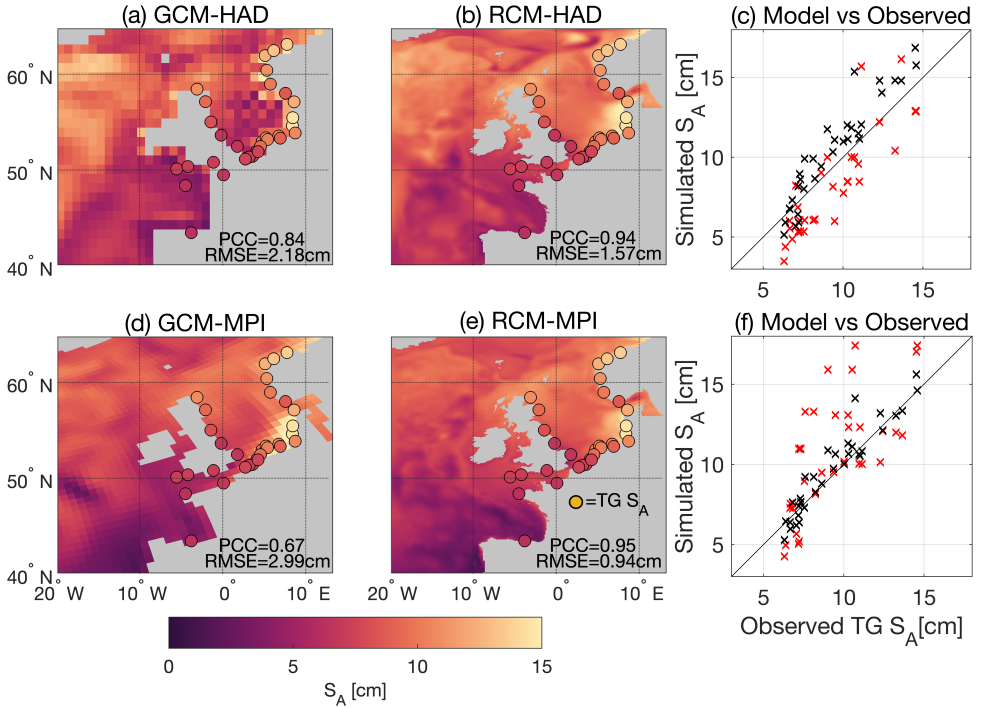


Figure 3.6: Simulated amplitude of the seasonal cycle of sea level S_A (1980-2017) calculated as half of the difference between the annual minimum and maximum sea level and averaged over all years for (a) GCM-HAD, (b) RCM-HAD, (d) GCM-MPI and (e) RCM-MPI, with colored circles depicting the observed seasonal amplitude at TGs. The historical simulations are extended with the RCP8.5 scenario for 2006-2017. The PCCs and RMSEs of simulations v.s. observations are indicated in the panels; scatter plots of the simulated v.s. observed seasonal amplitude at TGs for (c) GCM-HAD (red) and RCM-HAD (black) and for (f) GCM-MPI (red) and RCM-MPI (black).

Summarizing, dynamical downscaling generally improves the historical GCM simulations with respect to observations (i.e., reduces biases). We expect that dynamical downscaling will improve the simulations of other CMIP5 GCMs as well, especially since most CMIP5 GCMs have a lower horizontal resolution than MPI-ESM-LR in the NWES region. The evaluation shows that the bathymetry and land mask of GCM-HAD is too coarse to resolve the circulation on and along the shelf. This can influence sea-level projections as well, which we will investigate next.

3.4. The impact of dynamical downscaling on future DSLC

In this section we assess the effect of dynamical downscaling on simulations of future DSLC (Section 3.4.1) and its different components (Section 3.4.2). Additionally, we investigate the time of emergence (Hawkins and Sutton, 2012; Lyu et al., 2014) of SLC above background variability (Section 3.4.3).

3.4.1. DSLC projections for the 21st century

We compute 21st century DSLC as the difference between time-mean sea level in the historical period (1980-2005) and at the end of the century (2074-2099). The global-mean thermosteric SLC 'zostoga' is excluded (see Section 3.2.4). For RCP8.5, all models project a relative sea-level rise on the NWES (Figure 3.7), with the strongest increase for GCM-HAD (Figure 3.7a). The results for RCP4.5 are spatially similar to the results for RCP8.5, but have smaller magnitudes (Figure S3.4).

The differences in DSLC between GCM-HAD and RCM-HAD (Figures 3.7a & b) are large, especially in the North Sea (Figure 3.7c): DSLC is up to 15.5 cm larger in GCM-HAD than in RCM-HAD along the southeastern coast (up to 8 cm larger for RCP4.5). This difference is approximately 30% of the sterodynamic SLC (DSLC plus 'zostoga', Gregory et al., 2019) simulated by GCM-HAD for the North Sea. It is of a magnitude similar to the inter-model uncertainty of CMIP5 ensembles used for previous ocean dynamic sea-level projections (e.g., Slangen et al., 2012, 2014; de Vries et al., 2014; Kopp et al., 2014; Palmer et al., 2018b). DSLC in GCM-HAD is 5-7 cm larger than in RCM-HAD north of the UK, 3-4 cm larger along the coastline of France and Spain, and 2-4 cm smaller along parts of the Irish coast. In the Irish Sea, differences in DSLC between GCM-HAD and RCM-HAD are also large, since the Irish Sea is not resolved in GCM-HAD and interpolated values are used instead. Unlike GCM-HAD, RCM-HAD simulates a distinct sea-level rise in the Norwegian Trench despite the climatology used for the Baltic outflow. This points toward changes in shelf circulation or in the Atlantic inflow into the North Sea (Holt et al., 2018).

In contrast to GCM-HAD and RCM-HAD, the spatial patterns of DSLC in GCM-MPI (Figure 3.7d) and RCM-MPI (Figure 3.7e) generally agree well. DSLC in GCM-MPI is up to 3.5 cm smaller than in RCM-MPI in the Bay of Biscay (Fig. 7f). In the North Sea, GCM-MPI simulates slightly larger DSLC, but differences with RCM-MPI do not exceed 2.5 cm (7% of the sterodynamic SLC simulated by GCM-MPI). The differences are much smaller than for GCM-HAD, which points to the importance of a realistic bathymetry and land mask for sea-level projections.

In the deep ocean, the differences between the original and downscaled simulations of DSLC can exceed the differences on the shelf for both driving GCMs (Figures 3.7c & f). The currents east of Iceland and along the Faroe Islands show a sea-level fall relative to the global mean in RCM-HAD, but not in GCM-HAD. DSLC in GCM-MPI around the Faroe Islands is smaller than on the shelf, but in RCM-MPI it is larger.

Near the western boundary of the NWES region, GCM-HAD (Figure 3.7a) shows a large sea-level rise, whereas in GCM-MPI (Figure 3.7d) sea level falls relative to the global mean change. This is likely caused by changes in the gyre circulation west of the region, which are inherited in the downscaled simulations through the lateral boundary conditions (Figures 3.7b & e).

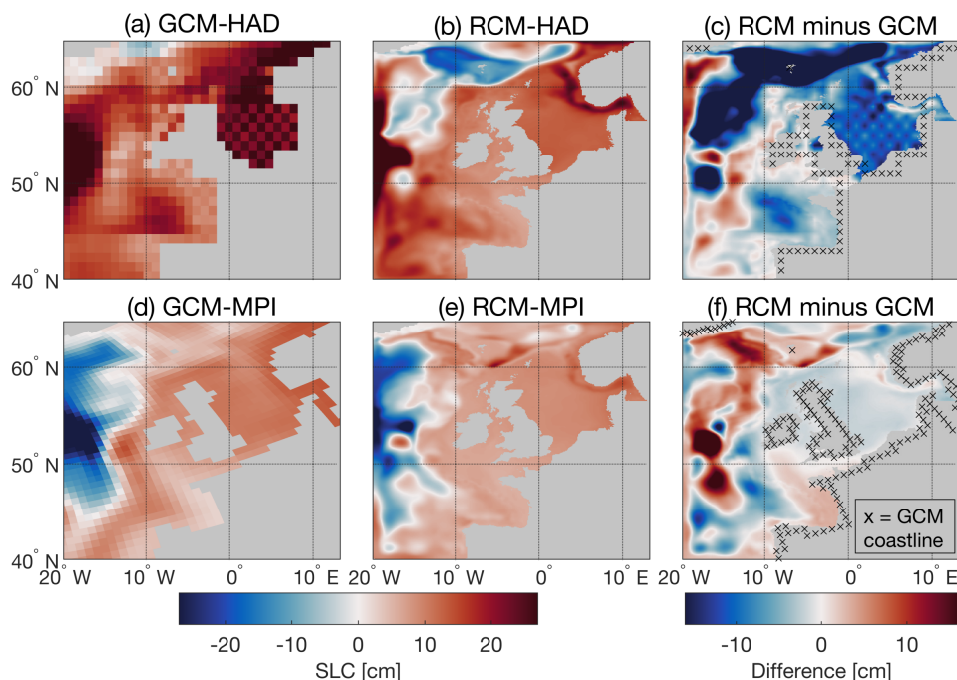


Figure 3.7: Projected DSLC between 1980-2005 and 2074-2099 (RCP8.5) for (a) GCM-HAD, (b) RCM-HAD, (c) RCM-HAD minus GCM-HAD, (d) GCM-MPI, (e) RCM-MPI and (f) RCM-MPI minus GCM-MPI. The differences in (c) and (f) are computed on the AMM7 grid; black crosses indicate the original GCM coastline.

In GCM-HAD there is a large contrast (≈ 18 cm) between DSLC northeast and southwest of the English Channel (Figure 3.7a). Apparently, the closed English Channel in GCM-HAD prohibits circulation into the North Sea via its southern entrance. The DSLC gradient across the closed English Channel reduces by approximately 13 cm after dynamical downscaling (Figure 3.7b). For GCM-MPI, which has an open English Channel, dynamical downscaling hardly affects the SLC gradient. To explore the effect of a closed English Channel on DSLC further, we assess the difference between DSLC on either side of the English Channel in 18 additional CMIP5 GCMs (Figure 3.8). For all 20 GCMs and the downscaled simulations, 21st century DSLC is larger near Vlissingen (northeast of the channel) than near Brest (southwest of the channel). The difference is largest for HadGEM2-ES (≈ 18 cm, closed English Channel) and smallest for EC-EARTH (≈ 0.55 cm, open English Channel). On average, the difference between DSLC near Vlissingen and Brest is 4.2 cm for the

10 CMIP5 models with an open English Channel (squares), and 8.5 cm for the 10 CMIP5 models with a closed English Channel (circles). Like HadGEM2-ES, other CMIP5 models with a closed English Channel and a large gradient in DSLC across the channel might benefit substantially from dynamical downscaling.

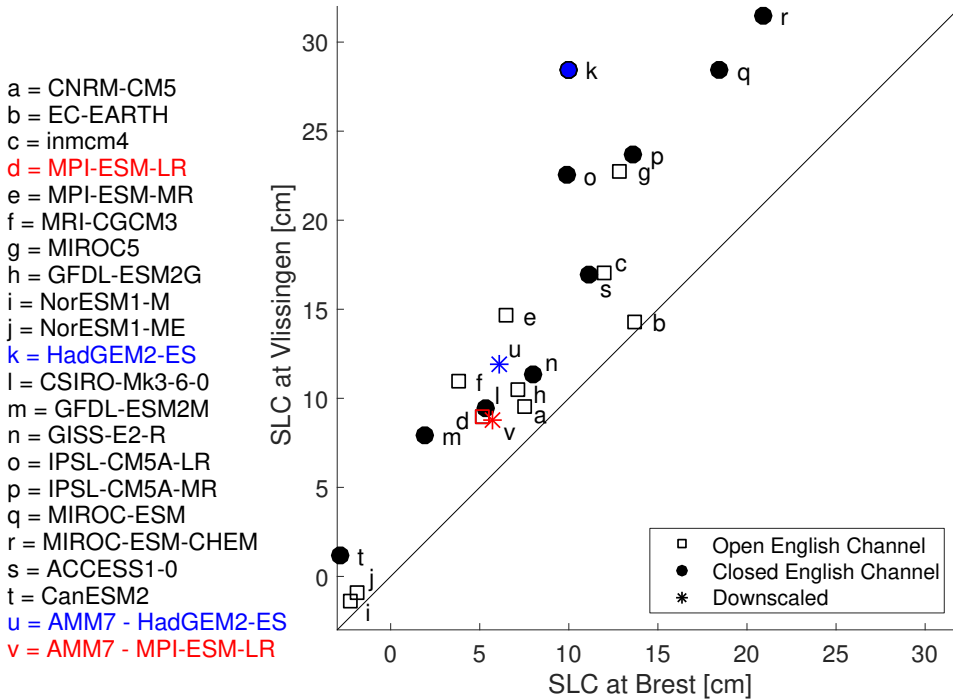


Figure 3.8: Simulated DSLC (excluding the IB effect) between 1980-2005 and 2074-2099 (RCP8.5) near Vlissingen v.s. near Brest for 20 CMIP5 models with a closed English Channel (circles) or open English Channel (squares), and for our downscaled simulations (asterisks). The CMIP5 models downscaled in this study are indicated in red (HadGEM2-ES) and blue (MPI-ESM-LR). The solid 1:1 line denotes equal DSLC in Vlissingen and Brest.

3.4.2. Drivers of projected DSLC

To better understand which processes drive the DSLC differences between the original and downscaled simulations (Figure 3.7), we decompose DSLC into local steric SLC (Figure 3.9) and SLC related to bottom pressure changes (manometric SLC, Figure 3.10) following Equation 3.1 (Section 3.2.3). We exclude the IB effect here, since it is small on centennial timescales (Church et al., 2013) and differences in DSLC due to the IB effect between our models are less than 0.5 cm.

All models project the largest steric change in the deep ocean (Figures 3.9a, b, d & e), because when heated a deeper water column expands more than a shallow one. If no other forces balance the resulting SSH gradient, these volume anomalies are redistributed from the deep ocean toward the shelf (Landerer et al., 2007). This mass redistribution leads to a slight bottom pressure decrease in the deep ocean

and to an increase on the shelf (Figures 3.10a, b, d & e). The dependency of local steric and bottom pressure change on water column depth means that differences between models will depend partially on differences in bathymetry. The imprint of bathymetry is indeed visible in Figures 3.9c & f and Figures 3.10c & f, for example in the North Sea, the Norwegian Trench and along the shelf break. Note that these steric and bottom pressure change differences often have opposite signs.

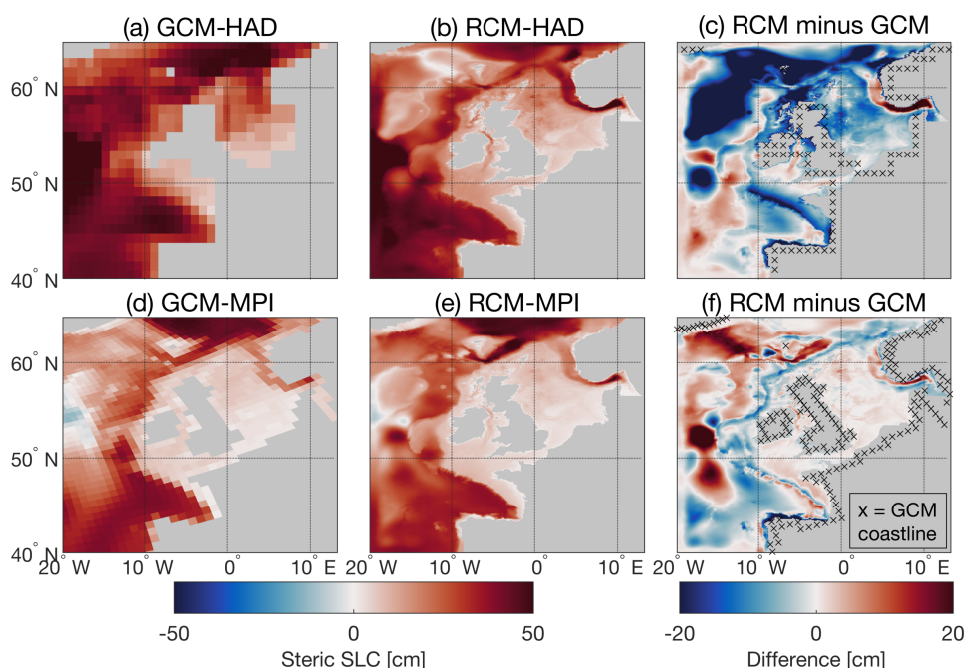


Figure 3.9: Local steric SLC (derived in Section 3.2.3) between 1980-2005 and 2074-2099 (RCP8.5) for (a) GCM-HAD, (b) RCM-HAD, (c) RCM-HAD minus GCM-HAD, (d) GCM-MPI, (e) RCM-MPI and (f) RCM-MPI minus GCM-MPI. The differences in (c) and (f) are computed on the AMM7 grid; black crosses indicate the original GCM coastline.

On the shelf, the differences in local steric and manometric SLC between GCM-HAD and RCM-HAD are large (Figures 3.9c & 3.10c). The local steric change in GCM-HAD can be over 15 cm larger than in RCM-HAD in the northern North Sea. GCM-HAD also simulates a much larger local steric change north of Scotland, where the representation of the shelf break is crude (Figure 3.1). SLC due to bottom pressure changes is up to 13 cm larger in GCM-HAD than in RCM-HAD in the North Sea. These effects combined lead to the large DSLC differences in the North Sea between GCM-HAD and RCM-HAD (Figure 3.7c). The DSLC differences between GCM-MPI and RCM-MPI (Figure 3.7f) on the shelf are the result of a slightly larger local steric change on the Armorican and Aquitaine shelves (Figure 3.9f), and a slightly smaller bottom pressure change mainly in the North Sea and Irish Sea in RCM-MPI (Figure 3.10f).

Off the shelf, the differences in local steric and manometric SLC display a complex spatial pattern and partially cancel out. Differences in the local steric change between the GCM and downscaled simulations are largest in the north and northwest of the domain. The decrease in sea level with respect to the global mean change in RCM-HAD and the increase in RCM-MPI east of Iceland and around the Faroe Islands (Figures 3.7b & e), and the resulting differences with the GCMs, are mainly driven by local steric changes (Figures 3.9c & f).

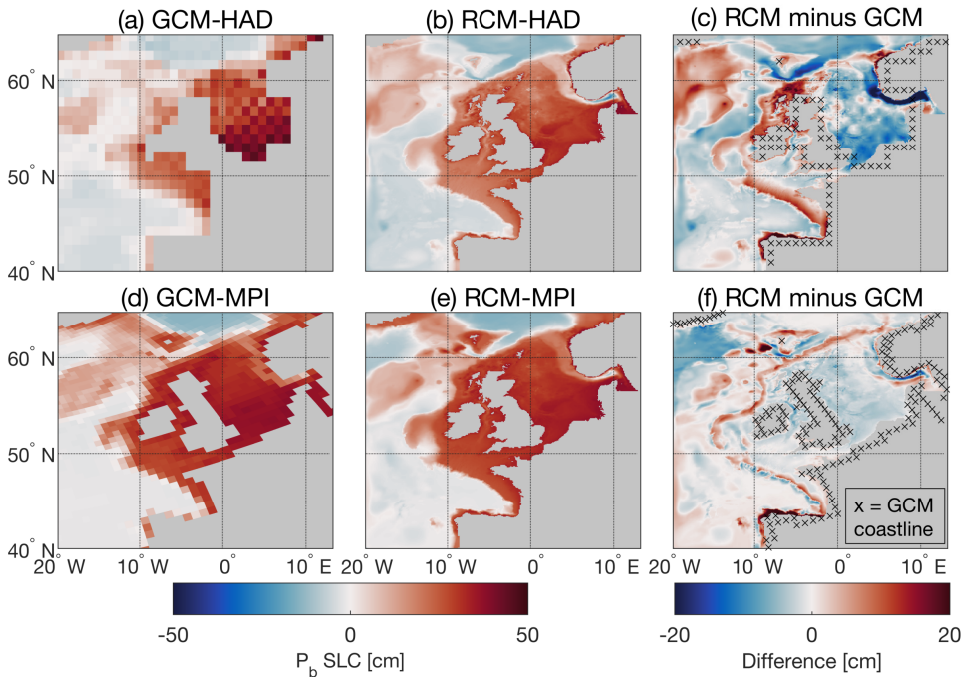


Figure 3.10: Manometric SLC (SLC related to bottom pressure changes, as derived in Section 3.2.3) between 1980-2005 and 2074-2099 (RCP8.5) for **(a)** GCM-HAD, **(b)** RCM-HAD, **(c)** RCM-HAD minus GCM-HAD, **(d)** GCM-MPI, **(e)** RCM-MPI and **(f)** RCM-MPI minus GCM-MPI. The differences in (c) and (f) are computed on the AMM7 grid; black crosses indicate the original GCM coastline. The global-mean thermosteric change 'zostoga' has been added to all fields to correct for the spurious bottom pressure change of the GCMs due to the Boussinesq approximation (Section 3.2.4).

Despite the shallow depth of the North Sea, the differences in local steric changes between GCM-HAD and RCM-HAD (Figure 3.9c) in the North Sea are large (10-17 cm). To see if this is the result of differences in temperature change or differences in salinity change, we further decompose steric change into thermosteric (Figure 3.11) and halosteric (Figure 3.12) SLC (explained in Section 3.2.3). All models simulate large thermosteric sea-level rise in the deep ocean, except RCM-HAD southeast of Iceland (Figures 3.11a, b, d & e). Halosteric SLC partially cancels out thermosteric SLC and is negative in the southwest of the NWES region and positive elsewhere in all models (Figures 3.12a, b, d & e). On the shelf, thermosteric SLC is in the order

of a few cm, and the differences between GCM-HAD and RCM-HAD (Figure 3.11c) and between GCM-MPI and RCM-MPI (Figures 3.11f) are mostly below 1 cm.

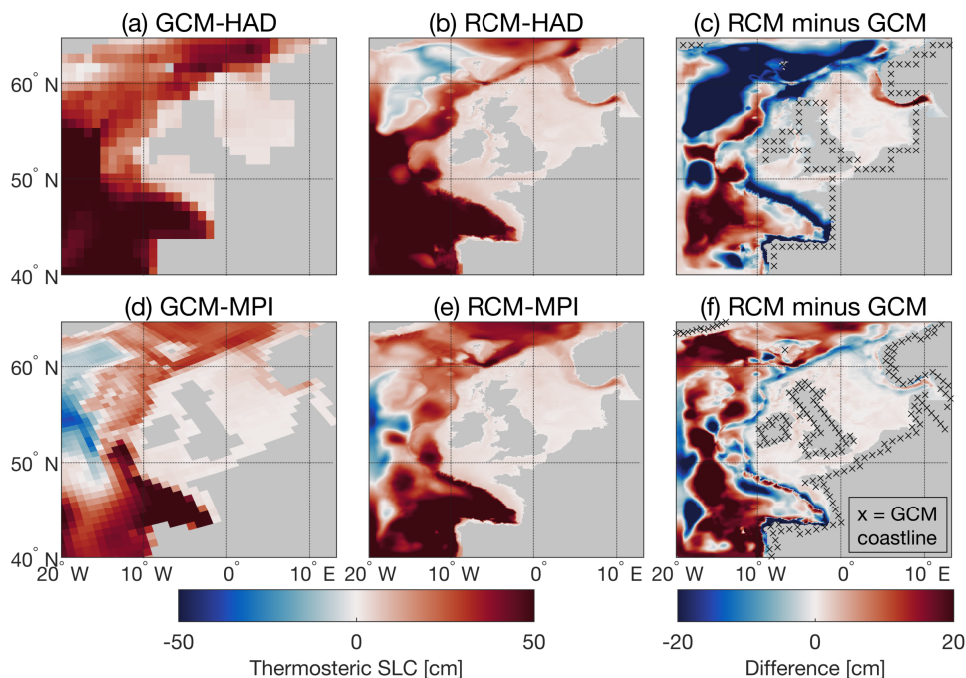


Figure 3.11: Thermosteric SLC between 1980-2005 and 2074-2099 (RCP8.5) for (a) GCM-HAD, (b) RCM-HAD, (c) RCM-HAD minus GCM-HAD, (d) GCM-MPI, (e) RCM-MPI and (f) RCM-MPI minus GCM-MPI. The differences in (c) and (f) are computed on the AMM7 grid; black crosses indicate the original GCM coastline.

The differences in halosteric SLC between GCM-HAD and RCM-HAD are up to 15 cm (Figure 3.12c) on the shelf. This indicates that DSLC in the northern North Sea in GCM-HAD is larger than in RCM-HAD (Figure 3.7c) mainly because of the differences in depth-integrated salinity change. This can be the result of (a combination of) differences in the projected changes in river run-off, evaporation minus precipitation, Atlantic inflow and shelf circulation that are introduced by dynamical downscaling. Halosteric SLC is also larger in RCM-MPI than in GCM-MPI, especially in the Bay of Biscay (Figure 3.12f). As shown in Section 3.3, the bathymetry and land mask of GCM-HAD are too coarse to model the Atlantic inflow through the Norwegian Trench and English Channel, affecting the simulated climatological salinity on the shelf (Figure 3.4) and likely also DSLC.

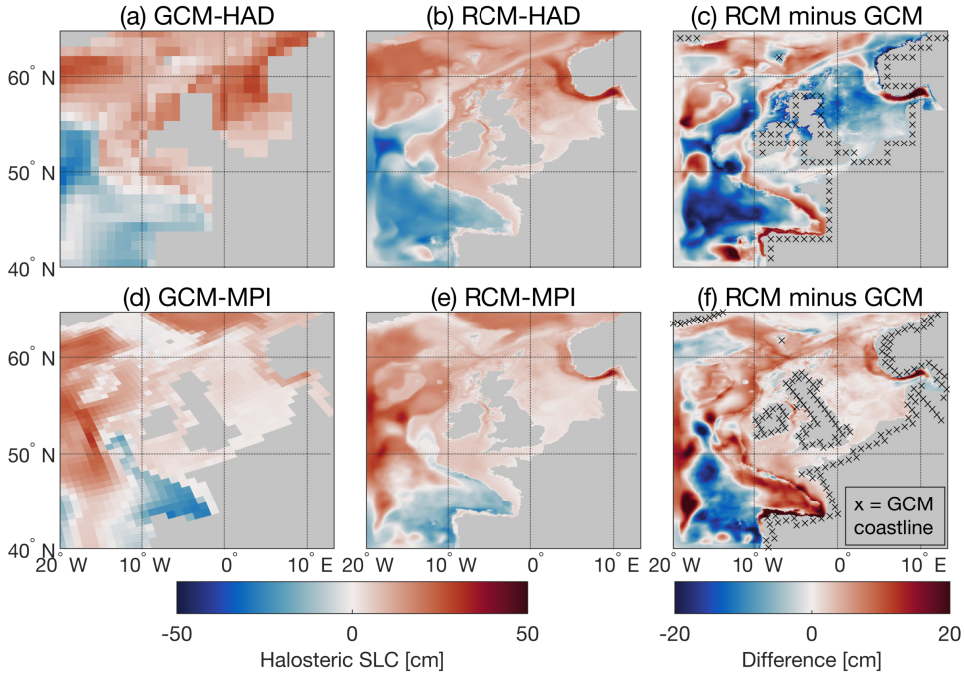


Figure 3.12: Halosteric SLC between 1980-2005 and 2074-2099 (RCP8.5) for **(a)** GCM-HAD, **(b)** RCM-HAD, **(c)** RCM-HAD minus GCM-HAD, **(d)** GCM-MPI, **(e)** RCM-MPI and **(f)** RCM-MPI minus GCM-MPI. The differences in **(c)** and **(f)** are computed on the AMM7 grid; black crosses indicate the original GCM coastline.

3.4.3. Time of emergence of sea-level change

In addition to the DSLC over the 21st century, we investigate the impact of dynamical downscaling on the time of emergence (ToE) of sterodynamic SLC (Hawkins and Sutton, 2012; Lyu et al., 2014), which is a measure of the magnitude of forced SLC relative to internal sea-level variability. The detection of SLC relative to background noise is useful for impact assessments and adaption planning (Kirtman et al., 2013). We calculate the ToE of sterodynamic SLC relative to the simulated historical time-mean sea level (1980-2005). We define ToE as the time in the middle of a 26-yr window following the 26-yr historical period, in which the change in time-mean sea level relative to the historical window exceeds and remains outside the bands of one standard deviation of detrended annual-mean sea level in both this and the historical window.

For all models sterodynamic SLC has emerged above variability on most of the shelf before 2020 (Figures 3.13a, b, d & e). The emergence in the German Bight occurs later than elsewhere in the North Sea because of the high local interannual sea-level variability (Figure 3.5). Compared to RCM-HAD, ToE in GCM-HAD is up to 6 years earlier in the North Sea and along the coast of France and Scotland, 3 years later south of the UK and up to 8 years later in the Norwegian Trench (Figure 3.13c).

These differences are relatively small despite the large differences in DSLC between GCM-HAD and RCM-HAD by the end of the 21st century (Figure 3.7c). Since the differences in historical interannual variability on the shelf between both models are not very large (Figures 3.5a & b), this indicates that DSLC in the North Sea in RCM-HAD starts to diverge from DSLC in GCM-HAD mainly after the ToE. In the deep ocean, sterodynamic SLC emerges later than on the shelf for both models since interannual sea-level variability in the deep ocean is larger (Figures 3.5a & b). The sea-level fall east of Iceland and around the Faroe Islands in RCM-HAD (Figure 3.7b) is not detectable above sea-level variability before the end of the 21st century (Figure 3.13b).

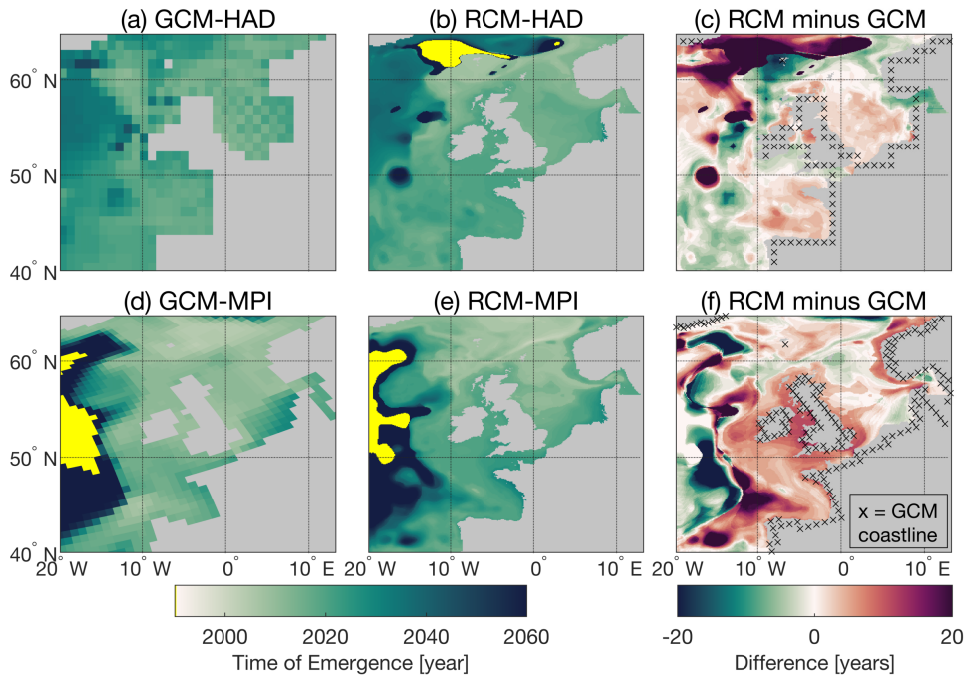


Figure 3.13: ToE of sterodynamic SLC (RCP8.5) relative to the historical period 1980-2005 for (a) GCM-HAD, (b) RCM-HAD, (c) RCM-HAD minus GCM-HAD, (d) GCM-MPI, (e) RCM-MPI and (f) RCM-MPI minus GCM-MPI. The differences in (c) and (f) are computed on the AMM7 grid; black crosses indicate the original GCM coastline. Yellow grid cells indicate no emergence before the end of the century. For these grid cells we use the value 2099 in (c) and (f).

On the shelf, differences in ToE between GCM-MPI and RCM-MPI (Figure 3.13f) are larger than between GCM-HAD and RCM-HAD, especially along the coasts of the UK and Norway. For example, the ToE in the Irish Sea in GCM-MPI is up to 12 years earlier than in RCM-MPI, despite differences in 21st century DSLC between GCM-MPI and RCM-MPI of less than 2.5 cm (Figure 3.7f). Since sea-level variability and the timing of SLC differ between GCM and RCM, the effect of dynamical downscaling on ToE on the NWES can be large, even if differences in DSLC by the end of the 21st

century are relatively small. The ToE on the shelf is similar for RCP4.5 and RCP8.5 since emergence occurs mostly before the RCPs start to significantly diverge. The emergence for RCP4.5 occurs somewhat earlier in RCM-HAD than in GCM-HAD in the German Bight and south of the UK (Figure S3.5). Similar to GCM-HAD and RCM-HAD, the emergence in GCM-MPI and RCM-MPI occurs later in the deep ocean than on the shelf. West of the shelf, stericodynamic SLC does not emerge before the end of the 21st century, indicating that the projection of a sea-level fall there (Figures 3.7d & e) is strongly affected by interannual variability.

3.5. Projected changes in the seasonal sea-level cycle

In Section 3.3.3, we showed that dynamical downscaling improved the fit with the observed amplitude of the seasonal sea-level cycle at TGs. Therefore, we also analyze the impact of dynamical downscaling on the projected changes in seasonal amplitude. Changes in the seasonal sea-level cycle may heighten the risk associated to sea-level rise on sub-annual timescales. In most of the domain, the linear trends of the seasonal amplitude over the 21st century are not significantly different from 0 (yellow) for any of the models (Figures 3.14a, b, d & e). For RCP4.5 an even smaller part of the NWES region displays significant trends (Figure S3.6). In locations with significant trends, differences between GCM-HAD and RCM-HAD can be as large as the trends themselves (Figure 3.14c). The trends in GCM-HAD are up to 0.33 mm/yr smaller than in RCM-HAD in the southern North Sea, which is a large difference compared to the observed historical seasonal amplitude of around 7 cm (Figure 3.6). For GCM-MPI and RCM-MPI, the trends are mostly significant and positive around the north of the UK (Figures 3.14d & e). A large difference in trends is displayed in the southwest of the NWES region. In the northern North Sea, trends in GCM-MPI can be up to 0.19 mm/yr smaller than in RCM-MPI (Figure 3.14f). The large differences in trends between the GCM and downscaled simulations suggest that RCMs can be used to improve projections of the change in the amplitude of the seasonal sea-level cycle on the NWES region.

Next, we use the linear trends in Figure 3.14 to detrend the amplitude of the seasonal sea-level cycle. The magnitude of the remaining variability of the amplitude over the 21st century can be calculated by taking the standard deviation of the detrended signal (Figure 3.15). The amplitude of the seasonal sea-level shows substantial interannual variability for all models (Figures 3.15a, b, d & e), especially when compared to the linear trends in Figure 3.14. The variability is largest in the German Bight, and smaller at the British coast of the North Sea. This is in line with the 20th century observations at TG stations around the North Sea (Dangendorf et al., 2013b; Frederikse and Gerkema, 2018). The results are similar for RCP4.5 (Figure S3.7).

On the shelf, differences in the interannual variability of the seasonal amplitude between GCM-HAD and RCM-HAD (Figure 3.15c) can be up to 1.6cm ($\approx 40\%$ of the standard deviation in GCM-HAD), and up to 2.6 cm ($\approx 32\%$ of the standard

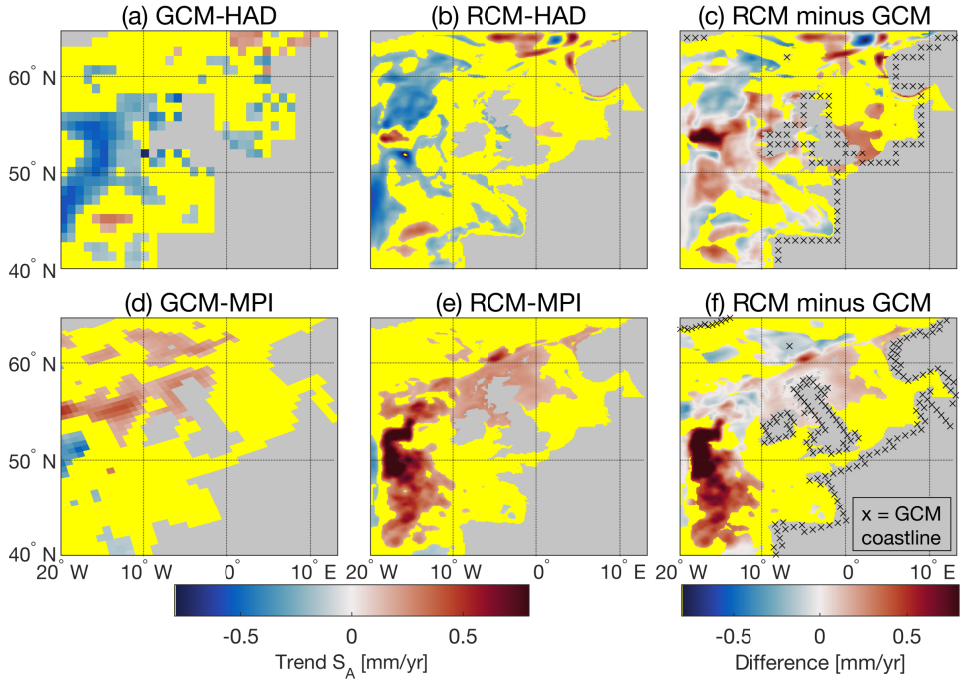


Figure 3.14: Linear trends in the amplitude of the seasonal cycle of sea level S_A (1980-2099, RCP8.5) for (a) GCM-HAD, (b) RCM-HAD, (c) RCM-HAD minus GCM-HAD, (d) GCM-MPI, (e) RCM-MPI and (f) RCM-MPI minus GCM-MPI. Yellow grid cells indicate linear regression coefficients that are not significantly different from 0 (2 standard errors; 95% confidence). The differences in (c) and (f) are computed on the AMM7 grid; black crosses indicate the original GCM coastline. Differences are yellow when both simulations have insignificant trends.

deviation in GCM-MPI) between GCM-MPI and RCM-MPI (Figure 3.15f). The high variability in the German Bight simulated by GCM-MPI extends further along the southeastern coast of the North Sea than in RCM-MPI, similar to the bias of its historical mean seasonal amplitude relative to observations (Figure 3.6). Hence, dynamical downscaling is important to better project the variability of the amplitude of the seasonal sea-level cycle in the NWES region.

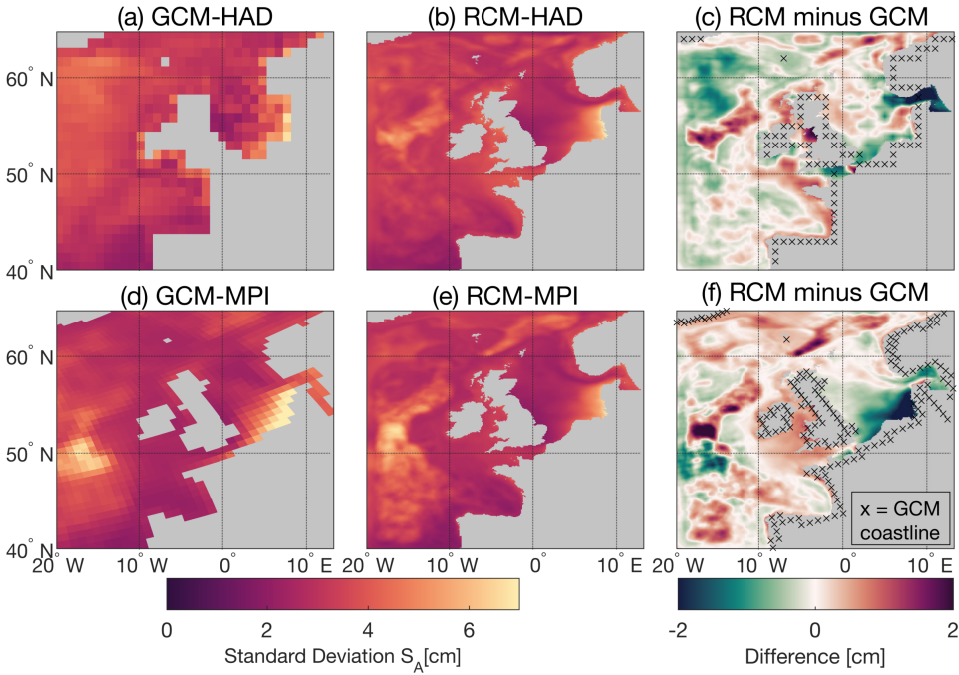


Figure 3.15: Interannual variability of the amplitude of the seasonal cycle of sea level s_A (1980-2099) calculated as the standard deviation of the detrended timeseries of s_A (RCP8.5), for (a) GCM-HAD, (b) RCM-HAD, (c) RCM-HAD minus GCM-HAD, (d) GCM-MPI, (e) RCM-MPI and (f) RCM-MPI minus GCM-MPI. The differences in (c) and (f) are computed on the AMM7 grid; black crosses indicate the original GCM coastline.

3.6. Discussion and conclusions

Previous projections of regional sea level have been constructed with the output of CMIP5 GCMs (e.g., [Slangen et al., 2012, 2014](#); [Church et al., 2013](#); [de Vries et al., 2014](#); [Kopp et al., 2014](#); [Palmer et al., 2018b](#)). However, such GCMs have a horizontal ocean resolution in the order of 100 km and exclude some of the key processes relevant to shelf seas. Therefore, GCMs might not be the most appropriate means of providing sea-level projections for coastal regions. The objective of this study was to explore the use of dynamical downscaling with the regional model AMM7 to refine the CMIP5 GCM simulations of the ocean dynamic sea-level change and variability for the NWES region.

In agreement with previous dynamical downscaling studies for the NWES (e.g., [Ådlandsvik and Bentsen, 2007](#)), we find that dynamical downscaling improves historical GCM simulations with respect to observations of SST, SSS and MDT. Additionally, we show that dynamical downscaling provides a better representation of sea-level variability on seasonal and interannual timescales (Section 3.3). The improvements reflect the importance of a realistic bathymetry and land mask to resolve important

topographically-steered currents along and on the shelf, which requires a sufficient horizontal and vertical resolution. MPI-ESM-LR has a relatively high horizontal resolution and reproduces observations better than HadGEM2-ES. Related to this, we find that the improvement after dynamical downscaling is generally larger for HadGEM2-ES than for MPI-ESM-LR.

The inclusion of key processes for the NWES and the improvement in reproducing observed ocean properties and sea-level characteristics that was demonstrated in Section 3.3 promotes greater confidence in the emergent patterns of DSLC in our dynamically downscaled simulations. Depending on the driving GCM, the impact of dynamical downscaling on 21st century DSLC can be substantial (Section 3.4). For MPI-ESM-LR, differences between the GCM and downscaled simulations are in the order of a few cm on the shelf. For HadGEM2-ES the downscaled DSLC is up to 15.5 cm (RCP8.5) smaller along the North Sea coastline than in the original GCM simulations (up to 8 cm for RCP4.5). This is as large as the inter-model uncertainty in the CMIP5 ensembles used for previous dynamic sea-level projections (e.g., Church et al., 2013; Slangen et al., 2014). To draw more general conclusions, additional CMIP5 models need to be dynamically downscaled. However, since the horizontal resolution of HadGEM2-ES is more typical for the CMIP5 ensemble than the horizontal resolution of MPI-ESM-LR, we expect the results of dynamical downscaling for HadGEM2-ES to be representative of other CMIP5 models as well.

Part of the differences in projected 21st century DSLC between the original and downscaled simulations are caused by the differences in bathymetry and land mask between the models. Our results show that it is important for DSLC projections that models resolve the main topographic features such as the English Channel, the Norwegian Trench and the transition from the deep ocean to the shelf. This is further supported by the finding that the impact of dynamical downscaling is larger for HadGEM2-ES than for MPI-ESM-LR. Therefore, sea-level projections for the NWES constructed with an ensemble of GCMs could be improved by weighting or excluding models based on their bathymetry and land mask or skill at reproducing observations regionally (e.g., McSweeney et al., 2015). This can have a substantial effect on model spread (Little et al., 2015).

Besides the magnitude of simulated DSLC, dynamical downscaling also affects the projected time of emergence of sterodynamic SLC. When including the global-mean thermosteric change, the SLC signal emerges above internal variability before 2020 for most of the NWES in all of our models. The ToE is later in the deep ocean. Spatially, this compares well with the results of Lyu et al. (2014) obtained with CMIP5 GCMs. However, dynamical downscaling delayed the emergence of sterodynamic SLC on the shelf by up to 12 years (Section 3.4.3). Instead of using preindustrial control runs to estimate (unforced) internal sea-level variability (Lyu et al., 2014), dynamical downscaling can be used to estimate the ToE of SLC more realistically, accounting for both the mean state and the variability around the mean state that can both evolve over time.

We have also shown that historical GCM simulations of the amplitude of the seasonal cycle of sea level strongly improve after dynamical downscaling (Section 3.3.3). The projected trends and interannual variability of the seasonal amplitude over the 21st century can differ substantially between the GCM and downscaled simulations (Section 3.5). This means that dynamical downscaling offers the ability to investigate DSLC on sub-annual timescales. The primary driver for sea-level projections is coastal flood risk. A stronger seasonal cycle of sea level, or for instance of tidal amplitudes, may exacerbate the in-year risk associated with the annual mean increase in sea level. This can be relevant to sediment transport and the recoverability of ecological systems in coastal wetlands.

Our dynamical downscaling setup does not include a two-way coupling between AMM7 and the atmosphere nor between AMM7 and the ocean component of the driving GCMs, which would allow the RCM to influence the simulations outside the NWES region. Although we find that dynamical downscaling improves the SST simulations of the GCMs relative to the observations (Section 3.3.2), a two-way atmosphere-ocean coupling was found to be important for downscaled SST to evolve more independently from the atmospheric forcing provided by the parent model (Mathis et al., 2017). Future studies could investigate the sensitivity of the results of dynamical downscaling to two-way coupling, to the implementation of the boundary conditions and to using different regional models, or isolate the role of tides in the simulations. The DSLC output can be combined with other SLC contributors to construct comprehensive downscaled sea-level projections. Monte Carlo approaches such as used by Palmer et al. (2018b) can readily accommodate this new information.

A few CMIP6 models will have an increased horizontal ocean resolution of $1/4^\circ$ (Haarsma et al., 2016) and are expected to better resolve the topographic scales in the NWES region. Despite these advancements, the vertical resolution of most GCMs remains limited in shallow shelf seas. Additionally, to fully resolve eddy-induced sea-level variability, mixing and coastal upwelling, the horizontal ocean resolution needs to be increased beyond the first baroclinic Rossby radius on the shelf (≈ 4 km). GCMs operating at such small scales are decades away in terms of computational feasibility (Holt et al., 2017), while the latest generation of 3D regional ocean models can resolve these scales already (e.g., Graham et al., 2018). Our results show the importance of improving the representation of coastal regions in GCMs for regional sea-level projections for the NWES, and support a role for dynamical downscaling in improving projections for coastal regions.

3.7. Supplementary information

3.7.1. Supplementary figures

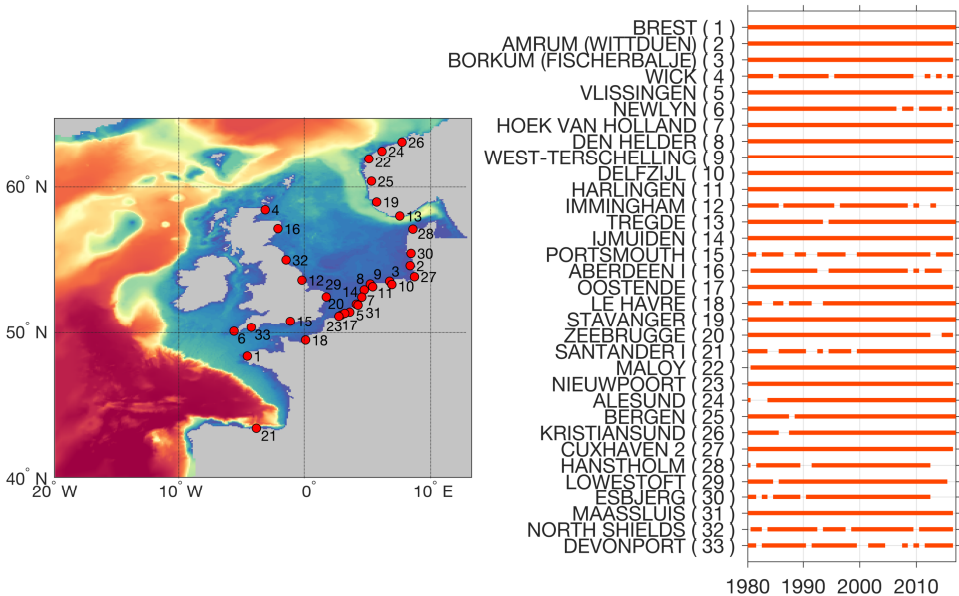


Figure S3.1: Location and temporal coverage of selected tide gauges (TG) from the revised local reference dataset of the Permanent Service for Mean Sea Level (PSMSL).

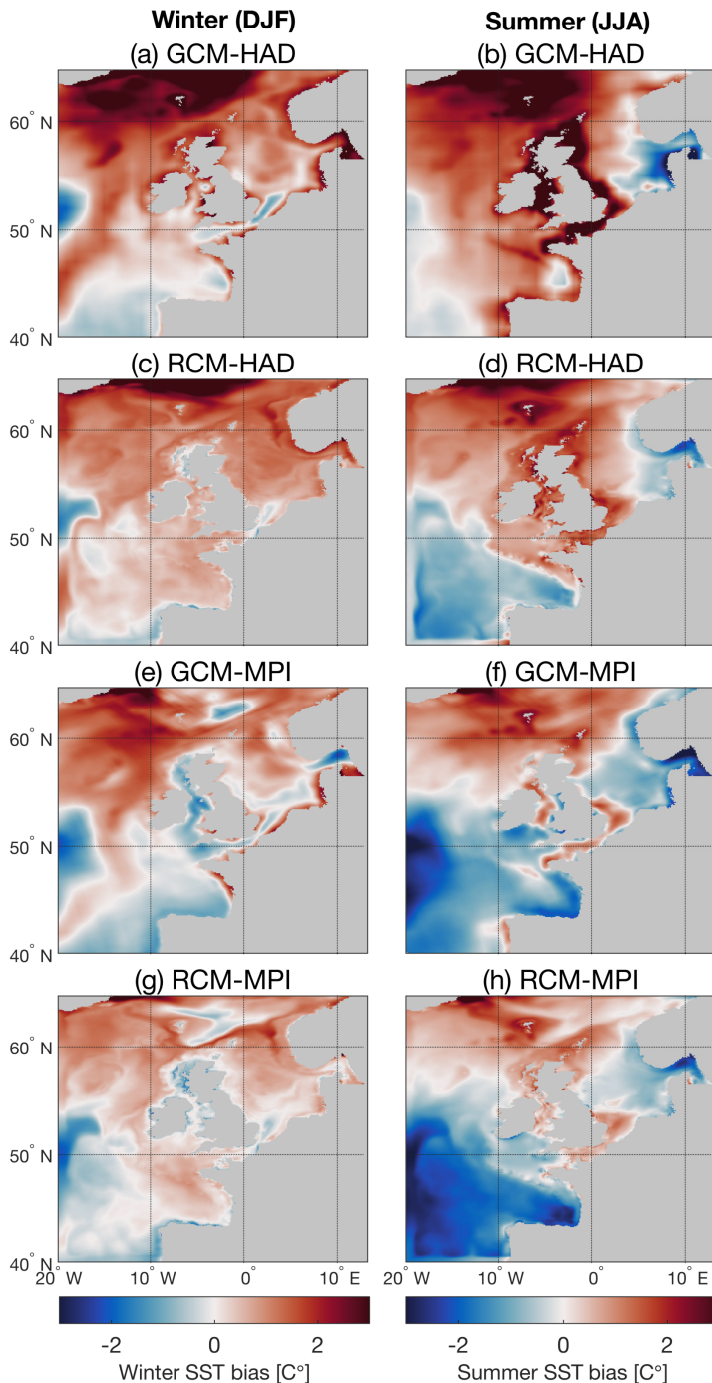


Figure S3.2: Biases of climatological SST (1992-2010) in winter (DJF) and summer (JJA) with respect to the observational dataset OSTIA (simulations minus observations) for **(a-b)** GCM-HAD, **(c-d)** RCM-HAD, **(e-f)** GCM-MPI and **(g-h)** RCM-MPI. The historical simulations are extended with the RCP8.5 scenario for 2006-2010. The differences are calculated on the AMM7 grid.

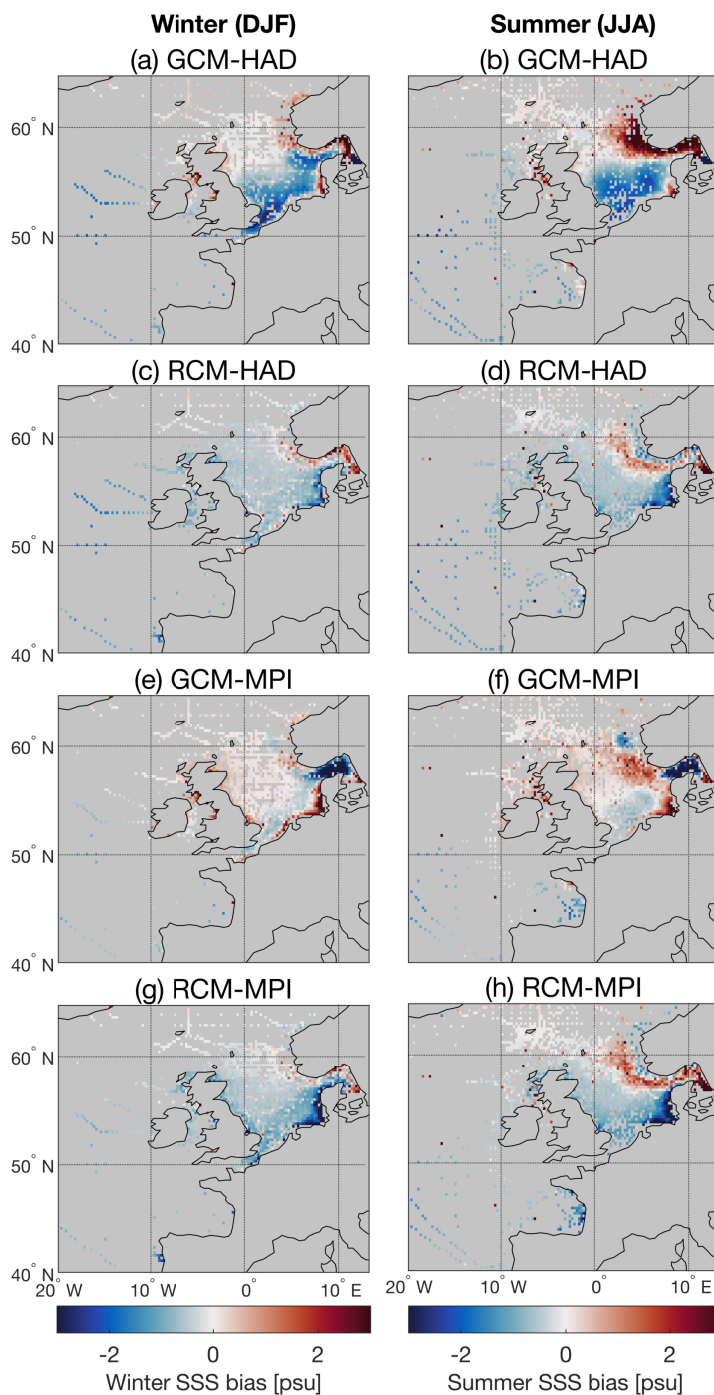


Figure S3.3: Biases of climatological SSS (1980-2017) in winter (DJF) and summer (JJA) with respect to the observational dataset EN4.2.0 (simulations minus observations) for **(a-b)** GCM-HAD, **(c-d)** RCM-HAD, **(e-f)** GCM-MPI and **(g-h)** RCM-MPI. The historical simulations are extended with the RCP8.5 scenario for 2006-2017. Differences with EN4 are taken from the nearest AMM7 grid cell.

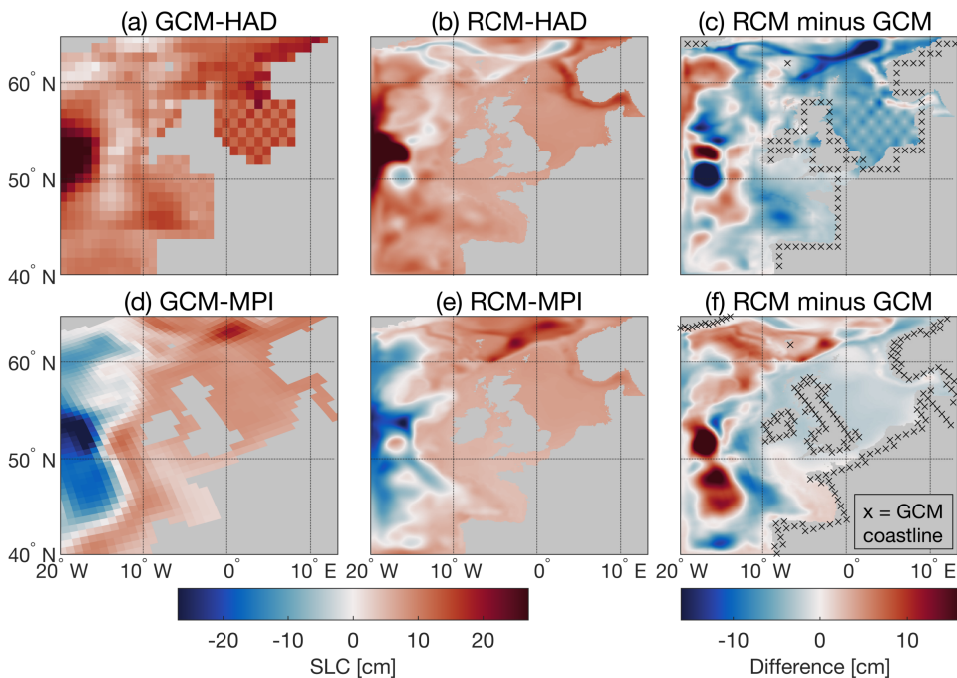


Figure S3.4: Projected DSLC between 1980-2005 and 2074-2099 (RCP4.5) for **(a)** GCM-HAD, **(b)** RCM-HAD, **(c)** RCM-HAD minus GCM-HAD, **(d)** GCM-MPI, **(e)** RCM-MPI and **(f)** RCM-MPI minus GCM-MPI. The differences in **(c)** and **(f)** are computed on the AMM7 grid; black crosses indicate the original GCM coastline.

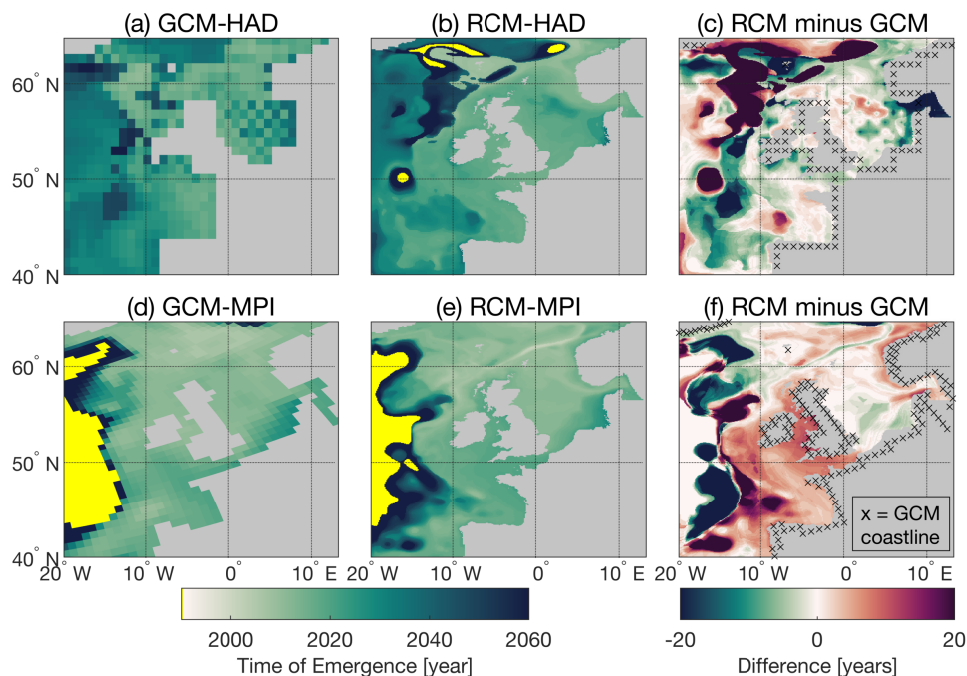


Figure S3.5: ToE of sterodynamic SLC (RCP4.5) relative to the historical period 1980-2005 for **(a)** GCM-HAD, **(b)** RCM-HAD, **(c)** RCM-HAD minus GCM-HAD, **(d)** GCM-MPI, **(e)** RCM-MPI and **(f)** RCM-MPI minus GCM-MPI. The differences in (c) and (f) are computed on the AMM7 grid; black crosses indicate the original GCM coastline. Yellow grid cells indicate no emergence before the end of the century. For these grid cells we use the value 2099 in **(c)** and **(f)**.

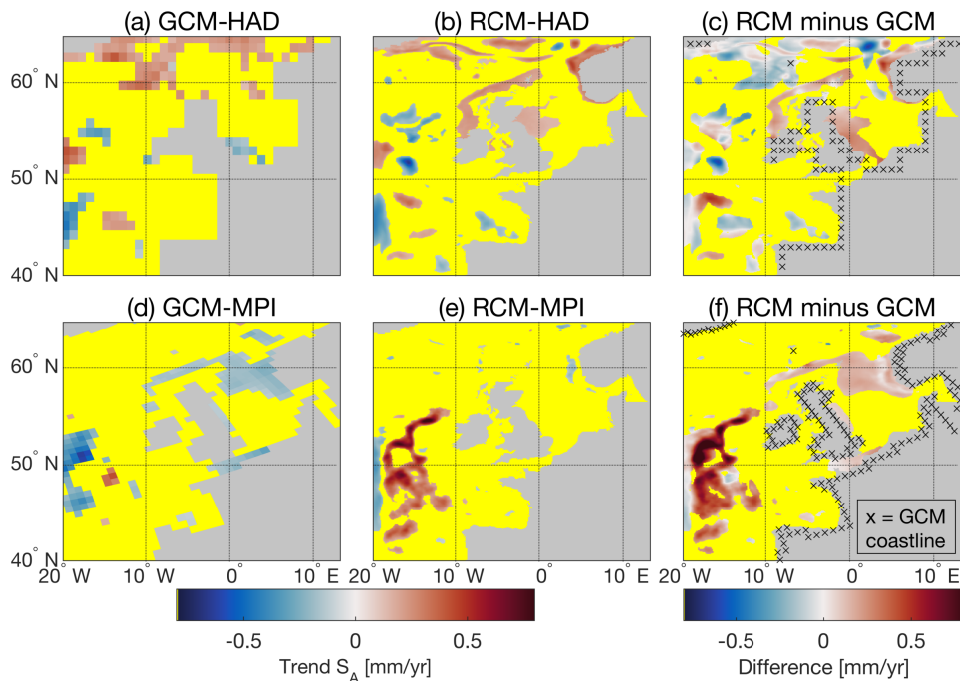


Figure S3.6: Linear trends in the amplitude of the seasonal cycle of sea level S_A (1980-2099, RCP4.5) for **(a)** GCM-HAD, **(b)** RCM-HAD, **(c)** RCM-HAD minus GCM-HAD, **(d)** GCM-MPI, **(e)** RCM-MPI and **(f)** RCM-MPI minus GCM-MPI. Yellow grid cells indicate linear regression coefficients that are not significantly different from 0 (2 standard errors; 95% confidence). The differences in **(c)** and **(f)** are computed on the AMM7 grid; black crosses indicate the original GCM coastline. Differences are yellow when both simulations have insignificant trends.

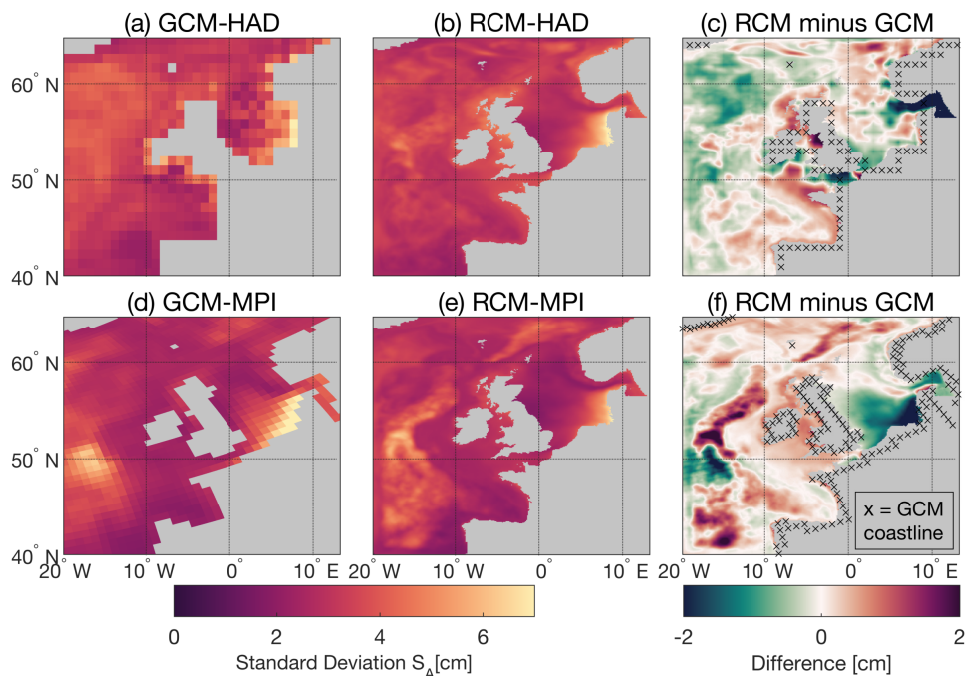


Figure S3.7: Interannual variability of the amplitude of the seasonal cycle of sea level S_A (1980-2099) calculated as the standard deviation of the detrended timeseries of S_A (RCP4.5), for **(a)** GCM-HAD, **(b)** RCM-HAD, **(c)** RCM-HAD minus GCM-HAD, **(d)** GCM-MPI, **(e)** RCM-MPI and **(f)** RCM-MPI minus GCM-MPI. The differences in **(c)** and **(f)** are computed on the AMM7 grid; black crosses indicate the original GCM coastline.

4

Drivers of Interannual Sea-Level Variability

Abstract

Sea level on the Northwestern European Shelf (NWES) varies substantially from year to year. Removing explained parts of interannual sea-level variability from observations helps to improve estimates of long-term sea-level trends. To this end, the contributions of the different drivers to interannual sea-level variability need to be understood and quantified. We analyzed these contributions for the entire NWES by performing sensitivity experiments with a high-resolution configuration of the Regional Ocean Modeling System (ROMS). The lateral and atmospheric boundary conditions were derived from reanalyses. We compared our model results with satellite altimetry data, and used our sensitivity experiments to show that non-linear feedbacks cause only minor interannual sea-level variability on the shelf. This indicates that our model experiments can be used to separate the effects of different drivers. We find that the variability of wind dominates the variability of annual mean sea level in the southern and eastern North Sea (up to 4.7 cm standard deviation), whereas the inverse barometer effect dominates elsewhere on the NWES (up to 1.7 cm standard deviation). In contrast, the forcing at the lateral ocean boundaries of the model results in small and coherent sea-level variability on the shelf (0.5 cm standard deviation). The sea-level variability driven by the variability of buoyancy fluxes ranges from 0.5 to 1.3 cm standard deviation. The results of our sensitivity experiments explain the (anti)correlation between interannual sea-level variability at different locations on the NWES and can be used to estimate forced sea-level rise from observations in this region with a higher accuracy.

4.1. Introduction

Sea level on the Northwestern European Shelf (NWES) has been rising since the 19th century (Wahl et al., 2013), and this rise is projected to accelerate in the coming centuries (e.g., Church et al., 2013; Oppenheimer et al., 2019). Fluctuations of sea level on various timescales complicate detecting forced sea-level change from observations, and sea-level variability will continue to be the dominant source of uncertainty of sea-level change for the coming decades (Palmer et al., 2018b). Removing explained parts of variability from sea-level records can lead to more accurate estimates of trends and accelerations (e.g., Thompson, 1986; Calafat and Chambers, 2013; Wahl et al., 2013; Dangendorf et al., 2014a; Gerkema and Duran-Matute, 2017; Hogarth et al., 2020). Therefore, the processes driving interannual to multi-decadal sea-level variability on the NWES need to be understood.

4

The drivers of sea-level variability on the NWES have mainly been studied using the long tide gauge (TG) records that are available in the region. Wahl et al. (2013) found that interannual sea-level variability is largest at TGs in the southeastern North Sea. Using linear regression, Dangendorf et al. (2014a) showed that a large part of the interannual sea-level variability at TGs in the southeastern North Sea can be explained by the variability of wind stress, and at the western UK and Norwegian coastlines by the inverse barometer (IB) effect (Stammer and Hüttemann, 2008). Additionally, a link has been found between the North Atlantic Oscillation (NAO) and sea level on the NWES (Wakelin et al., 2003; Woolf et al., 2003; Tsimplis et al., 2005, 2008; Chen et al., 2014).

On annual to multi-decadal timescales, sea level at several locations on the NWES is significantly correlated with sea level along the eastern boundary of the North Atlantic. Miller and Douglas (2007) and Woodworth et al. (2010) correlated sea level at Brest (France) and Cascais (Portugal) to sea-level pressure (SLP) over the subtropical North Atlantic, and suggested a link between multi-decadal sea-level variability and mass redistribution related to gyre-scale adjustments. Others showed that sea-level variability is coherent from northwestern Africa to the NWES, and strongly correlated with integrated longshore winds (LSWs) on timescales of one year to decades (Sturges and Douglas, 2011; Calafat et al., 2012). This suggests an important role of boundary dynamics, and in particular wind-driven coastally trapped waves (CTWs). Dangendorf et al. (2014a) hypothesized that CTWs also affect sea-level variability in the North Sea. Using the correlation between sea level in the North Sea and the eastern North Atlantic, Frederikse et al. (2016) closed the sea-level budget for the North Sea for 1958–2014. More recently, Chafik et al. (2019) argued that steric anomalies in the North Atlantic are communicated to the NWES through Ekman transport and affect interannual to decadal sea-level variability, since sea level, along-slope winds and the properties of the North Atlantic subpolar gyre co-varied during 1993–2016.

These studies have explained sea-level variability on the NWES at interannual to multi-decadal timescales using statistical relationships between observed sea level at different locations, and between sea level and a variety of oceanic and atmo-

spheric drivers. Many of these drivers, such as SLP, winds, gyre circulation, precipitation and the NAO, are correlated themselves (Woodworth et al., 2009). This makes the correlations between observed sea level and sea-level drivers challenging to interpret. Additionally, since TGs are sparsely distributed and located at the coast, TGs alone do not allow us to characterize sea-level variability spatially and determine whether observed signals are purely coastal or originate in the open ocean. Satellite altimetry has a better spatial coverage than TGs, but can be less accurate in coastal zones due to altimetric corrections and land contamination (i.e., the distortion of altimetric waveforms by the presence of land).

Instead of using observations, Roberts et al. (2016) ran numerical sensitivity experiments with a global ocean model to link interannual sea-level variability to different modes of climate variability. More recently, Tinker et al. (2020) used a high-resolution regional ocean model to explore the influence of atmospheric forcing and lateral ocean boundary conditions on interannual sea-level variability on the NWES. However, they used a climate control simulation and did not investigate the effect of specific drivers. Hence, the contributions of different drivers to interannual sea-level variability in the satellite altimetry era are not yet fully clear for the entire NWES region.

Here, we investigate different drivers of interannual sea-level variability for a period in the satellite altimetry era (1995-2018). To this end, we developed a high-resolution set-up of the Regional Oceanic Modeling System (ROMS; Shchepetkin and McWilliams, 2005) for the NWES. We derived boundary conditions for our model from ocean and atmosphere reanalyses (GLORYS12v1 and ERA5, respectively). By separately varying the lateral ocean boundaries, SLP, winds and buoyancy fluxes in our model, we quantify the effects of these drivers on interannual sea-level variability.

We explain our ROMS set-up and methods in Section 4.2 and show that our model simulations agree well with satellite altimetry data in Section 4.3. We show the influence of forcing at the lateral ocean boundaries, SLP, winds and buoyancy fluxes on interannual sea-level variability and discuss the correlations between annual mean sea level at different coastal locations in Section 4.4. We end with a discussion in Section 4.5 and our conclusions in Section 4.6.

4.2. Data and methods

We first introduce our ROMS set-up for the NWES (Section 4.2.1) and the reanalysis data that we prescribed at the boundaries of ROMS (Section 4.2.2). Additionally, we discuss the satellite altimetry data that we used to evaluate our model (Section 4.2.3) and present the sensitivity experiments that were used to study the influences of different drivers of interannual sea-level variability (Section 4.2.4).

4.2.1. ROMS set-up for the Northwestern European Shelf

ROMS is a primitive-equation, curvilinear, hydrostatic, Boussinesq and free-surface regional ocean modeling system (Shchepetkin and McWilliams, 2005). It runs on a

staggered Arakawa C grid and has stretched terrain-following vertical coordinates (Song and Haidvogel, 1994). Terrain-following coordinates are particularly suited for modeling regions with large bottom topography gradients such as the slope from the deep ocean toward the NWES.

Our model domain extends from 36°N to 62°N and from 20°W to 10°E, and has four lateral open boundaries (Figure 4.1). Our model has 30 vertical levels and a horizontal resolution of $1/8^\circ$ by $1/8^\circ$ (≈ 11 km), so resolves eddies in the open ocean. With this resolution, the English Channel and Irish Sea are at least 4 to 5 grid points wide. The bathymetry (Figure 4.1), derived from ETOPO1 (Amante and Eakins, 2009), was smoothed with grid stiffness $rx_0 = 0.13$, which reduces horizontal pressure gradient errors (Beckmann and Haidvogel, 1993). We used mixing along geopotential surfaces.

4

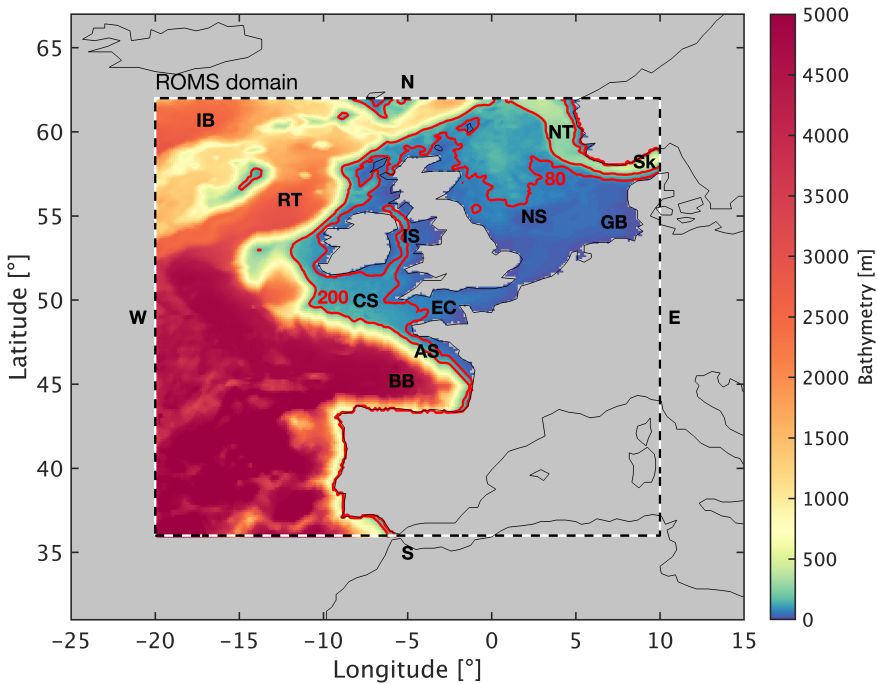


Figure 4.1: Map of the ROMS domain showing the smoothed ETOPO1 bathymetry [m] and the land mask (grey) of the model set-up. The red contours indicate the 80 and 200 m isobaths. The abbreviations denote the American Shelf (AS), Bay of Biscay (BB), Celtic Sea (CS), English Channel (EC), German Bight (GB), Iceland Basin (IB), Irish Sea (IS), North Sea (NS), Norwegian Trench (NT), Rockall Trough (RT) and Skagerrak (Sk) (see also Figure 1.8).

4.2.2. ROMS boundary conditions from reanalysis data

We derived surface and lateral boundary conditions for ROMS from reanalysis data for 1993-2018. For the lateral ocean boundaries, we obtained monthly mean values of sea-surface height (SSH), zonal and meridional currents, and temperature and

salinity from GLORYS12v1 (Fernandez and Lellouche, 2018). GLORYS12v1 is a global ocean reanalysis with a horizontal resolution of $1/12^\circ$ by $1/12^\circ$ (≈ 8 km), and covers the period 1993–2018. Its model component NEMO (Madec and NEMO Team, 2016) is driven by atmospheric forcing from the ERA-Interim reanalysis (Dee et al., 2011). GLORYS12v1 assimilates satellite sea-surface temperature and in-situ temperature and salinity profiles. It also assimilates along-track satellite altimetry data, corrected for the IB effect and the 18.61-year lunar nodal cycle (Fernandez and Lellouche, 2018).

We imposed Chapman conditions for the free surface (Chapman, 1985), Flather radiation conditions for barotropic velocities (Flather, 1976), and mixed-radiation nudging for baroclinic velocities and ocean temperature and salinity (Orlanski, 1976; Marchesiello et al., 2001). We applied outgoing nudging to temperature and salinity at a timescale of one year, and ingoing nudging at a timescale of one day, using a 20-point relaxation zone at the lateral boundaries of the domain. Baroclinic velocities were nudged at the boundaries only. To suppress computational noise, we also applied a 20-point sponge layer, multiplying the diffusion and viscosity by a factor that linearly increases from 1 to 10 at the lateral boundaries.

ROMS and NEMO (GLORYS12v1) are both Boussinesq ocean models, meaning that local steric effects are modeled prognostically but non-Boussinesq steric effects are not (Griffies and Greatbatch, 2012). Although non-Boussinesq steric effects have a negligible imprint on monthly or longer regional sea-level patterns, they do impact global mean sea level (Greatbatch, 1994; Griffies and Greatbatch, 2012). The global mean sea level in GLORYS12v1 was corrected by adding the global mean steric effect to the SSH diagnostically (Lellouche et al., 2018). This signal may enter our model via the lateral boundary conditions, but has only small interannual variability.

The atmospheric boundary conditions were derived from ERA5 (CDS, 2019). ERA5 is based on the IFS41r2 Earth-system model and is available for 1979 to a few months before present. The atmospheric forcing was applied using bulk formulae based on (Fairall et al., 1996). We prescribed solar radiation daily using an idealized diurnal cycle, and precipitation 12-hourly. Winds at 10 m above sea level, atmospheric pressure, cloud coverage, air temperature, and relative air humidity at 2 m above sea level were prescribed on a 6-hourly basis.

We also applied a climatological river run-off based on the river discharge dataset of Dai (2017). This means that our model does not capture interannual variability due to the freshwater inflow from rivers. We also omit tides in our model. River run-off and tides may contribute to interannual sea-level variability, but require a model set-up with a higher horizontal resolution to be fully resolved.

4.2.3. Satellite altimetry data used for model evaluation

We evaluated model results against sea-level observations from the level-4 gridded Ssalto/Duacs multi-mission satellite product ($1/4^\circ$ by $1/4^\circ$) of AVISO (AVISO, 2019). This product is available for 1993 to a few months before present. It has

been corrected for the IB effect, and for the nodal cycle through standard tidal corrections. Furthermore, we assume that barystatic effects on interannual sea-level variability are small compared to the effects of regional ocean dynamics, allowing for direct comparison with ROMS.

In addition, we evaluated our simulation of mean dynamic topography (MDT), which reflects the average strength of geostrophic currents. We used the CNES MDT CLS18 product (CNES, 2019), which is an estimate of the mean SSH above the geoid, and is given at a $1/8^\circ$ by $1/8^\circ$ resolution. It is based on altimetry data, in-situ measurements of temperature and salinity, and the GOCO5S geoid model, and covers the period 1993-2012.

Although the satellite altimetry data is given on $1/4^\circ$ and $1/8^\circ$ grids respectively, its effective resolution is lower than our model resolution. Hence, small-scale features in the model results are difficult to evaluate. Additionally, land contamination leads to a lower accuracy of satellite altimetry in coastal regions (Andersen and Scharroo, 2011). Finally, satellite altimetry products are usually corrected for the IB effect, tides and high-frequency winds (e.g., Ponte and Ray, 2002), leading to reduced accuracy in regions on the NWES where these corrections are difficult to model. Therefore, in Section 4.3 we also compare our model results with GLORYS12v1.

4.2.4. ROMS sensitivity experiments

We decomposed sea-level variability using six sensitivity experiments with different lateral and surface boundary conditions (Table 4.1). For the reference experiment, we varied all lateral and surface boundary conditions (*Exp_AllVar*). For the sensitivity experiments, we prescribed ROMS with an interannually varying annual cycle for the driver under investigation and with a repeated mean annual cycle for the others.

We decomposed the total interannual sea-level variability (*Exp_AllVar*) into variability due to the lateral ocean boundary conditions, atmospheric forcing, and intrinsic variability (*Exp_OceanVar*, *Exp_AtmosVar* and *Exp_NoneVar*). The influence of atmospheric forcing was further decomposed into the influences of SLP, winds and buoyancy fluxes (*Exp_SLPVar*, *Exp_WindVar* and *Exp_BuoyVar*). The SSH from GLORYS12v1 does not include the IB effect. Hence, when we include SLP in ROMS, the lateral boundary conditions from GLORYS12v1 are compensated using the *PRESS_COMPENSATE* option in ROMS.

All runs were initialized with the final year of *Exp_NoneVar*, i.e., the sensitivity experiment in which both the atmospheric forcing and the lateral ocean boundary conditions are a repeated mean annual cycle. We calculated the mean annual cycle of the reanalysis data from the years 1993-1998, instead of the full period 1993-2018. This was done to minimize spin-up effects toward a changed climate state, as the mean state of 1993-1998 is more compatible with the boundary conditions in 1993. Additionally, we discarded the first two model years (1993 and 1994) to avoid any remaining spin-up effects. Therefore, in this chapter we show model results

Table 4.1: Overview of the ROMS sensitivity experiments. We used a climatological annual cycle for river run-off in every model experiment.

Experiment	Interannually varying	Repeated annual cycle	Discussed in
<i>Exp_AllVar</i> (reference)	All boundaries	None	Sections 4.4.1-4.4.4
<i>Exp_AtmosVar</i> <i>Exp_OceanVar</i>	Surface boundaries Lateral boundaries	Lateral boundaries Surface boundaries	Sections 4.4.1, 4.4.2 Sections 4.4.1, 4.4.3, 4.4.4
<i>Exp_NoneVar</i>	None	Lateral & surface boundaries	Section 4.4.1
<i>Exp_SLPVar</i>	SLP	Winds, buoyancy fluxes, lateral boundaries	Sections 4.4.2-4.4.4
<i>Exp_WindVar</i>	Winds	SLP, buoyancy fluxes, lateral boundaries	Sections 4.4.2-4.4.4
<i>Exp_BuoyVar</i>	Buoyancy fluxes	SLP, winds, lateral boundaries	Sections 4.4.2-4.4.4

for 1995-2018 (24 years). Spun-up sensitivity experiments show that the results depend marginally on the period used to derive the climatological forcing.

Some of the bulk parameterizations of atmospheric forcing (Section 4.2.2) depend on variables that vary in all sensitivity experiments. Thus, buoyancy fluxes may still vary interannually in sensitivity experiments other than *Exp_BuoyVar*. For example, the variability of SLP (*Exp_SLPVar*) affects air density and specific humidity, which in turn affect heat and freshwater fluxes. Since these feedbacks are ultimately caused by the interannual variability of the driver under investigation (SLP in this example), we do not consider them part of *Exp_BuoyVar*.

Additionally, the response of the ocean to the various components of forcing at the lateral and surface boundaries depends on its state (temperature, salinity, circulation). For example, the heat taken up by the ocean varies interannually in *Exp_BuoyVar*, but is redistributed by the same wind-driven circulation each year. Hence, due to non-linear feedbacks the interannual sea-level variability in *Exp_BuoyVar* may differ from the actual buoyancy-driven variability in *Exp_AllVar*. This applies to the other sensitivity experiments as well. However, we show in Section 4.4 that such non-linear feedbacks result in only small interannual sea-level variability on the shelf.

4.3. Evaluation of model results

In this section, we evaluate simulated MDT against CNES MDT CLS18 (both as anomalies with respect to their area-weighted regional mean) and interannual sea-level variability against the AVISO product. Additionally, we compare our simulations with the GLORYS12v1 reanalysis. We evaluate a variant of *Exp_AllVar* that excludes the effect of SLP. We compared the different fields quantitatively using pattern correlation coefficients (PCCs - the spatial equivalent of Pearson's correla-

tion coefficient) and root mean square errors (RMSEs). We used a hypothesis test to determine statistical significance ($p < 0.05$, with p calculated using a two-sided t -distribution).

ROMS MDT matches well with GLORYS12v1 MDT and CNES MDT CLS18 (Figure 4.2, left panels). It has PCCs of 0.95 and 0.93 and RMSEs of 3.76 and 4.34 cm with the other products, respectively. All three fields have a north to south gradient of low to high MDT anomalies. The MDT is higher than the regional mean on most of the shelf, and largest in the southeastern North Sea. All fields show lower MDT in the Norwegian Trench and the northern North Sea. In ROMS and GLORYS12v1, the 0 cm MDT contour realistically follows the northern coast of Scotland and approximately traces the 80-m isobath into the North Sea.

4

Since GLORYS12v1 assimilates along-track satellite altimetry, its MDT is similar to the satellite altimetry data. However, in some areas, ROMS and GLORYS12v1 MDT match well, but differ from CNES MDT CLS18. For example, ROMS and GLORYS12v1 differ only 1 cm near the coast of Scotland and Denmark, whereas CNES MDT CLS18 is up to 6 cm lower. This could be due to limitations of the satellite altimetry data (see Section 4.2.3).

ROMS MDT differs from the other products near the Rockall Bank and in the southwest of the domain, so here geostrophic currents may not be well reproduced. Our model also has stronger MDT gradients across the shelf break, particularly at the Celtic and Armorican slopes. Such gradients indicate along-slope geostrophic currents, which have indeed been identified in this region with moorings and numerical models (Friocourt et al., 2008; Pingree and Cann, 1989) and may be affected by bathymetry smoothing. CNES MDT CLS18 shows no gradient in this area, but its resolution is likely insufficient to assess such a feature. Despite its data assimilation, GLORYS12v1 has a somewhat lower MDT along this part of the shelf break. Other high-resolution regional ocean models with different boundary conditions also show, to various extents, reduced MDT along the Celtic and Armorican slopes (e.g., Hermans et al., 2020b; Tinker et al., 2020).

Next, we compare the magnitude of interannual sea-level variability in our model with the observations. To this end, we calculated the standard deviation (SD) of linearly detrended, annual mean sea level. *Exp_AllVar* reproduces the observed SDs well (Figure 4.2, right panels). It has PCCs of 0.80 and 0.78 and RMSEs of 0.49 and 0.53 cm with respect to GLORYS12v1 and AVISO. All three fields have large interannual sea-level variability in deep waters, such as the Iceland Basin, the Rockall Trough and the Bay of Biscay. However, the variability in ROMS (Figure 4.2b) is larger than in GLORYS12v1 and AVISO (Figures 4.2d & f) northwest of Portugal, and generally smaller in the rest of the open ocean. Sea-level variability is small near the shelf break and the Norwegian Trench, with all three fields showing a similar magnitude of 0.7–1.0 cm SD. This is encouraging, since the shelf break might play an important role for (decadal) sea-level variability on the shelf (Dangendorf et al., 2014a).

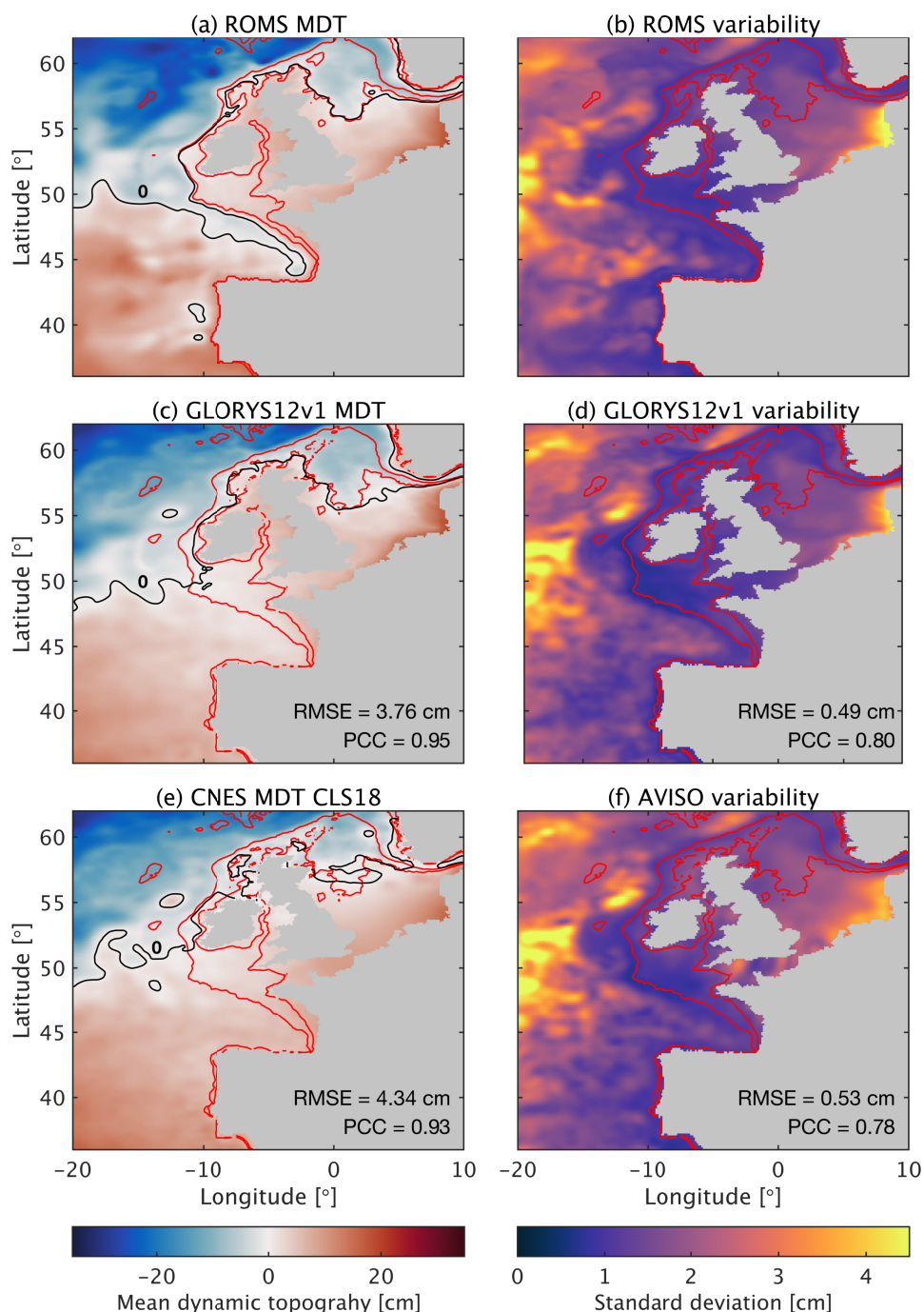


Figure 4.2: Mean dynamic topography anomalies with respect to the area-weighted regional mean [cm] (left panels) and interannual sea-level variability as the SD of detrended, annual mean sea level [cm] (right panels) for **(a-b)** ROMS, **(c-d)** GLORYS12v1 and **(e-f)** CNES MDT CLS18 and AVISO. All products have been interpolated to the $1/8^\circ$ grid of ROMS. The PCCs and RMSEs of ROMS with respect to GLORYS12v1 and the satellite altimetry products are indicated. The black contours indicate 0 cm MDT, and the red contours indicate the 80 and 200 m isobaths of ROMS **(a-b)** and GLORYS12v1 **(c-f)**.

The spatial patterns of interannual sea-level variability also agree well on the shelf. As in GLORYS12v1 and AVISO, the largest variability in ROMS is found in the German Bight. The variability in the German Bight is somewhat higher in ROMS than in GLORYS12v1 and AVISO (up to 4.9, 4.3 and 4 cm SD, respectively). In the central North Sea, ROMS is closer to AVISO, whereas AVISO has somewhat larger sea-level variability in the northern North Sea and around the UK than both ROMS and GLORYS12v1. Additionally, unlike ROMS and GLORYS12v1, AVISO shows a few patches of high variability (up to ≈ 3 cm SD) in the English Channel. These differences could be the result of inaccurate tidal corrections or processes that are not represented in ROMS and GLORYS12v1.

The high pointwise correlation between ROMS and AVISO (Figure 4.3a) corroborates the agreement seen in Figure 4.2. Correlation coefficients are high and statistically significant in most of the domain. The insignificant correlations in the deep parts of the open ocean (Figure 4.1) are likely because of the intrinsic variability in these regions (see Section 4.4.1 and Figure 4.5b). Intrinsic variability in ROMS does not have exactly the same spatial pattern as in the observations, and is not expected to have the same phase. In the English Channel, the Irish Sea and along parts of the shelf break, the correlations between ROMS and AVISO are lower than on the rest of the shelf, which could be due to limitations of the satellite altimetry data (see Section 4.2.3). This is further supported by the pointwise correlation between GLORYS12v1 and AVISO, which is also reduced around the UK and parts of the shelf break (Figure 4.3b).

To further demonstrate the high correlations between sea level in ROMS and AVISO, we show the time series for a few sample locations at the coast (Figure 4.3c). Correlation coefficients range from 0.64 to 0.84 for these coastal locations, despite the potential land contamination of the altimetry. The time series in Figure 4.3c also show how much sea level varies. For example, interannual variations are up to 11.14 cm (Cuxhaven), while long-term trends are only in the order of mm/yr (Wahl et al., 2013).

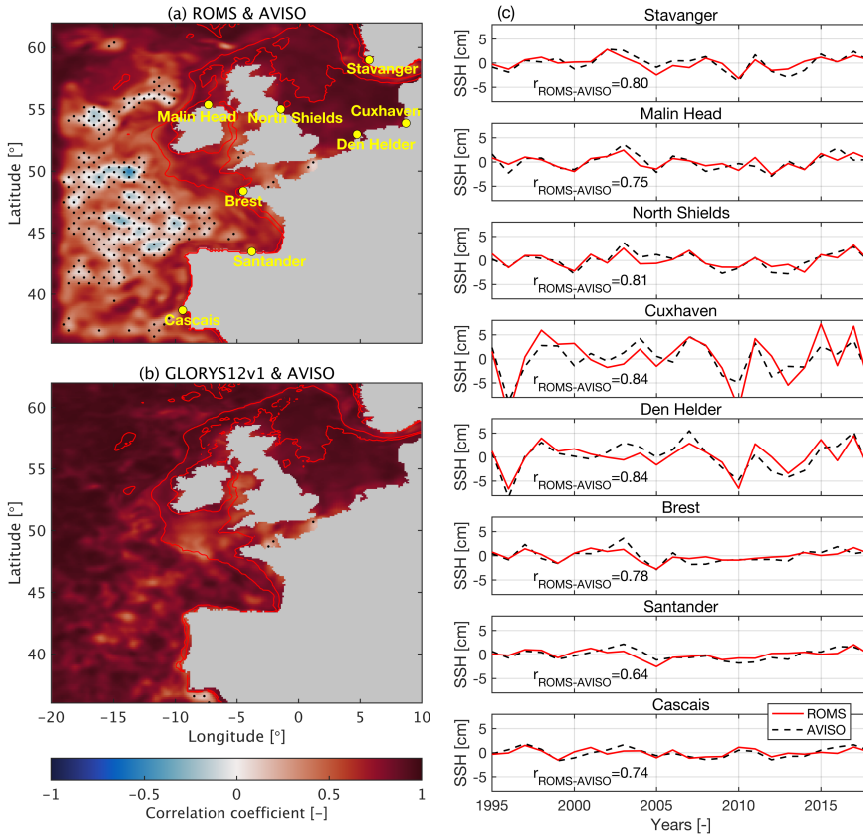


Figure 4.3: Pointwise correlation coefficients [-] between detrended, annual mean sea level (1995–2018) in **(a)** ROMS and AVISO and **(b)** GLORYS12v1 and AVISO, and **(c)** detrended sea level with respect to the time-mean [cm] at sample locations for ROMS (red, solid) and AVISO (black, dashed), with their correlation coefficients. The black stipples in **(a)** and **(b)** indicate statistically insignificant correlation coefficients ($p \geq 0.05$); isobaths as in Figure 4.2.

Finally, we compare the correlations of detrended sea level at Brest with detrended sea level at all other grid cells in ROMS and AVISO (Figures 4.4a & b), since the spatial correlation pattern in the eastern North Atlantic and on the NWES has been discussed in a number of previous studies (Sturges and Douglas, 2011; Calafat et al., 2012, 2013; Dangendorf et al., 2014a; Chafik et al., 2019; Frederikse et al., 2016; Hogarth et al., 2020). The resulting patterns of ROMS and AVISO agree well within the model domain. High correlations (>0.6) with sea level at Brest extend from northwestern Africa to Norway, with the highest correlations found primarily along the continental slope. In both ROMS and AVISO, sea level at Brest becomes progressively less correlated with sea level toward the southern and eastern North Sea. It is negatively correlated with sea level in the open ocean in the west and northwest of the domain, although in most places this anticorrelation is statistically insignificant. To highlight the unique character of the spatial coherence of the

sea-level variability in the region, we compare the cross-correlations of observed sea level along the continental slope and along a meridional transect in the open ocean (25°W) (Figures 4.4c & d). This shows that the correlation scales along the slope are several times longer than those in the open ocean, suggesting shelf-sea dynamics play an important role in driving spatial coherence on the NWES.

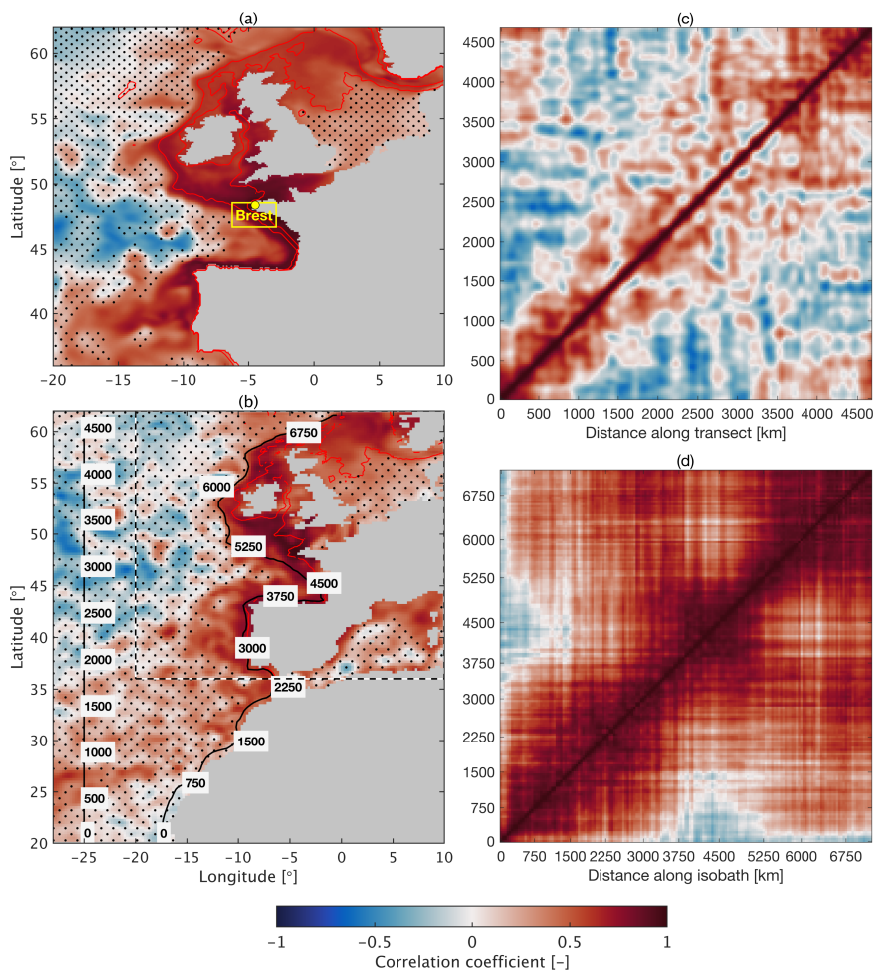


Figure 4.4: Correlation coefficients [-] between detrended annual mean sea level (1995-2018) at Brest and at all other grid cells for **(a)** ROMS and **(b)** AVISO, and cross-correlations for AVISO along **(c)** a meridional transect in the open ocean (25°W) and **(d)** along the 200m isobath. Distances [km] along the transect and isobath are indicated. Stipples and isobaths as in Figure 4.3.

We conclude that, overall, interannual sea-level variability in ROMS, GLORYS12v1 and AVISO are in good agreement (Figures 4.2, 4.3 & 4.4). Next, we use our ROMS set-up to investigate the different drivers of interannual sea-level variability in the NWES region (Section 4.4).

4.4. The contributions of different drivers

Using the sensitivity experiments in Table 4.1, we first isolate the contributions of intrinsic sea-level variability, atmospheric forcing and the lateral ocean boundaries (Section 4.4.1). Then, we split up the contribution of atmospheric forcing into the effects of the variability of SLP, winds and buoyancy fluxes (Section 4.4.2). Finally, we show the relative contribution of different drivers to sea level at a few coastal locations (Section 4.4.3) and relate these to the correlation between sea level at different locations (Section 4.4.4).

4.4.1. Intrinsic variability, atmospheric forcing and lateral ocean boundaries

In contrast to Section 4.3, here we included the effect of SLP in *Exp_AllVar* (Figure 4.5a). The spatial patterns of sea-level variability in Figures 4.2b & 4.5a are similar, but due to covariance, not exactly the same. For example, including SLP leads to larger sea-level variability in most locations, but to slightly lower sea-level variability in the central North Sea.

The interannual sea-level variability in *Exp_NoneVar* (Figure 4.5b) has SDs of up to 2.7 cm in the deep ocean (Rockall Trough), but is negligible (<0.1 cm SD) on the shelf. Since all forcing in *Exp_NoneVar* is a repeated mean annual cycle, the resulting variability must be due to spontaneously generated non-linear processes, such as mesoscale eddies. Therefore, we refer to this variability as intrinsic. A model with tides and sufficient resolution to resolve shelf-sea eddies may simulate larger intrinsic sea-level variability on the shelf. The open ocean variability in *Exp_NoneVar* is lower than the intrinsic variability found in previous studies (e.g., Sérazin et al., 2015), and is negligible at the lateral boundaries. This is the result of the lateral boundary conditions, which were prescribed as a repeated annual cycle in *Exp_NoneVar*. The other sensitivity experiments also have intrinsic variability, so the sea-level variability due to forcing at the lateral and surface boundaries is easier to identify on the shelf than in the open ocean.

Exp_AtmosVar (Figure 4.5c), in which only the atmospheric forcing varies inter-annually, shows that the atmospheric forcing is the dominant driver of sea-level variability on the shelf. The resulting spatial pattern on the shelf compares well to *Exp_AllVar* (Figures 4.2b & 4.5a) and the observations (Figure 4.2f). Sea-level variability in *Exp_AtmosVar* is highest in the German Bight (≈ 5.6 cm SD) and is also relatively high around Scotland and Norway (≈ 2.4 cm SD). Intrinsic sea-level variability is present in the open ocean, and is enhanced by the local effects of atmospheric variability. At the lateral boundaries, the interannual sea-level variability is nudged toward the variability due to SLP, since a repeated annual cycle from GLORYS12v1 was used combined with the PRESS_COMPENSATE option (explained in Section 4.2.4).

Exp_OceanVar (Figure 4.5d), in which only the lateral boundary conditions vary inter-annually, has only minor interannual sea-level variability of around 0.5 cm SD on the shelf. The variability is mostly uniform on the shelf, as demonstrated by the high

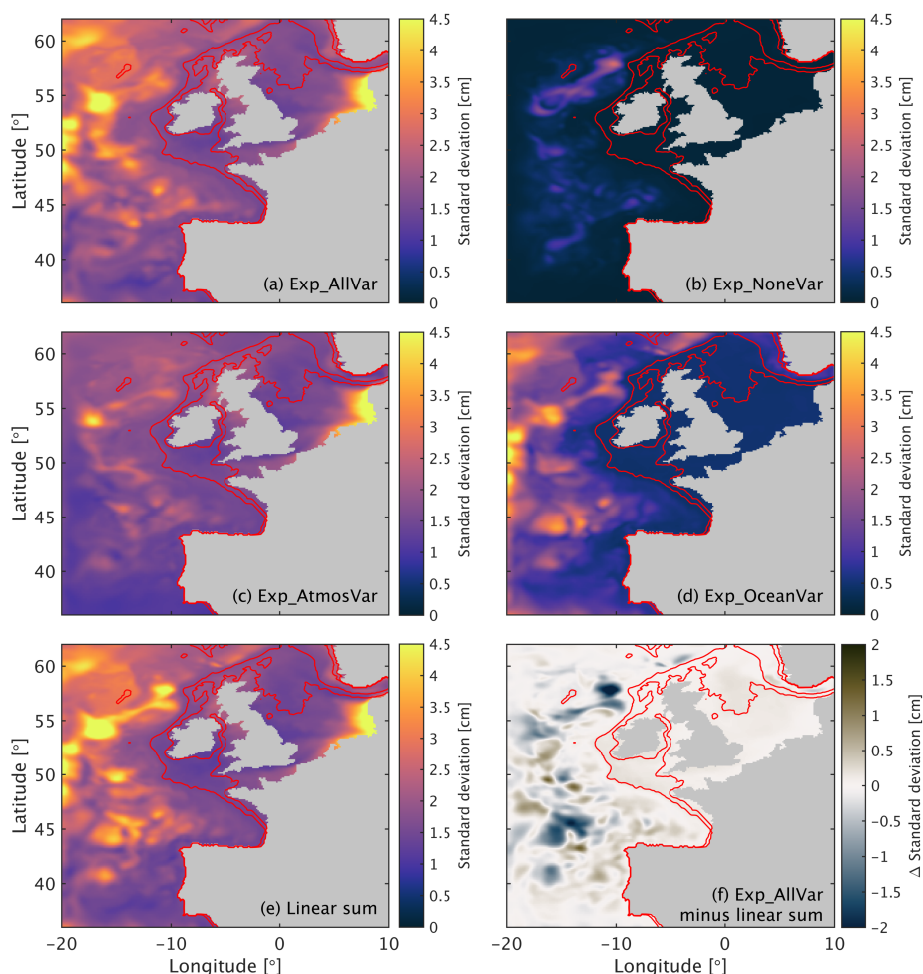


Figure 4.5: Sea-level variability in different ROMS experiments (Table 4.1) as the SD [cm] of detrended annual means (1995-2018) for **(a)** *Exp_AllVar*, **(b)** *Exp_NoneVar*, **(c)** *Exp_AtmosVar*, **(d)** *Exp_OceanVar*, **(e)** the linear sum of time series in *Exp_NoneVar*, *Exp_AtmosVar* and *Exp_OceanVar* and **(f)** the residual SD of *Exp_AllVar* minus the linear sum of components. Isobaths as in Figure 4.1.

correlations between detrended sea level at Brest and elsewhere shown in Figure S4.1. By interannually varying the boundary conditions at each lateral boundary separately, we find that the sea-level variability on the shelf is caused mostly by the variation of the western and southern boundaries of our model domain (see Figure S4.2). Variations in subtropical gyre strength may affect transport through the western and southern boundaries, but we did not find a significant correlation between sea level in *Exp_OceanVar* and the North Atlantic barotropic streamfunction in GLORYS12v1. In the open ocean, interannual sea-level variability due to the varying lateral boundary conditions is much larger than on the shelf. Geostrophic

currents along the continental slope can hinder the propagation of open ocean signals to the coast (Huthnance, 1981). In addition to the intrinsic sea-level variability in the open ocean, the lateral ocean boundaries drive strong sea-level variability along the western boundary, in the Iceland Basin (≈ 4 cm SD) and east of the Faroe Islands (≈ 2.6 cm SD).

Next, we calculated SDs for the linear sum of the detrended sea level time series in *Exp_NoneVar*, *Exp_AtmosVar* and *Exp_OceanVar* (Figure 4.5e). We compared this to the variability in *Exp_AllVar* (Figure 4.5a), in which all forcing varies interannually simultaneously. The SDs for *Exp_AllVar* and the linear sum are similar on the shelf (Figures 4.5a & e), with differences well below 0.2 cm (Figure 4.5f). The linear sum also has the same phase, as indicated by the high pointwise correlation with *Exp_AllVar* (see Figure S4.3). This indicates that to first order, sea-level variability due to the atmospheric and oceanic drivers combines linearly on the shelf. This also holds for the forcing at the separate lateral ocean boundaries (Figures S4.2 & S4.3). Since all sensitivity experiments include intrinsic sea-level variability, the differences between *Exp_AllVar* and the linear sum are larger in the open ocean (Figure 4.5f).

4.4.2. Sea-level pressure, winds and buoyancy fluxes

We further decomposed the interannual sea-level variability in *Exp_AtmosVar* (Figure 4.5c, repeated in Figure 4.6a) into the variability induced by the variability of SLP (*Exp_SLPVar*), winds (*Exp_WindVar*) and buoyancy fluxes (*Exp_BuoyVar*).

Exp_SLPVar (Figure 4.6b) shows the effect of SLP on interannual sea-level variability. Except for the intrinsic variability in the open ocean, the resulting variability agrees with the variability of SLP in ERA5 (≈ 1 cm sea level for 100 Pa SLP, see Figure S4.4). Therefore, the interannual sea-level variability in *Exp_SLPVar* is mainly due to the IB effect. The resulting sea-level variability is smallest in the south of the domain and in the southeastern North Sea (≈ 1 cm SD), and increases toward the Icelandic Low northwest of the domain (≈ 2.1 cm SD).

Exp_WindVar (Figure 4.6c) shows that winds drive large sea-level variability in the North Sea, and around Scotland, Ireland and Norway (up to 1.4 cm SD). Wind-induced sea-level variability is largest in the southern and eastern North Sea (up to ≈ 4.7 cm SD), and is also large in the open ocean. The large SDs in the open ocean and on the shelf are separated by much smaller sea-level variability along the shelf break (0.3-0.55 cm SD), west of France (0.6 cm SD) and southwest of the UK (0.5-0.7 cm SD).

Exp_BuoyVar (Figure 4.6d) results in spatially relatively smooth sea-level variability that varies from 0.5 to 1.3 cm SD on the shelf. Apart from the intrinsic sea-level variability, the magnitude of the variability in the open ocean is comparable to that on the shelf. The sea-level variability in *Exp_BuoyVar* tends toward zero at the lateral boundaries because of the repeated annual cycle of GLORYS12v1. The interaction of buoyancy fluxes with river run-off and winds may explain the pattern of buoyancy-driven sea-level variability in the German Bight.

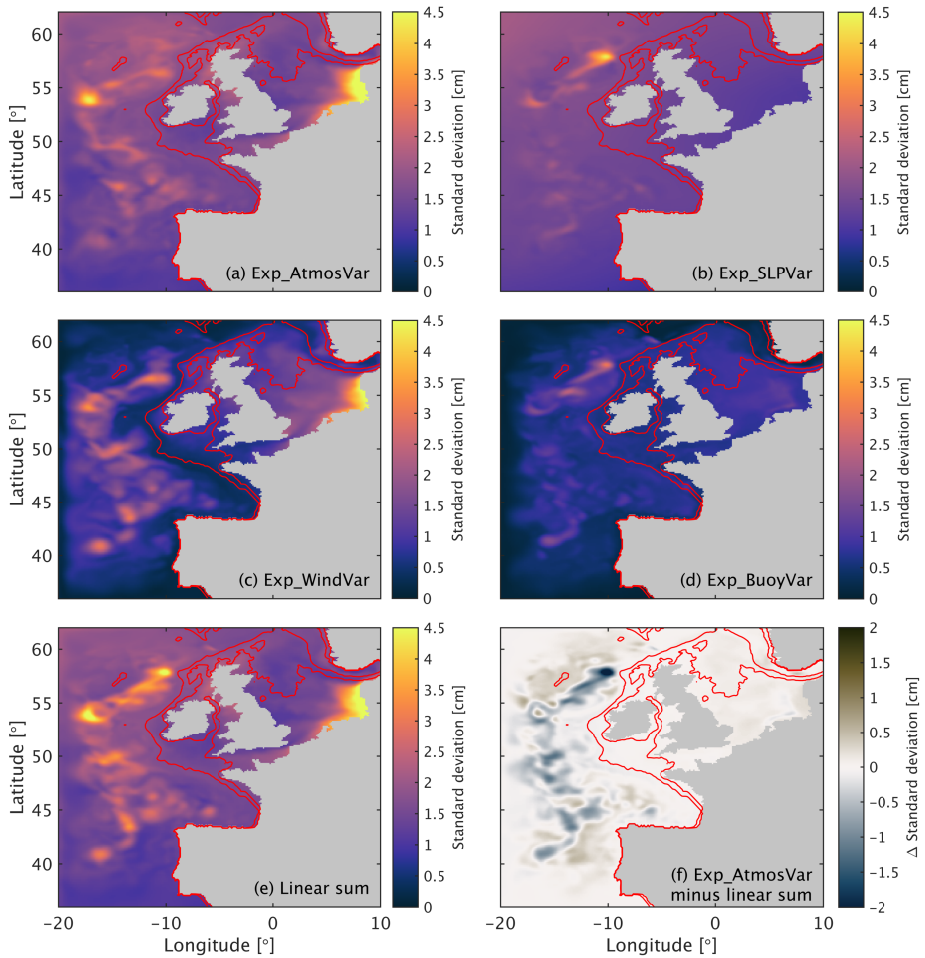


Figure 4.6: Sea-level variability in different ROMS experiments (Table 4.1) as the SD [cm] of detrended annual means (1995-2018) for **(a)** *Exp_AtmosVar*, **(b)** *Exp_SLPVar*, **(c)** *Exp_WindVar*, **(d)** *Exp_BuoyVar*, **(e)** the linear sum of time series in *Exp_SLPVar*, *Exp_WindVar* and *Exp_BuoyVar* and **(f)** the residual SD of *Exp_AtmosVar* minus the linear sum of components. Isobaths as in Figure 4.1.

Similar to Section 4.4.1, we linearly summed the detrended sea-level time series in *Exp_SLPVar*, *Exp_WindVar* and *Exp_BuoyVar*, and computed the resulting SDs (Figure 4.6e). The residual SDs relative to *Exp_AtmosVar* are less than 0.24 cm on the shelf (Figure 4.6f). Additionally, the pointwise correlation with the time series of *Exp_AtmosVar* is high (Figure S4.3). The residual SD is around 0.23 cm in the German Bight, which indicates that non-linear feedbacks between buoyancy fluxes and winds, or buoyancy fluxes and river run-off, can have a small effect on the interannual sea-level variability in this area. The generally small effect of non-linear feedbacks suggests that, to first order, the influences of different drivers of sea-level variability on the shelf can be studied separately. This justifies the use of

multiple linear regression methods in observation-based studies (e.g., Calafat and Chambers, 2013; Dangendorf et al., 2013a, 2014a; Wahl et al., 2013; Frederikse et al., 2016; Gerkema and Duran-Matute, 2017).

4.4.3. Relative magnitudes of sea-level variability at coastal locations

To compare the sea-level variability in each sensitivity experiment, we display the time series for the sample coastal locations of Figure 4.3 (Figure 4.7, left panels). Additionally, we calculated the relative magnitudes of interannual sea-level variability by dividing the SDs of the detrended sea level in each sensitivity experiment by those in *Exp_AllVar* (Figure 4.7, right panels). These ratios do not necessarily add up to one for a given location, because the sea-level variability in one sensitivity experiment may reinforce or interfere with that in another sensitivity experiment.

In most locations, the variability of SLP drives the largest interannual sea-level variability (red). This is especially the case for Brest, Santander and Cascais (Figures 4.7f, g & h, red). In Stavanger, Malin Head and North Shields, both SLP (red) and winds (green) play a dominant role (Figures 4.7a, b & c). Wind variability is the primary driver of interannual sea-level variability at Cuxhaven and Den Helder (Figures 4.7d & e); there is large overlap between the time series of *Exp_WindVar* (green) and *Exp_AllVar* (black, dashed). The effects of winds at the western and eastern North Sea coasts clearly differ (Figures 4.7c, d & e). Sea-level variability due to the variability of SLP, buoyancy fluxes and the lateral boundary conditions is smaller than wind-driven variability at Cuxhaven and Den Helder, but not negligible. Using linear regression, Dangendorf et al. (2013a) obtained similar results for the Cuxhaven TG record.

Since the interannual sea-level variability in *Exp_OceanVar* is approximately uniform on the shelf (Section 4.4.1), the relative importance of the forcing at the lateral boundaries depends on the spatial pattern of sea-level variability in the other experiments in Figure 4.7. Hence, although sea-level variability in *Exp_OceanVar* is small (≈ 0.5 cm SD, Figure 4.5d), the forcing at the lateral ocean boundaries is still a relatively important driver at Stavanger, North Shields, Santander and Cascais. It results in SD ratios of 0.41, 0.33, 0.36 and 0.42, respectively (Figures 4.7a, c, g & h, blue).

Especially Cascais is situated close to the lateral boundaries of our ROMS domain. Because of the nudging layer, the sea-level variability in *Exp_WindVar* and *Exp_BuoyVar* tends toward the repeated mean annual cycle of GLORYS12v1 at the lateral boundaries (Figures 4.6c & d). Therefore, the SD ratios of the sensitivity experiments should be interpreted with caution at locations close to the lateral boundaries. Nevertheless, we expect that the drivers of sea-level variability at Cascais, Santander and Brest are similar, since sea level at these locations is highly correlated in both ROMS and the observations.

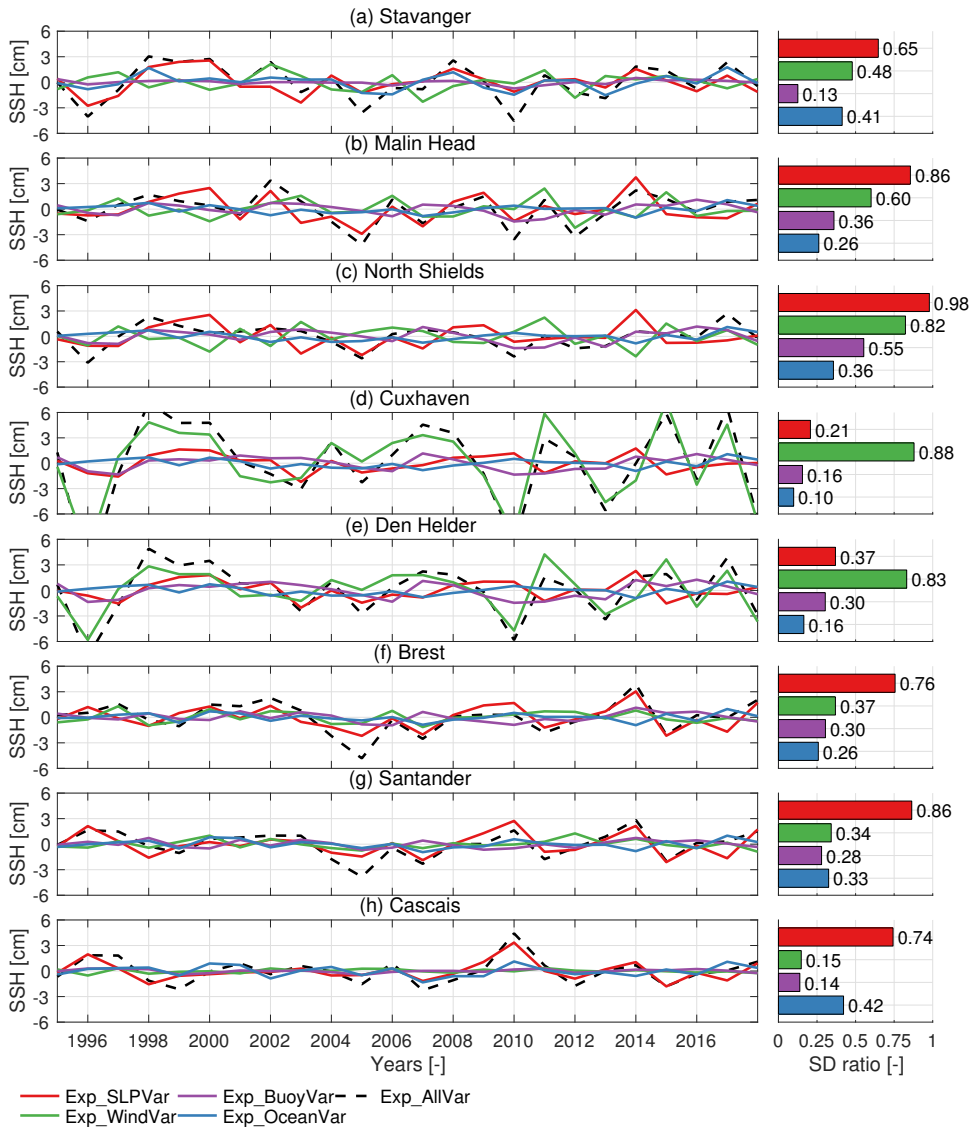


Figure 4.7: Detrended sea-level anomalies with respect to time-mean sea level [cm] and the ratio of SDs [-] with respect to *Exp_AllVar* (black, dashed) for *Exp_SLPVar* (red), *Exp_WindVar* (green), *Exp_BuoyVar* (purple) and *Exp_OceanVar* (blue) at the coastal locations in Figure 4.3: **(a)** Stavanger (Norway), **(b)** Malin Head (Ireland), **(c)** North Shields (United Kingdom), **(d)** Cuxhaven (Germany), **(e)** Den Helder (The Netherlands), **(f)** Brest (France), **(g)** Santander (Spain) and **(h)** Cascais (Portugal).

4.4.4. Correlation between sea level at coastal locations

To relate the spatially varying effect of different drivers to the correlation between sea level at different locations, we calculated the correlation between detrended annual mean sea level in *Exp_AllVar* at several coastal locations in the region (Figure 4.8a, lower triangle). In Section 4.4.2 we showed that wind variability is an important driver of interannual sea-level variability in the North Sea (Figure 4.6c). Consequently, sea level along the North Sea coast is highly correlated (e.g., at Wick, Aberdeen, North Shields, Esbjerg, Cuxhaven, Den Helder and Oostende). The sea level at locations on the southwest of the NWES is also correlated (e.g., Brest, Newlyn, Santander and Cascais), which is where SLP dominates (Figure 4.6b). The sea level at Malin Head is strongly influenced by both SLP and winds (Figure 4.7b) and has high correlations with sea level at Bergen, Stavanger, and the northeast UK coastline. It has reduced correlations with the sea level at locations in the North Sea, since these are predominantly controlled by wind variability. Correlations between the sea level at locations in the North Sea and the English Channel, and in the North Sea and on the southwestern NWES, are low or even negative (e.g., Santander and Brest).

The correlation pattern for *Exp_AllVar* generally agrees with that for the TGs of PSMSL (Holgate et al., 2013; PSMSL, 2020) (Figure 4.8a, upper triangle), but the correlations between the sea level observed at TGs are generally lower, possibly due to data gaps and the influence of local unmodelled processes. We excluded TGs with less than 18 years of data (75%, grey) and corrected for the nodal cycle following Woodworth (2012), neglecting self-attraction and loading effects. Both ROMS and the TG observations show that the sea level on the southwestern part of the NWES has low or negative correlations with the sea level in the southern and eastern North Sea. This can be explained by the sensitivity of shelf sea level to the NAO (Wakelin et al., 2003; Woolf et al., 2003; Tsimplis et al., 2005, 2008; Chen et al., 2014). For example, a high SLP anomaly at Santander depresses sea level locally. This coincides with stronger southwesterly winds over the North Sea, which induce higher sea level at the North Sea coast through Ekman transport (Tsimplis et al., 2008). This mechanism becomes apparent from *Exp_SLPVar* and *Exp_WindVar*, (Figures 4.6b & c).

Complementing Figure 4.8a, we repeat Figure 4.4a, now incorporating the effect of SLP (Figure 4.8b). This leads to increased and statistically significant correlations between sea level at Brest and in the open ocean, because SLP has long correlation scales and the coastal region and open ocean respond to SLP similarly. As discussed earlier, SLP also enhances the contrast between sea-level variability on the southwestern part of the NWES and in the North Sea. As a consequence, the coherence of sea-level variability along the shelf break extends less far north in Figure 4.8b than in Figure 4.4a.

To investigate the role of LSWs inside our domain in driving the coherence of sea level on the NWES, we integrated the winds from ERA5 along the 400 m isobath from the southern lateral boundary (36°N) to the respective latitudes of Stavanger, Malin Head, Brest, Santander and Cascais. The LSW integrals are significantly cor-

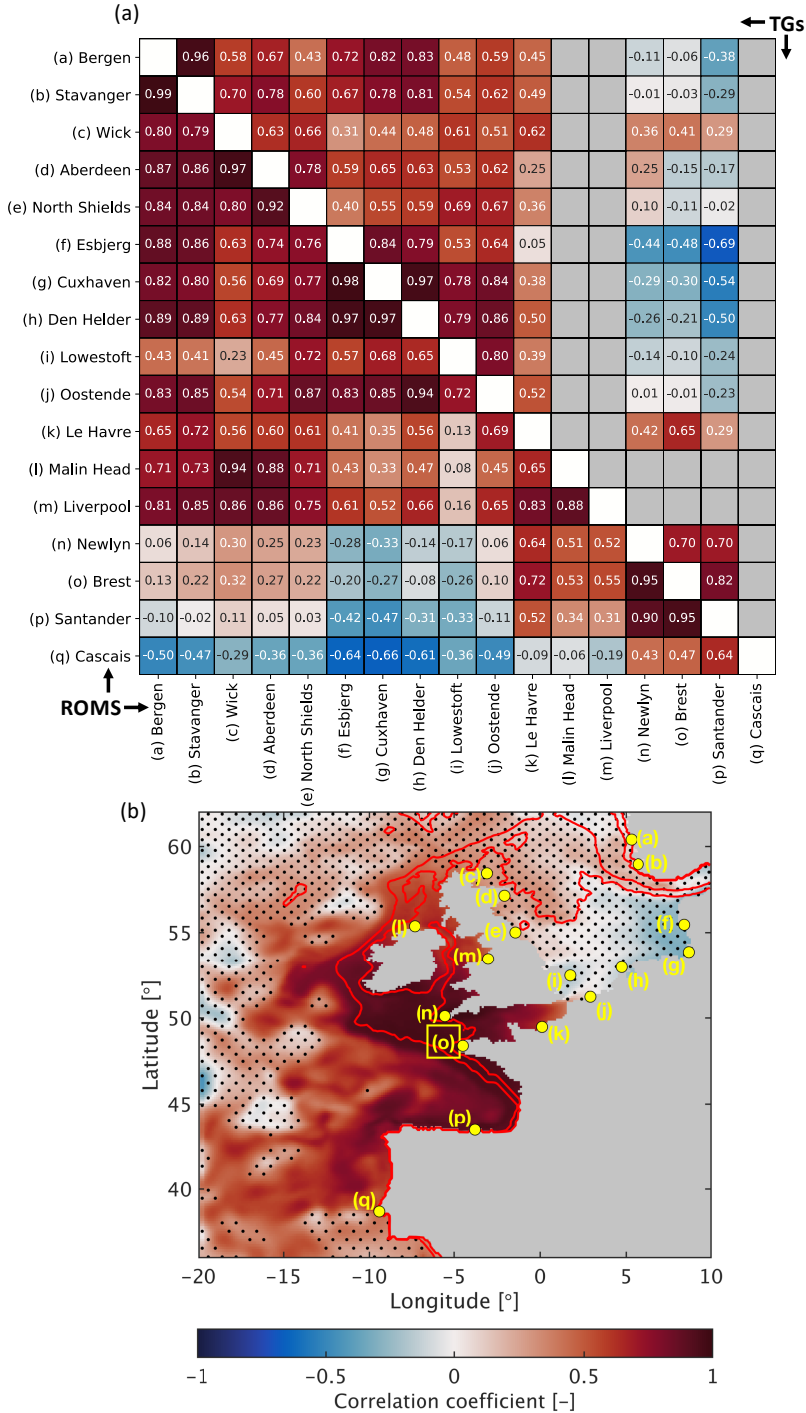


Figure 4.8: Correlation coefficients [-] between **(a)** detrended annual mean sea level (1995-2018) at several coastal locations across the region for *Exp_AllVar* (lower triangle) and for tide gauges with $\geq 75\%$ data available (upper triangle), and between **(b)** detrended sea level at Brest (label o) and detrended sea level at all other grid cells for *Exp_AllVar*. Stipples and isobaths in **(b)** as in Figure 4.2.

related with the detrended annual mean sea level in *Exp_AllVar* (excluding the IB effect) at these locations, which appears to primarily reflect the high correlations between integrated LSWs and sea level in *Exp_WindVar* (Table S4.1). The correlations between the integrated LSWs and sea level are higher than those between local winds and sea level, supporting the premise of signals propagating along the boundary (Sturges and Douglas, 2011; Calafat et al., 2012). The LSW integral up to Stavanger has relatively low correlations with sea level at North Shields, Cuxhaven and Den Helder. In line with Figure 4.8b, including SLP changes the correlation between integrated LSWs and annual mean sea level (Table S4.1), reflecting the important role of the IB effect at most locations.

4.5. Discussion

Our sensitivity experiments showed that atmospheric forcing is the main driver of interannual sea-level variability on the NWES. This agrees with previous studies for different time periods (e.g., Wakelin et al., 2003; Dangendorf et al., 2014a; Tinker et al., 2020). Additionally, we found that ocean-driven variability is small and coherent on the shelf, and combines with atmospheric-driven variability nearly linearly. Similar spatial patterns of sea-level variability were obtained by Tinker et al. (2020) with a different regional ocean model, indicating some robustness to model design. Because Tinker et al. (2020) derived boundary conditions from a 200-yr control run of HadGEM3 GC3.0 (Williams et al., 2018), the magnitude of sea-level variability in their atmospheric and ocean-driven simulations differs from that in *Exp_AtmosVar* and *Exp_OceanVar* (Figures 4.5c & d). Since we used reanalysis data as boundary conditions instead, our results can be compared directly with satellite altimetry, but may not be fully representative of (multi-)decadal sea-level variability.

We have separated the effect of atmospheric forcing on interannual sea-level variability into the effects of SLP, winds and buoyancy fluxes for the entire NWES. This complements the analysis of Dangendorf et al. (2014a), which focused on tide gauges in the North Sea. Dangendorf et al. (2014a) found that a linear regression on winds explains around 50-85% of the observed sea-level variability from Oostende (Belgium) to Hirtshals (Denmark), and on SLP around 50-65% from Tregde to Bergen (Norway) and Aberdeen to Lerwick (UK). *Exp_WindVar* confirms that wind-driven interannual sea-level variability is largest in the southern and eastern North Sea. Our results also show that wind-driven variability is large around Norway, Scotland and north of Ireland, and small on the southwest of the NWES and along the shelf break. In line with Dangendorf et al. (2014a), we showed that SLP is the dominant driver of interannual sea-level variability along the northeast UK coastline. Our sensitivity experiments show that this is also the case on the southwestern part of the NWES. Much of the interannual variability observed at TGS in the North Sea can be explained with barotropic models (Dangendorf et al., 2014a; Piecuch et al., 2019). The baroclinic response to winds could be further investigated by comparing our results to the results of a barotropic set-up under the same atmospheric forcing.

Since the NWES-seas are shallow, local steric sea-level variability is limited (Roberts et al., 2016; Tinker et al., 2020). We showed that buoyancy fluxes result in interannual sea-level variability with SDs varying from 0.5–1.3 cm on the shelf (*Exp_BuoyVar*, Figure 4.6d). At the sample locations in Figure 4.7, the relative magnitude of buoyancy-driven variability roughly agrees with the finding of Tinker et al. (2020) that the local steric component explains up to 35% of the total variability on the shelf. A large fraction of the steric sea-level variability on the NWES in the global model of Roberts et al. (2016) was indeed explained by buoyancy fluxes.

The coherence of sea level along the eastern boundary of the North Atlantic and in the North Sea was previously attributed to wind-driven CTWs (Sturges and Douglas, 2011; Calafat et al., 2012, 2013; Dangendorf et al., 2014a). The long correlation scales along the shelf break compared to in the deep ocean (Figures 4.4c & d) suggest that boundary dynamics are indeed at play. This is further supported by the significant correlations of integrated LSWs with simulated coastal sea level (Table S4.1), which are similar to the correlations with observed sea level (Calafat et al., 2012, 2013; Dangendorf et al., 2014a). That these correlations remain high when only the wind forcing is varied interannually (*Exp_WindVar*) confirms that the wind variability has a causative role, and the reduced correlations between local winds and sea level suggest that LSWs drive a part of the variability in *Exp_WindVar*. The correlation between integrated LSWs and sea level in the North Sea is low, mirroring the correlation pattern of a common mode of British TGs with satellite altimetry in (Hogarth et al., 2020) and indicating the dominance of local winds over the North Sea (Figure 4.6c).

Since wind-driven interannual sea-level variability is relatively small at the shelf break and on the southwestern NWES (*Exp_WindVar*, Figure 4.6c), the coherence of sea level there could partially be explained by the relatively uniform sea-level variability due to the forcing at the lateral ocean boundaries and due to buoyancy fluxes (*Exp_OceanVar* and *Exp_BuoyVar*, Figures 4.5d & 4.6d). The correlation scales in Figure 4.4 as well as the correlation between sea level and integrated LSWs strongly suggest that wind-driven CTWs influence sea level on the NWES, but do not necessarily rule out an effect of open ocean steric anomalies (Chafik et al., 2019), which may be represented in *Exp_OceanVar*. The variability driven by the southern boundary conditions may also reflect northward propagating CTWs triggered south of the domain (Calafat et al., 2012; Fukumori et al., 2015). However, quantifying this remote contribution accurately would require enlarging the model domain and increasing the simulation period.

4.6. Conclusions

We have used a high-resolution ($1/8^\circ$ by $1/8^\circ$) configuration of ROMS for the NWES to identify the contribution of different drivers of interannual sea-level variability during 1995–2018. The interannual sea-level variability in our model matches well with that observed with satellite altimetry. Based on sensitivity experiments in which we isolated the effect of atmospheric and oceanic drivers, we conclude that atmospheric variability is the main driver of interannual sea-level variability, with

the largest SDs in the German Bight (up to 5.6 cm). On the other hand, the forcing at the lateral ocean boundaries causes coherent sea-level variability on the shelf, with an SD of only 0.5 cm. The ocean-driven variability on the shelf is mainly caused by the variation of the western and southern boundary conditions, but the driving physical mechanism requires further investigation, for instance by comparing against simulations with a barotropic model, further decomposing the lateral boundary conditions or studying the ocean bottom pressure on the shelf. In our model, intrinsic sea-level variability has an SD of up to 2.7 cm in the open ocean, but is negligible on the shelf.

Our results show that, to first order, the interannual sea-level variability induced by the variability of SLP, winds, buoyancy fluxes and the lateral ocean boundaries combines linearly on the NWES. Thus, the contributions of these drivers can be studied separately, which supports the use of multiple linear regression analysis. Wind variability has a large influence on sea-level variability in the North Sea, and around Scotland, Norway and north of Ireland. It is the dominant driver in the southern and eastern North Sea, whereas the IB effect dominates at other coastal locations shown in this study. Wind also drives large mesoscale variability in the open ocean, but wind-driven sea-level variability is suppressed along the shelf break. At the sample locations in Figure 4.7, buoyancy-driven sea-level variability can have a relative magnitude of up to 55% (North Shields). Sea-level variability driven by the lateral ocean boundary conditions can have a relative magnitude of up to 42% (Cascais).

Sea-level variability on the southwestern part of the NWES is predominantly driven by the IB effect. As a consequence, detrended annual mean sea level on the southwestern part of the shelf has low or even negative correlations with that in the southern and eastern North Sea, where sea-level variability is predominantly driven by local winds. This agrees with the sensitivity of shelf sea level to the NAO (e.g., [Tsimplis et al., 2008](#); [Wakelin et al., 2003](#)). The significantly positive correlations between wind-driven sea-level variability on the NWES and winds integrated along the continental slope in our model indicate that LSWs and the consequent propagation of signals along the eastern boundary of the North Atlantic are partly responsible for the coherence of sea-level variability on the NWES.

To conclude, our results improve the understanding of the drivers of interannual sea-level variability on the NWES, which vary in importance depending on location. Explicitly decomposing the contribution of different drivers using ROMS increases confidence in previous observation-based studies and is useful for sea-level budget studies. The results of our sensitivity experiments can be used to remove known variability from observations to estimate sea-level rise or time of emergence with a higher accuracy. This will help coastal decision makers to monitor and detect early warning signals more reliably.

4.7. Supplementary information

4.7.1. Supplementary figures

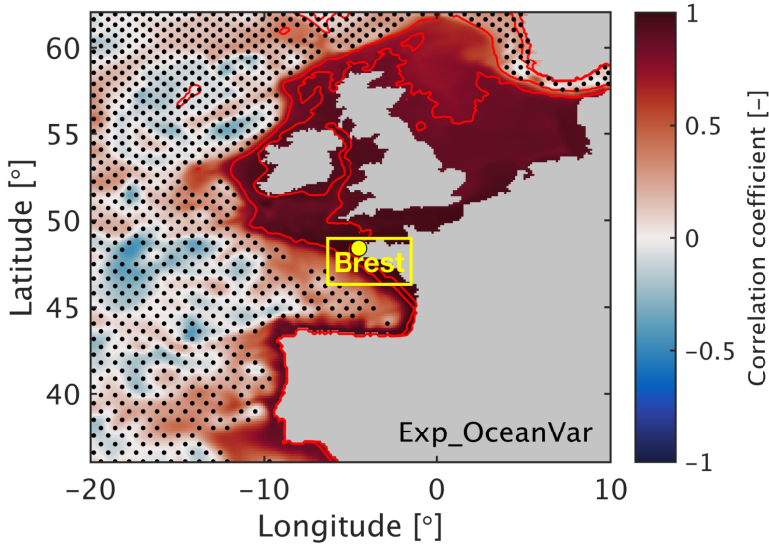


Figure S4.1: Correlation coefficients [-] of the detrended annual mean sea level (1995-2018) at Brest with that at all other grid cells in *Exp_OceanVar* (Figure 4.5d). The black stipples indicate statistically insignificant correlation coefficients ($p \geq 0.05$). The red contours indicate the 80 and 200 m isobaths of ROMS.

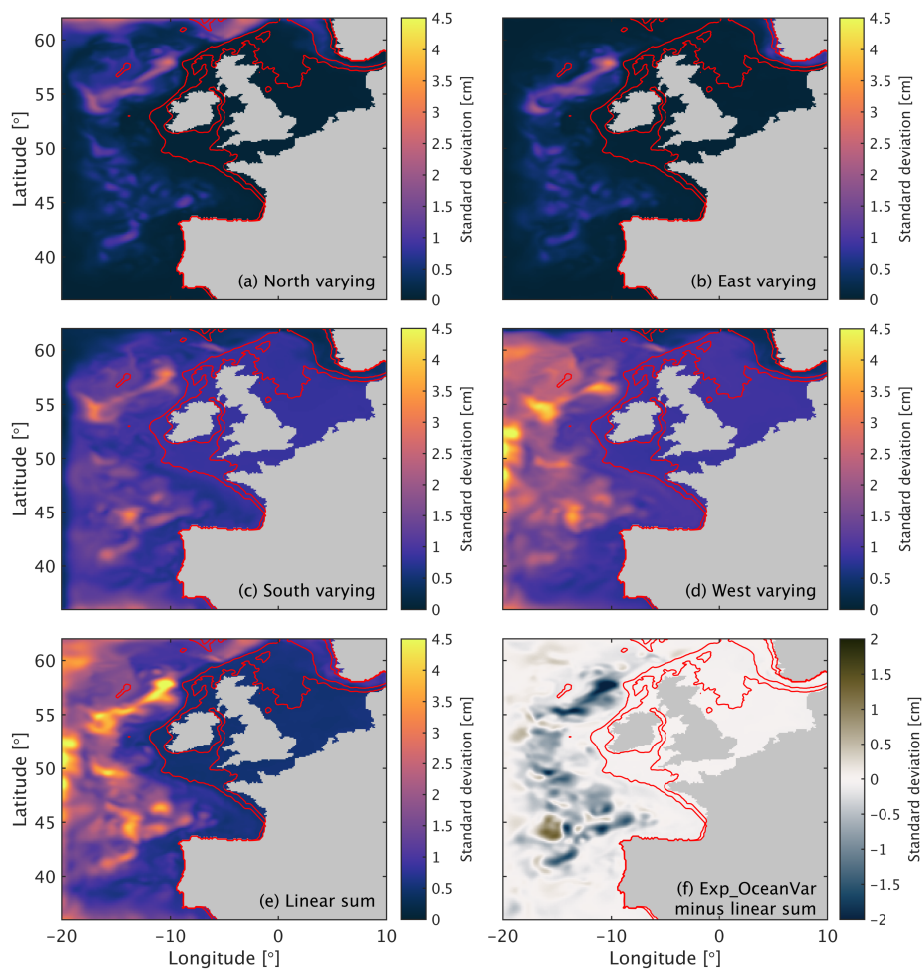


Figure S4.2: Sea-level variability as the SD [cm] of detrended annual means (1995-2018) for four variants of *Exp_OceanVar* (Figure 4.5d) in which there is only interannual variation of forcing at (a) the northern boundary, (b) the eastern boundary, (c) the southern boundary, and (d) the western boundary; for (e) the linear sum of time series of these four variants; and (f) the residual SD of *Exp_OceanVar* minus the linear sum of components. Isobaths as in Figure S4.1.

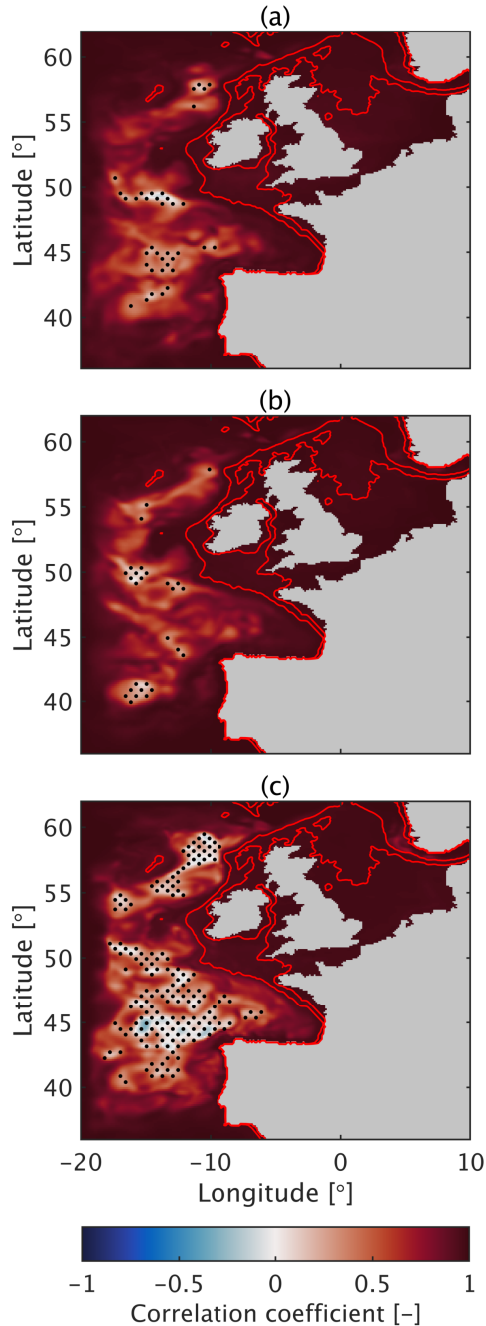


Figure S4.3: Correlation coefficients [-] between the detrended annual mean sea level in **(a)** *Exp_AllVar* and the linear sum of time series in *Exp_AtmosVar*, *Exp_OceanVar* and *Exp_NoneVar* (Figure 4.5), **(b)** *Exp_AtmosVar* and the linear sum of time series in *Exp_SLPVar*, *Exp_WindVar* and *Exp_BuoyVar* (Figure 4.6), and **(c)** *Exp_OceanVar* and the linear sum of time series in the model experiments in which boundary conditions are varied interannually separately for each lateral boundary (Figure S4.2). Stipples and isobaths as in Figure S4.1.

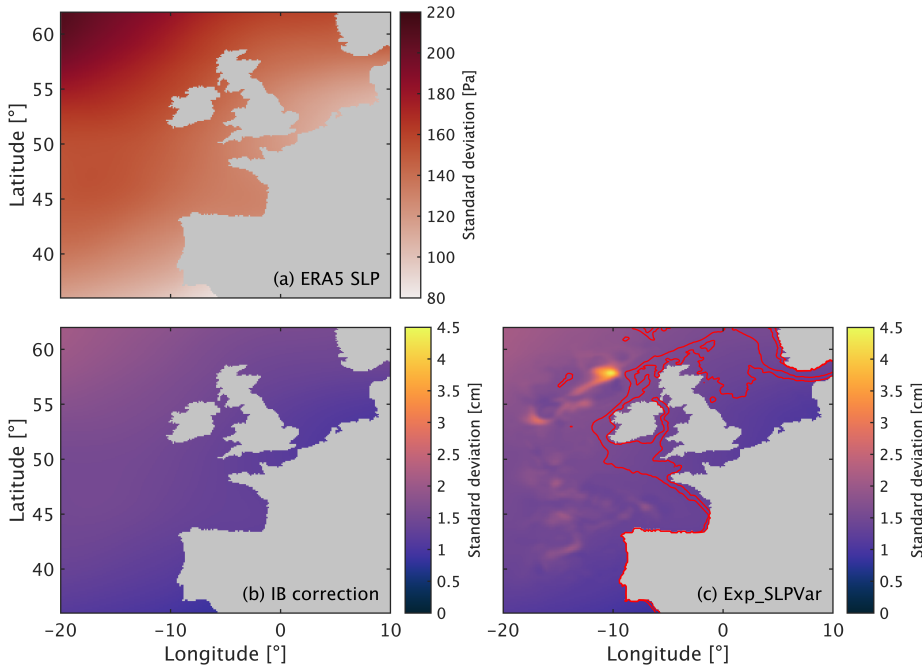


Figure S4.4: Interannual variability expressed as the SD of detrended annual means (1995-2018), for **(a)** SLP in ERA5 [Pa], **(b)** the IB correction $\eta_{IB}(x, y, t) = \frac{-(P_{sl}(x, y, t) - P_{sl}(t))}{\rho_0 g}$ [cm] following [Stammer and Hüttemann \(2008\)](#) and using SLP from ERA5, with $\overline{P_{sl}} = 101,000$ Pa, $g = 9.81$ m/s² and $\rho_0 = 1025$ kg/m³, and **(c)** sea level in *Exp_SLPVar* [cm] (Figure 4.6c). Isobaths as in Figure S4.1.

4.7.2. Supplementary tables

Table S4.1: Correlation coefficients [-] between detrended annual mean sea level in the various ROMS experiments with the integral of winds along the 400 m isobath from 36N to the respective latitudes of sample coastal locations in Figures 4.3 & 4.7 (up to the latitude of Stavanger for North Shields, Cuxhaven and Den Helder). Bold correlation coefficients are statistically significant ($p < 0.05$).

Location	Experiment					
	AllVar (no IB)	AllVar	SLPVar	WindVar	BuoyVar	OceanVar
Stavanger	0.51	0.09	-0.38	0.75	-0.07	-0.02
Malin Head	0.61	0.56	0.14	0.75	0.01	-0.17
North Shields	0.31	0.20	-0.14	0.38	0.00	-0.16
Cuxhaven	0.07	-0.05	-0.59	0.08	-0.02	-0.17
Den Helder	0.12	-0.06	-0.44	0.13	-0.02	-0.13
Brest	0.56	0.68	0.45	0.82	0.09	0.00
Santander	0.46	0.49	0.23	0.67	0.05	-0.04
Cascais	0.56	0.24	-0.07	0.64	0.31	0.18

5

The Effect Of Wind Stress on Seasonal Sea-Level Change

Abstract

Projections of relative sea-level change (RSLC) are commonly reported at an annual mean basis. The seasonality of RSLC is often not considered, even though it may modulate the impacts of annual mean RSLC. Here, we study seasonal differences in 21st-century ocean dynamic sea-level change (DSL_C, 2081-2100 minus 1995-2014) on the Northwestern European Shelf (NWES) and their drivers, using an ensemble of 33 CMIP6 models complemented with experiments performed with a regional ocean model. For the high-end emissions scenario SSP5-8.5, we find substantial seasonal differences in ensemble mean DSL_C, especially in the southeastern North Sea. For example, at Esbjerg (Denmark) winter mean DSL_C is on average 8.4 cm higher than summer mean DSL_C. Along all coasts on the NWES, DSL_C is higher in winter and spring than in summer and autumn. For the low-end emissions scenario SSP1-2.6, these seasonal differences are smaller. Our model experiments indicate that the changes in winter and summer sea-level anomalies are mainly driven by regional changes in wind-stress anomalies, which are generally southwesterly and east-northeasterly over the NWES, respectively. In spring and autumn, regional wind-stress changes play a smaller role. We also show that CMIP6 models not resolving currents through the English Channel cannot accurately simulate the effect of seasonal wind-stress changes on the NWES. Our results imply that using projections of annual mean rather than seasonal mean RSLC may underestimate the RSLC-driven changes in the frequency of extreme coastal sea levels in spring and winter. Additionally, changes in the seasonal sea-level cycle may affect groundwater dynamics and the inundation characteristics of intertidal ecosystems.

Published as: Hermans, T.H.J., Katsman, C.A., Camargo, C.M.L., Garner, G.G., Kopp, R.E., & Slangen, A.B.A. (2021). *The Effect Of Wind Stress on Seasonal Sea-Level Change on the Northwestern European Shelf*, Journal of Climate, 1-31. [10.1175/JCLI-D-21-0636.1](https://doi.org/10.1175/JCLI-D-21-0636.1)

5.1. Introduction

Probabilistic regional sea-level projections are crucial for coastal adaptation planning (e.g., [Hinkel et al., 2019](#)). New sea-level projections are continuously being developed for a range of emissions scenarios, building on the latest understanding of the physical processes contributing to relative sea-level change (RSLC) ([Fox-Kemper et al., 2021](#), and references therein). Most of these projections focus on annual mean RSLC. However, the seasonal sea-level cycle may also change over time, which has the potential to modulate the impacts of RSLC in particular seasons.

[Widlansky et al. \(2020\)](#) recently showed that seasonal sea-level variability will increase in many regions in which the ocean warms. The authors argue that this is at least partially because of the larger thermal expansion of the ocean at higher temperatures, which implies that steric sea-level variability will increase even if the temperature variability stays constant. In shallow coastal regions, however, barotropic processes also contribute substantially to the seasonal sea-level cycle ([Roberts et al., 2016](#); [Vinogradov et al., 2008](#); [Vinogradova et al., 2007](#)). The effect of barotropic processes on future changes of the seasonal sea-level cycle in coastal regions has not been extensively studied yet.

This study focuses on seasonal changes in the coastal region northwest of Europe. The Northwestern European Shelf (NWES) harbors shallow shelf seas, such as the North Sea, with low-lying and densely populated coasts. On the NWES, atmospheric forcing is the dominant driver of the interannual variability of annual mean sea level ([Dangendorf et al., 2014a](#); [Hermans et al., 2020a](#); [Tinker et al., 2020](#)). Atmospheric forcing also affects the temporal variability of the seasonal sea-level cycle on the NWES ([Plag and Tsimplis, 1999](#)). The magnitude of the interannual to multi-decadal variability of seasonal mean sea level and the extent to which that variability can be explained by atmospheric forcing are larger for autumn and winter than for spring and summer ([Dangendorf et al., 2012, 2013a](#); [Frederikse and Gerkema, 2018](#)). For example, a regression on local wind stress explains 80-90% of the observed interannual sea-level variability at Cuxhaven (Germany) in autumn and winter, compared to 50-60% in spring and summer ([Dangendorf et al., 2013a](#)). This reflects the seasonality of atmospheric variability and introduces seasonal differences in sea-level trends computed over a few decades, especially in the southeastern North Sea ([Dangendorf et al., 2012, 2013b](#); [Frederikse and Gerkema, 2018](#); [Marcos and Tsimplis, 2007](#)).

At centennial timescales, seasonal differences in RSLC on the NWES have also been observed. For example, along the Dutch coast, [Gerkema and Duran-Matute \(2017\)](#) found differences of 0.35-0.81 mm/yr between 100-year trends of sea level in winter and summer half-years. Also in the Baltic Sea, seasonal differences in RSLC of several centimeters were observed ([Ekman, 1998](#)). These were linked to seasonal differences in the change of southwesterly winds over the entrance to the Baltic Sea. Although these findings suggest that RSLC may also have seasonal differences in the future, only a few studies have investigated the seasonality of sea-level projections

for the NWES (Dangendorf et al., 2014b; Hermans et al., 2020b; Mathis, 2013). Moreover, the results of these studies were based on a limited number of models and/or were obtained for only a part of the NWES.

Here, we explore the seasonal differences in ocean dynamic sea-level change (DSLCL) over the 21st century as simulated by a large ensemble of state-of-the-art global climate models from the Coupled Model Intercomparison Project 6 (CMIP6; Eyring et al., 2016). Additionally, we investigate if these seasonal differences can be attributed to the projected wind-stress changes over the region. To better understand the effect of wind-stress changes, we complement the CMIP6 simulations with experiments performed with a high-resolution regional ocean model for the NWES (Hermans et al., 2020a). Section 5.2 describes both these datasets. Section 5.3 shows that, depending on the emissions scenario, CMIP6 models simulate substantial seasonal differences in DSLCL. In Section 5.4, we present seasonal differences in ensemble-mean wind-stress change and test the effect of wind-stress changes on sea level in individual CMIP6 models using the regional model. We also study the importance of the representation of the English Channel. We end with a discussion and our conclusions in Section 5.5.

5.2. CMIP6 simulations and regional model experiments

Section 5.2.1 details how we obtained and processed the CMIP6 output. In Section 5.2.2, we introduce the high-resolution regional ocean model and the experiments that we performed with it.

5.2.1. Downloading and processing the CMIP6 output

We use simulations of dynamic sea level and wind stress from an ensemble of 33 CMIP6 models (see the overview in Table S5.1), downloaded from the Earth System Grid Federation database in July 2021. The variables used are monthly mean dynamic sea level above the geoid ('zos' variable) and the zonal and meridional wind stress components at the surface ('tauu' & 'tauv' variables). Since we use 'zos', we study DSLCL as defined by Gregory et al. (2019) and therefore exclude the inverse barometer effect (Stammer and Hüttemann, 2008).

All simulation realizations that provide both sea level and wind stress for the historical period (1850-2014) and the high-end shared socioeconomic pathway scenario SSP5-8.5 (O'Neill et al., 2014) (2015-2100) are used. For sea level, we also obtain the same realizations for the low-end emissions scenario SSP1-2.6, if available. We focus on the output for the SSP5-8.5 scenario, since it has the highest signal-to-noise ratio. To indicate the range within which seasonal differences in DSLCL for other SSPs may fall, we present results for the SSP1-2.6 scenario in Section 5.6. Additionally, we download preindustrial control simulations of 'zos', which are required to correct DSLCL for ocean model drift. Finally, for our regional model experiments (Section 5.2.2), we also download the wind velocity components at a height of 10 m ('uas' & 'vas' variables) for a subset of CMIP6 models.

The CMIP6 'zos' output first needs to be corrected for ocean model drift (Sen Gupta et al., 2013). We do so by applying a linear fit to 'zos' over the full length of the preindustrial control run of each model and by subtracting these fits from the historical and SSP runs. This commonly used procedure implicitly assumes that the model drift and the forced changes are linearly separable (Hobbs et al., 2016; Sen Gupta et al., 2013). Since 'zos' is defined as sea level above the geoid, and the geoid is time-invariant in CMIP6 models, we also remove the global area-weighted mean of 'zos' at each time step using the grid cell area variable 'areacello'. For the analysis of gridded ensemble projections (e.g., Figures 5.1 & 5.3), we bi-linearly interpolate the CMIP6 simulations to a common 1° by 1° grid using ESMValTool routines (Eyring et al., 2020).

5

Before adding each model to the multi-model ensemble, we first take the mean of all available realizations of each model, following Yin (2012). Since each realization of a simulation of a given model is branched from its preindustrial control run at a different time, the phase of the internal sea-level variability differs between each realization. Averaging over the available realizations reduces the effect of internal sea-level variability on the projections of each model, leading to a better representation of the externally forced response. In Section 5.5, we will show that this moderately reduces the multi-model ensemble spread. Projections derived from models with relatively few realizations will be affected by internal variability the most. However, using only models with an equal number of multiple realizations would substantially reduce the ensemble size. Table S5.1 provides an overview of the CMIP6 output that we used. We exclude simulations that do not provide the complete (meta)data required for the processing steps described above. Additionally, we exclude the models MIROC6 and MIROC-ES2L, because their minimum ocean depth on the NWES is 150 m. This is unrealistically deep compared to the other CMIP6 models (10-60 m). At 90 and 193 km, the average native ocean and atmosphere grid resolution of the CMIP6 models in the NWES region is relatively coarse (Table S5.1), but large ensembles of high-resolution models are currently not available.

From the processed monthly mean CMIP6 output, we compute seasonal means by averaging over December to February (DJF), March to May (MAM), June to August (JJA) and September to November (SON). To study the seasonal differences in DSLC, we then compute seasonal anomalies by subtracting the annual mean of each year from the seasonal means of that year, with the annual mean calculated over December to November. We abbreviate the seasonal anomalies of sea level, wind stress and wind velocity as SSLA, SWSA and SWVA, respectively. We compute the projected change of these anomalies (Δ SSLA, Δ SWSA and Δ SWVA) from the difference between the future mean (2081-2100) and the historical mean (1995-2014) anomalies.

5.2.2. Regional ocean model and model experiments

To test the effect of wind-stress changes in CMIP6 models on sea level (Sections 5.4.2 & 5.4.3), we perform experiments with a regional ocean model for the NWES

(Hermans et al., 2020a). This model is a configuration of the Regional Ocean Modeling System (ROMS; Shchepetkin and McWilliams, 2005) and covers the region 36°N–62°N by 20°W–10°E with a 1/8° by 1/8° horizontal resolution. At the surface and lateral boundaries, the ROMS model is forced with atmosphere (ERA5; CDS, 2019) and ocean reanalysis data (GLORYS12v; Lellouche et al., 2018). Climatological river run-off is prescribed based on the dataset of Dai (2017). Simulations with this model compare well with satellite altimetry data and were used to study the drivers of interannual sea-level variability on the NWES (Hermans et al., 2020a).

Here, the reanalysis-forced model simulation is our reference experiment. For our sensitivity experiments (Table 5.1), we add the Δ SWVA derived from four example CMIP6 models (for SSP5–8.5) to the wind velocity boundary conditions from ERA5 at each timestep. We compute the resulting response of sea level and barotropic currents for a specific season as the difference relative to the reference experiment, averaged over 1993–1995. We use three CMIP6 models that span a wide range of Δ SSLA and provide at least five realizations each: CanESM5, UKESM1-0-LL and IPSL-CM6A-LR. Additionally, we use a model with a closed English Channel: ACCESS-ESM1-5. For further interpretation, we also simulate the effect of spatially uniform southwesterly and northeasterly wind-velocity changes. To test the importance of the representation of the English Channel, we repeat several experiments using a modified land mask in which the English Channel is closed at the Strait of Dover (Table 5.1).

Table 5.1: Model experiments discussed in Sections 5.4.2 & 5.4.3. The boundary conditions other than wind velocity are identical in all experiments.

Model experiments	Modifications of ERA5-based wind velocity boundary conditions	English Channel
<i>Exp_Ref</i>	-	Open
<i>Exp_Ref_cc</i>	-	Closed
<i>Exp_CAN</i>	+ Δ SWVA from CanESM5	Open
<i>Exp_UK</i>	+ Δ SWVA from UKESM1-0-LL	Open
<i>Exp_IPSL</i>	+ Δ SWVA from IPSL-CM6A-LR	Open
<i>Exp_ACC</i>	+ Δ SWVA from ACCESS-ESM1-5	Open
<i>Exp_ACC_cc</i>	+ Δ SWVA from ACCESS-ESM1-5	Closed
<i>Exp_SW</i>	+1 m/s southerly and 1 m/s westerly	Open
<i>Exp_SW_cc</i>	+1 m/s southerly and 1 m/s westerly	Closed
<i>Exp_NE</i>	+1 m/s northerly and 1 m/s easterly	Open
<i>Exp_NE_cc</i>	+1 m/s northerly and 1 m/s easterly	Closed

To add the wind-velocity changes from the CMIP6 models to the surface boundary conditions, we bi-linearly interpolate. To avoid prescribing the ROMS model with land-contaminated wind-velocity changes (Biol Kara et al., 2007), we first use nearest neighbor extrapolation to replace the wind-velocity change of (partially) over-land grid cells with the wind-velocity change of purely over-ocean grid cells in the CMIP6 models. We only extrapolate if it leads to larger wind-velocity changes, because over-land winds are weaker than over-ocean winds.

We emphasize that we only use the regional model experiments to qualitatively understand the effect of ΔSWSA on ΔSSLA and barotropic currents in the different CMIP6 models. Our model experiments are less well suited for a quantitative attribution because of the differences between the regional model and the global models, and because of the potential inconsistencies of combining coarse-resolution CMIP6 wind-velocity changes with ERA5 atmospheric forcing. For instance, the wind-velocity changes that we apply may not translate to exactly the same wind-stress changes as in the CMIP6 models, since the climatological wind velocities and the parameterization of air-sea fluxes may differ between the ROMS set-up and the CMIP6 models. Additionally, we ignore the results of the model experiments near Norway, because we do not modify the eastern lateral boundary conditions of the ROMS model that control the Norwegian Coastal Current.

5.3. Seasonal DSLC simulated by CMIP6 models

In this section we investigate seasonal differences in DSLC by analyzing ΔSSLA . First, we analyze CMIP6 projections of ΔSSLA on the NWES (Section 5.3.1). Then, we take a closer look at sea-level projections for Esbjerg (Section 5.3.2), which we find is a location on the NWES with large seasonal DSLC differences.

5.3.1. ΔSSLA on the NWES

Figures 5.1a-d show that for SSP5-8.5, the magnitude of the ensemble mean ΔSSLA reaches up to 4.9 cm on the NWES, which indicates how much seasonal mean DSLC may deviate from annual mean DSLC (Figure S5.1a). In the Celtic and Irish Seas, in part of the English Channel, along parts of the coast of Ireland and Scotland, and in the southern and eastern North Sea, ensemble mean ΔSSLA is most positive (DSLC is highest) in winter (Figure 5.1a). Elsewhere on the shelf, ΔSSLA is highest in spring (Figure 5.1b). The spatial patterns of summer and autumn ΔSSLA (Figures 5.1c & d) approximately oppose those of winter and spring (Figures 5.1a & b). Whereas spring and autumn ΔSSLA are spatially relatively uniform, winter and summer ΔSSLA show a dipole pattern in the North Sea. Along the coast of the southeastern North Sea, the seasonal differences are largest. For example, at Esbjerg (Denmark, location 8), winter and summer ΔSSLA are 3.7 and -4.7 cm, respectively. Therefore, on average, the CMIP6 models simulate an 8.4 cm (52%) increase in the difference between winter and summer mean sea level for SSP5-8.5 (see Figure S5.2 for historical and future SSLAs on the NWES).

The multi-model distributions of ΔSSLA reveal that DSLC is larger in spring than in autumn at all eight example coastal locations on the NWES (Figure 5.1e). However, especially at Den Helder, Cuxhaven and Esbjerg (locations 6-8), the difference between winter and summer mean DSLC exceeds the difference between spring and autumn mean DSLC. Together, these changes shift the phase and increase the amplitude of the seasonal sea-level cycle (Figure S5.2i). Additionally, at locations 6-8, the inter-model spread introduces large uncertainty in the projections. Consequently, studying the seasonality of DSLC is particularly relevant for the southeastern North Sea.

For the SSP1-2.6 scenario, the spatial patterns of Δ SSLA are comparable to those for the SSP5-8.5 scenario, but have a smaller magnitude (Figure S5.3). For example, the ensemble mean winter and summer Δ SSLA at Esbjerg are 0.1 and -1.0 cm, compared to 3.7 and -4.7 cm for SSP5-8.5. As for SSP5-8.5, the inter-model spread of Δ SSLA at locations 6-8 is larger than at the other locations. Since the signal-to-noise ratio is lower for SSP1-2.6, there is less agreement between models on the season of largest DSLC than for SSP5-8.5. In contrast to SSP5-8.5, DSLC for SSP1-2.6 is highest in spring and lowest in autumn on most of the NWES. Therefore, the projected seasonal differences in DSLC are scenario-dependent.

5.3.2. Seasonal sea-level projections at Esbjerg

The largest seasonal differences in DSLC occur in the southeastern North Sea, for example near Esbjerg (Figure 5.1). We therefore illustrate the seasonality of sea-level projections for Esbjerg in further detail. At Esbjerg, the CMIP6 ensemble has a median annual mean DSLC of 17.7 cm and a 5-95% range of 2.2 to 26.1 cm for SSP5-8.5 (Figure 5.2a, black bar). Spring and autumn mean DSLC have slightly higher and lower multi-model medians than annual mean DSLC (18.2 and 16.9 cm), respectively, and have differently shaped distributions (Figure 5.2a, light blue and light red bars). For winter, the ensemble projections are overall higher than for the annual mean, with a median of 21.1 cm and a 5-95% range of 2.9 to 31.6 cm (Figure 5.2a, dark blue bar). The projections for summer are substantially lower than for the annual mean, with a median of 11.1 cm and a 5-95% range of 0.8 to 20.7 cm (Figure 5.2a, dark red bar).

At Esbjerg, the changes in seasonal sea-level anomalies are most apparent for winter and summer (Figure 5.2b, dark blue and dark red bars). The CMIP6 ensemble projects a median winter Δ SSLA of 3.5 cm (5-95%: -0.5 to 9.2 cm) and a median summer Δ SSLA of -4.1 cm (5-95%: -9.9 to -1.3 cm). The finding that the multi-model distributions of Δ SSLA are not equal to the difference between the distributions of seasonal and annual mean DSLC indicates that models that simulate large/small seasonal differences in DSLC do not necessarily also simulate large/small annual mean DSLC. As noted in Section 5.3.1, the seasonal differences in the projections for Esbjerg are much smaller for SSP1-2.6 than for SSP5-8.5 (Figure S5.4).

The results in Sections 5.3.1 & 5.3.2 raise the question of what causes the scenario-dependent seasonality of DSLC. In Section 5.4 we therefore study the dynamics behind the seasonal differences in DSLC on the NWES. We focus on the effect of wind stress, motivated by the high correlation between observed seasonal mean sea level and wind stress on interannual to multi-decadal timescales (Dangendorf et al., 2013a, 2014b; Frederikse and Gerkema, 2018; Plag and Tsimplis, 1999).

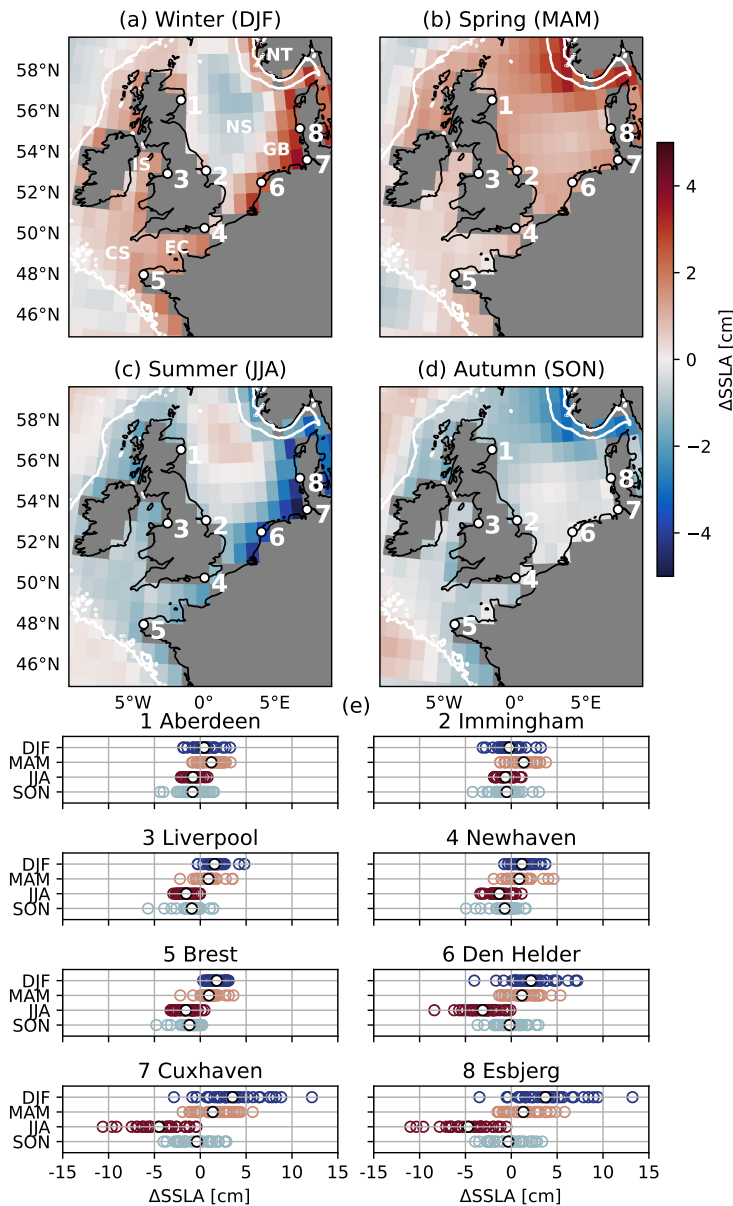


Figure 5.1: Ensemble mean changes of **(a)** winter (DJF), **(b)** spring (MAM), **(c)** summer (JJA) and **(d)** autumn (SON) sea-level anomalies [cm], for SSP5-8.5 (2081-2100 relative to 1995-2014); **(e)** the multi-model distributions of these changes in CMIP6 models at their ocean grid cells nearest to eight example coastal locations, for winter (dark blue), spring (light blue), summer (dark red) and autumn (light blue). Each colored circle represents the change in one model; the black-edged circle represents the ensemble mean. In **(a-d)**, ensemble mean results are shown only on grid cells for which at least 5 CMIP6 models provide ocean values on a common 1° by 1° grid. The white contour denotes the 200 m isobath from ETOPO1 (Amante and Eakins, 2009) approximating the shelf break. The abbreviations in **(a)** denote the Celtic Sea (CS), English Channel (EC), German Bight (GB), Irish Sea (IS), North Sea (NS) and Norwegian Trench (NT) (see also Figure 1.8).

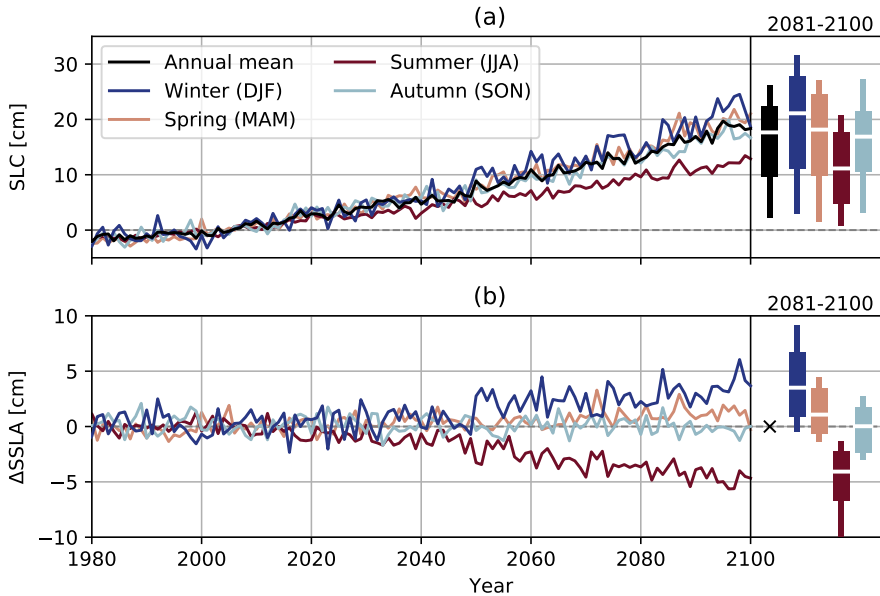


Figure 5.2: Ensemble median projections for Esbjerg of **(a)** annual mean and seasonal mean DSLC [cm] and of **(b)** the change in seasonal sea-level anomalies [cm] for SSP5-8.5 (relative to 1995-2014). The bars on the right indicate the 50% (horizontal white stripes), 17-83% (thick bars) and 5-95% (thin bars) percentiles of the multi-model distributions of the mean change in 2081-2100.

5.4. The effect of wind stress on the seasonality of DSLC

To study the effect of wind stress on seasonal differences in DSLC, we first investigate the ensemble mean changes in seasonal wind-stress anomalies (ΔSWSA) and discuss their relation to ensemble mean ΔSSLA (Section 5.4.1). Second, we compare ΔSSLA and ΔSWSA between individual CMIP6 models and test the effect of the wind-stress changes in these models on sea level using high-resolution model experiments (Section 5.4.2). Finally, in Section 5.4.3 we use model experiments to test the impact of the representation of the English Channel in CMIP6 models on simulating wind-driven ΔSSLA .

5.4.1. Ensemble mean ΔSWSA over the NWES

In winter the ensemble mean ΔSWSA for SSP5-8.5 is approximately southwesterly over the southern half of the NWES (Figure 5.3a). Toward the northwest of the domain, winter ΔSWSA decreases in magnitude and becomes southeasterly. The historical mean winter wind-stress anomalies are predominantly southwesterly over the NWES (see Figure S5.5 for historical and future SWSA s). Therefore, Figure 5.3a indicates that winter wind-stress anomalies will become more strongly southwesterly in the future over the Celtic Sea, the Irish Sea, the English Channel and most

of the North Sea. In contrast, summer Δ SWSA is approximately east-northeasterly (Figure 5.3c), which indicates that the historical, predominantly north-northeasterly wind-stress anomalies over the NWES in summer will become more strongly north-easterly. Spring Δ SWSA varies from northerly to westerly over the North Sea (Figure 5.3b) and autumn Δ SWSA is mainly southwesterly over the north and northwest of the NWES (Figure 5.3d). Over most of the NWES, spring and autumn Δ SWSA are lower in magnitude than winter and summer Δ SWSA. Ensemble mean Δ SWSA differs relatively little from seasonal mean wind-stress change because the annual mean wind-stress change is relatively small over the NWES (Figure S5.1b).

For a southwesterly wind-stress increase over the NWES as in Figure 5.3a, Ekman transport is expected to enhance sea level along the coasts to the right of the wind stress. Pingree and Griffiths (1980) modelled the effect of a spatially uniform southwesterly wind stress over the NWES and indeed found enhanced sea level in the English Channel, west of the United Kingdom (UK), around Scotland and Norway, and particularly in the southeastern North Sea (their Figure 3). This is qualitatively very similar to the ensemble mean winter Δ SSLA (Figure 5.1a). Pingree and Griffiths (1980) also found that the increased sea-level gradients perpendicular to the coast are accompanied by geostrophic changes in barotropic transport along the coast (their Figure 2).

Assuming linearity, the response to a northeasterly wind-stress change is approximately opposite to the response to a southwesterly wind-stress change. This is consistent with the ensemble mean summer Δ SSLA (Figure 5.1c), which is negative in the regions where winter Δ SSLA is positive (Figure 5.1a). These patterns strongly suggest that the ensemble mean southwesterly and (east-)northeasterly winter and summer Δ SWSA over the shelf cause a large part of the winter and summer Δ SSLA, respectively. Basic scaling relationships between wind-stress change and sea-level change based on Ekman transport are likely not easily applicable here, since Δ SWSA is spatially non-uniform and involves changes in both magnitude and direction. Nevertheless, summer Δ SSLA is likely larger than winter Δ SSLA (Figures 5.1a, c & e) because summer Δ SWSA is generally larger in magnitude than winter Δ SWSA (Figures 5.3a & c). A dynamical effect similar to the projected change can be found in observations of SSLAs in years with approximately southwesterly and northeasterly SWSAs (Figure S5.6).

The near shelf-wide positive and negative Δ SSLA in spring and autumn (Figures 5.1b & d) cannot be reconciled with the Ekman transport expected for the relatively small northwesterly and southwesterly spring and autumn Δ SWSA (Figures 5.3b & d), respectively. Instead, spring and autumn Δ SSLA may be more strongly affected by steric changes and mass redistribution between the shelf and the deep ocean than winter and summer Δ SSLA, since in the Northern Hemisphere the thermosteric component of the seasonal sea-level cycle has a minimum in spring and a maximum in autumn (Tsimplis and Woodworth, 1994; Vinogradov et al., 2008). We leave further investigation of steric effects on seasonal differences in DSLC, for instance by decomposing the DSLC on the NWES into local steric and manometric changes, to future work.

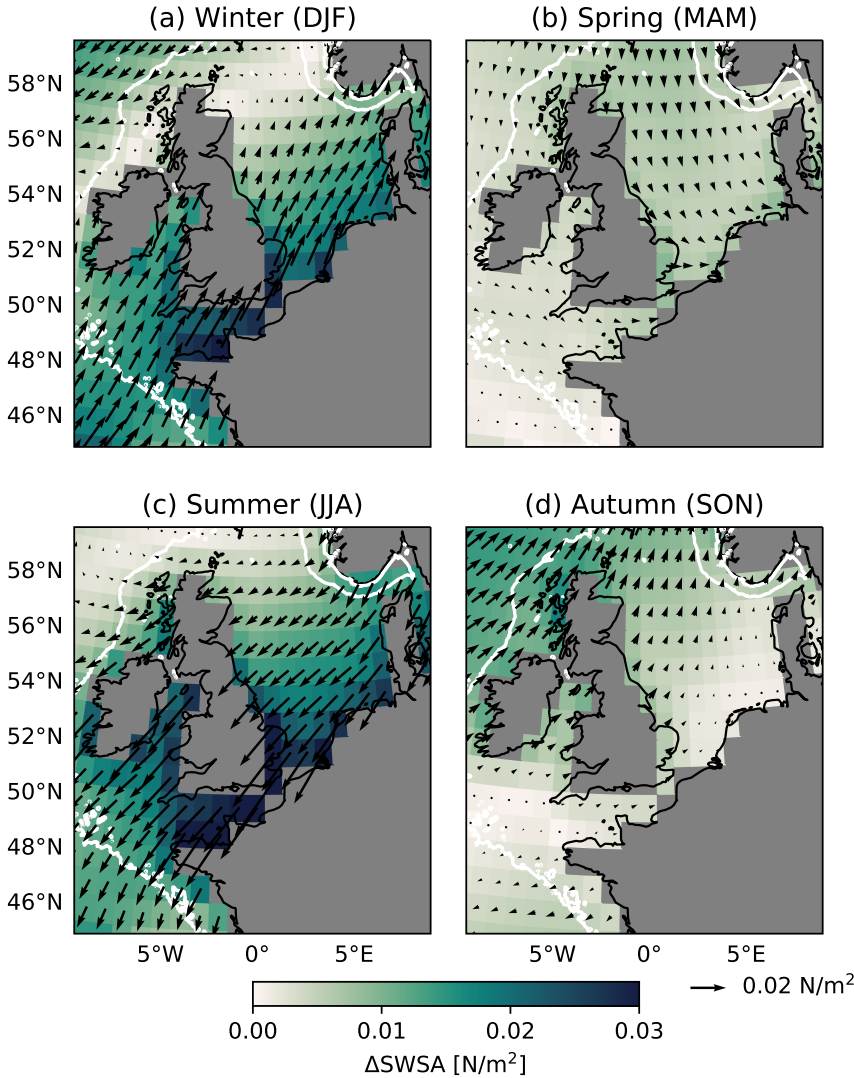


Figure 5.3: Ensemble mean changes of (a) winter (DJF), (b) spring (MAM), (c) summer (JJA) and (d) autumn (SON) wind-stress anomalies [N/m^2] for SSP5-8.5 (2081-2100 relative to 1995-2014). The colors represent the absolute change and the arrows the direction. White contours and land masks as in Figure 5.1.

5.4.2. The effect of ΔSWSA on ΔSSLA in individual CMIP6 models

In winter and summer, the ensemble mean ΔSSLA and ΔSWSA appear dynamically consistent (Section 5.4.1). However, Figures 5.1e & 5.2 reveal considerable inter-model differences in ΔSSLA . To understand the effect of the inter-model differences

in ΔSWSA on the inter-model differences in ΔSSLA , we compare winter and summer ΔSWSA and ΔSSLA between three example CMIP6 models: CanESM5, UKESM1-0-LL and IPSL-CM6A-LR. Additionally, as described in Section 5.2.2, we use our ROMS model to test the effect of the wind changes in these models on sea level and barotropic currents.

Winter and summer ΔSSLA vary in magnitude between CanESM5, UKESM1-0-LL and IPSL-CM6A-LR (Figures 5.4a-f, colors), but all three models resemble the ensemble mean spatial patterns (Figures 5.1a & c). ΔSWSA is also model-dependent and generally not spatially uniform over the region (Figures 5.4a-f, arrows). Nevertheless, ΔSWSA and ΔSSLA appear to be consistent in the models: the stronger and more southwesterly or northeasterly the ΔSWSA over the region, the higher the magnitude of winter and summer ΔSSLA . The contrast between the over-ocean and over-land ΔSWSA may be caused by the different surface roughness characteristics of the ocean and the land, affecting the translation of wind-velocity changes to wind-stress changes. The timeseries of ΔSSLA at Esbjerg reflect the model-dependent magnitudes of winter and summer ΔSSLA (Figures 5.4g-i). Although less of the internal variability is averaged out for UKESM1-0-LL and IPSL-CM6A-LR (5 & 6 realizations) than for CanESM5 (25 realizations), Figures 5.4g-i suggest that the projected changes in Figures 5.4a-f mostly represent forced responses rather than multi-decadal variability.

Next, we test the effect of winter and summer ΔSWSA in CanESM5, UKESM1-0-LL and IPSL-CM6A-LR on ΔSSLA by imposing the ΔSWVA derived from these models on the ROMS model (as explained in Section 5.2.2). The patterns of DSLC that the ROMS model simulates as a result (Figure 5.5, colors) are very similar to the patterns of winter and summer ΔSSLA in the CMIP6 models (Figure 5.4, colors). This confirms a causal relationship between ΔSWSA and ΔSSLA in winter and summer. Additionally, the model experiments imply that the ΔSSLA in the CMIP6 models are accompanied by changes in barotropic currents with opposite directions in winter and summer. For the experiments forced with winter ΔSWVA (Figures 5.5a-c), DSLC is smallest in *Exp_CAN*, intermediate in *Exp_UK* and largest in *Exp_IPSL*. This is consistent with the winter ΔSSLA in the CMIP6 models (Figures 5.4a-c) and suggests that the inter-model differences in ΔSWSA are responsible for the inter-model differences in ΔSSLA . For the experiments forced with summer ΔSWVA (Figures 5.5d-f), however, DSLC in *Exp_CAN* and *Exp_UK* are very similar despite the differences in summer ΔSWSA and ΔSSLA between CanESM5 and UKESM1-0-LL (Figures 5.4d & e). This may reflect that other factors besides regional ΔSWSA (e.g., changes in North Atlantic circulation) affect winter and summer ΔSSLA on the NWES in the CMIP6 models. It may also reflect differences in the translation of ΔSWVA to ΔSWSA between CanESM5 and UKESM1-0-LL due to differences in atmosphere-ocean coupling and the different atmosphere grid resolutions (Table S5.1).

The ensemble mean winter and summer ΔSSLA have a dipole pattern in the North Sea (Figures 5.1a & c). This is likely caused by the wind-driven redistribution of mass in the North Sea: the ensemble mean winter and summer ΔSWSA both have

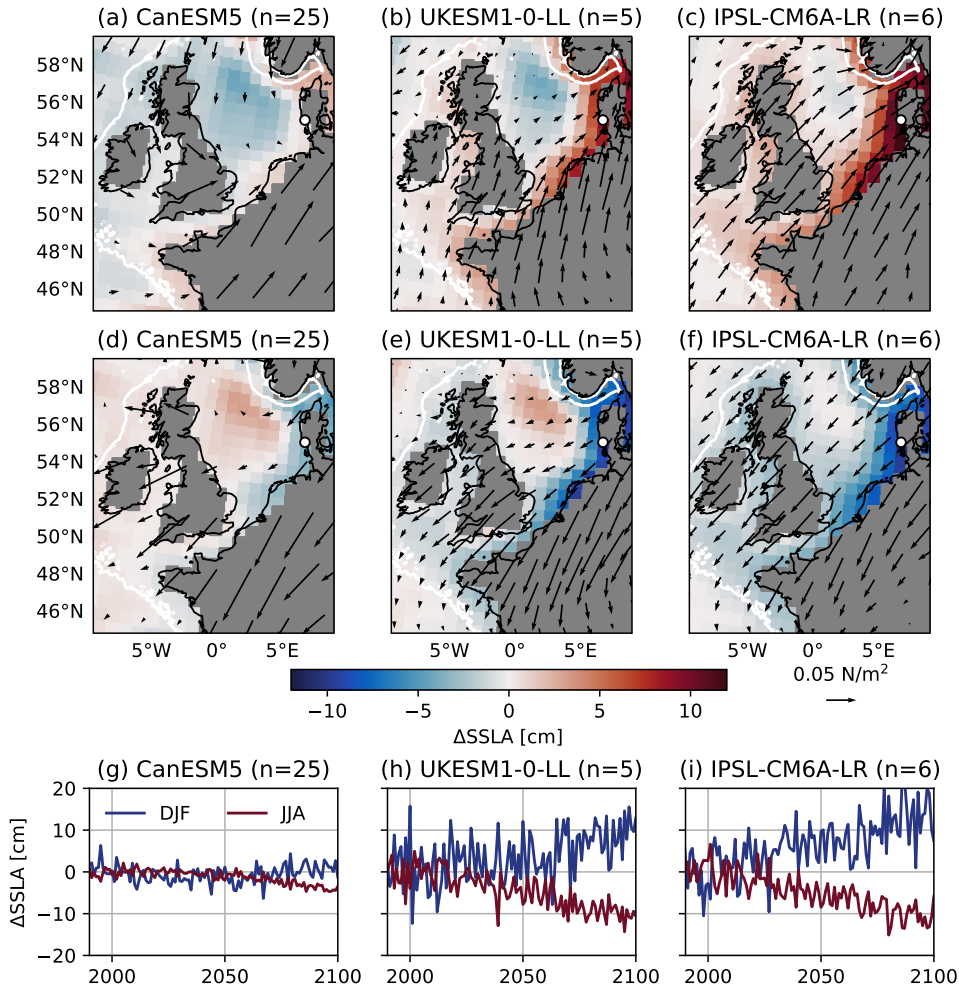


Figure 5.4: Composite plots of changes in winter (DJF, top row) and summer (JJA, middle row) sea-level anomalies [colors, cm] and wind-stress anomalies [arrows, N/m^2] for **(a & d)** CanESM5, **(b & e)** UKESM1-0-LL and **(c & f)** IPSL-CM6A-LR, for SSP5-8.5 (2081-2100 relative to 1995-2014); and timeseries of winter (blue) and summer (red) sea-level anomalies [cm] at Esbjerg for **(g)** CanESM5, **(h)** UKESM1-0-LL and **(i)** IPSL-CM6A-LR. The number of realizations used for each model is indicated in the title of each panel. For **(a-f)**, model specific grids are used (detailed in Table S5.1). The white circle in **(a-f)** denotes Esbjerg. White contours as in Figure 5.1.

a southeast to northwest gradient in magnitude and direction (Figures 5.3a & c), which may respectively drive a divergence and convergence of the flow in the central and northern North Sea. For IPSL-CM6A-LR, the dipole pattern of ΔSSLA in the North Sea is less apparent (Figures 5.4c & f). This appears to be consistent with the ΔSWSA in IPSL-CM6A-LR, which is spatially more uniform than in the other models (Figure 5.4). The absence of a dipole pattern in the sea-level responses to a

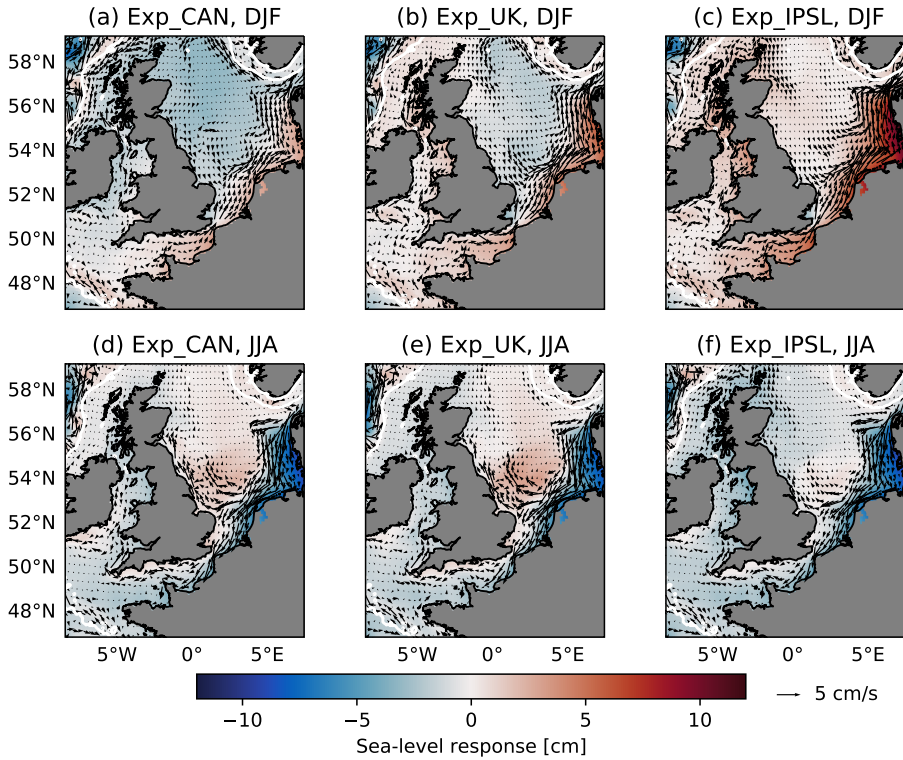


Figure 5.5: Composite plots of the response of sea level [colors, cm] and barotropic currents [arrows, cm/s] in ROMS to winter (top row) and summer (bottom row) Δ SWVA derived from **(a & d)** CanESM5 (*Exp_CAN*), **(b & e)** UKESM1-0-LL (*Exp_UK*) and **(c & f)** IPSL-CM6A-LR (*Exp_IPSL*), relative to *Exp_Ref* (Table 5.1). The arrows representing the response of barotropic currents are plotted every 9th grid cell. White contours as in Figure 5.1.

spatially uniform increase in southwesterly and northeasterly wind stress supports this interpretation (*Exp_SW* & *Exp_NE*, Figure 5.6). The results of *Exp_SW* are qualitatively very similar to the results of [Pingree and Griffiths \(1980\)](#), their Figures 2 & 3.

5.4.3. The effect of a closed English Channel on simulated Δ SSLA

Figures 5.6a & b show that increased southwesterly and northeasterly wind stress over the NWES induce changes in barotropic transport through the English Channel. However, the native land masks of at least 8 of the 33 CMIP6 models in our ensemble (see Table S5.1) are too coarse to allow these models to resolve currents through the English Channel. Therefore, we adjust the land mask of the ROMS model to test the effect of closing the English Channel at the Strait of Dover on the results of *Exp_SW* and *Exp_NW* (*Exp_SW_cc* & *Exp_NE_cc*, Figure 5.7).

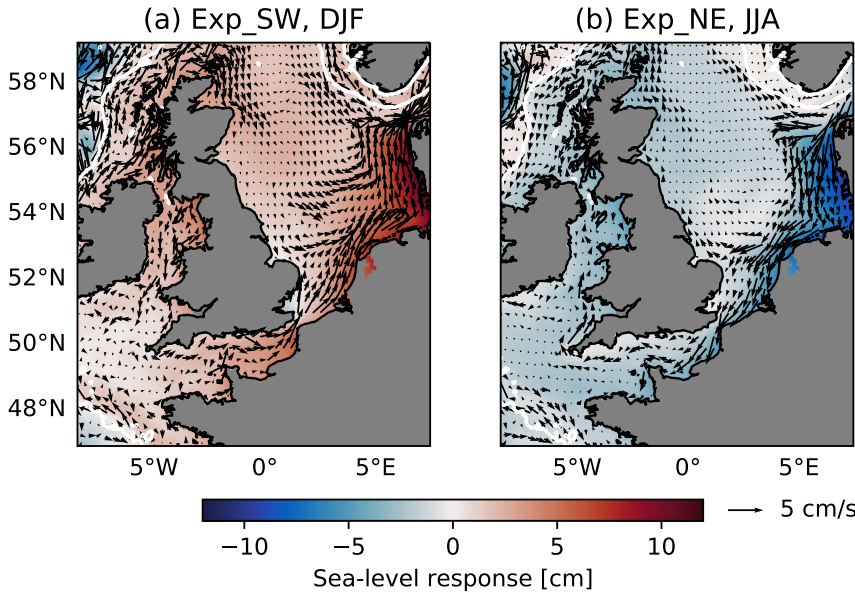


Figure 5.6: Composite plots of the response of sea level [colors, cm] and barotropic currents [arrows, cm/s] in ROMS in **(a)** *Exp_SW* in summer and **(b)** *Exp_NE* in winter, relative to *Exp_Ref* (Table 5.1). Arrows as in Figure 5.5, white contours as in Figure 5.1.

With a closed English Channel, the effect of a southwesterly wind-stress increase on sea-level rise in winter is reduced in the southern and eastern North Sea and enhanced elsewhere on the NWES, especially along the southern and western coastline of the UK (Figures 5.7a & c). The effect of a closed English Channel on the response to a northeasterly wind-stress increase in summer is similar to some extent (Figures 5.7b & d). That is, the sea-level fall in summer is mainly reduced in the southern and eastern North Sea and enhanced along the southern and western coastline of the UK, but also somewhat reduced in the Celtic Sea. Since direct transport of water between the English Channel and the southern North Sea is blocked in *Exp_SW_cc* and *Exp_NE_cc*, the response of barotropic currents to wind stress is reduced in the southern and eastern North Sea and enhanced on other parts of the shelf. Based on the results of these idealized experiments, we expect CMIP6 models with a closed English Channel to underestimate the difference between winter and summer DSLC in the southern and eastern North Sea and to overestimate it mainly along the coast of the UK.

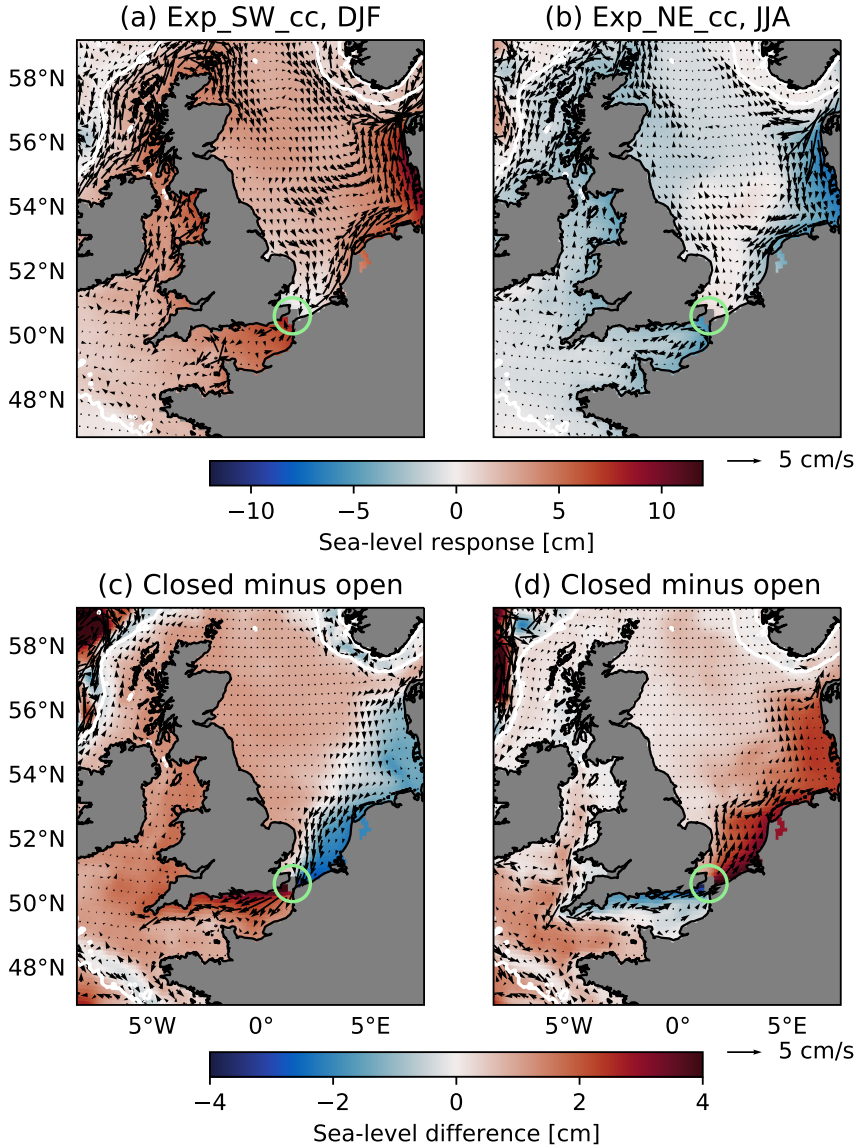


Figure 5.7: Composite plots of the response of sea level [colors, cm] and barotropic currents [arrows, cm/s] in ROMS in (a) *Exp_SW_cc* in summer and (b) *Exp_NE_cc* in winter, relative to *Exp_Ref_cc* (Table 5.1); (c-d) Figures 5.7a & b minus Figures 5.6a & b (response with a closed English Channel minus with an open English Channel). Arrows as in Figure 5.5, white contours as in Figure 5.1. The green circles indicate the closed English Channel in the modified land mask.

We illustrate the effect of a closed English Channel for the CMIP6 model ACCESS-ESM1-5 by applying the winter $\Delta SWVA$ derived from ACCESS-ESM1-5 to our ROMS model (Figure 5.8). When the English Channel is closed in the ROMS model, the

sea-level response is very similar to the winter Δ SSLA simulated by ACCESS-ESM1-5 itself (Figure 5.8a v.s. 5.8b). When the English Channel is open in the ROMS model, the sea-level response is higher in the southeastern North Sea and lower around the UK than in ACCESS-ESM1-5 (Figure 5.8a v.s. 5.8c). This indicates that the representation of the English Channel in CMIP6 models affects their simulation of Δ SSLA on the NWES. Excluding CMIP6 models with a closed English Channel from the ensemble increases the ensemble mean of winter Δ SSLA at Den Helder by 0.6 cm (28%).

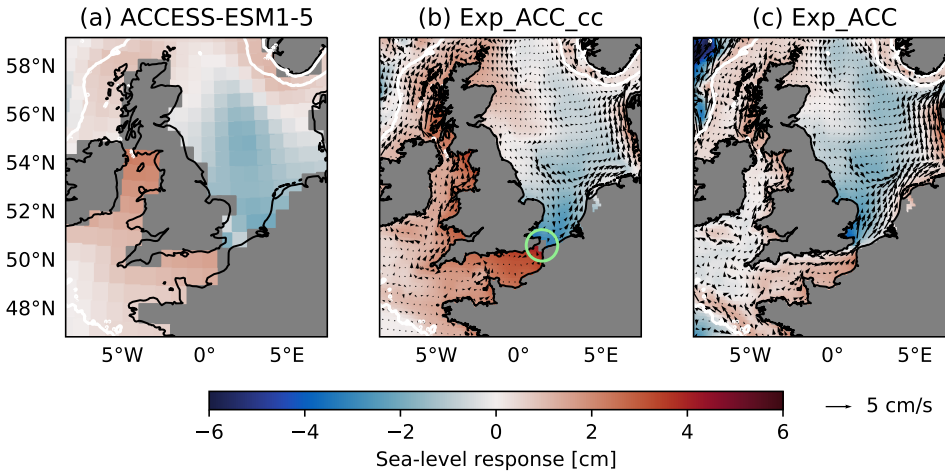


Figure 5.8: (a) Winter Δ SSLA [cm] simulated by ACCESS-ESM1-5 for SSP5-8.5 (2081-2100 relative to 1995-2104); (b-c) composite plots of the response of sea level [colors, cm] and barotropic currents [arrows, m/s] in ROMS to winter Δ SWVA derived from ACCESS-ESM1-5, with (b) a closed English Channel (*Exp_ACC_cc* relative to *Exp_Ref_cc*) and (c) an open English Channel (*Exp_ACC* relative to *Exp_Ref*) (Table 5.1). Arrows as in Figure 5.5, white contours as in Figure 5.1, green circles as in Figure 5.7.

5.5. Discussion and conclusions

Sea-level projections typically only consider annual mean RSLC, even though seasonal differences in DSLC may modulate the impacts of annual mean RSLC. Therefore, we studied the seasonal differences in DSLC on the NWES and investigated their causes. Based on an ensemble of 33 CMIP6 models, we find substantial changes in seasonal sea-level anomalies on the NWES for the SSP5-8.5 scenario, indicating substantial seasonal differences in DSLC. The seasonality of DSLC is largest in the southeastern North Sea, where sea level rises most in winter and least in summer (Figure 5.1). Our experiments with a regional ocean model indicate that the differences between winter and summer mean DSLC are for a large part caused by the differences in regional wind-stress change between these seasons (Section 5.4). For SSP1-2.6, seasonal differences in DSLC are much smaller, because atmospheric circulation changes are weaker for lower emissions scenarios (Collins et al., 2013).

To our knowledge, only one other study has investigated seasonal sea-level projections on the NWES using a multi-model ensemble (Dangendorf et al., 2014b). Although limited to the German Bight, Dangendorf et al. (2014b) found that the ensemble mean sea-level rise of 8 CMIP3 models was largest in winter and smallest in spring and summer. This partially agrees with our results, but we also find relatively large sea-level rise in spring (Figure 5.1b). The seasonal projections of Dangendorf et al. (2014b) were based on a sea-level pressure proxy reflecting the correlation between sea level and local zonal wind stress. In contrast, we find that the 21st-century changes in winter and summer sea-level anomalies are mainly caused by regional southwesterly and east-northeasterly wind-stress changes. The sea-level response is most likely governed by Ekman transport and accompanied by changes in barotropic transport on the shelf. The proxy of Dangendorf et al. (2014b) does not fully capture these regional dynamics, nor does it account for steric effects, which may influence Δ SSLA especially in spring and autumn (Section 5.4.1).

Since we find that the changes in winter and summer sea-level anomalies on the NWES are largely driven by regional changes in wind-stress anomalies, the large inter-model spread of projections of atmospheric circulation change (e.g., Oudar et al., 2020; Shepherd, 2014; Woollings, 2010) likely introduces substantial uncertainty in projected Δ SSLA (e.g., Figures 5.1, 5.2 & 5.4). It may be possible to constrain projections of Δ SSLA by weighting the CMIP6 models according to their performance and interdependence in simulating historical sea level or wind stress (e.g., Knutti et al., 2017; Lyu et al., 2020). Studies evaluating the seasonal sea-level cycle on the NWES in CMIP6 models are currently lacking, but they would be warranted in light of our results. Another part of the inter-model spread stems from internal variability, associated with the limited number of realizations available for some of the CMIP6 models. Although quantifying this uncertainty would require additional realizations, the differences between our projections of Δ SSLA and those derived by using only a single realization per model (Figure S5.7) suggest that the ensemble uncertainty due to internal variability is relatively modest.

While we focused on future changes and did not evaluate historical performance in this chapter, we do find that nearly 25% of the CMIP6 models in our ensemble do not resolve the currents through the English Channel (Table S5.1). This leads to an underestimation of seasonal differences in DSLC in the southern and eastern North Sea and an overestimation mainly along the southern and western coastline of the UK (Section 5.4.3). Not resolving currents through the English Channel likely affects simulations of annual mean DSLC as well (Hermans et al., 2020b). Therefore, we advocate excluding models that do not resolve currents through the English Channel when projecting DSLC for the NWES, unless the model simulations are dynamically downscaled first. Other resolution issues, such as related to resolving the inflow of the North Atlantic Current into the northern North Sea and the wind forcing near the coast, may further impact the CMIP6 simulations of Δ SSLA and need to be investigated.

We studied seasonal differences in DSLC for SSP5-8.5 and SSP1-2.6, and focused on the effect of wind-stress change to explain these. As a next step, results for SSP

scenarios in between SSP5-8.5 and SSP1-2.6 could be further investigated. Since changes in wind stress are coupled to changes in sea-level pressure, investigating the additional seasonal differences in DSLC that the inverse barometer effect (Stammer and Hüttemann, 2008) may introduce would also be useful. Additionally, follow-up studies could investigate steric effects in more detail by partitioning seasonal differences in DSLC into steric and manometric changes.

We see two potentially important implications of the seasonal differences in DSLC that we found. First, flood risk assessments and adaptation planning are currently based on projections of annual mean RSLC (e.g., Oppenheimer et al., 2019). We showed that coastal sea-level rise on the NWES exceeds the annual mean in spring and winter, which may cause a stronger shift in the distribution of extreme sea levels in these seasons than currently considered. Whether the increase in winter sea-level anomalies, which is mainly caused by increased southwesterly wind stress, can be superimposed on the height of the most severe storm surges in the southeastern North Sea, which occur for extreme northwesterly and westerly winds (de Winter et al., 2013; Sterl et al., 2009), is not yet clear. Second, mainly in the southeastern North Sea, the seasonal differences in DSLC imply a shift in the phase and an increase in the amplitude of the seasonal sea-level cycle (e.g., Figure S5.2i). This may impact coastal groundwater dynamics (Gonneea et al., 2013) and ecosystems in the intertidal zone. Whereas salt marshes with sufficient sediment accretion may keep up with centennial sea-level rise (Kirwan et al., 2016), even small changes in the seasonal sea-level cycle have the potential to significantly change the seasonal inundation characteristics of intertidal ecosystems, affecting the prospects for salt marsh development (Balke et al., 2016; Kim et al., 2011; Morris, 2000). Therefore, it is worth considering seasonal RSLC on the NWES and its impacts in addition to the annual mean change. This may apply to other regions as well.

5.6. Supplementary information

5.6.1. Supplementary figures

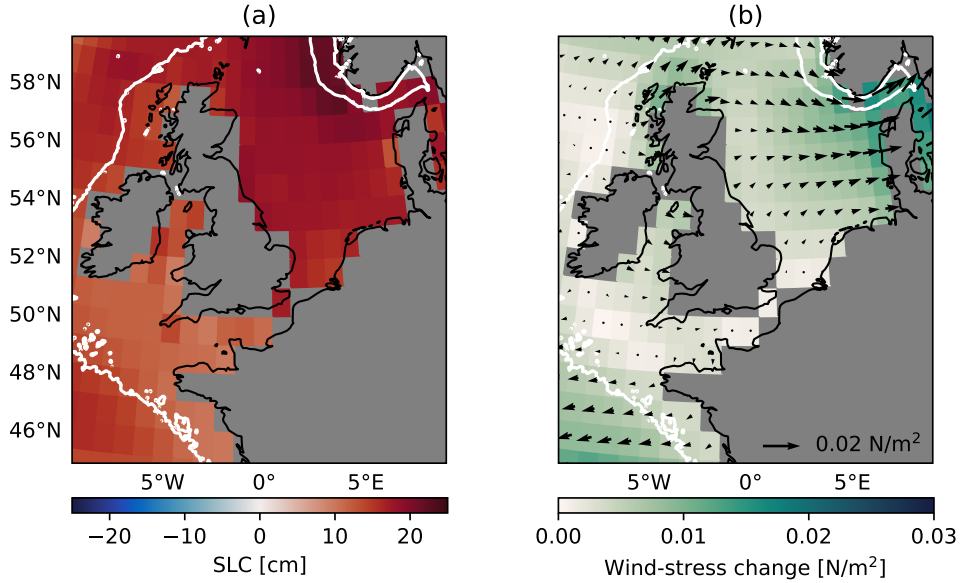


Figure S5.1: Ensemble mean changes of annual mean **(a)** ocean dynamic sea level [cm] and **(b)** wind stress [N/m²] for SSP5-8.5 (2081-2100 relative to 1995-2014). In **(a-b)**, ensemble mean results are shown only on grid cells for which at least 5 CMIP6 models provide ocean values on a common 1° by 1° grid. The white contour denotes the 200 m isobath from ETOPO1 ([Amante and Eakins, 2009](#)) approximating the shelf break.

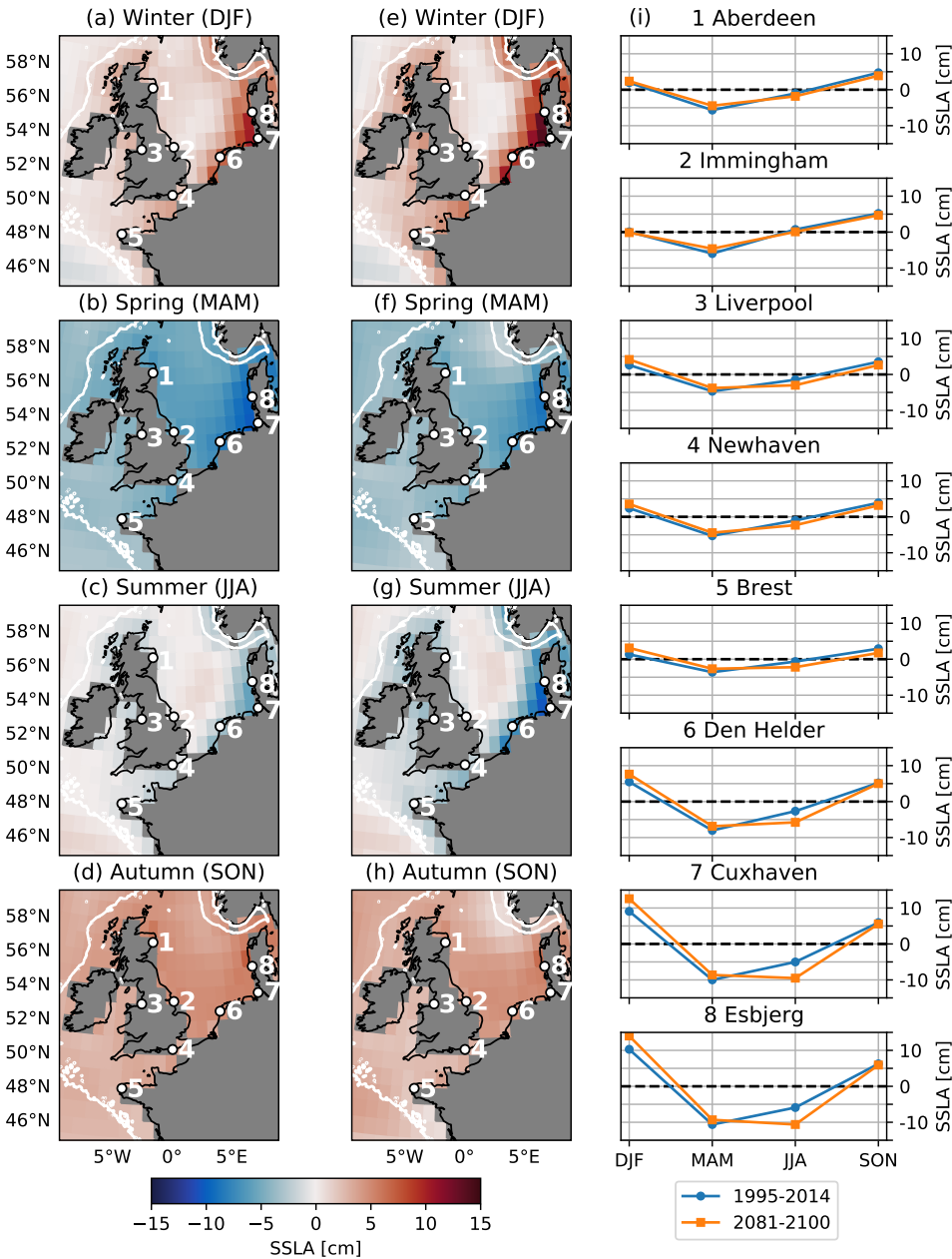


Figure S5.2: Ensemble mean (a-d) historical mean SSLA [cm] in winter (DJF), spring (MAM), summer (JJA) and autumn (SON) (1995-2014), (e-h) future mean SSLA [cm] in winter (DJF), spring (MAM), summer (JJA) and autumn (SON) for SSP5-8.5 (2081-2100), and (i) historical (blue) and future mean (orange) SSLA [cm] nearest to eight example coastal locations. White contours and land masks as in Figure S5.1.

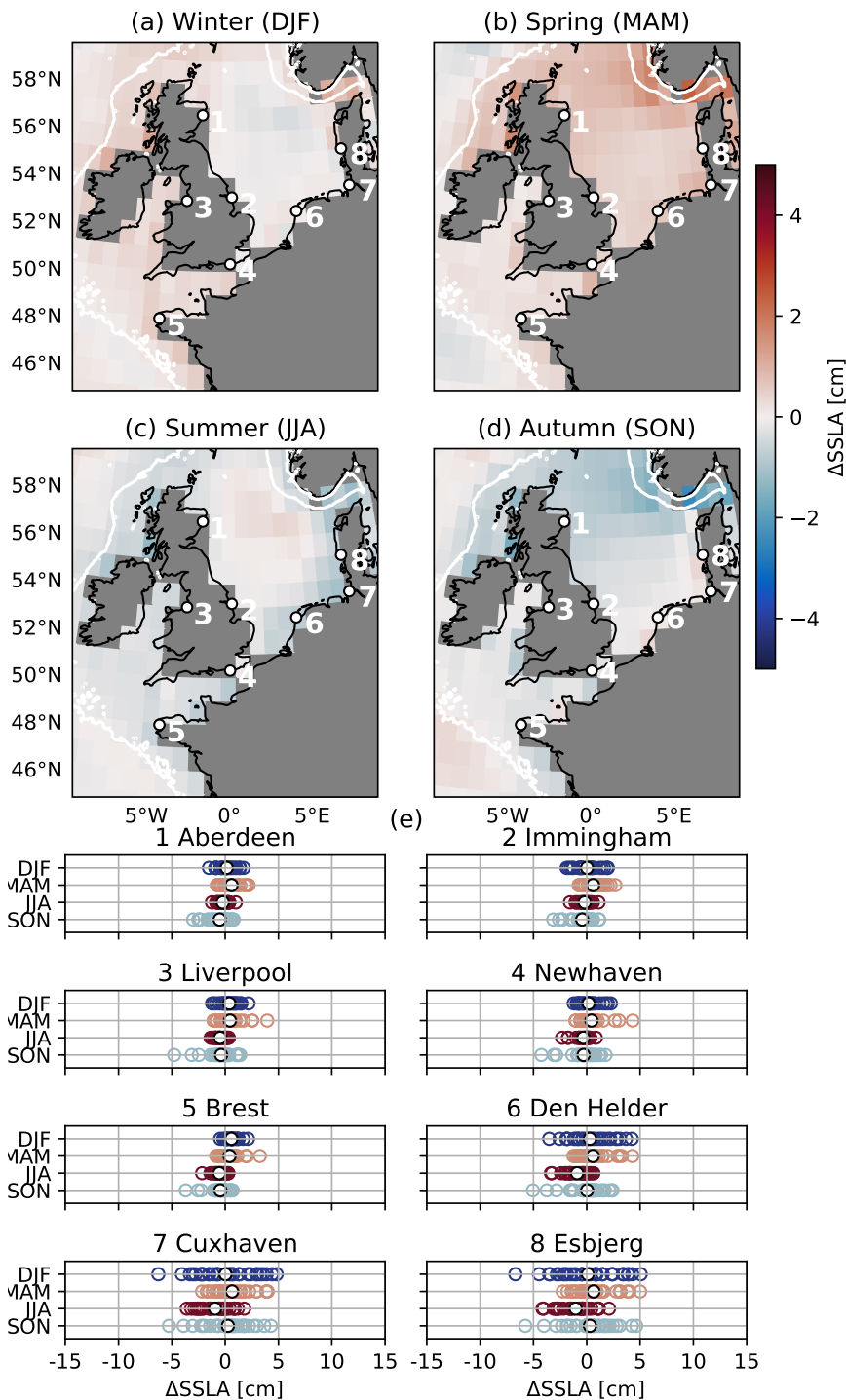


Figure S5.3: Ensemble mean changes of (a) winter (DJF), (b) spring (MAM), (c) summer (JJA) and (d) autumn (SON) sea-level anomalies [cm] for SSP1-2.6 (2081-2100 relative to 1995-2014); (e) the multi-model distributions of these changes in CMIP6 models at their ocean grid cells nearest to eight example coastal locations. Circles, white contours and land masks as in Figure S5.1.

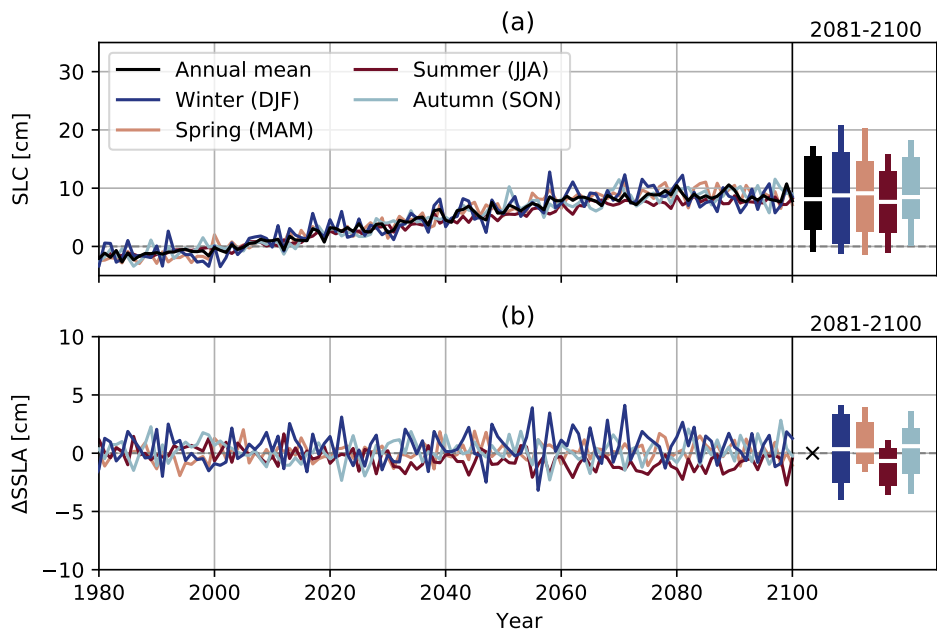


Figure S5.4: Ensemble median projections for Esbjerg of **(a)** annual mean and seasonal mean DS LC [cm] and of **(b)** the change in seasonal sea-level anomalies [cm] for SSP1-2.6 (relative to 1995-2014). The bars on the right indicate the 50% (horizontal white stripes), 17-83% (thick bars) and 5-95% (thin bars) percentiles of the multi-model distributions of the mean change in 2081-2100.

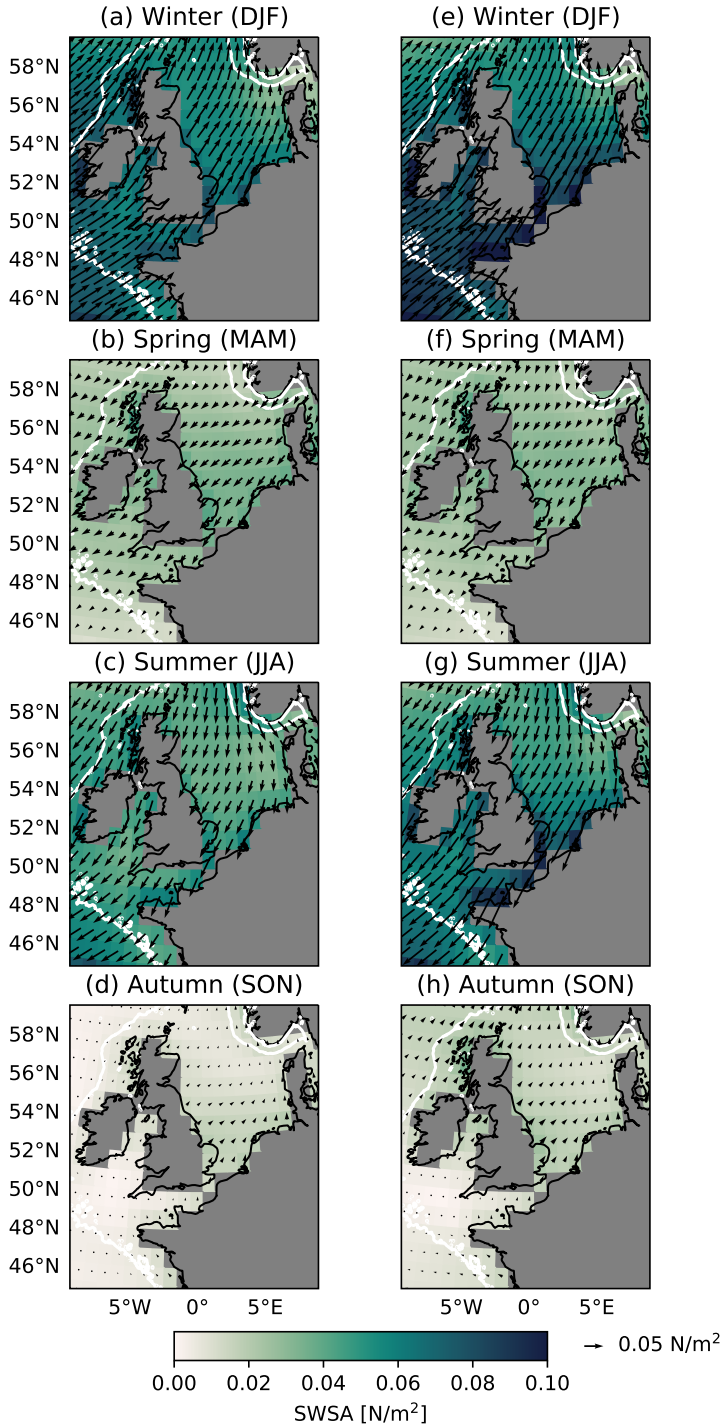


Figure S5.5: Ensemble mean (a-d) historical mean SWSA [N/m^2] in winter (DJF), spring (MAM), summer (JJA) and autumn (SON) (1995-2014); (e-h) future mean SWSA [N/m^2] in winter (DJF), spring (MAM), summer (JJA) and autumn (SON) for SSP5-8.5 (2081-2100). White contours and land masks as in Figure S5.1.

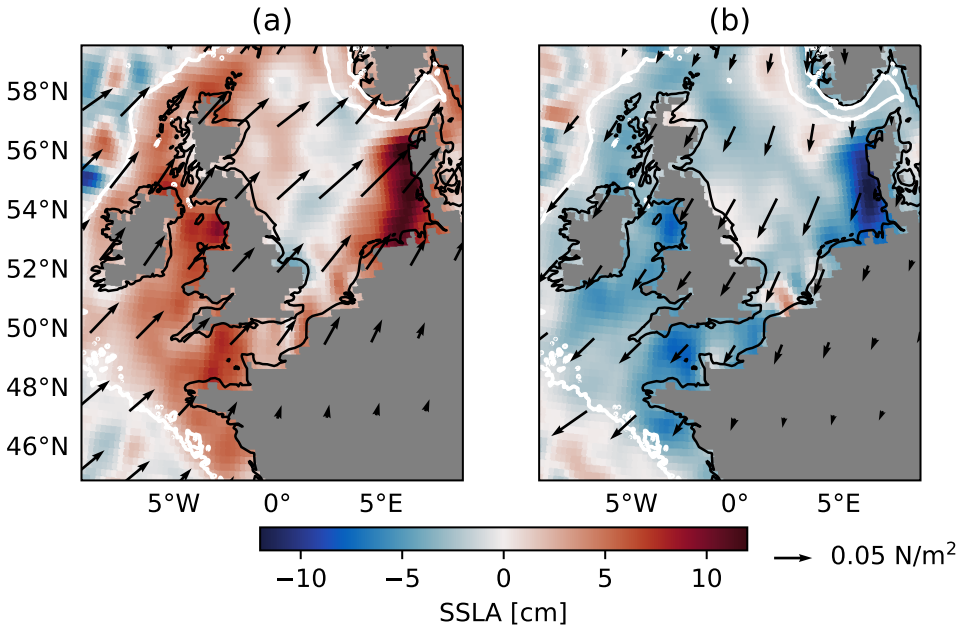


Figure S5.6: Observed sea-level anomalies [colors, cm] from AVISO ([AVISO, 2021](#)) and wind-stress anomalies [arrows, N/m²] derived from the NCEP reanalysis ([Kalnay et al., 1996](#)) in **(a)** winter 2007 and **(b)** summer 1995. As a first order approximation, the equation $\vec{\tau} = \rho_a C_D \vec{u} |\vec{u}|$ was used to convert wind speed to wind stress, with $\rho_a = 1.2 \text{ kg/m}^3$ and $C_D = 0.0015$. White contours as in Figure S5.1.

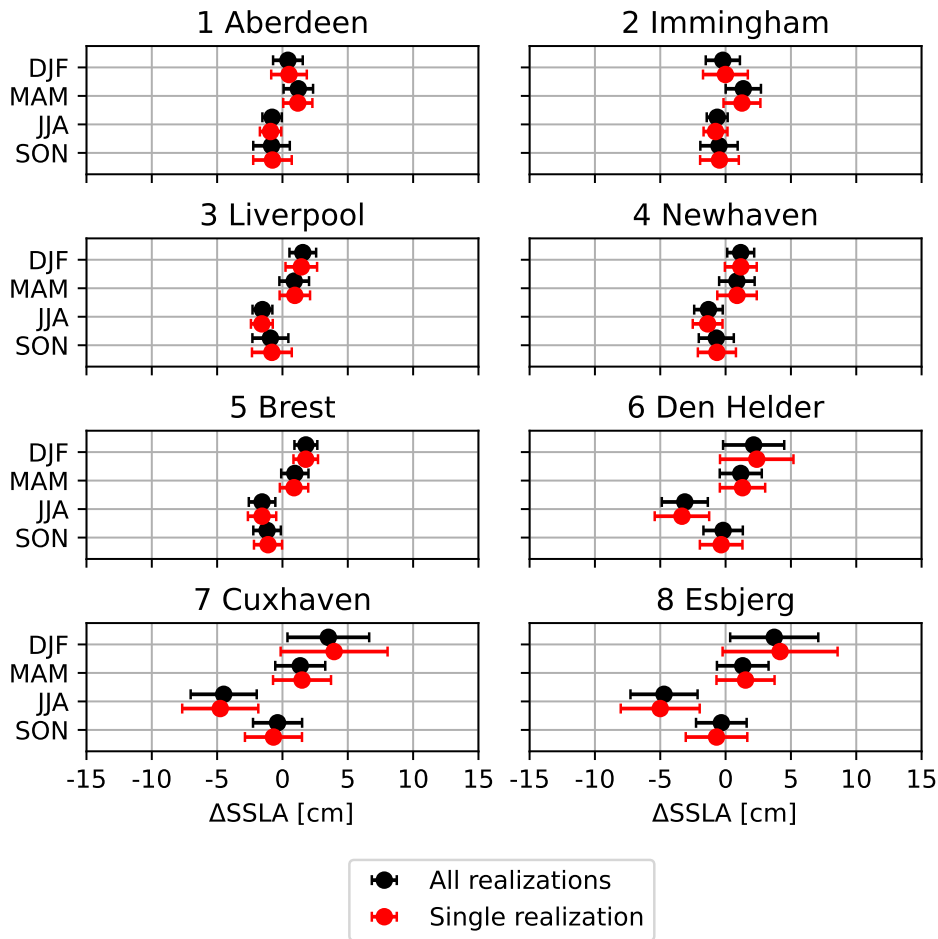


Figure S5.7: Multi-model mean (circles) and spread (whiskers, 1 standard deviation) of ΔSSLA at eight example coastal locations for a multi-model ensemble consisting of the mean of all available realizations for each model (black) and for a multi-model ensemble consisting of a single realization for each model (red).

5.6.2. Supplementary tables

Table S5.1: Overview of the CMIP6 models and realizations used for the ensemble projections. Model output on native grids ('gn') is used where possible. Otherwise, regridded ('gr') model output is used. The mean grid resolution in the NWES region was computed for the models providing the required metadata. We followed the routines prescribed for computing the 'nominal_resolution' CMIP6 attribute and used only grid cells in the region spanning from 45°N to 62°N and 15°W to 10°E. The mean grid resolution is defined as the area-weighted mean of the maximum great-circle distances between the vertices of each grid cell (see https://pcmdi.github.io/nominal_resolution/html/summary.html).

No.	Model	Realizations used for SSP5-8.5	Realizations used for SSP1-2.6	Mean ocean res. [km]	Mean atmos. res. [km]
1	ACCESS-CM2 ¹	r(1-3)i1p1f1	r(1-3)i1p1f1	99 (gn)	187 (gn)
2	ACCESS-ESM-1-5 ¹	r(1-10)i1p1f1	r(1-10)i1p1f1	99 (gn)	188 (gn)
3	CanESM5	r(1-25)i1p1f1	r(1-25)i1p1f1	100 (gn)	364 (gn)
4	CanESM5-CanOE	r(1-3)i1p1f1	r(1-3)i1p1f1	100 (gn)	364 (gn)
5	CAS-ESM2-0 ¹²	r(1,3)i1p1f1	r(1,3)i1p1f1	129 (gn)	n/a (gn)
6	CESM2 ¹	r(4,10,11)i1p1f1	r(4,10,11)i1p1f1	83 (gn)	134 (gn)
7	CESM2-WACCM ¹	r(1-3)i1p1f1	r1i1p1f1	83 (gn)	134 (gn)
8	CIESM ¹²	r1i1p1f1	r1i1p1f1	83 (gn)	n/a (gr)
9	CMCC-CM2-SR5 ²	r1i1p1f1	r1i1p1f1	100 (gn)	134 (gn)
10	CMCC-ESM2 ²	r1i1p1f1	r1i1p1f1	100 (gn)	134 (gn)
11	CNRM-CM6-1	r(1-6)i1p1f1	r(1-6)i1p1f1	100 (gn)	182 (gr)
12	CNRM-CM6-1-HR	r1i1p1f2	r1i1p1f2	25 (gn)	65 (gr)
13	CNRM-ESM2-1	r(1-5)i1p1f2	r(1-5)i1p1f2	100 (gn)	182 (gr)
14	E3SM-1-1	r1i1p1f1	-	129 (gr)	130 (gr)
15	EC-Earth3	r(1,3,4,6,11,13)i1p1f1	r(1,4,6,11,13)i1p1f1	99 (gn)	91 (gr)
16	EC-Earth3-CC	r1i1p1f1	-	99 (gn)	91 (gr)
17	EC-Earth3-Veg	r(1-3,4,6)i1p1f1	r(1-3,4,6)i1p1f1	99 (gn)	91 (gr)
18	EC-Earth3-Veg-LR	r(1-3)i1p1f1	r(1-3)i1p1f1	99 (gn)	146 (gr)
19	FIO-ESM-2-0 ¹²	r(1-3)i1p1f1	r(1-3)i1p1f1	83 (gn)	n/a (gn)
20	GFDL-ESM4	r1i1p1f1	r1i1p1f1	48 (gn)	139 (gr1)
21	GISS-E2-1-G ¹	r(1-5)i1p1f2	r(1-5)i1p1f2	138 (gn)	280 (gn)
22	HadGEM3-GC31-LL	r(1-4)i1p1f3	r1i1p1f3	100 (gn)	187 (gn)
23	HadGEM3-GC31-MM	(r1-4)i1p1f3	r1i1p1f3	25 (gn)	83 (gn)
24	INM-CM4-8	r1i1p1f1	r1i1p1f1	129 (gr1)	214 (gr1)
25	INM-CM5-0	r1i1p1f1	r1i1p1f1	129 (gr1)	214 (gr1)
26	IPSL-CM6A-LR	r(1-4,6,14)i1p1f1	r(1-4,6,14)i1p1f1	100 (gn)	219 (gr)
27	MPI-ESM1-2-HR	r(1,2)i1p1f1	r(1,2)i1p1f1	65 (gn)	122 (gn)
28	MPI-ESM1-2-LR	r(1-10)i1p1f1	r(1-10)i1p1f1	86 (gn)	243 (gn)
29	MRI-ESM2-0	r1i1p1f1	r1i1p1f1	86 (gn)	146 (gn)
30	NESM3	r(1,2)i1p1f1	r(1,2)i1p1f1	98 (gn)	n/a (gn)
31	NorESM2-LM	r1i1p1f1	r1i1p1f1	93 (gn)	268 (gn)
32	NorESM2-MM	r1i1p1f1	r1i1p1f1	93 (gn)	134 (gn)
33	UKESM1-0-LL	r(1-4,8)i1p1f2	r(1-4,8)i1p1f2	100 (gn)	187 (gn)

¹CMIP6 models with a closed English Channel on their native grid.

²CMIP6 models for which 'tauu' appears to be defined positive westward instead of eastward. For these models, 'tauu' was multiplied by -1.

6

Conclusions and Recommendations

The research presented in this thesis aims to improve our understanding of sea-level change and sea-level variability using global climate models and regional ocean models. Four different research questions were addressed, moving from the global mean (Chapter 2) to the regional scale (Chapters 3, 4 & 5). Here, I discuss to what extent these research questions have been answered (Section 6.1). Furthermore, I discuss how my research can be expanded and propose several new avenues for future work (Section 6.2).

6.1. Conclusions

6.1.1. Research question 1

How do the global mean sea-level projections based on CMIP5 and CMIP6 models differ?

In Chapter 2, global mean sea-level projections based on the latest generation of global climate models (CMIP6) were benchmarked against the projections based on the previous model generation (CMIP5). This ensures traceability to past sea-level projections. From the comparison, it can be concluded that despite its substantially higher mean climate sensitivity and surface air temperature increase, using the CMIP6 ensemble instead of the CMIP5 ensemble results in only modestly higher sea-level projections for 2100. Among others, this is caused by the thermal expansion of CMIP6, which was found not to be much larger than that of CMIP5. If this results from a lower mean ocean heat uptake and/or expansion efficiency is not yet clear. Another reason is the projected amount of glacier and ice sheet melt, which is a function of the time-integral of the surface air temperature. The CMIP5 and CMIP6 projections of the time-integrated surface air temperature differ less than their projections of the surface air temperature increase itself. Consequently, the projections of the sea-level rise by 2100 differ less than the projected rates of sea-level rise in 2100 (3-7% compared to 9-12% for the ensemble medians).

This implies that the inter-ensemble differences will affect sea-level projections for beyond 2100 (e.g., [Palmer et al., 2020](#)) more strongly.

Besides its higher mean, the climate sensitivity range of CMIP6 has a substantially higher upper end than that of CMIP5 (5.62 K compared to 4.67 K). When used individually, the CMIP6 models with the highest climate sensitivities also appear to yield the highest sea-level projections. Therefore, they can be used to explore high-end sea-level projections to a fuller extent than their CMIP5 counterparts (as recommended in Section 6.2.1). For both CMIP5 and CMIP6, the time-integrated global mean surface air temperature was found to be a good predictor of global mean sea-level rise. This implies that, while endpoint targets of cumulative emissions are useful to limit the global mean surface air temperature increase, the pathway of the emissions reduction needs to be considered to limit sea-level rise.

Since the CMIP5 and CMIP6 models were forced with different scenarios of greenhouse gas concentrations, the inter-ensemble differences found in Chapter 2 cannot be attributed solely to differences in model physics. Although the representative concentration pathways of CMIP5 and the shared socioeconomic pathways scenarios of CMIP6 were designed to yield the same approximate radiative forcing in 2100, their exact greenhouse gas concentrations differ ([Meinshausen et al., 2020](#)). To enable isolation of the differences in sea-level projections due to model physics, the CMIP5 and CMIP6 models would need to be forced with identical emissions scenarios and preferably using large ensembles to average out internal variability.

6

6.1.2. Research question 2

How does dynamical downscaling affect the simulations of ocean dynamic sea-level change of global climate models?

In Chapter 3, I investigated the ocean dynamic sea-level change on the Northwestern European Shelf. Motivated by the typical limitations of global climate models in coastal regions (see Section 1.5.3), I studied how dynamical downscaling affects the simulations of two CMIP5 models: HadGEM2-ES and MPI-ESM-LR. Dynamical downscaling was found to improve the representation of the ocean circulation and add spatial detail for both models, reflected by a better match between the historical simulations and the observations. The improvements are generally largest for HadGEM2-ES, which has a lower horizontal resolution and a less realistic land mask and bathymetry than MPI-ESM-LR. The HadGEM2-ES simulations of future sea-level change were also affected the most (up to 55% different from the original in the North Sea). Together, this shows that the added value of dynamical downscaling depends on the driving climate model. For example, whether a model resolves currents through the English Channel or not likely affects how accurately it simulates steric sea-level change in the North Sea. Also, Chapter 5 shows that CMIP6 models without an English Channel cannot accurately simulate how regional wind-stress change affects sea level, which dynamical downscaling would improve.

Only the simulations of two global climate models were dynamically downscaled. Nevertheless, since the horizontal resolution of HadGEM2-ES is typical for global

climate models, dynamical downscaling can be expected to affect the simulations of other CMIP5 and CMIP6 models to a similar extent. Ocean dynamic sea-level change is an important component of the total regional sea-level change (Fox-Kemper et al., 2021). My results therefore indicate that dynamical downscaling needs to be considered for sea-level projections for coastal regions like the North-western European Shelf, at least until the simulations of high-resolution global climate models become more widely available. In terms of computational feasibility, we are years to decades away from routinely running global climate models that well resolve small-scale coastal ocean processes (Holt et al., 2017).

6.1.3. Research question 3

What drives the interannual sea-level variability on the Northwestern European Shelf?

In Chapter 4, I used a high-resolution regional ocean model to investigate the drivers of interannual sea-level variability on the Northwestern European Shelf from 1995-2018. The atmospheric forcing that was applied to the regional model caused most of the interannual sea-level variability on the shelf, through the inverse barometer effect and the effects of wind stress and heat and freshwater fluxes. The resulting sea-level variability has a distinct spatial pattern. In contrast, varying the lateral ocean boundary conditions resulted in small and spatially highly coherent sea-level variability on the shelf. The sensitivity of these results to a different model configuration was not tested. However, similar conclusions were drawn by Tinker et al. (2020) using a different model, indicating that the results are relatively robust across the available studies and the methods used.

Furthermore, I separated the atmospherically driven sea-level variability into the contributions of the variability of wind, air pressure and heat and freshwater fluxes. Wind variability was found to be the dominant driver of interannual sea-level variability in the southern and eastern North Sea. Elsewhere on the shelf, the variability of air pressure dominates through the inverse barometer effect. Most of the spatial variation of sea-level variability on the shelf can be attributed to the wind variability. In contrast, the sea-level variability due to the variability of air pressure and buoyancy fluxes is spatially relatively smooth. The respective contributions of the different drivers of interannual sea-level variability therefore vary from location to location, which provides insight into the temporal correlation between sea level at different locations. Importantly, the model experiments indicate that the non-linear interactions between the different drivers that I studied have only a small impact on the interannual sea-level variability on the Northwestern European Shelf. This justifies reconstructing the sea-level variability in this region using multi-linear regression. The relations of the different boundary conditions with sea level that Chapter 4 exposed may also aid the prediction of seasonal to interannual sea-level variations, which is an emerging topic in the literature (Scaife et al., 2014; Miles et al., 2014; Roberts et al., 2016; Tinker et al., 2018).

6.1.4. Research question 4

How will seasonal mean sea level on the Northwestern European Shelf change in the future?

In Chapter 5, the focus shifted from annual to seasonal timescales. Potential changes in seasonal mean sea level on the Northwestern European Shelf were investigated. Based on the simulations of 33 CMIP6 models, it was found that seasonal sea-level anomalies are projected to change over the 21st century. Along the coasts on the shelf, the CMIP6 models simulate several centimeters larger sea-level rise in winter and spring than in summer and autumn. For a low emissions scenario these differences are small, but for higher emissions scenarios they increase. For example, under the SSP5-8.5 scenario, the projected dynamic sea-level rise in the eastern North Sea is 19.6 cm in winter and 11.2 cm in summer (ensemble means).

Tests with the regional model of Chapter 4 indicate that the deviations of sea-level rise in winter and summer are mainly caused by the seasonal deviations in regional wind-stress change simulated by the CMIP6 models. The projected deviations of sea-level rise in spring and autumn are likely more steric in nature, although this remains to be tested. The seasonal deviations in sea-level rise found in Chapter 5 imply that the seasonal sea-level cycle on the Northwestern European Shelf will change in amplitude and phase as a function of location and future emissions (Figure S5.2). The consequences that this may have for extreme sea levels, groundwater dynamics and ecosystems will need to be considered. While the results in Chapter 5 answer the research question above to a large extent, a caveat of the study is that the historical seasonal sea-level cycle in the CMIP6 models was not yet evaluated.

6.2. Recommendations

6.2.1. Climate sensitivity and high-end sea-level projections

In Chapter 2, I showed that individual CMIP6 models with a high effective climate sensitivity tend to yield high projections of global mean sea-level rise. Since some of these models overestimate observed surface warming and ocean heat uptake (Tokarska et al., 2020; Lyu et al., 2021) and their effective climate sensitivity falls outside assessed ranges (Sherwood et al., 2020; Forster et al., 2021), their projections may be considered less likely. However, higher climate sensitivities, outside of the assessed ranges, cannot be ruled out based on current scientific understanding (Forster et al., 2021). Based on the results of Chapter 2, I therefore propose to use the CMIP6 models with a high climate sensitivity to explore projections of global mean sea-level rise with a low probability and a high impact, which are very relevant for risk-averse stakeholders (Hinkel et al., 2019; Stammer et al., 2019). Such high-end global mean sea-level projections can be extended to the coast using dynamical downscaling.

6.2.2. Dynamical downscaling: the way forward

Chapters 3 & 5 demonstrate the value of dynamical downscaling for sea-level projections on the Northwestern European Shelf. Given the impact of dynamical downscaling, I recommend expanding the research in Chapter 3 to other coastal regions, such as the marginal seas near China and the United States. Additionally, dynamically downscaling the simulations of more global climate models will help to better understand the overall impact. I also recommend testing the sensitivity of dynamical downscaling results to methodological choices. This includes testing the influence of the regional ocean model used, the implementation of the boundary conditions, the incorporation of tides and dynamically downscaled atmospheric forcing, (the lack of) two-way coupling, and for the Northwestern European Shelf specifically, the representation of the exchange of water between the North Sea and the Baltic Sea.

To derive robust high-resolution projections, ideally the simulations of all models in the CMIP5 or CMIP6 ensemble would be dynamically downscaled. However, using the methods of Chapter 3 to downscale many century-long simulations is computationally expensive. If only the total change over a certain time window is of interest, computational cost can be reduced by dynamically downscaling only a few time slices of the full timeseries. Another approach worth exploring is dynamical downscaling using ensemble mean changes in forcing (e.g., Jin et al., 2021), although this does not readily provide estimates of multi-model uncertainty. In addition to dynamical downscaling, I recommend investigating statistical approaches to improve sea-level projections. For example, it may be possible to find robust statistical relationships between large-scale predictors and the dynamically downscaled simulations of only a subset of global climate models. These relationships can then be used to statistically downscale the simulations of other models and tested using cross-validation.

Apart from its value for regional sea-level projections, dynamical downscaling also offers a framework in which changes in mean sea level, tides, waves and surges can be simulated together in a dynamically consistent way. Such a high-resolution dataset can be used for local impact assessments, for example to assess dynamic changes in extreme sea levels or as boundary conditions to local hydrodynamic models. All in all, dynamical downscaling is a promising tool to tailor sea-level information to the needs of local stakeholders.

6.2.3. Model weighting for regional sea-level projections

Weighting the models in an ensemble based on their skill at reproducing observations and on their similarity (e.g. Knutti et al., 2017) has rarely been applied to regional sea-level projections. One of the main difficulties of model weighting is establishing weighting criteria that plausibly relate historical performance to simulated future change (see Section 1.5.2). The linkages between the historical mean atmospheric circulation and the ocean dynamic sea-level change in global climate models (Lyu et al., 2020) form a reasonable starting point. Since changes in atmospheric circulation affect the seasonal sea-level cycle on the Northwestern European

Shelf (Chapter 5), I recommend examining these linkages on seasonal timescales as well. In addition to emergent constraints, I argue that models should be weighted based on regional realism (e.g., [McSweeney et al., 2015](#)), which tests with regional models help to assess. For example, the results in Chapters 3 & 5 support giving less weight to models that do not resolve currents through the English Channel for their use for sea-level projections for the Northwestern European Shelf. Furthermore, the sea-level projections derived from models developed by the same modeling center tend to be more structurally similar. By accounting for the degree of model similarity in the ensemble, false confidence in the convergent results due to these similarities can be avoided.

6.2.4. Projecting changes in temporal sea-level variability

In Chapter 5, I found that the seasonal sea-level cycle on the Northwestern European Shelf is projected to change in addition to the annual mean sea-level change. This may be the case in other regions as well. I therefore recommend expanding Chapter 5 by studying seasonal sea-level change globally, and by studying potential changes in interannual to decadal sea-level variability. An increase in the variability around the long-term sea-level change can increase the height of extremes and lead to certain sea-level thresholds being exceeded earlier than expected, even if only temporarily. Externally forced changes in sea-level variability are therefore an important topic for future research. The roles that the variability of land-water storage and ice mass change may play in addition to the atmospheric and oceanic drivers of sea-level variability (Chapters 4 & 5) need to be considered in the process. The potential predictability of sea-level variability on shorter timescales is a related topic, which given its societal relevance, also deserves further investigation. It may be possible to use dynamical downscaling to improve the skill of global seasonal forecasting systems on the Northwestern European Shelf ([Tinker et al., 2018](#)) in a similar way to improving centennial sea-level projections (Chapter 3).

6.2.5. Final remarks

All in all, these recommendations make clear that there is still a lot to learn about sea-level change and its projections. However, mitigation and adaptation planning cannot wait until all existing uncertainties are resolved. Climate change is already underway, and we need adaptative plans that can be adjusted as new information about sea-level change comes in. This thesis has highlighted that regional ocean models are valuable tools to provide that information. Embedding regional modeling in sea-level science will help to improve the simulations of global climate models, to understand the mechanisms behind sea-level change and variability and to provide stakeholders with the local information they need.

Bibliography

- Amante, C. and Eakins, B. 1 Arc-Minute Global Relief Model: Procedures, Data Sources and Analysis. *NOAA Technical Memorandum NESDIS NGDC-24. National Geophysical Data Center, NOAA.*, 2009. [10.7289/V5C8276M](https://doi.org/10.7289/V5C8276M).
- Andersen, O. B. and Scharroo, R. Range and Geophysical Corrections in Coastal Regions: And Implications for Mean Sea Surface Determination. In Vignudelli, S., Kostianoy, A., Cipollini, P., and Benveniste, J., editors, *Coastal Altimetry*. Springer, Berlin, Heidelberg, 2011. ISBN 9783642127960.
- Andrews, T., Gregory, J. M., Webb, M. J., and Taylor, K. E. Forcing, feedbacks and climate sensitivity in CMIP5 coupled atmosphere-ocean climate models. *Geophysical Research Letters*, 39:1–7, 2012. [10.1029/2012GL051607](https://doi.org/10.1029/2012GL051607).
- Arns, A., Dangendorf, S., Jensen, J., Talke, S., Bender, J., and Pattiaratchi, C. Sea-level rise induced amplification of coastal protection design heights. *Scientific Reports*, 7:1–9, 2017. [10.1038/srep40171](https://doi.org/10.1038/srep40171).
- AVISO. The Ssalto/Duacs altimeter products were produced and distributed by the Copernicus Marine and Environment Monitoring Service (CMEMS), 2019. URL <https://doi.org/10.48670/moi-00148>. Accessed on: 30-03-2019.
- AVISO. The Ssalto/Duacs altimeter products were produced and distributed by the Copernicus Marine and Environment Monitoring Service (CMEMS), 2021. URL <https://doi.org/10.48670/moi-00148>. Accessed on: 01-03-2021.
- Baart, F., Rongen, G., Hijma, M., Kooi, H., de Winter, R., and Nicolai, R. Zeespiegelmonitor 2018, 2018.
- Balke, T., Stock, M., Jensen, K., Bouma, T., and Kleyer, M. A global analysis of the seaward salt marsh extent: The importance of tidal range. *Water Resources Research*, 52:3775–3786, 2016. [10.1002/2015WR018318](https://doi.org/10.1002/2015WR018318).
- Bamber, J. L. and Aspinall, W. P. An expert judgement assessment of future sea level rise from the ice sheets. *Nature Climate Change*, 3:424–427, 1 2013. [10.1038/nclimate1778](https://doi.org/10.1038/nclimate1778).
- Bamber, J. L., Oppenheimer, M., Kopp, R. E., Aspinall, W. P., and Cooke, R. M. Ice sheet contributions to future sea-level rise from structured expert judgment. *PNAS*, 116, 2019. [10.1073/pnas.1817205116](https://doi.org/10.1073/pnas.1817205116).
- Beckmann, A. and Haidvogel, D. Numerical Simulation of Flow around a Tall Isolated Seamount. Part 1: Problem Formulation and Model Accuracy. *Journal of Physical Oceanography*, 23:1736–1753, 1993. [10.1175/1520-0485\(1993\)023<1736:NSOFAA>2.0.CO;2](https://doi.org/10.1175/1520-0485(1993)023<1736:NSOFAA>2.0.CO;2).
- Bilbao, R. A. F., Gregory, J. M., and Bouttes, N. Analysis of the regional pattern of sea level change due to ocean dynamics and density change for 1993-2099 in observations and CMIP5 AOGCM's. *Climate Dynamics*, 2015. [10.1007/s00382-015-2499-z](https://doi.org/10.1007/s00382-015-2499-z).
- Birol Kara, A., Wallcraft, A. J., and Hurlburt, H. A Correction for Land Contamination of Atmospheric Variables near Land – Sea Boundaries. *Journal of Physical Oceanography*, 37:803–818, 2007. [10.1175/JPO2984.1](https://doi.org/10.1175/JPO2984.1).
- Bjorndal, J., Storelvmo, T., and Carlsen, T. Equilibrium climate sensitivity above 5C plausible due to state-dependent cloud feedback. *Nature Geoscience*, 13:718–721, 2020. [10.1038/s41561-020-00649-1](https://doi.org/10.1038/s41561-020-00649-1).

- Bodas-Salcedo, A., Mulcahy, J., Andrews, T., Williams, K., Ringer, M., Field, P., and Elsaesser, G. Strong Dependence of Atmospheric Feedbacks on Mixed-Phase Microphysics and Aerosol-Cloud Interactions in HadGEM3. *Journal of Advances in Modeling Earth Systems*, 11:1735–1758, 2019. [10.1029/2019MS001688](https://doi.org/10.1029/2019MS001688).
- Brain, M. J. Past, Present and Future Perspectives of Sediment Compaction as a Driver of Relative Sea Level and Coastal Change. *Current Climate Change Reports*, 2:75–85, 2016. [10.1007/s40641-016-0038-6](https://doi.org/10.1007/s40641-016-0038-6).
- Brunner, L., Pendergrass, A. G., Lehner, F., Merrifield, A. L., Lorenz, R., and Knutti, R. Reduced global warming from CMIP6 projections when weighting models by performance and independence. *Earth System Dynamics*, 11:995–1012, 2020. [10.5194/esd-11-995-2020](https://doi.org/10.5194/esd-11-995-2020).
- Calafat, F. M. and Chambers, D. P. Quantifying recent acceleration in sea level unrelated to internal climate variability. *Geophys. Res. Lett.*, 40:3661–3666, 2013. [10.1002/grl.50731](https://doi.org/10.1002/grl.50731).
- Calafat, F. M., Chambers, D. P., and Tsimplis, M. N. Mechanisms of decadal sea level variability in the eastern North Atlantic and the Mediterranean Sea. *Journal of Geophysical Research: Oceans*, 117: 1–14, 2012. [10.1029/2012JC008285](https://doi.org/10.1029/2012JC008285).
- Calafat, F. M., Chambers, D. P., and Tsimplis, M. N. Inter-annual to decadal sea-level variability in the coastal zones of the Norwegian and Siberian Seas: The role of atmospheric forcing. *Journal of Geophysical Research: Oceans*, 118:1287–1301, 2013. [10.1002/jgrc.20106](https://doi.org/10.1002/jgrc.20106).
- Cannaby, H., Palmer, M. D., Howard, T., Brichenon, L., Calvert, D., Krijnen, J., Wood, R., Tinker, J., Bunney, C., Harle, J., Saulter, A., Neill, C. O., Bellingham, C., and Lowe, J. Projected sea level rise and changes in extreme storm surge and wave events during the 21st century in the region of Singapore. *Ocean Science*, 12:613–632, 2016. [10.5194/os-12-613-2016](https://doi.org/10.5194/os-12-613-2016).
- Cao, A., Esteban, M., Paolo, V., Valenzuela, B., Onuki, M., Takagi, H., Thao, N. D., and Tsuchiya, N. Future of Asian Deltaic Megacities under sea level rise and land subsidence: current adaptation pathways for Tokyo, Jakarta, Manila, and Ho Chi Minh City. *Current Opinion in Environmental Sustainability*, 50: 87–97, 2021. [10.1016/j.cosust.2021.02.010](https://doi.org/10.1016/j.cosust.2021.02.010).
- Caron, L., Ivins, E. R., Larour, E., Adhikari, S., Nilsson, J., and Blewitt, G. GIA Model Statistics for GRACE Hydrology, Cryosphere, and Ocean Science. *Geophysical Research Letters*, 45:2203–2212, 3 2018. [10.1002/2017GL076644](https://doi.org/10.1002/2017GL076644).
- CDS. ERA5 hourly data on single levels from 1979 to present, 2019. URL <https://doi.org/10.24381/cds.adbb2d47>. Accessed on: 03-10-2019.
- Chafik, L., Nilsen, J., Dangendorf, S., Reverdin, G., and Frederikse, T. North Atlantic Ocean Circulation and Decadal Sea Level Change During the Altimetry Era. *Scientific Reports*, 9:1041, 2019. [10.1038/s41598-018-37603-6](https://doi.org/10.1038/s41598-018-37603-6).
- Chapman, D. Numerical Treatment of Cross-Shelf Open Boundaries in a Barotropic Coastal Ocean Model. *Journal of Physical Oceanography*, 15:1060–1074, 1985. [10.1175/1520-0485\(1985\)015<1060:NTOCSO>2.0.CO;2](https://doi.org/10.1175/1520-0485(1985)015<1060:NTOCSO>2.0.CO;2).
- Chen, X., Dangendorf, S., Narayan, N., O'Driscoll, K., Tsimplis, M. N., Su, J., Mayer, B., and Pohlmann, T. On sea level change in the North Sea influenced by the North Atlantic Oscillation: Local and remote steric effects. *Estuarine, Coastal and Shelf Science*, 151:186–195, 2014. [10.1016/j.ecss.2014.10.009](https://doi.org/10.1016/j.ecss.2014.10.009).
- Church, J. A., Clark, P. U., Cazenave, A., Gregory, J. M., Jevrejeva, S., Levermann, A., Merrifield, M. A., Milne, G. A., Nerem, R. S., Nunn, P. D., Payne, A. J., Pfeffer, W. T., Stammer, D., and Unnikrishnan, A. S. Sea Level Change. In Stocker, T. F., Qin, D., Plattner, G.-K., Tignor, M., Allen, S. K., Boschung, J., Nauels, A., Xia, Y., Bex, V., and Midgley, P. M., editors, *Climate Change 2013: The Physical Science Basis. Contribution of Working Group I to the Fifth Assessment Report of the Intergovernmental Panel on Climate Change*. Cambridge University Press, Cambridge, United Kingdom and New York, NY, USA., 2013.

- Cipollini, P., Benveniste, J., Birol, F., Joana, M., Obligis, E., Passaro, M., Strub, P. T., Valladeau, G., Vignudelli, S., and Wilkin, J. Satellite Altimetry in Coastal Regions. In Stammer, D. and Cazenave, A., editors, *Satellite Altimetry over Oceans and Land Surfaces*, 2017. ISBN 9781315151779. [10.1201/9781315151779](https://doi.org/10.1201/9781315151779).
- CNES. MDT CNES CLS18 was produced by CLS and distributed by Aviso+, with support from Cnes., 2019. URL <https://www.aviso.altimetry.fr/en/data/products/auxiliary-products/mdt/mdt-global-cnes-cls18.html>. Accessed on: 01-02-2019.
- Collins, M., Knutti, R., Arblaster, J., Dufresne, J.-L., Fichet, T., Friedlingstein, P., Gao, X., Gutowski, W. J., Johns, T., Krinner, G., Shongwe, M., Tebaldi, C., Weaver, A. J., and Wehner, M. Long-term Climate Change: Projections, Commitments and Irreversibility. In Stocker, T. F., Qin, D., Plattner, G.-K., Tignor, M., Allen, S. K., Boschung, J., Nauels, A., Xia, Y., Bex, V., and Midgley, P. M., editors, *Climate Change 2013: The Physical Science Basis. Contribution of Working Group I to the Fifth Assessment Report of the Intergovernmental Panel on Climate Change*. Cambridge University Press, Cambridge, United Kingdom and New York, NY, USA, 2013.
- Collins, W. J., Bellouin, N., Gedney, N., Halloran, P., Hinton, T., Hughes, J., and Jones, C. D. Development and evaluation of an Earth-System model – HadGEM2. *Geoscientific Model Development*, 4:1051–1075, 2011. [10.5194/gmd-4-1051-2011](https://doi.org/10.5194/gmd-4-1051-2011).
- Collins, W. J., Frame, D. J., Fuglestad, J. S., and Shine, K. Stable climate metrics for emissions of short and long-lived species—combining steps and pulses. *Environmental Research Letters*, 15, 2020. [10.1088/1748-9326/ab6039](https://doi.org/10.1088/1748-9326/ab6039).
- Dai, A. Dai and Trenberth Global River Flow and Continental Discharge Dataset, 2017. URL <https://doi.org/10.5065/D6V69H1T>. Accessed on: 24-10-2019.
- Dangendorf, S., Wahl, T., Hein, H., Jensen, J., Mai, S., and Muddersbach, C. Mean Sea Level Variability and Influence of the North Atlantic Oscillation on Long-Term Trends in the German Bight. *Water*, 4: 170–195, 2012. [10.3390/w4010170](https://doi.org/10.3390/w4010170).
- Dangendorf, S., Calafat, F. M., Arns, A., Wahl, T., Haigh, I. D., and Jensen, J. Mean sea level variability in the North Sea: Processes and implications. *Journal of Geophysical Research : Oceans*, 119:6820–6841, 2014a. [10.1002/2014JC009901](https://doi.org/10.1002/2014JC009901).
- Dangendorf, S., Muddersbach, C., Wahl, T., and Jensen, J. Characteristics of intra-, inter-annual and decadal sea-level variability and the role of meteorological forcing: the long record of Cuxhaven. *Ocean Dynamics*, 63:209–224, 2013a. [10.1007/s10236-013-0598-0](https://doi.org/10.1007/s10236-013-0598-0).
- Dangendorf, S., Wahl, T., Muddersbach, C., and Jensen, J. The Seasonal Mean Sea Level Cycle in the Southeastern North Sea. *Journal of Coastal Research*, 65:1915–1920, 2013b. [10.2112/SI65-324.1](https://doi.org/10.2112/SI65-324.1).
- Dangendorf, S., Wahl, T., Nilsson, E., Klein, B., and Jensen, J. A new atmospheric proxy for sea level variability in the southeastern North Sea: Observations and future ensemble projections. *Climate Dynamics*, 43:447–467, 2014b. [10.1007/s00382-013-1932-4](https://doi.org/10.1007/s00382-013-1932-4).
- Dangendorf, S., Marcos, M., Wöppelmann, G., Conrad, C. P., Frederikse, T., and Riva, R. Reassessment of 20th century global mean sea level rise. *PNAS*, 114:5946–5951, 2017. [10.1073/pnas.1616007114](https://doi.org/10.1073/pnas.1616007114).
- DeConto, R. M. and Pollard, D. Contribution of Antarctica to past and future sea-level rise. *Nature*, 531: 591–597, 2016. [10.1038/nature17145](https://doi.org/10.1038/nature17145).
- DeConto, R. M., Pollard, D., Alley, R. B., Velicogna, I., Gasson, E., Gomez, N., Sadai, S., Condron, A., Gilford, D. M., Ashe, E. L., Kopp, R. E., Li, D., and Dutton, A. The Paris Climate Agreement and future sea-level rise from Antarctica. *Nature*, 593:83–89, 2021. [10.1038/s41586-021-03427-0](https://doi.org/10.1038/s41586-021-03427-0).

- Dee, D. P., Uppala, S. M., Simmons, A. J., Berrisford, P., Poli, P., Kobayashi, S., Andrae, U., Balmaseda, M. A., Balsamo, G., Bauer, P., Bechtold, P., Beljaars, A. C. M., Berg, L. V. D., Bidlot, J., Bormann, N., Delsol, C., Dragani, R., Fuentes, M., Geer, A. J., and Dee, D. P. The ERA-Interim reanalysis: configuration and performance of the data assimilation system. *Quarterly Journal of the Royal Meteorological Society*, pages 553–597, 2011. [10.1002/qj.828](https://doi.org/10.1002/qj.828).
- Deng, X., Featherstone, W., Hwang, C., and Berry, P. Estimation of Contamination of ERS-2 and POSEIDON Satellite Radar Altimetry Close to the Coasts of Australia. *Marine Geodesy*, 25:249–271, 2002. [10.1080/01490410214990](https://doi.org/10.1080/01490410214990).
- Donlon, C. J., Martin, M., Stark, J., Roberts-jones, J., Fiedler, E., and Wimmer, W. The Operational Sea Surface Temperature and Sea Ice Analysis (OSTIA) system. *Remote Sensing of Environment*, 116: 140–158, 2012. [10.1016/j.rse.2010.10.017](https://doi.org/10.1016/j.rse.2010.10.017).
- Edwards, T. L., Brandon, M. A., Durand, G., Edwards, N. R., Golledge, N. R., Holden, P. B., Nias, I. J., Payne, A. J., Ritz, C., and Wernecke, A. Revisiting Antarctic ice loss due to marine ice-cliff instability. *Nature*, 566:58–64, 2019. [10.1038/s41586-019-0901-4](https://doi.org/10.1038/s41586-019-0901-4).
- Ekman, M. Secular Change of the Seasonal Sea Level Variation in the Baltic Sea and Secular Change of the Winter Climate. *Geophysica*, 34:131–140, 1998.
- Escudier, P., Couhert, A., Mercier, F., Mallet, A., Thibaut, P., Tran, N., Amarouche, L., Picard, B., Carrere, L., Dibarboure, G., Ablain, M., Richard, J., Steunou, N., Dubois, P., Rio, M.-H., and Dorandeu, J. Satellite Radar Altimetry - Principle, Accuracy, and Precision. In Stammer, D. and Cazenave, A., editors, *Satellite Altimetry over Oceans and Land Surfaces*, page 617. Taylor and Francis Group, 2017. ISBN 13:978-1-4987-4345-7. [10.1201/9781315151779](https://doi.org/10.1201/9781315151779).
- Eyring, V., Bony, S., Meehl, G. A., Senior, C. A., Stevens, B., Stouffer, R. J., Taylor, K. E., Dynamique, D. M., Pierre, I., Laplace, S., and Ipsl, L. M. D. Overview of the Coupled Model Intercomparison Project Phase 6 (CMIP6) experimental design and organization. *Geoscientific Model Development*, 9: 1937–1958, 2016. [10.5194/gmd-9-1937-2016](https://doi.org/10.5194/gmd-9-1937-2016).
- Eyring, V., Cox, P. M., Flato, G. M., Gleckler, P. J., Abramowitz, G., Caldwell, P., Collins, W. D., Gier, B. K., Hall, A. D., Hoffman, F. M., Hurtt, G. C., Jahn, A., Jones, C. D., Klein, S. A., Krasting, J. P., Kwiatkowski, L., Lorenz, R., Maloney, E., Meehl, G. A., Pendergrass, A. G., Pincus, R., Ruane, A. C., Russell, J. L., Sanderson, B. M., Santer, B. D., Sherwood, S. C., Simpson, I. R., Stouffer, R. J., and Williamson, M. S. Taking climate model evaluation to the next level. *Nature Climate Change*, 9:102–110, 2019. [10.1038/s41558-018-0355-y](https://doi.org/10.1038/s41558-018-0355-y).
- Eyring, V., Bock, L., Lauer, A., Righi, M., Schlund, M., Andela, B., Arnone, E., Bellprat, O., Brötz, B., philippe Caron, L., Carvalhais, N., Cionni, I., Cortesi, N., Crezee, B., Davin, E. L., Davini, P., Debeire, K., Mora, L. D., Deser, C., Docquier, D., Earnshaw, P., Ehbrecht, C., Gier, B., Gonzalez-Reviriego, N., Goodman, P., Hagemann, S., Hardiman, S., Hassles, B., Hunter, A., Kadow, C., Kindermann, S., Koirala, S., Koldunov, N., Lejeune, Q., Lembo, V., Lovato, T., Lucarini, V., Massonnet, F., Muller, B., Pandde, A., Perez-Zanon, N., Phillips, A., Predoi, V., Russell, J., Sellar, A., Serva, F., Stacke, T., Swaminathan, R., Torralba, V., Vegas-Regidor, J., Hardenberg, J. V., Weigel, K., and Zimmerman, K. Earth System Model Evaluation Tool (ESMValTool) v2. 0 – an extended set of large-scale diagnostics for quasi-operational and comprehensive evaluation of Earth system models in CMIP. *Geoscientific Model Development*, 13:3383–3438, 2020. [10.5194/gmd-13-3383-2020](https://doi.org/10.5194/gmd-13-3383-2020).
- Fairall, C. W., Bradley, E. F., Rogers, D. P., Edson, J. B., and Young, G. S. Bulk parameterization of air-sea fluxes for Tropical Ocean-Global Atmosphere Coupled-Ocean Atmosphere Response Experiment. *Journal of Geophysical Research*, 101:3747–3764, 1996. [10.1029/95JC03205](https://doi.org/10.1029/95JC03205).
- Farrell, W. E. and Clark, J. A. On Postglacial Sea Level. *Geophysical Journal of the Royal Astronomical Society*, 46:647–667, 1976. [10.1111/j.1365-246X.1976.tb01252.x](https://doi.org/10.1111/j.1365-246X.1976.tb01252.x).
- Fasullo, J. T. and Nerem, R. S. Altimeter-era emergence of the patterns of forced sea-level rise in climate models and implications for the future. *Proceedings of the National Academy of Sciences*, 115:12944–12949, 12 2018. [10.1073/pnas.1813233115](https://doi.org/10.1073/pnas.1813233115).

- Fernandez, E. and Lellouche, J. Product User Manual: For the GLOBAL Ocean Sea Physical Reanalysis product GLOBAL_REANALYSIS_PHY_001_030, 2018. URL <https://doi.org/10.48670/moi-00021>. Accessed on: 01-11-2019.
- Flather, R. A tidal model for the northwest European shelf. *Mem. Soc. R. Sci Liege*, 10:141–164, 1976.
- Forster, P., Storelvmo, T., Armour, K., Collins, W., Dufresne, J.-L., Frame, D., Lunt, D., Mauritsen, T., Palmer, M., Watanabe, M., Wild, M., and Zhang, H. The Earth's Energy Budget, Climate Feedbacks, and Climate Sensitivity. In Masson-Delmotte, V., Zhai, P., Pirani, A., and Connors, S., editors, *Climate Change 2021: The Physical Science Basis. Contribution of Working Group I to the Sixth Assessment Report of the Intergovernmental Panel on Climate Change*. Cambridge University Press, Cambridge, United Kingdom and New York, NU, USA, 2021.
- Forster, P. M., Andrews, T., Good, P., Gregory, J. M., Jackson, L. S., and Zelinka, M. Evaluating adjusted forcing and model spread for historical and future scenarios in the CMIP5 generation of climate models. *Journal of Geophysical Research Atmospheres*, 118:1139–1150, 2013. [10.1002/jgrd.50174](https://doi.org/10.1002/jgrd.50174).
- Forster, P., Maycock, A., McKenna, C., and Smith, C. Latest climate models confirm need for urgent mitigation. *Nature Climate Change*, 19:7–10, 2020. [10.1038/s41558-019-0660-0](https://doi.org/10.1038/s41558-019-0660-0).
- Fox-Kemper, B., Hewitt, H., Xiao, C., Aðalgeirsdóttir, Drijfhout, G., Edwards, T., Golledge, N., Hemer, M., Kopp, R. E., Krinner, G., Mix, A., Notz, D., Nowicki, S., Nurhati, I. S., Ruiz, L., Sallée, J.-B., Slangen, A. B. A., and Yu, Y. Chapter 9: Ocean, Cryosphere and Sea Level Change. In Masson-Delmotte, V., Zhai, P., Pirani, A., Connors, S., Péan, C., Berger, S., Caud, N., Chen, Y., Goldfarb, L., Gomis, M., Huang, M., Leitzell, K., Lonnoy, E., Matthews, J., Maycock, T., Waterfield, T., Yelekçi, O., Yu, R., and Zhou, B., editors, *Climate Change 2021: The Physical Science Basis. Contribution of Working Group I to the Sixth Assessment Report 13 of the Intergovernmental Panel on Climate Change*. Cambridge University Press, Cambridge, United Kingdom and New York, NU, USA, 2021.
- Frederikse, T. and Gerkema, T. Multi-decadal variability in seasonal mean sea level along the North Sea coast. *Ocean Science*, 14:1491–1501, 2018. <https://doi.org/10.5194/os-14-1491-2018>.
- Frederikse, T., Riva, R., Kleinherenbrink, M., Wada, Y., van den Broeke, M., and Marzeion, B. Closing the sea level budget on a regional scale: Trends and variability on the Northwestern European continental shelf. *Geophysical Research Letters*, 43:10,864–10,872, 2016. [10.1002/2016GL070750](https://doi.org/10.1002/2016GL070750).
- Frederikse, T., Jevrejeva, S., Riva, R. E., and Dangendorf, S. A Consistent Sea-Level Reconstruction and Its Budget on Basin and Global Scales over 1958–2014. *Journal of Climate*, 31:1267–1280, 2018. [10.1175/JCLI-D-17-0502.1](https://doi.org/10.1175/JCLI-D-17-0502.1).
- Friocourt, Y., Drijfhout, S., and Blanke, B. On the Dynamics of the Slope Current System along the West European Margin. Part I: Analytical Calculations and Numerical Simulations with Steady-State Forcing. *Journal of Physical Oceanography*, 38:2597–2618, 2008. [10.1175/2008JPO3744.1](https://doi.org/10.1175/2008JPO3744.1).
- Fu, L., Christensen, E., Yamarone, C., Lefebvre, M., Mnard, Y., Dorrer, M., and Escudier, P. TOPEX/POSEIDON mission overview. *JGR Oceans*, 99:369–381, 1994. [doi:10.1029/94JC01761](https://doi.org/10.1029/94JC01761).
- Fukumori, I., Wang, O., Llovel, W., Fenty, I., and Forget, G. A near-uniform fluctuation of ocean bottom pressure and sea level across the deep ocean basins of the Arctic Ocean and the Nordic Seas. *Progress in Oceanography*, 134:152–172, 2015. [10.1016/j.pocean.2015.01.013](https://doi.org/10.1016/j.pocean.2015.01.013).
- Garner, A. J., Weiss, J. L., Parris, A., Kopp, R. E., Overpeck, J. T., and Horton, B. P. Evolution of 21st Century Sea Level Rise Projections. *Earth's Future*, pages 1603–1615, 2018. [10.1029/2018EF000991](https://doi.org/10.1029/2018EF000991).
- Geoffroy, O. and Saint-Martin, D. Transient Climate Response in a Two-Layer Energy-Balance Model. Part I: Analytical Solution and Parameter Calibration Using CMIP5 AOGCM Experiments. *Journal of Climate*, 26:1841–1857, 2013. [10.1175/JCLI-D-12-00195.1](https://doi.org/10.1175/JCLI-D-12-00195.1).
- Gerkema, T. and Duran-Matute, M. Interannual variability of mean sea level and its sensitivity to wind climate in an inter-tidal basin. *Earth System Dynamics*, 8:1223–1235, 2017. [10.5194/esd-8-1223-2017](https://doi.org/10.5194/esd-8-1223-2017).

- Gettelmann, A., Hannay, C., Bacmeister, J. T., Neale, R. B., Pendergrass, A. G., Danabasoglu, G., Lamarque, J., Fasullo, J., Baily, D., Lawrence, D., and Mills, M. High Climate Sensitivity in the Community Earth System Model Version 2 (CESM2). *Geophysical Research Letters*, 2:8329–8337, 2019. [10.1029/2019GL083978](https://doi.org/10.1029/2019GL083978).
- Gill, A. *Atmosphere-ocean dynamics*. Academic Press, 1 edition, 1983. ISBN 9788578110796. [10.1016/0141-1187\(83\)90039-1](https://doi.org/10.1016/0141-1187(83)90039-1).
- Giorgetta, M. A., Jungclaus, J., Reick, C. H., Legutke, S., Bo, M., Brovkin, V., Crueger, T., Esch, M., Fieg, K., Glushak, K., Gayler, V., Haak, H., Dieter Hollweg, H., Ilyina, T., Kinne, S., Kornblueh, L., Matei, D., Mauritsen, T., Mikolajewicz, U., Mueller, W., Notz, D., Pithan, F., Raddatz, T., Rast, S., Redler, R., Roeckner, E., Schmidt, H., Schnur, R., Segschneider, J., Six, K. D., Stockhause, M., Timmreck, C., Widmann, H., h Wiens, K., and Claussen, M. Climate and carbon cycle changes from 1850 to 2100 in MPI-ESM simulations for the Coupled Model Intercomparison Project phase 5. *Journal of Advances in Modeling Earth Systems*, 5:572–597, 2013. [10.1002/jame.20038](https://doi.org/10.1002/jame.20038).
- Giorgi, F., Jones, C., and Asrar, G. R. Addressing climate information needs at the regional level: the CORDEX framework. *WMO Bulletin*, 58, 2009.
- Goelzer, H., Nowicki, S., Payne, A., Larour, E., Seroussi, H., Lipscomb, W. H., Gregory, J., Abe-Ouchi, A., Shepherd, A., Simon, E., Agosta, C., Alexander, P., Aschwanden, A., Barthel, A., Calov, R., Chambers, C., Choi, Y., Cuzzzone, J., Dumas, C., Edwards, T., Felikson, D., Fettweis, X., Golledge, N. R., Greve, R., Humbert, A., Huybrechts, P., Clec'h, S. L., Lee, V., Leguy, G., Little, C., Lowry, D., Morlighem, M., Nias, I., Quiquet, A., Rückamp, M., Schlegel, N. J., Slater, D. A., Smith, R., Straneo, F., Tarasov, L., van de Wal, R., and van den Broeke, M. The future sea-level contribution of the Greenland ice sheet: a multi-model ensemble study of ISMIP6. *Cryosphere*, 14:3071–3096, 9 2020. [10.5194/tc-14-3071-2020](https://doi.org/10.5194/tc-14-3071-2020).
- Golledge, N. R., Keller, E. D., Gomez, N., Naughten, K. A., Bernales, J., Trusel, L. D., and Edwards, T. L. Global environmental consequences of twenty-first-century ice-sheet melt. *Nature*, 566:65–72, 2019. [10.1038/s41586-019-0889-9](https://doi.org/10.1038/s41586-019-0889-9).
- Gonneea, M. E., Mulligan, A. E., and Charette, M. A. Climate-driven sea level anomalies modulate coastal groundwater dynamics and discharge. *Geophysical Research Letters*, 40:2701–2706, 2013. [10.1002/grl.50192](https://doi.org/10.1002/grl.50192).
- Good, P., Gregory, J. M., and Lowe, J. A. A step-response simple climate model to reconstruct and interpret AOGCM projections. *Geophysical Research Letters*, 38:1–5, 2011. [10.1029/2010GL045208](https://doi.org/10.1029/2010GL045208).
- Good, S. A., Martin, M. J., and Rayner, N. A. EN4: Quality controlled ocean temperature and salinity profiles and monthly objective analyses with uncertainty estimates. *Journal of Geophysical Research: Oceans*, 118:6704–6716, 2013. [10.1002/2013JC009067](https://doi.org/10.1002/2013JC009067).
- Graham, J. A., Dea, E. O., Holt, J., Polton, J., Hewitt, H. T., Furner, R., Guihou, K., Brereton, A., Arnold, A., Wakelin, S., Manuel, J., Sanchez, C., and Adame, C. G. M. AMM15: a new high-resolution NEMO configuration for operational simulation of the European north-west shelf. *Geoscientific Model Development Discussions*, 11:1–23, 2018. [10.5194/gmd-11-681-2018](https://doi.org/10.5194/gmd-11-681-2018).
- Greatbatch, J. A note on the representation of steric sea level in models that conserve volume rather than mass. *Journal of Geophysical Research: Oceans*, 99:767–771, 1994. [10.1029/94JC00847](https://doi.org/10.1029/94JC00847).
- Gregory, J. M. and Mitchell, J. F. B. The climate response to CO₂ of the Hadley Centre coupled AOGCM with and without flux adjustment. *Geophysical Research Letters*, 24:1943–1946, 1997. [10.1029/97GL01930](https://doi.org/10.1029/97GL01930).
- Gregory, J. M., Banks, H. T., Stott, P. A., Lowe, J. A., and Palmer, M. D. Simulated and observed decadal variability in ocean heat content. *Geophys. Res. Lett.*, 31, 2004. [10.1029/2004GL020258](https://doi.org/10.1029/2004GL020258).
- Gregory, J. M., Andrews, T., and Good, P. The inconstancy of the transient climate response parameter under increasing CO₂. *Phil. Trans. R. Soc. A*, 373, 2015. [10.1098/rsta.2014.0417](https://doi.org/10.1098/rsta.2014.0417).

- Gregory, J. and Lowe, J. Predictions of global and regional sea-level rise using AOGCMs with and without flux adjustment. *Geophysical Research Letters*, 27:3069–3072, 2000. [10.1029/1999GL011228](https://doi.org/10.1029/1999GL011228).
- Gregory, J. M., Griffies, S. M., Hughes, C. W., Lowe, J. A., Church, J. A., Fukimori, I., Gomez, N., Kopp, R., Landerer, F., Cozannet, G. L., Ponte, R., Stammer, D., Tamisiea, M. E., and van de Wal, R. Concepts and Terminology for Sea Level: Mean Variability and Change, Both Local and Global. *Survey in Geophysics*, 2019. [10.1007/s10712-019-09525-z](https://doi.org/10.1007/s10712-019-09525-z).
- Griffies, S. M. and Greatbatch, R. J. Physical processes that impact the evolution of global mean sea level in ocean climate models. *Ocean Modelling*, 51:37–72, 2012. [10.1016/j.ocemod.2012.04.003](https://doi.org/10.1016/j.ocemod.2012.04.003).
- Griffies, S. M., Yin, J., Durack, P. J., Goddard, P., Bates, S. C., Behrens, E., Bentsen, M., Bi, D., Biastoch, A., Böning, C. W., Bozec, A., Chassignet, E., Danabasoglu, G., Danilov, S., Domingues, C. M., Drange, H., Farneti, R., Fernandez, E., Greatbatch, R. J., Holland, D. M., Ilıcak, M., Large, W. G., Lorbacher, K., Lu, J., Marsland, S. J., Mishra, A., Nurser, A. J. G., Salas, D., Palter, J. B., Samuels, B. L., Schröter, J., Schwarzkopf, F. U., Sidorenko, D., Marie, A., heng Tseng, Y., Tsujino, H., Uotila, P., Valcke, S., Voldoire, A., Wang, Q., Winton, M., and Zhang, X. An assessment of global and regional sea level for years 1993–2007 in a suite of interannual CORE-II simulations. *Ocean Modelling*, 78:35–89, 2014. [10.1016/j.ocemod.2014.03.004](https://doi.org/10.1016/j.ocemod.2014.03.004).
- Grose, M. R., Colman, R., Bhend, J., and Moise, A. F. Limits to global and Australian temperature change this century based on expert judgment of climate sensitivity. *Climate Dynamics*, 48:3325–3339, 2016. [10.1007/s00382-016-3269-2](https://doi.org/10.1007/s00382-016-3269-2).
- Grose, M., Gregory, J., Colman, R., and Andrews, T. What Climate Sensitivity Index Is Most Useful for Projections? *Geophysical Research Letters*, 45:1559–1566, 2018. [10.1002/2017GL075742](https://doi.org/10.1002/2017GL075742).
- Haarsma, R. J., Roberts, M. J., Vidale, P. L., Senior, C. A., Bellucci, A., Bao, Q., Chang, P., Corti, S., Fučkar, N. S., Guemas, V., von Hardenberg, J., Hazeleger, W., Kodama, C., Koenigk, T., Leung, L. R., Lu, J., Luo, J.-J., Mao, J., Mizielinski, M., Mizuta, R., Nobre, P., Satoh, M., Scoccimarro, E., Semmler, T., Small, J., and von Storch, J.-S. High Resolution Model Intercomparison Project (HighResMIP v1.0) for CMIP6. *Geosci. Model Dev.*, 9:4185–4208, 2016. [10.5194/gmd-9-4185-2016](https://doi.org/10.5194/gmd-9-4185-2016).
- Haasnoot, M., Kwadijk, J., van Alphen, J., Le Bars, D., van den Hurk, B., Diermanse, F., van der Spek, A., Essink, G. O., Delsman, J., and Mens, M. Adaptation to uncertain sea-level rise; how uncertainty in Antarctic mass-loss impacts the coastal adaptation strategy of the Netherlands. *Environmental Research Letters*, 2019. [10.1088/1748-9326/ab666c](https://doi.org/10.1088/1748-9326/ab666c).
- Haasnoot, M., Van, S., and Alphen, J. V. Designing a monitoring system to detect signals to adapt to uncertain climate change. *Global Environmental Change*, 52:273–285, 2018. [10.1016/j.gloenvcha.2018.08.003](https://doi.org/10.1016/j.gloenvcha.2018.08.003).
- Haigh, I. D., Wahl, T., Rohling, E. J., Price, M., Pattiaratchi, C. B., Calafat, F., and Dangendorf, S. Timescales for detecting a significant acceleration in sea level rise. *Nature Communications*, 5:1–11, 2014. [10.1038/ncomms4635](https://doi.org/10.1038/ncomms4635).
- Hamlington, B. D., Fasullo, J., Nerem, R., Kim, K.-Y., and Landerer, F. Uncovering the Pattern of Forced Sea Level Rise in the Satellite Altimeter Record *Geophysical Research Letters*. *Geophys Res Lett*, 46: 4844–4853, 2019. [10.1029/2018GL081386](https://doi.org/10.1029/2018GL081386).
- Hamlington, B. D., Frederikse, T., Nerem, R. S., Fasullo, J. T., and Adhikari, S. Investigating the Acceleration of Regional Sea Level Rise During the Satellite Altimeter Era. *Geophysical Research Letters*, 47, 3 2020. [10.1029/2019GL086528](https://doi.org/10.1029/2019GL086528).
- Hawkins, E. and Sutton, R. Time of emergence of climate signals. *Geophysical Research Letters*, 39: 1–6, 2012. [10.1029/2011GL050087](https://doi.org/10.1029/2011GL050087).
- Hawkins, E. and Sutton, R. The Potential to Narrow Uncertainty in Regional Climate Predictions. *Bulletin of the American Meteorological Society*, 90:1095–1107, 2009. [10.1175/2009BAMS2607.1](https://doi.org/10.1175/2009BAMS2607.1).

- Held, I., Winton, M., Takahasi, K., Delworth, T., Zeng, F., and Vallis, G. Probing the Fast and Slow Components of Global Warming by Returning Abruptly to Pre-Industrial Forcing. *Journal of Climate*, 23:2418–2427, 2010. [10.1175/2009JCLI3466.1](https://doi.org/10.1175/2009JCLI3466.1).
- Hermans, T. H. J., Le Bars, D., Katsman, C. A., and Camargo, C. M. L. Drivers of Interannual Sea Level Variability on the Northwestern European Shelf. *Journal of Geophysical Research: Oceans*, 125:1–18, 2020a. [10.1029/2020JC016325](https://doi.org/10.1029/2020JC016325).
- Hermans, T. H. J., Tinker, J., Palmer, M. D., Katsman, C. A., Vermeersen, B. L. A., and Slangen, A. B. A. Improving sea-level projections on the Northwestern European shelf using dynamical downscaling. *Climate Dynamics*, 54:1987–2011, 2020b. [10.1007/s00382-019-05104-5](https://doi.org/10.1007/s00382-019-05104-5).
- Hermans, T. H. J., Gregory, J. M., Palmer, M. D., Ringer, M., Katsman, C., and Slangen, A. Projecting Global Mean Sea-Level Using CMIP6 Models. *Geophysical Research Letters*, 48, 2021. [10.1029/2020GL092064](https://doi.org/10.1029/2020GL092064).
- Hinkel, J., Church, J. A., Gregory, J. M., Lambert, E., Cozannet, G. L., Lowe, J., McInnes, K., Nicholls, R. J., van der Pol, T. D., and van de Wal, R. Meeting User Needs for Sea Level Rise Information: A Decision Analysis Perspective. *Earth's Future*, 7:320–337, 2019. [10.1029/2018EF001071](https://doi.org/10.1029/2018EF001071).
- Hobbs, W., Palmer, M., and Monselesan, D. An Energy Conservation Analysis of Ocean Drift in the CMIP5 Global Coupled Models. *Journal of Climate*, 29:1639–1653, 2016. [10.1175/JCLI-D-15-0477.1](https://doi.org/10.1175/JCLI-D-15-0477.1).
- Hogarth, P., Hughes, C. W., Williams, S. D. P., and Wilson, C. Improved and extended tide gauge records for the British Isles leading to more consistent estimates of sea level rise and acceleration since 1958. *Progress in Oceanography*, 184:102333, 2020. [10.1016/j.pocean.2020.102333](https://doi.org/10.1016/j.pocean.2020.102333).
- Holgate, S. J., Matthews, A., Woodworth, P. L., Rickards, L. J., Tamsiea, E., Bradshaw, E., Foden, P. R., Gordon, K. M., Jevrejeva, S., Pugh, J., Journal, S., May, N., Holgate, S. J., Lesley, L. W., and Proudman, J. New Data Systems and Products at the Permanent Service for Mean Sea Level. *Journal of Coastal Research*, 29:493–504, 2013. [10.2112/JCOASTRES-D-12-00175.1](https://doi.org/10.2112/JCOASTRES-D-12-00175.1).
- Holt, J., Wakelin, S., Lowe, J., and Tinker, J. The potential impacts of climate change on the hydrography of the northwest European continental shelf. *Progress in Oceanography*, 86:361–379, 2010. [10.1016/j.pocean.2010.05.003](https://doi.org/10.1016/j.pocean.2010.05.003).
- Holt, J., Schrum, C., Cannaby, H., Daewel, U., Allen, I., Artioli, Y., Bopp, L., Butenschon, M., Fach, B. A., Harle, J., Pushpadas, D., Salihoglu, B., and Wakelin, S. Potential impacts of climate change on the primary production of regional seas: A comparative analysis of five European seas. *Progress in Oceanography*, 140:91–115, 2016. [10.1016/j.pocean.2015.11.004](https://doi.org/10.1016/j.pocean.2015.11.004).
- Holt, J., Hyder, P., Ashworth, M., Harle, J., Hewitt, H. T., Liu, H., New, A. L., Pickles, S., Porter, A., Popova, E., Allen, J. I., Siddorn, J., and Wood, R. Prospects for improving the representation of coastal and shelf seas in global ocean models. *Geoscientific Model Development*, 10:499–523, 2017. [10.5194/gmd-10-499-2017](https://doi.org/10.5194/gmd-10-499-2017).
- Holt, J., Polton, J., Huthnance, J., Wakelin, S., O'Dea, E., Harle, J., Yool, A., Artioli, Y., Blackford, J., Siddorn, J., and Inall, M. Climate-Driven Change in the North Atlantic and Arctic Oceans Can Greatly Reduce the Circulation of the North Sea. *Geophysical Research Letters*, 2018. [10.1029/2018GL078878](https://doi.org/10.1029/2018GL078878).
- Howard, T., Lowe, J., and Horsburgh, K. Interpreting Century-Scale Changes in Southern North Sea Storm Surge Climate Derived from Coupled Model Simulations. *Journal of Climate*, 23:6234–6247, 2010. [10.1175/2010JCLI3520.1](https://doi.org/10.1175/2010JCLI3520.1).
- Howard, T., Palmer, M. D., and Brichenno, L. M. Contributions to 21st century projections of extreme sea-level change around the UK. *Environmental Research Letters*, 1, 2019. [10.1088/2515-7620/ab42d7](https://doi.org/10.1088/2515-7620/ab42d7).

- van den Hurk, B., Siegmund, P., Tank, A. E. K., Attema, J., Bakker, A., Beersma, J., Bessembinder, J., Boers, R., Brandsma, T., van den Brink, H., Drijfhout, S., Eskes, H., Haarsma, R., Hazeleger, W., Jilderda, R., Katsman, C., Lenderink, G., Loriaux, J., van Meijgaard, E., van Noije, T., van Oldenborgh, G., Selten, F., Siebesma, P., Sterl, A., de Vries, H., van Weerle, M., de Winter, R., and van Zadelhoff, G. KNMI'14: Climate Change scenarios for the 21st Century – A Netherlands perspective, 2014. URL <http://www.climatescenarios.nl/>.
- Huthnance, J. M. Waves and currents near the continental shelf edge. *Progress in Oceanography*, 10: 193–226, 1981. [10.1016/0079-6611\(81\)90004-5](https://doi.org/10.1016/0079-6611(81)90004-5).
- Huthnance, J. M. Slope Currents and “JEBAR”. *Journal of Physical Oceanography*, 14:795–810, 1984. [10.1175/1520-0485\(1984\)014<0795:SCA>2.0.CO;2](https://doi.org/10.1175/1520-0485(1984)014<0795:SCA>2.0.CO;2).
- Huthnance, J. M. Physical oceanography of the North Sea. *Ocean and Shoreline Management*, 16: 199–231, 1991. [10.1016/0951-8312\(91\)90005-M](https://doi.org/10.1016/0951-8312(91)90005-M).
- Huthnance, J. Circulation, exchange and water masses at the ocean margin: the role of physical processes at the shelf edge. *Progress in Oceanography*, 35:353–431, 1995. [10.1016/0079-6611\(95\)80003-C](https://doi.org/10.1016/0079-6611(95)80003-C).
- Idier, D., Paris, F., Cozannet, G. L., Boulahya, F., and Dumas, F. Sea-level rise impacts on the tides of the European Shelf. *Continental Shelf Research*, 137:56–71, 2017. [10.1016/j.csr.2017.01.007](https://doi.org/10.1016/j.csr.2017.01.007).
- Idžanovic, M. and Ophaug, V. The coastal mean dynamic topography in Norway observed by CryoSat-2 and GOCE. *Geophysical Research Letters*, 44:5609–5617, 2017. [10.1002/2017GL073777](https://doi.org/10.1002/2017GL073777).
- Jackson, L. P. and Jevrejeva, S. A probabilistic approach to 21st century regional sea-level projections using RCP and High-end scenarios. *Global and Planetary Change*, 146:179–189, 2016. [10.1016/j.gloplacha.2016.10.006](https://doi.org/10.1016/j.gloplacha.2016.10.006).
- Jacob, D., Teichmann, C., Sobolowski, S., Katragkou, E., Anders, I., Belda, M., Benestad, R., Boberg, F., Buonomo, E., Cardoso, R. M., Casanueva, A., Christensen, O. B., Christensen, J. H., Coppola, E., Cruz, L. D., Davin, E. L., Dobler, A., Domínguez, M., Fealy, R., Fernandez, J., Gaertner, M. A., García-Díez, M., Giorgi, F., Gobiet, A., Goergen, K., Gómez-Navarro, J. J., Alemán, J. J. G., Gutiérrez, C., Gutiérrez, J. M., Güttler, I., Haensler, A., Halenka, T., Jerez, S., Jiménez-Guerrero, P., Jones, R. G., Keuler, K., Kjellström, E., Knist, S., Kotlarski, S., Maraun, D., van Meijgaard, E., Mercogliano, P., Montávez, J. P., Navarra, A., Nikulin, G., de Noblet-Ducoudré, N., Panitz, H. J., Pfeifer, S., Piazza, M., Pichelli, E., Pietikäinen, J. P., Prein, A. F., Preuschmann, S., Rechid, D., Rockel, B., Romera, R., Sánchez, E., Sieck, K., Soares, P. M., Somot, S., Srnec, L., Sørland, S. L., Termonia, P., Truhetz, H., Vautard, R., Warrach-Sagi, K., and Wulfmeyer, V. Regional climate downscaling over Europe: perspectives from the EURO-CORDEX community. *Regional Environmental Change*, 20, 6 2020. [10.1007/s10113-020-01606-9](https://doi.org/10.1007/s10113-020-01606-9).
- Jin, Y., Zhang, X., Church, J. A., and Bao, X. Projected Sea Level Changes in the Marginal Seas near China Based on Dynamical Downscaling. *Journal of Climate*, pages 1–52, 6 2021. [10.1175/JCLI-D-20-0796.1](https://doi.org/10.1175/JCLI-D-20-0796.1).
- Kalnay, E., Kanamitsu, M., Kistler, R., Collins, W., Deaven, D., and Gandin, L. The NCEP / NCAR 40-Year Reanalysis Project. *Bull Am Meteorol Soc*, 77:437–472, 1996. [10.1175/1520-0477\(1996\)077<0437:TNYRP>2.0.CO;2](https://doi.org/10.1175/1520-0477(1996)077<0437:TNYRP>2.0.CO;2).
- Kim, D., Cairns, D. M., Bartholdy, J., Kim, D., Cairns, D. M., and Bartholdy, J. Wind-Driven Sea-Level Variation Influences Dynamics of Salt Marsh Vegetation. *Annals of the Association of American Geographers*, 102:231–248, 2011. [10.1080/00045608.2010.544933](https://doi.org/10.1080/00045608.2010.544933).
- Kirtman, B., Power, S., Adedoyin, J., Boer, G., Bojariu, R., Camilloni, I., Doblas-Reyes, F., Fiore, A., Kimoto, M., Meehl, G., Prather, M., Sarr, A., Kimoto, M., Schär, C., Sutton, R., van Oldenborgh, G., Vecchi, G., and Wang, H. Near-term Climate Change: Projections and Predictability. In Stocker, T., Qin, D., Plattner, G.-K., Tignor, M., Allen, S., Bosschung, J., Nauels, A., Xia, Y., Bex, V., and Midgley, P., editors, *Climate Change 2013: The Physical Science Basis. Contribution of Working Group I to the Fifth Assessment Report of the Intergovernmental Panel on Climate Change*. Cambridge University Press, Cambridge, United Kingdom and New York, NY, USA., 2013.

- Kirwan, M., Temmerman, S., Skeeahan, E., Guntenspergen, G., and Fagherazzi, S. Overestimation of marsh vulnerability to sea level rise. *Nature Climate Change*, 6:253–260, 2016. [10.1038/nclimate2909](https://doi.org/10.1038/nclimate2909).
- Klos, A., Kusche, J., Fenoglio, L., Machiel, M., and Janusz, S. B. Introducing a vertical land motion model for improving estimates of sea level rates derived from tide gauge records affected by earthquakes. *GPS Solutions*, 23:1–12, 2019. [10.1007/s10291-019-0896-1](https://doi.org/10.1007/s10291-019-0896-1).
- Knutti, R., Sedlacek, J., Sanderson, B., Lorenz, R., Fischer, E., and Eyring, V. A climate model projection weighting scheme accounting for performance and interdependence. *Geophys Res Lett*, pages 1909–1918, 2017. [10.1002/2016GL072012](https://doi.org/10.1002/2016GL072012).
- Konikow, L. F. Contribution of global groundwater depletion since 1900 to sea-level rise. *Geophys Res Lett*, 38, 2011. [10.1029/2011GL048604](https://doi.org/10.1029/2011GL048604).
- Kopp, R. E., Horton, R. M., Little, C. M., Mitrovica, J. X., Oppenheimer, M., Rasmussen, D. J., Strauss, B. H., and Tebaldi, C. Probabilistic 21st and 22nd century sea-level projections at a global network of tide-gauge sites. *Earth's Future*, 2:383–406, 2014. [10.1002/2014EF000239](https://doi.org/10.1002/2014EF000239).
- Kopp, R. E., Gilmore, E. A., Little, C. M., Ramenzoni, V. C., and Sweet, W. V. Usable Science for Managing the Risks of Sea-Level Rise. *Earth's Future*, 7:1235–1269, 2019. [10.1029/2018EF001145](https://doi.org/10.1029/2018EF001145).
- Kuhlbrodt, T. and Gregory, J. M. Ocean heat uptake and its consequences for the magnitude of sea level rise and climate change. *Geophysical Research Letters*, 39:1–6, 2012. [10.1029/2012GL052952](https://doi.org/10.1029/2012GL052952).
- Lambeck, K., Rouby, H., Purcell, A., Sun, Y., and Sambridge, M. Sea level and global ice volumes from the Last Glacial Maximum to the Holocene. *Proceedings of the National Academy of Sciences of the United States of America*, 111:15296–15303, 10 2014. [10.1073/pnas.1411762111](https://doi.org/10.1073/pnas.1411762111).
- Landerer, F. W., Jungclauss, J. H., and Marotzke, J. Ocean bottom pressure changes lead to a decreasing length-of-day in a warming climate. *Geophys. Res. Lett.*, 34, 2007. [10.1029/2006GL029106](https://doi.org/10.1029/2006GL029106).
- Landerer, F., Gleckler, P., and Lee, T. Evaluation of CMIP5 dynamic sea surface height multi-model simulations against satellite observations. *Climate Dynamics*, 43:1271–1283, 2014. [10.1007/s00382-013-1939-x](https://doi.org/10.1007/s00382-013-1939-x).
- Lellouche, J.-M., Greiner, E., Galloudec, O. L., Garric, G., Regnier, C., Drevillon, M., Benkiran, M., Emmanuel Testut, C., Bourdalle-Badie, R., Gasparin, F., Hernandez, O., Levier, B., Drillet, Y., Remy, E., and Traon, P. L. Recent updates to the Copernicus Marine Service global ocean monitoring and forecasting real-time 1/12th degree high-resolution system. *Ocean Science*, 14:1093–1126, 2018. [10.5194/os-14-1093-2018](https://doi.org/10.5194/os-14-1093-2018).
- Levermann, A., Griesel, A., Hofmann, M., Montoya, M., and Rahmstorf, S. Dynamic sea level changes following changes in the thermohaline circulation. *Climate Dynamics*, 24:347–354, 2005. [10.1007/s00382-004-0505-y](https://doi.org/10.1007/s00382-004-0505-y).
- Levermann, A., Winkelmann, R., Nowicki, S., Fastook, J. L., Frieler, K., Greve, R., Hellmer, H. H., Martin, M., Meinshausen, M., Mengel, M., Payne, A., Pollard, D., Sato, T., Timmermann, R., Wang, W., and Bindshadler, R. Projecting Antarctic ice discharge using response functions from SeaRISE ice-sheet models. *Earth System Dynamics*, 5:271–293, 2014. [10.5194/esd-5-271-2014](https://doi.org/10.5194/esd-5-271-2014).
- Levermann, A., Winkelmann, R., Albrecht, T., Goelzer, H., Golledge, N., Greve, R., Huybrechts, P., Jordan, J., Leguy, G., Martin, D., Morlighem, M., Pattyn, F., Pollard, D., Quiquet, A., Rodehacke, C., Seroussi, H., Sutter, J., Zhang, T., Breedam, J. V., Calov, R., DeConto, R., Dumas, C., Garbe, J., Gudmundsson, G. H., Hoffman, M., Humbert, A., Kleiner, T., Lipscomb, W., Meinshausen, M., Ng, E., Nowicki, S., Perego, M., Price, S., Saito, F., Schlegel, N.-J., Sun, S., and van de Wal, R. Projecting Antarctica's contribution to future sea level rise from basal ice shelf melt using linear response functions of 16 ice sheet models (LARMIP-2). *Earth System Dynamics*, 11:35–76, 2020. <https://doi.org/10.5194/esd-11-35-2020>.

- Lidberg, M., Johansson, J. M., Scherneck, H.-G., and Davis, J. An improved and extended GPS-derived 3D velocity field of the glacial isostatic adjustment (GIA) in Fennoscandia. *J Geod*, 81:213–230, 2007. [10.1007/s00190-006-0102-4](https://doi.org/10.1007/s00190-006-0102-4).
- Little, C. M., Horton, R. M., Kopp, R. E., Oppenheimer, M., and Yip, S. Uncertainty in Twenty-First-Century CMIP5 Sea Level Projections. *Journal of Climate*, 28:838–852, 2015. [10.1175/JCLI-D-14-00453.1](https://doi.org/10.1175/JCLI-D-14-00453.1).
- Liu, Z. J., Minobe, S., Sasaki, Y. N., and Terada, M. Dynamical downscaling of future sea level change in the western North Pacific using ROMS. *Journal of Oceanography*, 72:905–922, 2016. [10.1007/s10872-016-0390-0](https://doi.org/10.1007/s10872-016-0390-0).
- Lorbacher, K., Nauels, A., and Meinshausen, M. Complementing thermosteric sea level rise estimates. *Geoscientific Model Development*, 8:2723–2734, 2015. [10.5194/gmd-8-2723-2015](https://doi.org/10.5194/gmd-8-2723-2015).
- Lowe, J. A. and Gregory, J. M. Understanding projections of sea level rise in a Hadley Centre coupled climate model. *J Geophys Res*, 111, 11 2006. [10.1029/2005JC003421](https://doi.org/10.1029/2005JC003421).
- Lyu, K., Zhang, X., Church, J. A., Slangen, A. B. A., and Hu, J. Time of emergence for regional sea-level change. *Nature Climate Change*, 4:1006–1010, 2014. [10.1038/nclimate2397](https://doi.org/10.1038/nclimate2397).
- Lyu, K., Zhang, X., Church, J. A., and Hu, J. Quantifying internally generated and externally forced climate signals at regional scales in CMIP5 models. *Geophysical Research Letters*, 42:9394–9403, 2015. [10.1002/2015GL065508](https://doi.org/10.1002/2015GL065508).
- Lyu, K., Zhang, X., and Church, J. A. Regional Dynamic Sea Level Simulated in the CMIP5 and CMIP6 Models: Mean Biases, Future Projections, and Their Linkages. *Journal of Climate*, 33:6377–6398, 8 2020. [10.1175/JCLI-D-19-1029.1](https://doi.org/10.1175/JCLI-D-19-1029.1).
- Lyu, K., Zhang, X., and Church, J. A. Projected ocean warming constrained by the ocean observational record. *Nature Climate Change*, 11:834–839, 10 2021. [10.1038/s41558-021-01151-1](https://doi.org/10.1038/s41558-021-01151-1).
- Madec, G. and NEMO Team. *NEMO ocean engine*. 2016. [10.5281/zenodo.1472492](https://doi.org/10.5281/zenodo.1472492).
- Marchesiello, P., McWilliams, J. C., and Shchepetkin, A. Open boundary conditions for long-term integration of regional oceanic models. *Ocean Modelling*, 3:1–20, 2001. [10.1016/S1463-5003\(00\)00013-5](https://doi.org/10.1016/S1463-5003(00)00013-5).
- Marcos, M. and Tsimplis, M. N. Forcing of coastal sea level rise patterns in the North Atlantic and the Mediterranean Sea. *Geophysical Research Letters*, 34:1–6, 2007. [10.1029/2007GL030641](https://doi.org/10.1029/2007GL030641).
- Marzeion, B., Hock, R., Anderson, B., Bliss, A., Champollion, N., Fujita, K., Huss, M., Immerzeel, W., Kraaijenbrink, P., Malles, J.-H., Maussion, F., Radic, V., Rounce, D., Sakai, A., Shannon, S., van de Wal, R., and Zekollari, H. Partitioning the Uncertainty of Ensemble Projections of Global Glacier Mass Change. *Earth's Future*, 8:1–25, 2020. [10.1029/2019EF001470](https://doi.org/10.1029/2019EF001470).
- Masson-Delmotte, V., Zhai, P., Pirani, A., Connors, S., Péan, C., Berger, S., Caud, N., Chen, Y., Goldfarb, L., Gomis, M., Huang, M., Leitzell, K., Lonnoy, E., Matthews, J., Maycock, T., Waterfield, T., Yelekçi, O., Yu, R., and Zhou, B. IPCC, 2021: Summary for Policymakers. In Masson-Delmotte, V., Zhai, P., Pirani, A., Connors, S., Péan, C., Berger, S., Caud, N., Chen, Y., Goldfarb, L., Gomis, M., Huang, M., Leitzell, K., Lonnoy, E., Matthews, J., Maycock, T., Waterfield, T., Yelekçi, O., Yu, R., and Zhou, B., editors, *Climate Change 2021: The Physical Science Basis. Contribution of Working Group I to the Sixth Assessment Report of the Intergovernmental Panel on Climate Change*. Cambridge University Press, 2021.
- Mathis, M. Projected Forecast of Hydrodynamic Conditions in the North Sea for the 21st Century, 2013. Dissertation, University of Hamburg.
- Mathis, M., Elizalde, A., and Mikolajewicz, U. Which complexity of regional climate system models is essential for downscaling anthropogenic climate change in the Northwest European Shelf? *Climate Dynamics*, 50:2637–2659, 2017. [10.1007/s00382-017-3761-3](https://doi.org/10.1007/s00382-017-3761-3).

- McDougall, T. and Barker, P. *Getting started with the TEOS-10 and the Gibbs Seawater (GSW) Oceanographic Toolbox*. SCOR/IAPSO WG127, 2011. ISBN 9780646556215.
- McSweeney, C., Jones, R., Lee, R., and Rowell, D. Selecting CMIP5 GCMs for downscaling over multiple regions. *Climate Dynamics*, 44:3237–3260, 2015. [10.1007/s00382-014-2418-8](https://doi.org/10.1007/s00382-014-2418-8).
- Meehl, G. A., Senior, C. A., Eyring, V., Flato, G., Lamarque, J.-F., Stouffer, R. J., Taylor, K. E., and Schlund, M. Context for interpreting equilibrium climate sensitivity and transient climate response from the CMIP6 Earth system models. *Science Advances*, 6:1–10, 2020. [10.1126/sciadv.aba1981](https://doi.org/10.1126/sciadv.aba1981).
- Meinshausen, M., Smith, S. J., Calvin, K., Daniel, J. S., Kainuma, M. L. T., Lamarque, J.-F., Matsumoto, K., Montzka, S. A., Raper, S. C. B., Riahi, K., Thomson, A., Velders, G. J. M., and van Vuuren, D. P. P. The RCP greenhouse gas concentrations and their extensions from 1765 to 2300. *Climatic Change*, 109:210–241, 2011. [10.1007/s10584-011-0156-z](https://doi.org/10.1007/s10584-011-0156-z).
- Meinshausen, M., Nicholls, Z., Lewis, J., Gidden, M. J., Vogel, E., Freund, M., Beyerle, U., Gessner, C., Bauer, N., Canadell, J. G., Daniel, J. S., John, A., Luderer, G., Meinshausen, N., Montzka, S. A., Rayner, P., Reimann, S., Smith, S., den Berg, M. V., Velders, G., Vollmer, M., and Wang, R. The shared socio-economic pathway (SSP) greenhouse gas concentrations and their extensions to 2500. *GMD*, 13: 3571–3605, 2020. [10.5194/gmd-13-3571-2020](https://doi.org/10.5194/gmd-13-3571-2020).
- Melet, A. and Meyssignac, B. Explaining the Spread in Global Mean Thermosteric Sea Level Rise in CMIP5 Climate Models. *Journal of Climate*, 28:9918–9940, 2015. [10.1175/JCLI-D-15-0200.1](https://doi.org/10.1175/JCLI-D-15-0200.1).
- Mengel, M., Levermann, A., Frieler, K., Robinson, A., Marzeion, B., and Winkelmann, R. Future sea level rise constrained by observations and long-term commitment. *PNAS*, 113:2597–2602, 2016. [10.1073/pnas.1500515113](https://doi.org/10.1073/pnas.1500515113).
- Mengel, M., Nauels, A., Rogelj, J., and Schleussner, C.-F. Committed sea-level rise under the Paris Agreement and the legacy of delayed mitigation action. *Nature Communications*, 9:1–10, 2018. [10.1038/s41467-018-02985-8](https://doi.org/10.1038/s41467-018-02985-8).
- Meyssignac, B., Slangen, A. B., Melet, A., Church, J., Fettweis, X., Marzeion, B., Agosta, C., Ligtenberg, S., Spada, G., Richter, K., Palmer, M. D., Roberts, C. D., and Champollion, N. Evaluating Model Simulations of Twentieth-Century Sea-Level Rise. Part II: Regional Sea-Level Changes. *Journal of Climate*, 30: 8539–8563, 2017. [10.1175/JCLI-D-17-0112.1](https://doi.org/10.1175/JCLI-D-17-0112.1).
- Miles, E. R., Spillman, C. M., Church, J. A., and McIntosh, P. C. Seasonal prediction of global sea level anomalies using an ocean–atmosphere dynamical model. *Climate Dynamics*, 43:2131–2145, 10 2014. [10.1007/s00382-013-2039-7](https://doi.org/10.1007/s00382-013-2039-7).
- Miller, L. and Douglas, B. C. Gyre-scale atmospheric pressure variations and their relation to 19th and 20th century sea level rise. *Geophysical Research Letters*, 34:1–5, 2007. [10.1029/2007GL030862](https://doi.org/10.1029/2007GL030862).
- Mitrovica, J. X., Tamisiea, M. E., Davis, J. L., and Milne, G. A. Recent mass balance of polar ice sheets inferred from patterns of global sea-level change. *Nature*, 409:1026–1029, 2001. [10.1038/35059054](https://doi.org/10.1038/35059054).
- Mitrovica, J. X., Gomez, N., Morrow, E., Hay, C., Latychev, K., and Tamisiea, M. E. On the robustness of predictions of sea level fingerprints. *Geophys. J. Int.*, 187:729–742, 2011. [10.1111/j.1365-246X.2011.05090.x](https://doi.org/10.1111/j.1365-246X.2011.05090.x).
- Morris, J. T. Effects of sea level anomalies on estuarine processes. In Hobbie, J., editor, *Estuarine Science: A synthetic Approach to Research and Practice*, pages 107–127. Island Press, 2000. ISBN 1559637005.
- Muis, S., Apecechea, M. I., Dullaart, J., de Lima Rego, J., Madsen, K. S., Su, J., Yan, K., and Verlaan, M. A High-Resolution Global Dataset of Extreme Sea Levels, Tides, and Storm Surges, Including Future Projections. *Frontiers in Marine Science*, 7:263, 4 2020. [10.3389/fmars.2020.00263](https://doi.org/10.3389/fmars.2020.00263).

- Muntjewerf, L., Petrini, M., Vizcaino, M., da Silva, C. E., Sellevold, R., Scherrenberg, M. D., Thayer-Calder, K., Bradley, S. L., Lenaerts, J. T., Lipscomb, W. H., and Lofverstrom, M. Greenland Ice Sheet Contribution to 21st Century Sea Level Rise as Simulated by the Coupled CESM2.1-CISM2.1. *Geophysical Research Letters*, 47, 5 2020. [10.1029/2019GL086836](https://doi.org/10.1029/2019GL086836).
- Nauels, A., Meinshausen, M., Mengel, M., Lorbacher, K., and Wigley, T. M. L. Synthesizing long-term sea level rise projections – the MAGICC sea level model v2.0. *Geoscientific Model Development*, 10: 2495–2524, 2017. [10.5194/gmd-10-2495-2017](https://doi.org/10.5194/gmd-10-2495-2017).
- Newsom, E., Zanna, L., Khatiwala, S., and Gregory, J. The Influence of Warming Patterns on Passive Ocean Heat Uptake. *Geophysical Research Letters*, 47:71–75, 2020. [10.1029/2020GL088429](https://doi.org/10.1029/2020GL088429).
- Nicholls, R. J. and Cazenave, A. Sea-Level Rise and Its Impact on Coastal Zones. *Science*, 328:1517–1520, 2010. [10.1126/science.1185782](https://doi.org/10.1126/science.1185782).
- Nijse, F. J. M. M., Cox, P. M., and Williamson, M. S. Emergent constraints on transient climate response (TCR) and equilibrium climate sensitivity (ECS) from historical warming in CMIP5 and CMIP6 models. *Earth System Dynamics*, 11:737–750, 2020. [10.5194/esd-11-737-2020](https://doi.org/10.5194/esd-11-737-2020).
- Nowicki, S., Goelzer, H., Seroussi, H., Payne, A. J., Lipscomb, W. H., Abe-Ouchi, A., Agosta, C., Alexander, P., Asay-Davis, X., Barthel, A., Bracegirdle, T., Cullater, R., Felikson, D., Fettweis, X., Gregory, J., Hattermann, T., Jourdain, N., Munneke, P. K., Larour, E., Little, C., Morlighem, M., Nias, I., Shepherd, A., Simon, E., Sltar, D., Smith, R., Straneo, F., Trusel, L., den Broeke, M. V., and van de Wal, R. Experimental protocol for sea level projections from ISMIP6 stand-alone ice sheet models. *The Cryosphere*, 14:2331–2368, 2020. [10.5194/tc-14-2331-2020](https://doi.org/10.5194/tc-14-2331-2020).
- O'Dea, E., Furner, R., Wakelin, S., Siddorn, J., While, J., Sykes, P., King, R., Holt, J., and Hewitt, H. The CO5 configuration of the 7km Atlantic Margin Model: large-scale biases and sensitivity to forcing, physics options and vertical resolution. *Geoscientific Model Development*, 10:2947–2969, 2017. [10.5194/gmd-10-2947-2017](https://doi.org/10.5194/gmd-10-2947-2017).
- Oki, T. and Sud, Y. C. Design of Total Runoff Integrating Pathways (TRIP) - A Global River Channel Network. *Earth Interactions*, 2:7–22, 1998. [10.1175/1087-3562\(1998\)002<0001:DOTRIP>2.3.CO;2](https://doi.org/10.1175/1087-3562(1998)002<0001:DOTRIP>2.3.CO;2).
- Olivié, D. and Peters, G. Variation in emission metrics due to variation in CO2 and temperature impulse response functions. *Earth System Dynamics*, 4:267–286, 2013. [10.5194/esd-4-267-2013](https://doi.org/10.5194/esd-4-267-2013).
- O'Neill, B. C., Kriegler, E., Riahi, K., Ebi, K. L., Hallegatte, S., Carter, T., Mathur, R., and Vuuren, D. V. A new scenario framework for climate change research: the concept of shared socioeconomic pathways. *Climatic Change*, 122:387–400, 2014. [10.1007/s10584-013-0905-2](https://doi.org/10.1007/s10584-013-0905-2).
- Ophaug, V., Breili, K., and Gerlach, C. A comparative assessment of coastal mean dynamic topography in Norway by geodetic and ocean approaches. *Journal of Geophysical Research: Oceans*, 120:7807–7826, 2015. [10.1002/2015JC011145](https://doi.org/10.1002/2015JC011145).
- Oppenheimer, M., Glavovic, B., Hinkel, J., van de Wal, R., Magnan, A., Abd-Elgawad, A., Cai, R., Cifuentes-Jara, M., DeConto, R., Ghosh, T., Hay, J., Isla, F., Marzeion, B., Meyssignac, B., and Sebesvari, Z. Sea Level Rise and Implications for Low Lying Islands, Coasts and Communities. In Pörtner, H.-O., Roberts, D., Masson-Delmotte, V., Zhai, P., Yihnot, M., Poloczanska, E., Mintenbeck, K., Alegria, A., Nicolai, M., Okem, A., Petzold, J., Rama, B., and Weyer, N., editors, *IPCC Special Report on the Ocean and Cryosphere in a Changing Climate*. Cambridge University Press, 2019.
- Orlanski, I. A simple boundary condition for unbounded hyperbolic flows. *Journal of Computational Physics*, 21:251–269, 1976. [10.1016/0021-9991\(76\)90023-1](https://doi.org/10.1016/0021-9991(76)90023-1).
- Oudar, T., Cattiaux, J., and Douville, H. Drivers of the Northern Extratropical Eddy-Driven Jet Change in CMIP5 and CMIP6 Models. *Geophys Res Lett*, 47:1–9, 2020. [10.1029/2019GL086695](https://doi.org/10.1029/2019GL086695).

- O'Dea, E. J., Arnold, A. K., Edwards, K. P., Furner, R., Hyder, P., Martin, M. J., Siddorn, J. R., Storkey, D., While, J., Holt, J. T., and Liu, H. An operational ocean forecast system incorporating NEMO and SST data assimilation for the tidally driven European North-West shelf. *Journal of Operational Oceanography*, 5:3–17, 2012. [10.1080/1755876X.2012.11020128](https://doi.org/10.1080/1755876X.2012.11020128).
- Palmer, M. D., Harris, G. R., and Gregory, J. M. Extending CMIP5 projections of global mean temperature change and sea level rise due to thermal expansion using a physically-based emulator. *Environmental Research Letters*, 13, 2018a. [10.1088/1748-9326/aad2e4](https://doi.org/10.1088/1748-9326/aad2e4).
- Palmer, M. D., Howard, T., Tinker, J. M., Lowe, J., Bricheno, L., Calvert, D., Gregory, J., Harris, G., Krijnen, J., Pickering, M., Roberts, C., and Wolf, J. UKCP18 Marine report, 2018b.
- Palmer, M., Gregory, J., Bagge, M., Calvert, D., Hagedoorn, J., Howard, T., Klemann, V., Lowe, J., Roberts, C., Slangen, A., and Spada, G. Exploring the Drivers of Global and Local Sea-Level Change over the 21st Century and Beyond. *Earth's Future*, 8, 2020. [10.1029/2019EF001413](https://doi.org/10.1029/2019EF001413).
- Palmer, M., Domingues, C., Slangen, A., and Dias, F. B. An ensemble approach to quantify global mean sea-level rise over the 20th century from tide gauge reconstructions. *Environmental Research Letters*, 16:1–10, 2021. [10.1088/1748-9326/abdaec](https://doi.org/10.1088/1748-9326/abdaec).
- Pelling, H. E. and Green, J. A. M. Impact of flood defences and sea-level rise on the European Shelf tidal regime. *Continental Shelf Research*, 34:96–105, 2014. [10.1016/j.csr.2014.04.011](https://doi.org/10.1016/j.csr.2014.04.011).
- Pelling, H. E., Green, J. A. M., and Ward, S. L. Modelling tides and sea-level rise: To flood or not to flood. *Ocean Modelling*, 38:21–29, 2013. [10.1016/j.ocemod.2012.12.004](https://doi.org/10.1016/j.ocemod.2012.12.004).
- Peltier, W. R., Argus, D. F., and Drummond, R. Space geodesy constrains ice age terminal deglaciation: The global ICE-6G_C (VM5a) model. *Journal of Geophysical Research: Solid Earth*, 119:450–487, 2014. [10.1002/2014JB011176](https://doi.org/10.1002/2014JB011176).
- Penduff, T., Juza, M., Brodeau, L., Smith, G. C., Barnier, B., Molines, J. M., Treguier, A. M., and Madec, G. Impact of global ocean model resolution on sea-level variability with emphasis on interannual time scales. *Ocean Science*, 6:269–284, 2010. [10.5194/os-6-269-2010](https://doi.org/10.5194/os-6-269-2010).
- Pickering, M. D., Wells, N. C., Horsburgh, K. J., and Green, J. A. The impact of future sea-level rise on the European Shelf tides. *Continental Shelf Research*, 2012. [10.1016/j.csr.2011.11.011](https://doi.org/10.1016/j.csr.2011.11.011).
- Piecuch, C. G., Calafat, F. M., Dangendorf, S., and Jordà, G. The Ability of Barotropic Models to Simulate Historical Mean Sea Level Changes from Coastal Tide Gauge Data. *Surveys in Geophysics*, 40:1399–1435, 2019. [10.1007/s10712-019-09537-9](https://doi.org/10.1007/s10712-019-09537-9).
- Pingree, R. and Cann, B. L. Celtic and Armorican slope and shelf residual currents. *Progress in Oceanography*, 23:303–338, 1989. [10.1016/0079-6611\(89\)90003-7](https://doi.org/10.1016/0079-6611(89)90003-7).
- Pingree, R. and Griffiths, D. K. Currents driven by a steady uniform wind stress on the shelf seas around the British Isles. *Oceanologica Acta*, 3:227–236, 1980.
- Plag, H. and Tsimplis, M. N. Temporal variability of the seasonal sea-level cycle in the North Sea and Baltic Sea in relation to climate variability. *Global and Planetary Change*, 20:173–203, 1999. [10.1016/S0921-8181\(98\)00069-1](https://doi.org/10.1016/S0921-8181(98)00069-1).
- Ponte, R. M. and Ray, R. D. Atmospheric pressure corrections in geodesy and oceanography: A strategy for handling air tides. *Geophys Res Lett*, 29:2–5, 2002. [10.1029/2002GL016340](https://doi.org/10.1029/2002GL016340).
- Ponte, R. M. A preliminary model study of the larger-scale seasonal cycle in bottom pressure over the global ocean. *Journal of Geophysical Research: Oceans*, 104:1289–1300, 1999. [10.1029/1998JC900028](https://doi.org/10.1029/1998JC900028).

- Ponte, R. M., Carson, M., Cirano, M., Domingues, C. M., Jevrejeva, S., Marcos, M., Mitchum, G., van de Wal, R. S. W., Woodworth, P. L., Ablain, M., Ardhuin, F., Ballu, V., Becker, M., Benveniste, J., Birol, F., Bradshaw, E., Cazenave, A., Mey-Frémaux, P. D., Durand, F., Ezer, T., Fu, L.-L., Fukumori, I., Gordon, K., Gravelle, M., Griffies, S. M., Han, W., Hibbert, A., Hughes, C. W., Idier, D., Kourafalou, V. H., Little, C. M., Matthews, A., Melet, A., Merrifield, M., Meyssignac, B., Minobe, S., Penduff, T., Picot, N., Piecuch, C., Ray, R. D., Rickards, L., Santamaría-Gómez, A., Stammer, D., Staneva, J., Testut, L., Thompson, K., Thompson, P., Vignudelli, S., Williams, J., Williams, S. D. P., Wöppelmann, G., Zanna, L., and Zhang, X. Towards Comprehensive Observing and Modeling Systems for Monitoring and Predicting Regional to Coastal Sea Level. *Frontiers in Marine Science*, 6:1–25, 2019. [10.3389/fmars.2019.00437](https://doi.org/10.3389/fmars.2019.00437).
- PSMSL. Tide Gauge Data, 2018. URL <http://www.psmsl.org/data/obtaining/>. Accessed on: 15-03-2018.
- PSMSL. Tide Gauge Data, 2020. URL <http://www.psmsl.org/data/obtaining/>. Accessed on: 01-03-2020.
- Pugh, D. *Tides, Surges and Mean Sea-Level*. John Wiley & Sons Ltd., 1987. ISBN 978-0471915058.
- Rahmstorf, S., Cazenave, A., Church, J. A., Hansen, J. E., Keeling, R. F., Parker, D. E., and Somerville, R. C. J. Recent Climate Observations Compared to Projections. *Science*, 316:709–, 2007. [10.1126/science.1136843](https://doi.org/10.1126/science.1136843).
- Renshaw, C. R., Wakelin, S., Mahdon, R., O’Dea, E., and Tinker, J. North West European Shelf Production Centre NORTHWESTSHELF_REANALYSIS_PHY_004_009, 2019. URL <https://doi.org/10.48670/moi-00059>.
- Richter, K., Nilsen, J., Raj, P., Bethke, I., Johannessen, J., Slangen, A., and Marzeion, B. Northern North Atlantic Sea Level in CMIP5 Climate Models: Evaluation of Mean State, Variability, and Trends against Altimetric Observations. *Journal of Climate*, 30:9383–9398, 2017. [10.1175/JCLI-D-17-0310.1](https://doi.org/10.1175/JCLI-D-17-0310.1).
- Ricker, M. and Stanev, E. V. Circulation of the European northwest shelf: a Lagrangian perspective. *Ocean Science*, 16:637–655, 5 2020. [10.5194/os-16-637-2020](https://doi.org/10.5194/os-16-637-2020).
- Rio, M., Mulet, S., and Picot, N. Beyond GOCE for the ocean circulation estimate: Synergetic use of altimetry, gravimetry, and in situ data provides new insight into geostrophic and Ekman currents. *Geophysical Research Letters*, 41:8918–8925, 2014. [10.1002/2014GL061773](https://doi.org/10.1002/2014GL061773).
- Roberts, C., Calvert, D., Dunstone, N., Hermanson, L., Palmer, M., and Smith, D. On the Drivers and Predictability of Seasonal-to-Interannual Variations in Regional Sea Level. *Journal of Climate*, 2009: 7565–7585, 2016. [10.1175/JCLI-D-15-0886.1](https://doi.org/10.1175/JCLI-D-15-0886.1).
- Roberts-Jones, J., Fiedler, E., and Martin, M. Daily, Global, High-Resolution SST and Sea Ice Reanalysis for 1985–2007 Using the OSTIA System. *Journal of Climate*, 25:6215–6232, 2012. [10.1175/JCLI-D-11-00648.1](https://doi.org/10.1175/JCLI-D-11-00648.1).
- Rugenstein, M., Bloch-Johnson, J., Gregory, J., Mauritsen, T., Li, C., Frolicher, T., Paynter, D., Danabasoglu, G., Yang, S., Dufresne, J., Cao, L., Schmidt, G., Abe-Ouchi, A., Geoffroy, O., and Knutti, R. Equilibrium Climate Sensitivity Estimated by Equilibrating Climate Models. *Geophysical Research Letters*, 47, 2020. [10.1029/2019GL083898](https://doi.org/10.1029/2019GL083898).
- Rummukainen, M. State-of-the-art with regional climate models. *WIREs Climate Change*, 1:82–96, 2010. [10.1002/wcc.8](https://doi.org/10.1002/wcc.8).
- Scaife, A. A., Arribas, A., Blockley, E., Brookshaw, A., Clark, R. T., Dunstone, N., Eade, R., Fereday, D., Folland, C. K., Gordon, M., Hermanson, L., Knight, J. R., Lea, D. J., MacLachlan, C., Maidens, A., Martin, M., Peterson, A. K., Smith, D., Vellinga, M., Wallace, E., Waters, J., and Williams, A. Skillful long-range prediction of European and North American winters. *Geophysical Research Letters*, 41: 2514–2519, 4 2014. [10.1002/2014GL059637](https://doi.org/10.1002/2014GL059637).

- Schrum, C., Lowe, J., Meier, H. E. M., Grabemann, I., Holt, J., and Mathis, M. Projected Change—North Sea. In Quante, M. and Colijn, F., editors, *North Sea Region Climate Change Assessment*, pages 175–217. Springer, 2016. ISBN 9783319397436.
- Sen Gupta, A., Jourdain, N. C., Brown, J. N., and Monselesan, D. Climate Drift in CMIP5 Models. *Journal of Climate*, 26:8597–8615, 2013. [10.1175/JCLI-D-12-00521.1](https://doi.org/10.1175/JCLI-D-12-00521.1).
- Shchepetkin, A. F. and McWilliams, J. C. The regional oceanic modeling system (ROMS): a split-explicit, free-surface, topography-following-coordinate oceanic model. *Ocean Modelling*, 9:347–404, 2005. [10.1016/j.ocemod.2004.08.002](https://doi.org/10.1016/j.ocemod.2004.08.002).
- Shepherd, T. G. Atmospheric circulation as a source of uncertainty in climate change projections. *Nature Geoscience*, 7:703–708, 2014. [10.1038/ngeo2253](https://doi.org/10.1038/ngeo2253).
- Sherwood, A. S., Webb, M. J., Annan, J. D., Armour, K. C., Forster, P. M., Hargreaves, J., Hegerl, G., Klein, S., Marvel, K., Rohling, E., Watanabe, M., Andrews, T., Braconnot, P., Bretherton, C., Foster, G., Hausfather, Z., der Heydt, A. V., Knutti, R., Mauritsen, T., Norris, J., Proistosescu, C., Rugenstein, M., Schmidt, G., Tokarska, K., and Zelinka, M. An assessment of Earth's climate sensitivity using multiple lines of evidence. *Review of Geophysics*, 58:1–166, 2020. [10.1029/2019RG000678](https://doi.org/10.1029/2019RG000678).
- Siddorn, J. R. and Furner, R. An analytical stretching function that combines the best attributes of geopotential and terrain-following vertical coordinates. *Ocean Modelling*, 66:1–13, 2013. [10.1016/j.ocemod.2013.02.001](https://doi.org/10.1016/j.ocemod.2013.02.001).
- Slangen, A. B. A., Katsman, C. A., van de Wal, R. S. W., Vermeersen, L. L. A., and Riva, R. E. M. Towards regional projections of twenty-first century sea-level change based on IPCC SRES scenarios. *Climate Dynamics*, 38:1191–1209, 2012. [10.1007/s00382-011-1057-6](https://doi.org/10.1007/s00382-011-1057-6).
- Slangen, A. B. A., Carson, M., Katsman, C. A., van de Wal, R. S. W., Köhl, A., Vermeersen, L. L. A., Stammer, D., van de Wal, R. S. W., Köhl, A., Vermeersen, L. L. A., and Stammer, D. Projecting twenty-first century regional sea-level changes. *Climatic Change*, 124:317–332, 5 2014. [10.1007/s10584-014-1080-9](https://doi.org/10.1007/s10584-014-1080-9).
- Song, Y. and Haidvogel, D. A Semi-implicit Ocean Circulation Model Using a Generalized Topography-Following Coordinate System. *Journal of Computational Physics*, 115:228–244, 1994. [10.1006/jcph.1994.1189](https://doi.org/10.1006/jcph.1994.1189).
- Stammer, D. and Hüttemann, S. Response of Regional Sea Level to Atmospheric Pressure Loading in a Climate Change Scenario. *J. Clim.*, 21:2093–2101, 2008. [10.1175/2007JCLI1803.1](https://doi.org/10.1175/2007JCLI1803.1).
- Stammer, D., van De Wal, R. S. W., Nicholls, R. J., Church, J. A., Cozannet, G. L., Lowe, J., Horton, B., White, K., Behar, D., and Hinkel, J. Framework for High-End Estimates of Sea Level Rise for Stakeholder Applications. *Earth's Future*, 7:923–938, 2019. [10.1029/2019EF001163](https://doi.org/10.1029/2019EF001163).
- Sterl, A., van den Brink, H., de Vries, H., Haarsma, R., and Meijgaard, E. V. An ensemble study of extreme storm surge related water levels in the North Sea in a changing climate. *Ocean Science*, 5:369–378, 2009. [10.5194/os-5-369-2009](https://doi.org/10.5194/os-5-369-2009).
- Sterlini, P., de Vries, H., and Katsman, C. Sea surface height variability in the North East Atlantic from satellite altimetry. *Climate Dynamics*, 47:1285–1302, 2016. [10.1007/s00382-015-2901-x](https://doi.org/10.1007/s00382-015-2901-x).
- Strandberg, G., Barring, L., Hansson, U., Jansson, C., and Jones, C. CORDEX scenarios for Europe from the Rossby Centre regional climate model RCA4, 2014. SMHI, Report Meteorology and Climatology, No. 116.
- Sturges, W. and Douglas, B. C. Wind effects on estimates of sea level rise. *Journal of Geophysical Research: Oceans*, 116, 2011. [10.1029/2010JC006492](https://doi.org/10.1029/2010JC006492).

- Suzuki, T., Hasumi, H., Sakamoto, T. T., Nishimura, T., Abe-Ouchi, A., Segawa, T., Okada, N., Oka, A., and Emori, S. Projection of future sea level and its variability in a high-resolution climate model: Ocean processes and Greenland and Antarctic ice-melt contributions. *Geophys Res Lett*, 32, 2005. [10.1029/2005GL023677](https://doi.org/10.1029/2005GL023677).
- Swart, N. C., Cole, J. N. S., Kharin, V. V., Lazare, M., Scinocca, J. F., Gillett, N. P., Anstey, J., Arora, V., Christian, J. R., Hanna, S., Jiao, Y., Lee, W. G., Majaess, F., Saenko, O. A., Seiler, C., Seinen, C., Shao, A., Sigmond, M., Solheim, L., Salzen, K. V., Yang, D., and Winter, B. The Canadian Earth System Model version 5 (CanESM5.0.3). *Geoscientific Model Development*, 12:4823–4873, 2019. [10.5194/gmd-12-4823-2019](https://doi.org/10.5194/gmd-12-4823-2019).
- Syvitski, J. P. M., Kettner, A. J., Overeem, I., Hutton, E. W. H., Hannon, M. T., Brakenridge, G. R., Day, J., Vörösmarty, C., Saito, Y., Giosan, L., and Nicholls, R. J. Sinking deltas due to human activities. *Nature Geoscience*, 2:681–686, 2009. [10.1038/ngeo629](https://doi.org/10.1038/ngeo629).
- Sérazin, G., Penduff, T., Grégorio, S., Barnier, B., Molines, J.-M., and Terray, L. Intrinsic Variability of Sea Level from Global 1/12th Degree Ocean Simulations: Spatiotemporal Scales. *Journal of Climate*, 28: 4279–4292, 2015. [10.1175/JCLI-D-14-00554.1](https://doi.org/10.1175/JCLI-D-14-00554.1).
- Taylor, K., Stouffer, R. J., and Meehl, G. A. An Overview of CMIP5 and the Experiment Design. *Bull Am Meteorol Soc*, 93:485–498, 2012. [10.1175/BAMS-D-11-00094.1](https://doi.org/10.1175/BAMS-D-11-00094.1).
- Tebaldi, C. and Knutti, R. The use of the multi-model ensemble in probabilistic climate projections. *Philosophical Transactions of the Royal Society A: Mathematical, Physical and Engineering Sciences*, 365:2053–2075, 2007. [10.1098/rsta.2007.2076](https://doi.org/10.1098/rsta.2007.2076).
- Tebaldi, C., Debeire, K., Eyring, V., Fischer, E., Fyfe, J., Friedlingstein, P., Knutti, R., Lowe, J., O'Neill, B., Sanderson, B., Vuuren, D. V., Riahi, K., Meinshausen, M., Nicholls, Z., Tokarska, K., Hurtt, G., Kriegler, E., Meehl, G., Moss, R., Bauer, S., Boucher, O., Brovkin, V., Yhb, Y., Dix, M., Gualdi, S., Guo, H., John, J., Kharin, S., Kim, Y. H., Koshiro, T., Ma, L., Olivie, D., Panickal, S., Qiao, F., Rong, X., Rosenbloom, N., Schupfner, M., Séférian, R., Sellar, A., Semmler, T., Shi, X., Song, Z., Steger, C., Stouffer, R., Swart, N., Tachiiri, K., Tang, Q., Tatebe, H., Voldoire, A., Volodin, E., Wyser, K., Xin, X., Yang, S., Yu, Y., and Ziehn, T. Climate model projections from the Scenario Model Intercomparison Project (ScenarioMIP) of CMIP6. *Earth System Dynamics*, 12:253–293, 3 2021. [10.5194/esd-12-253-2021](https://doi.org/10.5194/esd-12-253-2021).
- Thompson, K. R. North Atlantic sea-level and circulation. *Geophys. J. R. Astron. Soc.*, 87:15–32, 1986. [10.1111/j.1365-246X.1986.tb04543.x](https://doi.org/10.1111/j.1365-246X.1986.tb04543.x).
- Thompson, P. R., Piecuch, C. G., Merrifield, M. A., McCreary, J. P., and Firing, E. Forcing of recent decadal variability in the Equatorial and North Indian Ocean. *Journal of Geophysical Research : Oceans*, 121: 6762–6778, 2016. [10.1002/2016JC012132](https://doi.org/10.1002/2016JC012132).
- Tinker, J., Lowe, J., Holt, J., Pardaens, A., and Wiltshire, A. Validation of an ensemble modelling system for climate projections for the northwest European shelf seas. *Progress in Oceanography*, 138:211–237, 2015. [10.1016/j.pocean.2015.07.002](https://doi.org/10.1016/j.pocean.2015.07.002).
- Tinker, J., Lowe, J., Pardaens, A., Holt, J., and Barciela, R. Uncertainty in climate projections for the 21st century northwest European shelf seas. *Progress in Oceanography*, 148:56–73, 2016. [10.1016/j.pocean.2016.09.003](https://doi.org/10.1016/j.pocean.2016.09.003).
- Tinker, J., Krijnen, J., Wood, R., Barciela, R., and Dye, S. R. What are the prospects for seasonal prediction of the marine environment of the North-west European Shelf? *Ocean Science*, 14:887–909, 8 2018. [10.5194/os-14-887-2018](https://doi.org/10.5194/os-14-887-2018).
- Tinker, J., Palmer, M. D., Copsey, D., Howard, T., Lowe, J. A., and Hermans, T. H. J. Dynamical downscaling of unforced interannual sea-level variability in the North-West European shelf seas. *Climate Dynamics*, 55:2207–2236, 2020. [10.1007/s00382-020-05378-0](https://doi.org/10.1007/s00382-020-05378-0).

- Tokarska, K. B., Stolpe, M. B., Sippel, S., Fischer, E. M., Smith, C. J., Lehner, F., and Knutti, R. Past warming trend constrains future warming in CMIP6 models. *Science Advances*, 6:1–14, 2020. [10.1126/sciadv.aaz9549](https://doi.org/10.1126/sciadv.aaz9549).
- Tsimplis, M., Marcos, M., Somot, S., and Barnier, B. Sea level forcing in the Mediterranean Sea between 1960 and 2000. *Global and Planetary Change*, 63:325–332, 2008. [10.1016/j.gloplacha.2008.07.004](https://doi.org/10.1016/j.gloplacha.2008.07.004).
- Tsimplis, M. N. and Woodworth, P. L. The global distribution of the seasonal sea level cycle calculated from coastal tide gauge data. *Journal of Geophysical Research Atmospheres*, 991:16031–16040, 1994. [10.1029/94JC01115](https://doi.org/10.1029/94JC01115).
- Tsimplis, M., Woolf, D., Osborn, T., Wakelin, S., Wolf, J., Flather, R., Shaw, A., Woodworth, P., Challenor, P., Blackman, D., Pert, F., Yan, Z., and Jevrejeva, S. Towards a vulnerability assessment of the UK and northern European coasts: the role of regional climate variability. *Phil. Trans. R. Soc. A*, 363: 1329–1358, 2005. [10.1098/rsta.2005.1571](https://doi.org/10.1098/rsta.2005.1571).
- Vega-Westhoff, B., Sriver, R. L., Hartin, C., Wong, T. E., and Keller, K. The Role of Climate Sensitivity in Upper-Tail Sea Level Rise Projections. *Geophysical Research Letters*, 47:1–8, 2020. [10.1029/2019GL085792](https://doi.org/10.1029/2019GL085792).
- Vinogradov, S. V., Ponte, R. M., Heimbach, P., and Wunsch, C. The mean seasonal cycle in sea level estimated from a data-constrained general circulation model. *Journal of Geophysical Research*, 113: 1–15, 2008. [10.1029/2007JC004496](https://doi.org/10.1029/2007JC004496).
- Vinogradova, N. T., Ponte, R. M., and Stammer, D. Relation between sea level and bottom pressure and the vertical dependence of oceanic variability. *Geophysical Research Letters*, 34:1–5, 2007. [10.1029/2006GL028588](https://doi.org/10.1029/2006GL028588).
- Vizcaino, M. Ice sheets as interactive components of Earth System Models: Progress and challenges. *Wiley Interdisciplinary Reviews: Climate Change*, 5:557–568, 2014. [10.1002/wcc.285](https://doi.org/10.1002/wcc.285).
- Voldoire, A., Martin, D. S., S  n  si, S., Decharme, B., Alias, A., Chevallier, M., Colin, J., Gu  r  my, J.-F., Michou, M., Moine, M.-P., Nabat, P., Roehrig, R., y M  lia, D. S., S  f  rian, R., Valcke, S., Beau, I., Belamari, S., Berthet, S., Cassou, C., Cattiaux, J., Deshayes, J., Douville, H., Eth  , C., Franchist  guy, L., Geoffroy, O., L  vy, C., Madec, G., Meurdesoif, Y., Msadek, R., Ribes, A., Sanchez-Gomez, E., Terray, L., and Waldman, R. Evaluation of CMIP6 DECK Experiments With CNRM-CM6-1. *Journal of Advances in Modeling Earth Systems*, 11:2177–2213, 2019. [10.1029/2019MS001683](https://doi.org/10.1029/2019MS001683).
- Volodin, E. M. and Gritsun, A. S. Simulation of Possible Future Climate Changes in the 21st Century in the INM-CM5 Climate Model. *Earth System Dynamics*, 9:1235–1242, 2018. [10.1134/S0001433820030123](https://doi.org/10.1134/S0001433820030123).
- Vousdoukas, M. I., Mentaschi, L., Voukouvalas, E., Verlaan, M., Jevrejeva, S., Jackson, L. P., and Feyen, L. Global probabilistic projections of extreme sea levels show intensification of coastal flood hazard. *Nature Communications*, 9:2360, 6 2018. [10.1038/s41467-018-04692-w](https://doi.org/10.1038/s41467-018-04692-w).
- de Vries, H., Katsman, C., and Drijfhout, S. Constructing scenarios of regional sea level change using global temperature pathways. *Environmental Research Letters*, 9, 2014. [10.1088/1748-9326/9/11/115007](https://doi.org/10.1088/1748-9326/9/11/115007).
- Wada, Y., Lo, M.-H., Yeh, P.-F., Reager, J. T., Famiglietti, J. S., Wu, R.-J., and Tseng, Y.-H. Fate of water pumped from underground and contributions to sea-level rise. *Nature Climate Change*, 6:8–13, 2016. [10.1038/NCLIMATE3001](https://doi.org/10.1038/NCLIMATE3001).
- Wada, Y., Reager, J. T., Chao, B. F., Wang, J., and Chunqiao, M.-H. L. Recent Changes in Land Water Storage and its Contribution to Sea Level Variations. *Surveys in Geophysics*, 38:131–152, 2017. [10.1007/s10712-016-9399-6](https://doi.org/10.1007/s10712-016-9399-6).
- Wahl, T., Haigh, I., Woodworth, P. L., Albrecht, F., Dillingh, D., Jensen, J., Nicholls, R., Weisse, R., and W  ppelmann, G. Observed mean sea level changes around the North Sea coastline from 1800 to present. *Earth Science Reviews*, 124:51–67, 2013. [10.1016/j.earscirev.2013.05.003](https://doi.org/10.1016/j.earscirev.2013.05.003).

- Wakelin, S. L., Woodworth, P. L., Flather, R. A., and Williams, J. A. Sea-level dependence on the NAO over the NW European Continental Shelf. *Geophysical Research Letters*, 30:1–4, 2003. [10.1029/2003GL017041](https://doi.org/10.1029/2003GL017041).
- Wakelin, S. L., Artioli, Y., Butenschön, M., Allen, J. I., and Holt, J. T. Modelling the combined impacts of climate change and direct anthropogenic drivers on the ecosystem of the northwest European continental shelf. *Journal of Marine Systems*, 152:51–63, 2015. [10.1016/j.jmarsys.2015.07.006](https://doi.org/10.1016/j.jmarsys.2015.07.006).
- Ward, S. L., Green, J. A., and Pelling, H. E. Tides, sea-level rise and tidal power extraction on the European shelf. *Ocean Dynamics*, 62:1153–1167, 2012. [10.1007/s10236-012-0552-6](https://doi.org/10.1007/s10236-012-0552-6).
- Whitehouse, P. Glacial isostatic adjustment modelling: historical perspectives, recent advances, and future directions. *Earth Surface Dynamics*, 6:401–429, 2018. [10.5194/esurf-6-401-2018](https://doi.org/10.5194/esurf-6-401-2018).
- Widlansky, M. J., Long, X., and Schloesser, F. Increase in sea level variability with ocean warming associated with the nonlinear thermal expansion of seawater. *Communications Earth & Environment*, 1:1–12, 2020. [10.1038/s43247-020-0008-8](https://doi.org/10.1038/s43247-020-0008-8).
- Williams, K. D., Copsey, D., Blockley, E. W., Bodas-Salcedo, A., Calvert, D., Comer, R., Davis, P., Graham, T., Hewitt, H. T., Hill, R., Hyder, P., Ineson, S., Johns, T. C., Keen, A. B., Lee, R. W., Megann, A., Milton, S. F., Rae, J. G. L., Roberts, M. J., Scaife, A. A., Schiemann, R., Storkey, D., Thorpe, L., Watterson, I. G., Walters, D. N., West, A., Wood, R. A., Woollings, T., and Xavier, P. K. The Met Office Global Coupled Model 3.0 and 3.1 (GC3.0 and GC3.1) Configurations. *Journal of Advances in Modeling Earth Systems*, 10:357–380, 2018. [10.1002/2017MS001115](https://doi.org/10.1002/2017MS001115).
- Williams, K., Hewitt, A., and Bodas-Salcedo, A. Use of Short-Range Forecasts to Evaluate Fast Physics Processes Relevant for Climate Sensitivity. *Journal of Advances in Modeling Earth Systems*, 12:1–9, 2020. [10.1029/2019MS001986](https://doi.org/10.1029/2019MS001986).
- de Winter, R. C., Sterl, A., and Ruessink, B. G. Wind extremes in the North Sea Basin under climate change: An ensemble study of 12 CMIP5 GCMs. *Journal of Geophysical Research Atmospheres*, 118: 1601–1612, 2013. [10.1002/jgrd.50147](https://doi.org/10.1002/jgrd.50147).
- Woodworth, P. L., White, N. J., Jevrejeva, S., Holgate, S. J., Church, J. A., and Gehrels, W. R. Evidence for the accelerations of sea level on multi-decade and century timescales. *Int. J. Climatol.*, 29:777–789, 2009. [10.1002/joc.1771](https://doi.org/10.1002/joc.1771).
- Woodworth, P. L., Pouvreau, N., and Wöppelman, G. The gyre-scale circulation of the North Atlantic and sea level at Brest. *Ocean Science*, 6:185–190, 2010. [10.5194/os-6-185-2010](https://doi.org/10.5194/os-6-185-2010).
- Woodworth, P. L. A Note on the Nodal Tide in Sea Level Records. *Journal of Coastal Research*, 28: 316–323, 2012. [10.2112/JCOASTRES-D-11A-00023.1](https://doi.org/10.2112/JCOASTRES-D-11A-00023.1).
- Woolf, D. K., Shaw, A., and Tsimplis, M. The influence of the North Atlantic Oscillation on sea-level variability in the North Atlantic region. *Journal of Atmospheric & Ocean Science*, 9:145–167, 2003. [10.1080/10236730310001633803](https://doi.org/10.1080/10236730310001633803).
- Woollings, T. Dynamical influences on European climate: an uncertain future. *Phil. Trans. R. Soc. A*, 368:3733–3756, 2010. [10.1098/rsta.2010.0040](https://doi.org/10.1098/rsta.2010.0040).
- Wöppelmann, G. and Marcos, M. Vertical land motion as a key to understanding sea level change and variability. *Reviews of Geophysics*, 54:64–92, 3 2016. [10.1002/2015RG000502](https://doi.org/10.1002/2015RG000502).
- Yin, J. Century to multi-century sea level rise projections from CMIP5 models. *Geophysical Research Letters*, 39, 2012. [10.1029/2012GL052947](https://doi.org/10.1029/2012GL052947).
- Yin, J., Griffies, S. M., and Stouffer, R. J. Spatial Variability of Sea-Level Rise in 21st Century Projections. *Journal of Climate*, 23:4585–4607, 2010. [10.1175/2010JCLI3533.1](https://doi.org/10.1175/2010JCLI3533.1).

- Zelinka, M. D., Myers, T. A., McCoy, D. T., Po-Chedley, S., Caldwell, P. M., Ceppi, P., Klein, S. A., and Taylor, K. E. Causes of Higher Climate Sensitivity in CMIP6 Models. *Geophysical Research Letters*, 47: 1–12, 2020. [10.1029/2019GL085782](https://doi.org/10.1029/2019GL085782).
- Zhang, X., Church, J. A., Monselesan, D., and McInnes, K. L. Sea level projections for the Australian region in the 21st century. *Geophysical Research Letters*, 44:8481–8491, 2017. [10.1002/2017GL074176](https://doi.org/10.1002/2017GL074176).
- Ådlandsvik, B. Marine downscaling of a future climate scenario for the North Sea. *Tellus, Series A: Dynamic Meteorology and Oceanography*, 60 A:451–458, 2008. [10.1111/j.1600-0870.2007.00311.x](https://doi.org/10.1111/j.1600-0870.2007.00311.x).
- Ådlandsvik, B. and Bentsen, M. Downscaling a twentieth century global climate simulation to the North Sea. *Ocean Dynamics*, 57:453–466, 2007. [10.1007/s10236-007-0125-2](https://doi.org/10.1007/s10236-007-0125-2).

Data Statements

Chapter 2

The CMIP6 data was extracted from ESGF on November 2, 2020. Chris Jones provided the CMIP6 GSAT time series, processed using JASMIN on November 1, 2020. The CMIP6 data and Monte Carlo GMSL projections produced for this chapter are available from the 4TU.ResearchData repository: <http://doi.org/10.4121/12958079>.

The WCRP, which, through its Working Group on Coupled Modeling, coordinated and promoted CMIP6, is hereby acknowledged. The climate modeling groups are thanked for producing and making available their model output, the ESGF for archiving the data and providing access, and the multiple funding agencies who support CMIP6 and ESGF.

Chapter 3

The dynamically downscaled simulations underlying the figures are available from the 4TU.ResearchData repository: <https://doi.org/10.4121/uuid:ef1c5cca-3900-49f3-9049-6719598a128d>.

The World Climate Research Programme's Working Group on Coupled Modeling, which is responsible for CMIP5, is hereby acknowledged. The associated climate modeling groups are thanked for producing and making available their model output used in this study. For CMIP5 the U.S. Department of Energy's Program for Climate Model Diagnosis and Intercomparison provides coordinating support and led development of software infrastructure in partnership with the Global Organization for Earth System Science Portals.

Chapter 4

The ROMS input and output files are available from the 4TU.ResearchData repository: <http://doi.org/10.4121/uuid:d9656541-ff40-45d0-8859-ac644b155dfb>.

This study has been conducted using E.U. Copernicus Marine Service Information (2019). Neither the European Commission nor ECMWF is responsible for any use that may be made of the Copernicus Information or Data it contains.

Chapter 5

The CMIP6 data was extracted from ESGF in July 2021. The processed CMIP6 output and the output of the ROMS model experiments underlying the figures can

be obtained from the 4TU.ResearchData repository: <https://doi.org/10.4121/16831918>.

The code used to obtain, process and analyze this data is available at Zenodo: <https://doi.org/10.5281/zenodo.5654667>.

This study has been conducted using E.U. Copernicus Marine Service Information (2019). Neither the European Commission nor ECMWF is responsible for any use that may be made of the Copernicus Information or Data it contains.

The WCRP, which, through its Working Group on Coupled Modeling, coordinated and promoted CMIP6, is hereby acknowledged. The climate modeling groups are thanked for producing and making available their model output, the ESGF for archiving the data and providing access, and the multiple funding agencies who support CMIP6 and ESGF.

Acknowledgements

Mijn dank gaat uit naar iedereen die direct of indirect heeft bijgedragen aan mijn proefschrift. Allereerst, Aimée: ontzettend bedankt voor je begeleiding in de laatste 4,5 jaar. Volgens mij zijn er weinig begeleiders zo betrokken als jij. Ik hoop dat we nog vele jaren kunnen samenwerken! Ook enorm bedankt voor jouw begeleiding, Caroline. Van jou heb ik geleerd dat het niet erg is om soms dingen niet te weten en dat dat juist is waar wetenschap over gaat. Het was een voorrecht om je handschrift te mogen ontcijferen. Bedankt Bert voor het in de gaten houden van de voortgang en je hulp bij het navigeren door de wirwar van administratie van de TU Delft. Thank you to Carolina for being my PhD Partner-In-Crime and helping me through the ups and downs of PhD life. Thank you to Lauren and Rosanna for being awesome office mates. Our conversations, tea-drinking contests and whiteboard doodling have been much appreciated distractions. Thank you to all the other PhDs and PostDocs at NIOZ as well for maintaining such a friendly and inspiring atmosphere. Thank you to the rest of my colleagues at NIOZ who have supported me in all kinds of ways, in particular Klaas, Theo, Suzanne, Anneke, Jan, Christine, Elly, Jan Thijs and Hans. Thank you to Victor, Theo, Johan, Long, Karen, Caroline, Carolina, Aimée, Annette, Bert, Esmee and others for attending the sea-level group meetings. Thank you to Annette for writing your MSc thesis with me.

Also the help of people outside of NIOZ has been invaluable. Thank you to Matt for hosting me at the Met Office and for being so supportive and inspiring. Thank you to Jon for sharing your simulations for my first paper and for the personal touch to our professional relationship. Thank you to Dewi for sharing your ocean model with me and enduring our lengthy conversations and e-mails. Thank you to Francisco, Jonathan, Bob and Greg for being patient and kind, answering my many questions. Thank you to Roderik for supervising Annette together with me. Thank you to Helene, Baylor, Bob, Aimée and Greg for giving me the opportunity to contribute to IPCC AR6. Thank you to Caroline, Julie, Lennart, Carine and Sotiria for the oceanography group meetings.

Writing this dissertation has been much more fun and bearable thanks to my friends and family. Thank you to all my housemates in the Keete who made it so fun to live there. Thank you to all the people that joined NIOZ soccer, which never disappoints. Thank you to Carolina, Roeland, Dunia, Zack, Marte, Lauren, Colin, Puck, Greg, Rosanna, Mo, Victor, Chiu and Jaco for all the good times in and around Bergen op Zoom. Bedankt Rogier, Maura, Marieke, Bastiaan, Belinda, Tim en Eva: jullie zijn stuk voor stuk superleuke mensen en dierbare vrienden. Bedankt Papa, Mama, Lieke, Tessa, Matthijs en Jelle: op jullie kan ik altijd rekenen en dat is een onmeetbaar voorrecht. Bedankt Martin, Margo en Thijs voor jullie enthousiasme en

interesse. Tot slot, Roos: in één dankwoord omschrijven wat je voor me betekent is onmogelijk, en waarschijnlijk zou je dat toch alleen maar ongemakkelijk vinden. Bedankt voor je onvoorwaardelijke steun, geduld en al het andere.

Curriculum Vitæ

Tim H.J. Hermans was born in Alphen aan den Rijn, The Netherlands, on the 15th of November, 1994. After graduating from Pre-University Secondary School at the OSG Erasmus in 2012, Tim started with a BSc program in Mechanical Engineering at the University of Twente, which he completed *cum laude* in 2015. He then moved to Delft and obtained his MSc degree in Aerospace Engineering *cum laude* in 2017. While writing his MSc thesis on glacial isostatic adjustment in Antarctica, Tim became interested in geoscience. He therefore started his PhD project on sea-level change at NIOZ and Delft University of Technology in 2018. During his PhD project, Tim also served as a contributing author and chapter scientist of the Sixth Assessment Report of the IPCC.



List of Publications

1. **Hermans, T.H.J.**, Van der Wal, W., & Broerse, T. (2018). Reversal of the Direction of Horizontal Velocities Induced by GIA as a Function of Mantle Viscosity, *Geophysical Research Letters*, 45, 9597-9604. [10.1029/2018GL078533](https://doi.org/10.1029/2018GL078533)
2. **Hermans, T.H.J.**, Tinker, J., Palmer, M.D., Katsman, C.A., Vermeersen, B.L.A., & Slangen, A.B.A. (2020). Improving sea-level projections on the Northwestern European shelf using dynamical downscaling, *Climate Dynamics*, 54, 1987-2011. [10.1007/s00382-019-05104-5](https://doi.org/10.1007/s00382-019-05104-5)
3. Tinker, J., Palmer, M.D., Copsey, D., Howard, T., Lowe, J.A., & **Hermans, T.H.J.** (2020). Dynamical downscaling of unforced interannual sea-level variability in the North-West European shelf seas, *Climate Dynamics*, 55, 2207-2236. [10.1007/s00382-020-05378-0](https://doi.org/10.1007/s00382-020-05378-0)
4. Romero-Calvo, A., Cano-Gómez, G., **Hermans, T.H.J.**, Parrilla Benítez, L., Herrada Gutiérrez, A.H., & Castro-Hernández, E. (2020). Total magnetic force on a ferrofluid droplet in microgravity, *Experimental Thermal and Fluid Science*, 117, 110124. [10.1016/j.expthermflusci.2020.110124](https://doi.org/10.1016/j.expthermflusci.2020.110124)
5. **Hermans, T.H.J.**, Le Bars, D., Katsman, C.A., Camargo, C.M.L., Gerkema, T., Calafat, F.M., Tinker, J., & Slangen, A.B.A. (2020). Drivers of Interannual Sea Level Variability on the Northwestern European Shelf, *Journal of Geophysical Research: Oceans*, 125, e2020JC016325. [10.1029/2020JC016325](https://doi.org/10.1029/2020JC016325)
6. Camargo, C.M.L., Riva, R.E.M., **Hermans, T.H.J.**, & Slangen, A.B.A. (2020). Exploring Sources of Uncertainty in Steric Sea-Level Change Estimates, *Journal of Geophysical Research: Oceans*, 125, e2020JC016551. [10.1029/2020JC016551](https://doi.org/10.1029/2020JC016551)
7. **Hermans, T.H.J.**, Gregory, J.M., Palmer, M.D., Ringer, M.A., Katsman, C.A., & Slangen, A.B.A. (2021). Projecting Global Mean Sea-Level Change Using CMIP6 Models, *Geophysical Research Letters*, 48, e2020GL092064. [10.1029/2020GL092064](https://doi.org/10.1029/2020GL092064)
8. Romero-Calvo, A., Herrada, A.H., **Hermans, T.H.J.**, Parrilla Benítez, L., Cano-Gómez, G., & Castro-Hernández, E. (2021). Axisymmetric Ferrofluid Oscillations in a Cylindrical Tank in Microgravity, *Microgravity Science and Technology*, 33, 50. [10.1007/s12217-021-09894-4](https://doi.org/10.1007/s12217-021-09894-4)
9. **Hermans, T.H.J.**, Katsman, C.A., Camargo, C.M.L., Garner, G.G., Kopp, R.E., & Slangen, A.B.A. (2022). The Effect Of Wind Stress On Seasonal Sea-Level Change On the Northwestern European Shelf, *Journal of Climate*, 1-31. [10.1175/JCLI-D-21-0636.1](https://doi.org/10.1175/JCLI-D-21-0636.1)
10. Camargo, C.M.L., Riva, R.E.M., **Hermans, T.H.J.**, & Slangen, A.B.A. (under review). Trends and Uncertainties of Regional Barystatic Sea-Level Change in the Satellite Altimetry Era, *Earth System Dynamics*. [10.5194/esd-2021-80](https://doi.org/10.5194/esd-2021-80)